Télédétection de couverts végétaux par interférométrie SAR polarimétrique multi-bases : modélisation et estimation de paramètres physiques.

Maxim Neumann

N° d'ordre : 3866

Thèse

présentée devant
l'UNIVERSITÉ DE RENNES I
pour obtenir le grade de

Docteur de l'Université de Rennes I

Mention : *Traitement du Signal et Télécommunications*

par
Maxim Neumann

Équipe d'accueil : Institut d'électronique et de télécommunications de Rennes
École doctorale : Matisse
Composante universitaire : UFR Structure et Propriétés de la Matière

Remote sensing of vegetation using multi-baseline polarimetric SAR interferometry: theoretical modeling and physical parameter retrieval

Soutenue le 14 janvier 2009 devant la commission d'examen

Composition du jury

Président du jury	
Olaf Hellwich	Technische Universität Berlin, Germany
Rapporteurs	
Fabio Rocca	Politecnico Milano, Italy
Shane Cloude	University of York, UK
Examinateurs	
Eric Pottier	Université de Rennes 1, France
Andreas Reigber	German Aerospace Center (DLR), Germany
Membres invités	
Robert Treuhaft	Jet Propulsion Laboratory (JPL), CALTEC, USA
Elise Colin	French Aerospace Lab (ONERA), France
Directeur de thèse	
Laurent Ferro–Famil	Université de Rennes 1, France

To Olga and Mark.

Acknowledgments

This thesis represents the work carried out in the Computer Vision and Remote Sensing Group at the Berlin University of Technology, Germany, and in the SAPHIR Team at the University of Rennes 1, France.

I had the privilege and the pleasure to have two supervisors, Dr. Andreas Reigber and Dr. Laurent Ferro-Famil. While in Berlin, Andreas supervised my initial steps in the field of SAR remote sensing, whereas Laurent took over the second part, becoming my "directeur de thèse" and helping me to finish the thesis. I sincerely thank for the confidence they showed in me, their support, and the company both in professional and in private matters.

I would like to thank the group leaders in Berlin and Rennes, Prof. Olaf Hellwich and Prof. Eric Pottier, respectively, for their interest in my work and for their support. It was thanks to Olaf, whom I initially asked for a Ph.D. position, that I got in contact with Dr. Andreas Reigber and started this work. I value a lot the cordiality of Eric, and his ability to explain complex things in an amazingly easy way.

I am thankful to the members of my thesis defense committee: The external reviewers, Prof. Fabio Rocca and Dr. Shane R. Cloude, for reading thoroughly my thesis manuscript and providing perceptive comments, and the invited members of the defense committee, Dr. Robert N. Treuhaft and Dr. Elise Colin, for their encouraging remarks and suggestions for clarifying my manuscript.

Special thanks are due to Marc Jäger, my first office–mate in Berlin, for being an example of a competent and critical researcher, who made a profound impact on my way of thinking about science in general.

I thank Dr. Carlos López Martinez for welcoming me during my stay at the Politecnical University of Catalonia in Barcelona, Spain. I also had a chance to visit the Chinese Academy of Forestry and the Chinese Academy of Science in Beijing, China, and I would like to thank Dr. Erxue Chen, Dr. Wen Hong, Dr. Fang Cao, Yong–sheng Zhou, Yang Li, and Lu Bai for their hospitality.

I would like to express my gratitude to the lab members both in Berlin and in Rennes, for the friendly atmosphere and the activities together: Adam S., Alexander V. (thanks for providing me with opportunities to practice my French), Anke B., Artem B. (*now* there should be some time for chess), Cécile L., Cédric L., Esra E. (see you in Istanbul at some time), Frank F. (impressive – doing a Ph.D. with 2 children! thanks also for all the expertise about cars), Frédéric B., Hongwei Z., Joëlle D. (thanks for your help and for never giving up teaching me French – Ça va aller !), Laurent L.C., Marc J. (thanks for the many fruitful conversations, both professional and personal; and the adventurous

endeavors together), Marco L. (thanks for the outgoing character), Marion D. (thanks for all the help with logistics and administration), Mathias H., Mauro E., Maxim Zh. (thanks for the help and many useful advises), Nicolas L. – Nico (Yep, man! – Konnichiwa!), Noelle L.B., Olivier D'H., Olivier H., Paul L. (thanks for the eco–education and all the storage room), Sandra R., Sandrine D. – Sandrinou (merci, Miss Comité Des Fêtes, pour tous les plaisanteries :) et la culture bretonne – yec'hed mat !), Sang-Eun P. (Ahn-young!), Shaharyar A.K. (thanks for our long discussions and the Pakistani specialties, especially the "green things" ;), Sophie A., Stefan S. (danke für die Hilfsbereitschaft), Stéphane G. (thanks for my first French lessons), Stéphane M. – Stef (Degemer mat !), Stéphane M. – Stéfou (ça roule – ça marche !), Thomas R., Tim S., Volker R. (thanks for computer matters), Wenju H., Xinwu L., and Yue H. (thanks for the always present good mood).

There are still a lot of people whom I met at conferences, and with whom I had interesting discussions and good times. I would like to thank them, especially all the Ph.D. students since we shared similar goals and faced similar difficulties.

I would like to express my profound gratitude to my parents, Valeri and Olga Neumann, and my two brothers, Eugen and Arthur, for their continuous support and encouragement.

Finally, I thank my wife, Olga, for her understanding and support, and our son, Mark, for being an unlimited source of inspiration and joy.

Поезда в этих краях все так же шли с запада на восток
и с востока на запад...

— Чингиз Айтматов, “И дольше века длится день”

Contents

Chapter 1

Introduction

The monitoring of the vegetation cover on a large scale is an important issue which is attracting a lot of research currently. Forest characteristics such as its biomass and species composition are of a vital importance in forestry and environmental science. Special attention to forest remote sensing has been generated by the explicit notice in the Kyoto protocol of the impact of forest activity on the global carbon cycle and the climate change, and of the need for monitoring of forests. The goal is to develop remote sensing techniques to provide accurate, reliable and complete information about forest parameters on a global scale with high temporal and spatial resolutions. Microwave remote sensing provides efficient means to accomplish this task, especially by combining polarimetric and interferometric techniques.

Microwave radar remote sensing is a tested technology which can be operated independently of weather conditions and time of the day. Active imaging radars transmit electromagnetic wave radiations from an antenna and receive the backscattered signal. Coherent sampling and processing of the returned signal permits to improve the azimuth resolution of a moving radar by constructing a synthetic aperture. A radar built on this principle is called synthetic aperture radar, or simply SAR. SAR interferometry (InSAR) is a technology, which uses the effect of wave interference between two SAR images. This permits to obtain additional information about the height dimension of the imaged scene. SAR polarimetry (PolSAR) is the extension of single–channel SAR technology to acquire the full polarimetric information about the scattering properties of the medium.

With respect to vegetation, polarimetry is sensitive to the morphology and the dielectric constant of plants. The dielectric constant is directly related to the water content and with it the consistency of the plants. Also, polarimetry permits to discriminate contributions, like for instance the ground and the vegetated parts of a forest. Interferometry can provide quantitative information about the layered structure of the vegetation, like the depth and the density. Polarimetric SAR interferometry (PolInSAR) has been envisaged, 10 years ago, to combine polarimetry and interferometry for enhanced parameter estimation. Since then, various applications using polarimetric SAR interferometry have been developed; for vegetation, snow, ice and urban area parameter estimation. For further information, brief and detailed overviews of polarimetric and interferometric technology and techniques can be found e.g. in [105, 6, 158, 10, 128, 50].

Two singular and most important articles for the developments in this thesis are the works on the foundations of PolInSAR in the form of "polarimetric vector interferometry" by

Shane R. Cloude and Kostas P. Papathanassiou in 1998 [22], and on vegetation properties as seen by polarimetric radar interferometry by Robert N. Treuhaft and Paul Siqueira in 2000 [154]. Also, to emphasize is the article by Treuhaft *et al.* in 1996 [153] providing great insight into the vegetation scattering problem for radar interferometry, and the PhD thesis of Papathanassiou in 1999 [105] delivering a coherent and valuable approach to the principles of PolInSAR. But of course many more works from these and other authors have been crucial in the development of the field under study, as for instance by Lang [69], Hagberg *et al.* [54], Askne *et al.* [5], Freeman and Durden [46], and Colin *et al.* [29], to name a few.
The scope of this thesis is to improve the understanding of polarimetric SAR interferometry observables and their utilization for vegetation parameter estimation. For this purpose, the thematic range of this thesis varies between mathematical formulations and derivations, physical reasoning, and experimental validation:

These different approaches are essential for the progress in the polarimetric SAR interferometry research field, with the physical reasoning component being the core theme in the center of the presented thesis.
In the first part of the thesis, the theory of polarimetric SAR interferometry is reexamined and questions are addressed in form of

- Which assumptions on polarimetry and interferometry in dependence of media characteristics can be applied to PolInSAR data? How does it affect PolInSAR observables?
- What is the mathematical background of PolInSAR coherence sets, and what physical meaning does it contain?
- What is the difference between different coherence optimization methods? Would the use of multi–baseline coherence optimization methods improve estimation performance? What could it be used for?

The deliveries of this theoretical PolInSAR analysis are:

- Interpretation of polarimetric stationarity (PS) and interferometrically polarimetric stationarity (IPS) conditions.
- Presentation of the properties of coherence sets, based on the mathematical numerical range theory and previous contributions by M. Tabb, T. Flynn *et al.* [143, 42] and E. Colin *et al.* [29]: coherence set interrelations with numerical ranges for different definitions, coherence set shape structures classification, statistical coherence set analysis.
- Development of multi–baseline coherence optimization methods. Evaluation of these methods on experimental multi–baseline multi–temporal PolInSAR data. These multi–baseline coherence optimization methods enable us for the first time to use coherence optimization techniques for polarimetric differential SAR interferometry applications, as well as for multi–temporal and multi–baseline change monitoring with PolInSAR data.

The second part of this thesis deals with forward and inverse modeling of vegetation. The state–of–the–art in vegetation parameter inversion for PolInSAR data uses the interferometric coherence dependence on polarization to estimate the linear ground–to–volume ratio relationship, which makes the inversion of the forest height and the ground topography phase possible. Two parameter inversion approaches based on this principle have been developed at the same time: by Treuhaft and Siqueira [154], in 2000, and by Papathanassiou and Cloude [106], in 2001. The scattering–model based approach by Treuhaft and Siqueira considers simple ground response components and coherence derivations for random and oriented volumes. The focus of this approach is on the estimation of structural parameters, and polarimetry has not been fully exploited, as [citation] "simply adding polarimetry adds too many new nonstructural parameters to improve estimation of structural parameters," [154], p. 155. The successional model presented by Papathanassiou and Cloude [106, 23] is simpler and consists only of 3 structural parameters (topography phase, forest height and extinction) and one additional degree of freedom in dependence of polarimetry, avoiding explicitly the estimation of the ground response.
This is in contrast to the modeling and parameter estimation approach presented in this work, where we seek to extend the limits of physical parameter inversion and especially concentrate on the information contained in polarization properties. The questions to be addressed are

- Can we improve in general the parameter estimation process performance by introducing more polarimetry?
- How to build an invertible scattering model that represents reliably the vegetation structure?
- Are multi–baseline PolInSAR acquisitions mandatory or are single–baseline data sufficient for accurate results?
- Can we cope with temporal decorrelation?
- Can scattering model based inversion schemes improve the estimation of structural parameters?
- Are we able to estimate more parameters, e.g. with respect to the vegetation type, or the underlying surface?

The contribution of this thesis consists in developing a simple invertible model for the vegetation layer, taking into account average particle characteristics and the distribution of particle orientations in the polarization plane. This model enables us to improve the estimation of forest height and ground topography, as well as to invert additional parameters related to particle anisotropy, the degree of orientation randomness, the main orientation of the particles, the attenuation coefficient of the canopy, and the ground scattering properties. The developed parameter inversion approach is validated on simulated and real air–borne SAR data with comparison to ground–truth measurements. In particular, it is reasoned that in some areas the obtained experimental results are better than the available ground–truth measurements in terms of spatial variability.
The presented PolInSAR vegetation model is initially developed for single–pass acquisitions. However, only repeat–pass multi–baseline and multi–temporal real SAR data is

available to us up to now. Therefore, the model needed to be adapted to repeat–pass acquisitions, and especially to deal with the temporal decorrelation of the data, which is the major noise source, caused on the given short temporal scale mostly by wind. In this thesis, a general parameter inversion framework is developed which is tolerant to temporal decorrelation and which permits to estimate the degree of temporal decorrelation in any particular baseline.
Today, there are two common acquisition modes for single–pass across–track SAR interferometry: the single–transmit and the alternate–transmit modes. They have been already previously combined to acquire single–polarization interferometric dual–baseline data [154]. In the theoretical study of interferometric coherence constituents in this thesis, the potential of a combined hybrid PolInSAR mode has been recognized for an improved separation of surface and double–bounce induced contributions. Up to now, no data is available which has been acquired in the given mode, which leaves these studies on a theoretical level.
The organization of the thesis is as follows:

- Chapter 2 outlines the basic theory of electromagnetic wave propagation and scattering, and describes the polarization of a wave. For the modeling of vegetation, the propagation and scattering in random volumetric media are presented for the distorted Born approximation. Finally, basic concepts of polarimetry are presented.

- Chapter 3 briefly introduces the functionality of SAR imaging. Data acquisition and processing methods are outlined in order to derive the system model function. SAR polarimetry and SAR interferometry are independently presented.

- Chapter 4 presents our own studies on fundamental PolInSAR data properties, its generic information content and restrictions. The aim is to present common PolInSAR properties, independently of the scattering medium under consideration. At the beginning of this chapter, PolInSAR data representations are presented as introduced by Cloude and Papathanassiou [22, 105], together with the whitened form and the coherency contraction [22, 105, 84], as well as the concept of polarimetric stationarity in SAR interferometry, recently formulated by Ferro–Famil and Neumann [39]. The concept of the PolInSAR coherence set, which relies on the works of Tabb and Flynn [142, 143, 42] and Colin [29], is extended by us to retrieve information on coherence set geometry, density, and distribution. The last topic of this chapter deals with PolInSAR coherence optimization. We re-examine the coherence optimization problem in order to improve the interpretation of the optimal coherences and optimal scattering mechanisms. Also, we introduce methods which extend single–baseline coherence optimization to the multiple baseline case. These optimization methods are evaluated on real SAR data consisting of 4 images.

- Chapter 5 presents a new polarimetric interferometric model for agricultural and forestry vegetation. This model has a low complexity in order to be invertible, but contains important parameters to characterize vegetation structures which are perceptible by radar polarimetry and interferometry: vegetation particles characteristics and orientation distribution, ground characteristics, and the vertical structure of the vegetation. At first, a polarimetric model for first–order scattering components is presented. We explicitly consider the modeled parameters under both

Born and distorted Born approximations. Complementarily, an interferometric coherence model for the same components is presented, enabling the construction of a PolInSAR model. Both single–transmit and alternate–transmit interferometric acquisition modes are analyzed. Based on the synergy of polarimetry and interferometry, it is recognized that a hybrid single–pass PolInSAR mode (alternate–transmit simultaneous–receive) will improve the distinction of surface scattering and the double–bounce scattering based on the interferometric coherence.

- Chapter 6 discusses at first the scattering inverse problem for vegetation parameter estimation. The developed model is used to estimate physical parameters based on the observed data. Four acquisition mode scenarios and two vegetation type scenarios are determined for further evaluation. Experimental results are presented for three data sources: synthetic simulations based on the presented forward model, structural simulations of forest stands by the PolSARPro simulator, and real SAR data at L–band. As the results indicate, most vegetation parameters can be reliably retrieved from the data.

- Chapter 7 concludes this thesis.

Chapter 2

Electromagnetic Scattering Basics

Every point in space at any time is pervaded by an electromagnetic field which is characterized by the strengths and the directions of the electric and magnetic forces for any frequency and polarization. Various frequency bands have been successfully used for remote sensing applications. Microwave frequencies provide the possibility of active remote sensing almost independently of the time of the day and the weather conditions, since microwaves are hardly influenced by cloud cover, rainfall or the sunlight level [147, 159, 157]. This chapter presents basic concepts and definitions of electromagnetic wave propagation and scattering as well as polarimetry with reference to active microwave remote sensing of geophysical media.

2.1 Electromagnetic Waves

The concept of electromagnetic wave propagation is derived from Maxwell's equations. These differential equations describe how variations of magnetic fields produce electric fields (Faraday's law of induction), how currents and changing electric fields produce magnetic fields (the Ampere-Maxwell law), how electric charges produce electric fields (Gauss' law), and the experimental absence of magnetic monopoles (Gauss' law for magnetism)[(1)]:

$$\text{Faraday's law of induction:} \quad \nabla \times \mathbf{E}_{(\boldsymbol{r},t)} = -\frac{\partial \mathbf{B}_{(\boldsymbol{r},t)}}{\partial t} \tag{2.1}$$

$$\text{Ampere's law:} \quad \nabla \times \mathbf{H}_{(\boldsymbol{r},t)} = \mathbf{J}_{(\boldsymbol{r},t)} + \frac{\partial \mathbf{D}_{(\boldsymbol{r},t)}}{\partial t} \tag{2.2}$$

$$\text{Gauss's law:} \quad \nabla \cdot \mathbf{D}_{(\boldsymbol{r},t)} = \rho_{(\boldsymbol{r},t)} \tag{2.3}$$

$$\text{Gauss's law for magnetism:} \quad \nabla \cdot \mathbf{B}_{(\boldsymbol{r},t)} = 0 \tag{2.4}$$

where $\mathbf{E}$ is the electric field vector in Volt/meter $[\frac{V}{m}]$, $\mathbf{H}$ the magnetic field vector in Ampere/meter $[\frac{A}{m}]$, $\mathbf{D}$ the electric displacement vector in Coulomb/meter^2 $[\frac{C}{m^2}]$, $\mathbf{B}$ the magnetic flux density vector in Tesla $[T = \frac{V \cdot s}{m^2}]$, $\mathbf{J}$ the current density vector in Ampere/meter^2 $[\frac{A}{m^2}]$, and ρ the volume charge density in Coulomb/meter^3 $[\frac{C}{m^3}]$. All these quantities are functions of space and time $(\boldsymbol{r}, t)$.

[(1)] Throughout the thesis, bold lowercase and capital letters represent vectors and matrices, respectively. Only a few exceptions are made because of common conventions: electromagnetic vectors $(\mathbf{E}, \mathbf{H}, \mathbf{B}, \mathbf{D}, \mathbf{J})$ are represented by bold capital letters, as is the Jones vector $\mathbf{E}$. The meaning depends on the context.

In addition to Maxwell's equations, the continuity equation represents the conservation of charge and the Lorentz force law represents the force on a charge q moving with a velocity vector v through an electromagnetic field:

$$\text{Continuity equation:} \quad \nabla \cdot \mathbf{J}_{(\boldsymbol{r},t)} = -\frac{\partial \rho_{(\boldsymbol{r},t)}}{\partial t} \tag{2.5}$$

$$\text{Lorentz force:} \quad \mathbf{F}_{(\boldsymbol{r},t)} = q_{(\boldsymbol{r},t)}[\mathbf{E}_{(\boldsymbol{r},t)} + \boldsymbol{v}_{(\boldsymbol{r},t)} \times \mathbf{B}_{(\boldsymbol{r},t)}] \tag{2.6}$$

In a *linear passive* medium, the field vectors are linearly related, as expressed in the following *constitutive relations*:

$$\mathbf{D}_{(\boldsymbol{r},t)} = \boldsymbol{\epsilon}'_{(\boldsymbol{r})}\mathbf{E}_{(\boldsymbol{r},t)}, \quad \mathbf{B}_{(\boldsymbol{r},t)} = \boldsymbol{\mu}_{(\boldsymbol{r})}\mathbf{H}_{(\boldsymbol{r},t)}, \quad \mathbf{J}_{(\boldsymbol{r},t)} = \boldsymbol{\sigma}_{(\boldsymbol{r})}\mathbf{E}_{(\boldsymbol{r},t)} + \mathbf{J}_{s(\boldsymbol{r},t)} \tag{2.7}$$

where $\boldsymbol{\epsilon}'$, $\boldsymbol{\mu}$ and $\boldsymbol{\sigma}$ are the electric *permittivity* (*dielectric constant*), magnetic *permeability* and *conductivity* tensors (which represent the time invariant characteristics of a material), and $\mathbf{J}_s$ is the *current density* of an externally applied electric source.
Often, permittivity and permeability are separated into scalar free space terms ϵ_0, μ_0 and dimensionless relative permittivity $\boldsymbol{\epsilon}'_r$ and permeability $\boldsymbol{\mu}_r$, as:

$$\boldsymbol{\epsilon}'_{(\boldsymbol{r})} = \epsilon_0\boldsymbol{\epsilon}'_{r(\boldsymbol{r})}, \quad \boldsymbol{\mu}_{(\boldsymbol{r})} = \mu_0\boldsymbol{\mu}_{r(\boldsymbol{r})} \tag{2.8}$$

with $\epsilon_0 = 8.854 \times 10^{-12}$ Farad/meter and $\mu_0 = 4\pi \times 10^{-7}$ Henry/meter.
The medium is said to be *homogeneous* if $\boldsymbol{\epsilon}', \boldsymbol{\mu}, \boldsymbol{\sigma}$ are constant ($\boldsymbol{\epsilon}'_{(\boldsymbol{r})} = \boldsymbol{\epsilon}'$, $\boldsymbol{\mu}_{(\boldsymbol{r})} = \boldsymbol{\mu}$, $\boldsymbol{\sigma}_{(\boldsymbol{r})} = \boldsymbol{\sigma}$). In an *isotropic* medium $\boldsymbol{\epsilon}', \boldsymbol{\mu}, \boldsymbol{\sigma}$ are independent of the field directions and they become scalars ϵ', μ, σ. The medium is called *dispersive* if these parameters depend on frequency. In the following, only linear isotropic electric materials for which $\mu_r = 1$ will be considered. Anisotropic effects will be taken into account later on and appropriate expressions using the permittivity tensor will be introduced.
Based on Maxwell's equations and the constitutive relations for linear materials one can derive the *inhomogeneous scalar wave equation* (*inhomogeneous Helmholtz equation*) which is caused by localized time–varying charge sources and rules the propagation of electromagnetic waves:

$$\nabla^2\mathbf{E}_{(\boldsymbol{r},t)} - \epsilon'\mu\frac{\partial^2}{\partial t^2}\mathbf{E}_{(\boldsymbol{r},t)} = \mu\frac{\partial}{\partial t}\mathbf{J}_{(\boldsymbol{r},t)} \tag{2.9}$$

In source–free medium ($\mathbf{J} = 0$) one obtains the *homogeneous wave equation* (*Helmholtz equation*) [105, 159]:

$$\nabla^2\mathbf{E}_{(\boldsymbol{r},t)} - \epsilon'\mu\frac{\partial^2}{\partial t^2}\mathbf{E}_{(\boldsymbol{r},t)} = 0 \tag{2.10}$$

Any wave can be expressed as a superposition of single–frequency waves through the Fourier transform. It is convenient to analyze a single–frequency wave, also called a *time–harmonic* or *monochromatic wave* with a *sinusoidal time dependence* $e^{\pm i\omega t}$, where ω is the angular frequency of the harmonic. The electric field is then given by

$$\mathbf{E}(\boldsymbol{r}, t) = \mathrm{Re}[\mathbf{E}(r)e^{i\omega t}] \tag{2.11}$$

where $\mathbf{E}(\boldsymbol{r})$ is the time independent *complex field amplitude*, also called *phasor*.

After differentiating over the time, the inhomogeneous wave equation can thus be reformulated into

$$\nabla^2\mathbf{E}(\boldsymbol{r}) + \omega^2(\epsilon' - i\frac{\sigma}{\omega})\mu\mathbf{E}(\boldsymbol{r}) = 0 \tag{2.12}$$

Introducing the complex dielectric constant

$$\epsilon = \epsilon' - i\frac{\sigma}{\omega} = \epsilon' - i\epsilon'' \tag{2.13}$$

one can express the inhomogeneous wave equation as

$$\nabla^2\mathbf{E}(\boldsymbol{r}) + k^2\mathbf{E}(\boldsymbol{r}) = 0 \quad \text{with } k = \omega\sqrt{\epsilon\mu} \tag{2.14}$$

where k is the wavenumber of the wave in the medium.
One particular solution of the wave equation leads to plane wave formulation

$$\mathbf{E}(\boldsymbol{r}) = \mathbf{E}_0 e^{i\boldsymbol{k}\cdot\boldsymbol{r}} \tag{2.15}$$

where $\mathbf{E}_0$ is a constant wave amplitude vector and $\boldsymbol{k} = k\hat{\boldsymbol{k}}$ is the wave vector. This relation represents the propagation of the wavefront in the direction of propagation $\hat{\boldsymbol{k}}$.
In free space, the wavenumber and the wavelength are given by

$$k_0 = \frac{2\pi}{\lambda} = \omega\sqrt{\epsilon_0\mu_0} = \frac{\omega}{c} = \frac{2\pi f}{c} \tag{2.16}$$

where c is the absolute speed of light, λ the wavelength, and f the frequency. The index $_0$ indicates in this case free–space propagation. In general,

$$k = k_0 n \tag{2.17}$$

where n is the complex index of refraction, which for electric materials ($\mu_r = 1$) is given by

$$n = n' - in'' = \frac{k}{k_0} = \sqrt{\frac{\epsilon}{\epsilon_0}} \tag{2.18}$$

The wavenumber k is sometimes also called the *propagation constant*. For complex dielectric constants the propagation constant is complex, too:

$$k = k' + ik'' = k_0 n' - ik_0 n'' \tag{2.19}$$

The real part of the complex propagation constant $k' = k_0 n' = \frac{\omega}{v}$ is known as the *phase constant* which determines the *phase velocity* v. The imaginary part $k'' = -k_0 n''$ is known as the *attenuation* or the *extinction coefficient* [63]. The reciprocal of the attenuation constant represents the *penetration depth* ($\frac{1}{k''}$) of the wave into the medium. This distance is also called *skin depth* because the wave magnitude is reduced by a factor of e^{-1}.
The propagation constant can also be decomposed into the sum of the free–space wavenumber and the *correction propagation constant* κ:

$$k = k_0 + \kappa \tag{2.20}$$

For active remote sensing applications it will prove useful to characterize the medium by the *two–way extinction* $\sigma_x = 2k'' = -2k_0 n''$ and the *refractivity* $\chi_x = n' - 1$ [153] so that

$$\kappa = k - k_0 = k_0(n-1) = k_0\chi_x + i\frac{\sigma_x}{2} \tag{2.21}$$

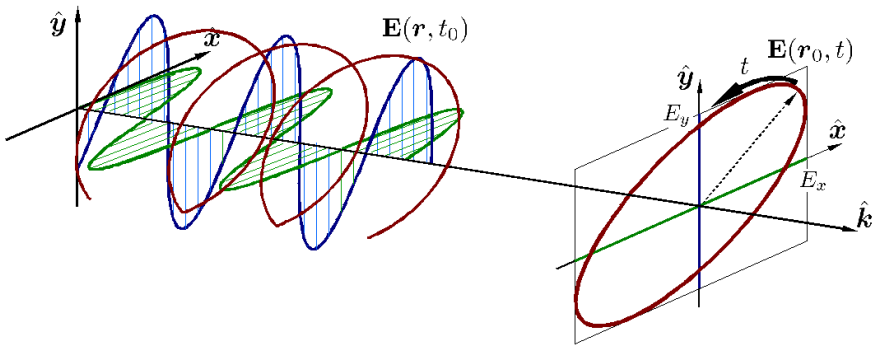

Figure 2.1: Propagation of an elliptically polarized plane wave $\mathbf{E}(\boldsymbol{r}, t)$ as a function of space $\boldsymbol{r}$ for a constant time $t = t_0$ (left), and as a function of time t for a constant position $r = r_0$ (right). The geometrical locus of the full wave (red) is given by the superposition of the linear components (green and blue).

2.2 Wave Polarization

Electromagnetic plane waves are *transverse* waves and satisfy

$$\mathbf{E}(\boldsymbol{r}, t) \cdot \hat{\boldsymbol{k}} = 0 \tag{2.22}$$

The plane containing the field oscillation is known as the *polarization plane*. The electric wave amplitude $\mathbf{E}_0$ at $\boldsymbol{r} = \mathbf{0}$ (also known as *Jones* vector) from equation (2.15) can be represented in the $(\boldsymbol{x}, \boldsymbol{y})$ orthonormal basis[(2)] of the polarization plane, cf. Fig. 2.1, [11, 111, 83] and is given by

$$\mathbf{E}_0 = \hat{\boldsymbol{x}} E_{0x} + \hat{\boldsymbol{y}} E_{0y} = \begin{bmatrix} E_{0x} \\ E_{0y} \end{bmatrix} = \begin{bmatrix} a_x e^{i\delta_x} \\ a_y e^{i\delta_y} \end{bmatrix} = a e^{i\delta_x} \begin{bmatrix} \cos\alpha \\ \sin\alpha e^{i\delta} \end{bmatrix} = E_{0x} \begin{bmatrix} 1 \\ \rho \end{bmatrix} \tag{2.23}$$

where several common wave polarization representations have been used. A completely polarized wave can be completely described by 4 real scalar parameters or degrees of freedom:

- absolute amplitude: $a = \sqrt{a_x^2 + a_y^2}$
- absolute phase: δ_x
- phase difference $\delta = \delta_y - \delta_x$
- amplitude ratio $a_d = \frac{a_y}{a_x}$, or alternatively the amplitude ratio angle $\alpha = \tan a_d$

Only the last two determine the polarization state of the wave. The angles α and δ are also known as *Deschamps parameters*. Also, a single complex number, the *complex polarization ratio* $\rho = \frac{E_{0y}}{E_{0x}} = a_d e^{i\delta}$ contains the same information.

[(2)] However, it is common to use the horizontal—vertical polarization basis and it will be the basis of choice if not otherwise stated in the following sections and chapters.

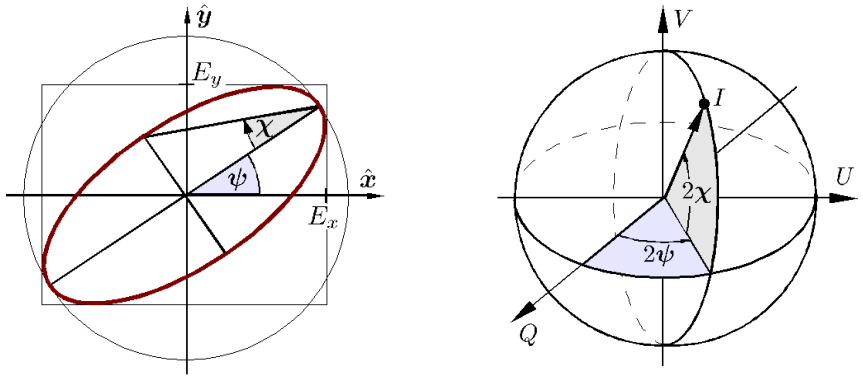

(a) Polarization ellipse (b) Poincaré shpere

Figure 2.2: Geometrical polarization representations.

The polarization state can be represented geometrically in the polarization ellipse, see Fig. 2.2(a), using the polarization orientation angle $\psi \in [-\frac{\pi}{2}, \frac{\pi}{2}]$ and the polarization ellipticity angle $\chi \in [-\frac{\pi}{4}, \frac{\pi}{4}]$ [11], where

$$\tan 2\psi = \tan(2a_d)\cos(\delta), \quad \sin 2\chi = \sin(2a_d)\sin(\delta) \tag{2.24}$$

In the general case the shape is an ellipse with ψ determining the direction of the major axis. For $\chi = 0$, the polarization ellipse degenerates to a line and represents linear polarizations, whereas for $\chi = \pm\frac{\pi}{4}$ it becomes a circle and represents circular polarizations. The sign of χ determines the *sense of rotation* in the polarization ellipse: $\chi > 0$ represents left–handed polarizations, and $\chi < 0$ represents right–handed polarizations.
An orthogonal polarization state ($\mathbf{E}_1^\dagger \mathbf{E}_2 = 0$) in terms of the polarization angles can be obtained using the substitutions

$$\psi_2 \leftarrow \psi_1 + \frac{\pi}{2}, \quad \chi_2 \leftarrow -\chi_1 \tag{2.25}$$

Also, the complex polarization ratio can be expressed using the polarization angles and vice versa:

$$\rho = \frac{\cos 2\chi \sin 2\psi + i \sin 2\chi}{1 + \cos 2\chi \cos 2\psi}, \quad \psi = \frac{1}{2}\arctan\left(\frac{2\,\mathrm{Re}\,\rho}{1-\rho\rho^*}\right), \quad \chi = \frac{1}{2}\arcsin\left(\frac{2\,\mathrm{Im}\,\rho}{1-\rho\rho^*}\right) \tag{2.26}$$

The angles 2ψ and 2χ can be interpreted as the spherical angular coordinates of the polarization state on the *Poincaré sphere*, as shown in Fig. 2.2(b). The Cartesian coordinates of the given point are at the same time a geometric representation of the completely polarized *Stokes parameters* Q, U, V:

$$\boldsymbol{g} = \begin{bmatrix} I \\ Q \\ U \\ V \end{bmatrix} = \begin{bmatrix} a^2 \\ a_x^2 - a_y^2 \\ 2a_x a_y \cos\delta \\ 2a_x a_y \sin\delta \end{bmatrix} = \begin{bmatrix} a^2 \\ a^2 \cos 2\psi \cos 2\chi \\ a^2 \sin 2\psi \cos 2\chi \\ a^2 \sin 2\chi \end{bmatrix} \tag{2.27}$$

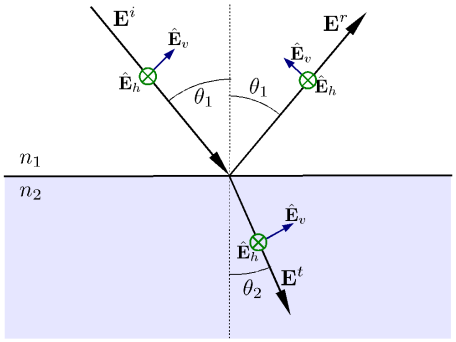

Figure 2.3: Reflection and refraction of a plane wave at a smooth dielectric interface.

2.3 Wave Propagation Phenomena

The main phenomena which might influence the propagation of microwaves are absorption, scattering, reflection, refraction, interference, and diffraction [11, 41]. The physical meaning and the effects of these phenomena are briefly discussed in this section.

2.3.1 Absorption and Scattering

As mentioned earlier, the attenuation of a wave propagating in a lossy medium is taken into account by the imaginary part in the propagation constant. Attenuation is caused by absorption and scattering by particles in inhomogeneous media.
The incident electromagnetic wave exerts forces on the atoms and electrons in the illuminated medium causing them to move. These motions can *absorb* energy. At the same time these motions are the source of new waves. The generation of these new waves is called *scattering* [41]. Absorption and scattering are important events for active microwave remote sensing and will be analyzed in more details in section 2.4.

2.3.2 Reflection and Refraction

Reflection is a special form of scattering at the boundary of two media with different dielectric properties. The curvature of the boundary needs to be large in comparison to the wavelength and the spacing of the charge particles small compared with the wavelength. In such case, the incident wave generates coherent motion in the charge particles in the second medium which generates a new wave. Under the given conditions, the direction of this new wave is specular to the incidence wave direction. This is the reflected wave.
Refraction modifies the phase velocity and causes the change of the direction of propagation. Reflection and refraction can be well explained based on the incidence of a plane wave $\mathbf{E}^i$ on a smooth boundary between two homogeneous media with different refractive indices[(3)] n_1, n_2. When an incident plane wave passes from one medium into another, it may be split into two waves: one reflected wave and one transmitted wave as presented in Fig. 2.3. According to the *law of reflection*, the reflected wave is scattered in the specular direction. *Snell's law*, which is a consequence of *Fermat's principle of least time*,

[(3)] At this point the indices of refraction are assumed to be real valued.

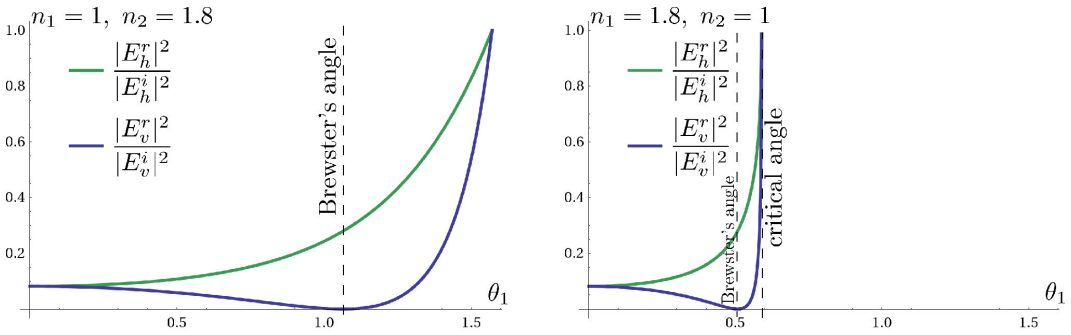

Figure 2.4: Examples of reflectivities representing Brewster's and critical angles.

determines the *angle of refraction* θ_2 for the given incidence angle θ_1:

$$\frac{n_2}{n_1} = \frac{\sin\theta_1}{\sin\theta_2} \tag{2.28}$$

The polarization dependent reflection and transmission coefficients $(R_{v/h}, T_{v/h})$ for the reflected and refracted waves are given by the *Fresnel equations*:

$$R_h = \frac{n_1\cos\theta_1 - n_2\cos\theta_2}{n_1\cos\theta_1 + n_2\cos\theta_2} \qquad R_v = \frac{n_2\cos\theta_1 - n_1\cos\theta_2}{n_2\cos\theta_1 + n_1\cos\theta_2} \tag{2.29}$$

$$T_h = \frac{2n_1\cos\theta_1}{n_1\cos\theta_1 + n_2\cos\theta_2} \qquad T_v = \frac{2n_1\cos\theta_1}{n_2\cos\theta_1 + n_1\cos\theta_2} \tag{2.30}$$

so that the reflected $\mathbf{E}^r$ and transmitted $\mathbf{E}^t$ waves can be represented by

$$\mathbf{E}^r = \begin{bmatrix} R_h & 0 \\ 0 & R_v \end{bmatrix} \mathbf{E}^i, \qquad \mathbf{E}^t = \begin{bmatrix} T_h & 0 \\ 0 & T_v \end{bmatrix} \mathbf{E}^i \tag{2.31}$$

If the first medium is free air ($n_1 = 1$) and the second medium is characterized by the complex relative permittivity ϵ_r, using Snell's law the reflection coefficients become

$$R_h = \frac{\cos\theta_1 - \sqrt{\epsilon_r - \sin^2\theta_1}}{\cos\theta_1 + \sqrt{\epsilon_r - \sin^2\theta_1}}, \qquad R_v = \frac{\epsilon_r\cos\theta_1 - \sqrt{\epsilon_r - \sin^2\theta_1}}{\epsilon_r\cos\theta_1 + \sqrt{\epsilon_r - \sin^2\theta_1}}, \tag{2.32}$$

For a certain incidence angle, known as *Brewster's angle*, the vertically polarized part of the wave can be perfectly transmitted, with no reflection. This effect appears when the sum of the incidence and the refracted angles equals 90 degrees.
If the wave passes the boundary to an optically less dense medium ($n_2 < n_1$), there exists a *critical angle*, above which all energy is reflected and nothing passes through the interface for all polarizations. Fig. 2.4 shows an example of Brewster's and critical angles.
Reflection and refraction are very important in layered dense natural media, such as snow or ice. Reflection is often the main scattering type for extended surfaces with low surface roughness. Reflection will be encountered as a constituent in the double bounce and the triple bounce scattering components between ground and vegetation.

2.3.3 Interference and Diffraction

An interference is caused by the coherent addition of two or more waves. Considering two monochromatic waves with the same angular frequency ω and different amplitudes and phases, $a_1 e^{i\phi_1}$ and $a_2 e^{i\phi_2}$, their sum is given by:

$$b = a_1 e^{i\phi_1} + a_2 e^{i\phi_2} \tag{2.33}$$

The intensity of the combined wave is

$$bb^* = a_1^2 + a_2^2 + 2a_1 a_2 \cos(\phi_2 - \phi_1) \tag{2.34}$$

The resulting intensity is the sum of the individual wave intensities plus a correction term, known as the *interference effect*. The interference term is called *constructive* if it is positive, and *destructive* if it is negative [41]. If a large number of waves interfere, one often speaks of *diffraction*.
In this work, among others, diffraction will be encountered in the form of the speckle effect, see appendix A.1.1. The wave interference is the fundamental effect which enables SAR interferometry, as discussed in section 3.4.

2.4 Scattering Process

In active remote sensing, electromagnetic waves are transmitted by an antenna and propagate through some media, get attenuated, refracted and scattered, and finally a small part of the transmitted energy propagates back to the receiving antenna. The analysis of these phenomena may reveal some of the characteristics of the illuminated media. One distinguishes at the top level between deterministic and random media (also called distributed targets). This thesis addresses wave propagation and scattering with respect to random media [62, 161, 157], which can be classified into two basic categories: random volumetric media and rough surfaces. These are problems whose random behavior is too complex and only statistical description can be given for the asymptotic electromagnetic behavior of the media. In this section, at first single particle scattering is addressed, followed by rough surface scattering and wave propagation and scattering in random volumetric media.

2.4.1 Deterministic Scattering

Let a single deterministic scatterer, located at position $\boldsymbol{r}_0$, be illuminated by an incident electromagnetic wave. The total field at any position $\boldsymbol{r}$ is the sum of the incident and scattered fields:

$$\mathbf{E}_{(\boldsymbol{r})} = \mathbf{E}^i_{(\boldsymbol{r})} + \mathbf{E}^s_{(\boldsymbol{r})} \tag{2.35}$$

If the illuminating source is located far away from the particle, the incidence field can be approximated by a plane wave

$$\mathbf{E}^i_{(\boldsymbol{r})} = \mathbf{E}^i_0 e^{i\boldsymbol{k}_i \cdot \boldsymbol{r}} \tag{2.36}$$

In the far field of the scatterer, characterized by the Fraunhoffer distance $R = |\boldsymbol{r} - \boldsymbol{r}_0| > D^2\lambda$ [62], the scattered field can be approximated by a spherical wave

$$\mathbf{E}^s_{(\boldsymbol{r})} = \frac{e^{ikR}}{R} \mathbf{F}_{(\hat{\boldsymbol{k}}_s, \hat{\boldsymbol{k}}_i)} \mathbf{E}^i_{(\boldsymbol{r}_0)} \tag{2.37}$$

where $\mathbf{F}_{(\hat{\boldsymbol{k}}_s,\hat{\boldsymbol{k}}_i)}$ is the *bistatic scattering amplitude matrix* representing the scattering behavior of the particle, $\hat{\boldsymbol{k}}_i$ stands for the direction of propagation of the incident plane wave and $\hat{\boldsymbol{k}}_s$ the considered direction of scattering. In the horizontal–vertical polarization basis, $\mathbf{F}$ is given by

$$\mathbf{F}_{(\hat{\boldsymbol{k}}_s,\hat{\boldsymbol{k}}_i)} = \begin{bmatrix} f_{hh(\hat{\boldsymbol{k}}_s,\hat{\boldsymbol{k}}_i)} & f_{hv(\hat{\boldsymbol{k}}_s,\hat{\boldsymbol{k}}_i)} \\ f_{vh(\hat{\boldsymbol{k}}_s,\hat{\boldsymbol{k}}_i)} & f_{vv(\hat{\boldsymbol{k}}_s,\hat{\boldsymbol{k}}_i)} \end{bmatrix} \tag{2.38}$$

where f_{ij} are scalar complex scattering amplitudes for different incidence and scattering polarizations [157]. It is a common convention to arrange the indices from right to left in relation to the process progression: the first index on the left denotes the considered scattering polarization channel, whereas the second index denotes the incident one.
The *bistatic scattering cross section* for a certain combination of transmit and receive polarizations $p, q \in \{h, v\}$ is given by [62]

$$\sigma^{bi}_{pq(\hat{\boldsymbol{k}}_s,\hat{\boldsymbol{k}}_i)} = 4\pi |f_{pq(\hat{\boldsymbol{k}}_s,\hat{\boldsymbol{k}}_i)}|^2 \tag{2.39}$$

The backscattering cross section (also known as *radar cross section* (RCS)) is simply

$$\sigma_{pq} = \sigma^{bi}_{pq(-\hat{\boldsymbol{k}}_i,\hat{\boldsymbol{k}}_i)} = 4\pi |f_{pq(-\hat{\boldsymbol{k}}_i,\hat{\boldsymbol{k}}_i)}|^2 \tag{2.40}$$

2.4.2 Rough Surface Scattering

The asymptotic electromagnetic properties of a rough surface can be characterized by its dielectric and roughness properties. The dielectric properties are most influenced by the moisture content. Surface roughness is described by the probability density and the autocorrelation functions of surface height with the main characteristics of surface root mean square (RMS) height s and the correlation length L_c. Since surface scattering depends on the wavelength of the incident electromagnetic wave, one multiplies s and L_c with the wavenumber to obtain the relative surface roughness descriptors: ks and kL_c. Two common correlation functions are the Gaussian and the exponential functions. The Fourier transform of the surface height correlation function represents the (positive, real valued) power spectral density function $W_{surf}(k_x, k_y)$, where k_x, k_y are the spatial wavenumbers.
Surface roughness determines how much of the wave energy is reflected in the specular direction (specular scattering), and how much is scattered in all directions (diffuse scattering) [62]. For smooth surfaces the specular "coherent" component dominates, whereas for rough surfaces the diffuse "incoherent" component gets more important. Different modeling approaches exist which are valid for certain ranges of roughness parameters. The small perturbation model (SPM) is applicable to slightly rough surfaces where the RMS height is much smaller than the wavelength ($s \ll \lambda$). Although this condition is often not satisfied for many natural surfaces, it is often applied because of the simplicity of the solution. The Kirchhoff model is applicable to surfaces with large curvature radius ($L_c \gg \lambda$) approximating the surface by a tangent plane. To solve the Kirchhoff model, two further approximations are applied: the geometrical optics (GO) and the physical optics (PO) approximations. A more general approach is the integral equation method (IEM) which fills in between the other approaches in the validity domain, as shown in Fig. 2.5. An alternative to the theoretical models are empirical models which were derived based on data analysis (e.g. [103, 33]).

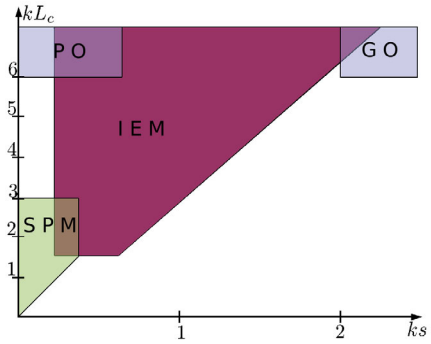

Figure 2.5: Approximate validity domains of common surface scattering models.

SPM Solution at Order 1

Small perturbation solution at first–order is also called Bragg scattering because of the similarity of phase effects in the solution to Bragg diffraction of x–rays from a crystal lattice [62]. The solution for an incidence angle θ_1 and the soil permittivity ϵ_r is given in terms of the backscattering coefficients and covariances by [62, 160]

$$\begin{aligned} \sigma_{pq} &= 4\pi k^4 \cos^4\theta_1 |\alpha_{pq}|^2 W_{surf}(k_x, k_y) \\ \sigma_{pqrs} &= 4\pi k^4 \cos^4\theta_1 (\alpha_{pq}\alpha_{rs}^*) W_{surf}(k_x, k_y) \end{aligned} \tag{2.41}$$

for $p, q, r, s \in \{h, v\}$ and where[(4)]

$$\alpha_{hh} = \frac{\cos\theta_1 - \sqrt{\epsilon_r - \sin^2\theta_1}}{\cos\theta_1 + \sqrt{\epsilon_r - \sin^2\theta_1}}, \qquad \alpha_{hv} = 0 \tag{2.42}$$

$$\alpha_{vv} = \frac{(1-\epsilon_r)(\sin^2\theta_1 - \epsilon_r(1+\sin^2\theta_1))}{(\epsilon_r\cos\theta_1 + \sqrt{\epsilon_r - \sin^2\theta_1})^2}, \qquad \alpha_{vh} = 0 \tag{2.43}$$

As it can be seen, the polarimetric properties of the SPM response depend only on the permittivity of the soil and the incidence angle; the surface roughness influences only the amplitude of the total backscattered power.

2.4.3 Random Volume Media

A random volumetric medium is a collection of randomly distributed scatterers embedded in a continuous background medium. Two main problems arise when dealing with random media: the propagation through the medium and the scattering including multiple order effects.

Vegetation, the object of study in this thesis, can be considered as partly tenuous medium at the frequencies used in this thesis. Because the phase is of fundamental importance for interferometry, the medium needs to be modeled by a coherent technique. A common approach is to consider the vegetation as a sparse random medium of discrete lossy dielectric scatterers. Lang [69] employed the *Foldy–Lax* approximation (also called *effective field*

[(4)] These terms are given in the forward scattering alignment (FSA) convention, see section 2.5.1. For the backscattering alignment (BSA) convention, α_{vv} needs to be multiplied by -1.

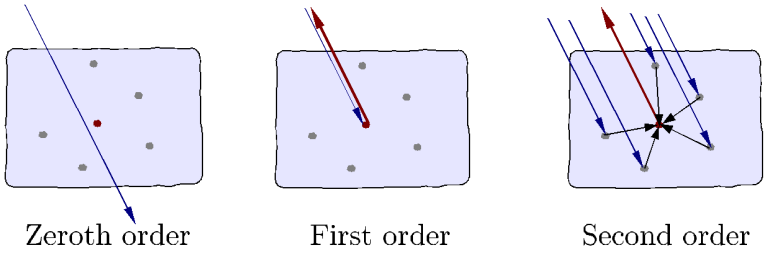

Figure 2.6: Illustration of the first three elements of the Born series for the backscattering case: zeroth order undisturbed wave propagation, first order taking into account single scattering, and second order taking into account pair–wise interactions between particles.

approximation (EFA)) [70,43] for the attenuation and the related *distorted Born* approximation for particle scattering in order to obtain backscattering coefficients for such media with random orientations and positions. In the following, the discrete scatterer approach using the Foldy–Lax and the distorted Born approximations are outlined [69,157,156,110]. The total field $\mathbf{E}_{(\boldsymbol{r})}$ at position $\boldsymbol{r}$ is the sum of the incidence field $\mathbf{E}^i$ and the scattered fields $\mathbf{E}^s_j$ from all particles j:

$$\mathbf{E}_{(\boldsymbol{r})} = \mathbf{E}^i_{(\boldsymbol{r})} + \sum_j \mathbf{E}^s_{j(\boldsymbol{r})} \tag{2.44}$$

The scattered field from a particle can be represented using the concept of the single–particle *transition operator* $\mathbf{T}$ [70, 109, 157]:

$$\mathbf{E}^s_{j(\boldsymbol{r})} = \mathbf{T}_{j(\boldsymbol{r})}\mathbf{E}^e_j \tag{2.45}$$

This transition operator is a generalization of the scattering matrix and it relates the exciting field $\mathbf{E}^e_j$ of the particle directly to the scattered field in the near or the far field of the scatterer. The exciting field is composed of the contributions originating from all the particles withing the medium, whereas $\mathbf{T}_{j(\boldsymbol{r})}$ is only a function of the particle j itself and the observation position $\boldsymbol{r}$. The exciting field of particle j is the total field at position $\boldsymbol{r}_j$ minus the scattered field of particle j:

$$\mathbf{E}^e_j = \mathbf{E}_{(\boldsymbol{r}_j)} - \mathbf{E}^s_{(\boldsymbol{r}_j)} \tag{2.46}$$

and therefore

$$\mathbf{E}^e_j = \mathbf{E}^i_{(\boldsymbol{r}_j)} + \sum_{l\neq j} \mathbf{E}^s_{l(\boldsymbol{r}_j)} = \mathbf{E}^i_{(\boldsymbol{r}_j)} + \sum_{l\neq j} \mathbf{T}_{l(\boldsymbol{r}_j)}\mathbf{E}^e_l \tag{2.47}$$

Equation (2.47) is the self–consistent *Foldy–Lax multiple scattering equation.*
The Born method, named after Max Born who applied this technique to quantum–mechanical scattering problems, consists in the iterative solution of (2.47). The zeroth order solution implies no excitation; the first order solution is given by approximating the exciting fields by the incidence fields, i.e. neglecting multiple scattering, and so on. Therefore, the initial condition and the recursive formulation for the exciting field are given by

$$\mathbf{E}^{e(0)}_j = \mathbf{0}, \qquad \mathbf{E}^{e(n+1)}_j = \mathbf{E}^i_{(\boldsymbol{r}_j)} + \sum_{l\neq j} \mathbf{T}_{l(\boldsymbol{r}_j)}\mathbf{E}^{e(n)}_l \tag{2.48}$$

The scattered field of order n is then given by

$$\mathbf{E}^{s(n)}_{(\boldsymbol{r})} = \sum_j \mathbf{T}_{j(\boldsymbol{r})} \mathbf{E}^{e(n)}_{j(\boldsymbol{r}_j)} \tag{2.49}$$

This is the *Born series* (also called the *Neumann series* [11]). Fig. 2.6 presents schematically the first three components of the series by means of a volume layer and the scattering contributions of one particle inside the volume. The truncation of the series at the first–order term is known as the *Born approximation*. It is a single–scattering approximation and is only applicable if the dielectric constant of the particles is similar to the dielectric constant of the background, so that the internal (exciting) field of the particles is similar to the external field [155].
In the *effective field approximation* (EFA), also called the Foldy or the Foldy–Lax approximation, the exciting fields for all scatterers are approximated by the average "effective" field in the random medium, thus obtaining an *effective medium*. The index of refraction of the effective isotropic medium can be related to scatterer properties via [99]

$$n = 1 + \frac{2\pi n_0}{k_0^2} \left\langle f_{(\hat{\boldsymbol{k}},\hat{\boldsymbol{k}})} \right\rangle \tag{2.50}$$

where $\left\langle f_{(\hat{\boldsymbol{k}},\hat{\boldsymbol{k}})} \right\rangle$ is the isotropic average forward scattering amplitude of a single particle and n_0 is the number of particles per unit volume. Therefore, the propagation correction constant κ from (2.21) for the effective medium can be given by

$$\kappa = M_{iso} = \frac{2\pi n_0}{k_0} \left\langle f_{(\hat{\boldsymbol{k}},\hat{\boldsymbol{k}})} \right\rangle \tag{2.51}$$

In case of possibly anisotropic average forward scattering amplitude, the propagation correction constant can be generalized to a tensor [157, 80]

$$\boldsymbol{\kappa} = \begin{bmatrix} M_{hh} & M_{hv} \\ M_{vh} & M_{vv} \end{bmatrix} = \frac{2\pi n_0}{k_0} \left\langle \mathbf{F}_{(\hat{\boldsymbol{k}},\hat{\boldsymbol{k}})} \right\rangle, \quad \text{where } M_{pq} = \frac{2\pi n_0}{k_0} \left\langle f_{pq(\hat{\boldsymbol{k}},\hat{\boldsymbol{k}})} \right\rangle,\ p,q \in \{h,v\} \tag{2.52}$$

Therefore, the effective field after a propagation of a distance s inside the medium becomes

$$\mathbf{E}_{(s)} = \begin{bmatrix} e^{is(k_0+M_{hh})} & e^{isM_{vh}} \\ e^{isM_{hv}} & e^{is(k_0+M_{vv})} \end{bmatrix} \mathbf{E}_{(s=0)} \tag{2.53}$$

Using the single–scattering Born approximation and considering the attenuation of the wave in the medium using the effective field is called the *distorted Born* approximation. The components of the Born and the distorted Born approximations for a volumetric layer over the ground are presented schematically in Fig. 2.7.
The presented approximations can only be applied to sparsely distributed scatterers. For dense media, the interactions between the particles have to be taken into account more explicitly. One possible approach is the *quasi–crystalline approximation* (QCA), which accounts for up to second–order scatterer interactions considering particle pair distribution functions [157, 136].

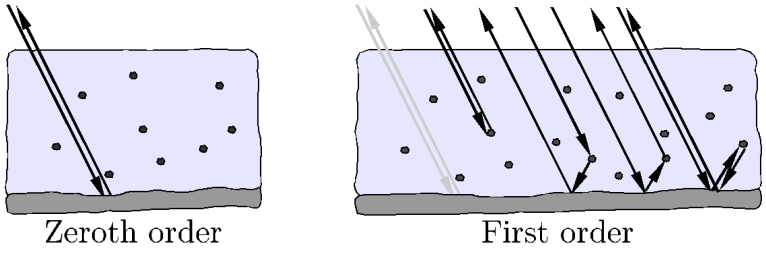

Figure 2.7: Illustration of random volume over ground approximations: zeroth order wave propagation until the ground (surface scattering), and first order scattering components (direct volume scattering, volume–ground and ground–volume double bounce scattering, and ground–volume–ground triple bounce scattering).

2.4.4 Forward Scattering Theorem

The *forward scattering theorem*, also called the *optical theorem*, states that the total power loss of a particle due to scattering and absorption, represented by σ_t, is related to the imaginary part of the forward scattering amplitude [11, 62]:

$$\sigma_t = \frac{4\pi}{k} \operatorname{Im} f_{(\hat{\boldsymbol{k}}_i, \hat{\boldsymbol{k}}_i)} \tag{2.54}$$

This theorem is related to (2.50) and it enables the computation of the total cross section. It will be used to determine the extinction of the wave inside vegetation.

2.5 Polarimetry

As shown in the previous section, scattering modifies the polarization state of the incidence wave. These effects are studied by polarimetry in order to characterize the scattering targets based on their interaction with polarized electromagnetic waves. In the following, basic definitions of polarimetry are presented.

2.5.1 Backscattering Geometry and Reciprocity

The change in polarization due to scattering by a single particle is represented by the particle's scattering amplitude matrix $\mathbf{F}$. When observing a scattering scene from distance by an instrument (see next chapter) one can also acquire the scattering matrix of the whole (focused) scene consisting of scattering contributions from different scatterers, wave propagation effects, and system acquisition and processing effects. To distinguish between the single particle scattering amplitude matrix and the observed scattering matrix, we will denote the later by $\mathbf{S}$

$$\mathbf{S} = \begin{bmatrix} S_{hh} & S_{hv} \\ S_{vh} & S_{vv} \end{bmatrix} \tag{2.55}$$

There exist two conventions for the scattering coordinate systems alignment. The *Forward Scattering Alignment* (FSA) convention is defined with respect to the wave propagation

direction (the local coordinate systems $(\hat{\boldsymbol{h}}, \hat{\boldsymbol{v}}, \hat{\boldsymbol{k}})$ point always in the direction of propagation) and is best suited for bistatic and multi–scattering problems.
Alternatively, the *Backscatter Alignment* (BSA) convention is defined with respect to the transmit and receive antennas so that the local coordinate systems always point away from the antennas. The backscattering matrices in FSA and BSA conventions are called *Jones matrix* and *Sinclair matrix*, respectively. The scattering matrix transformation between these two conventions is given by

$$\mathbf{S}_{FSA} = \begin{bmatrix} 1 & 0 \\ 0 & -1 \end{bmatrix} \mathbf{S}_{BSA} \tag{2.56}$$

For linear media we can assume *scattering reciprocity* which states that for the same propagation path the sense of wave propagation does not change the scattering contribution. Practically, for the two scattering alignment conventions it implies that

$$\text{FSA: } S_{hv} = -S_{vh} \qquad \text{BSA: } S_{hv} = S_{vh} \tag{2.57}$$

$$\Longleftrightarrow \text{FSA: } \mathbf{S}_{FSA} = \begin{bmatrix} S_{hh} & S_{hv} \\ -S_{hv} & S_{vv} \end{bmatrix} \qquad \text{BSA: } \mathbf{S}_{BSA} = \begin{bmatrix} S_{hh} & S_{hv} \\ S_{hv} & S_{vv} \end{bmatrix} \tag{2.58}$$

For convenience, from now on the BSA convention will be used for all global backscattering problems together with the matrix $\mathbf{S}$, whereas the FSA convention will be used for single particle bistatic scattering problems.

2.5.2 Polarimetric Covariance and Coherency Matrices

The scattering matrix can be vectorized using a set of complex basis matrices [16, 24]. Two common matrix sets are the lexicographic $\boldsymbol{\Psi}_L$ and the Pauli $\boldsymbol{\Psi}_P$ basis matrices:

$$\boldsymbol{\Psi}_L = \left\{ 2\begin{bmatrix} 1 & 0 \\ 0 & 0 \end{bmatrix}, 2\begin{bmatrix} 0 & 1 \\ 0 & 0 \end{bmatrix}, 2\begin{bmatrix} 0 & 0 \\ 1 & 0 \end{bmatrix}, 2\begin{bmatrix} 0 & 0 \\ 0 & 1 \end{bmatrix} \right\} \tag{2.59}$$

$$\boldsymbol{\Psi}_P = \left\{ \sqrt{2}\begin{bmatrix} 1 & 0 \\ 0 & 1 \end{bmatrix}, \sqrt{2}\begin{bmatrix} 1 & 0 \\ 0 & -1 \end{bmatrix}, \sqrt{2}\begin{bmatrix} 0 & 1 \\ 1 & 0 \end{bmatrix}, \sqrt{2}\begin{bmatrix} 0 & -i \\ i & 0 \end{bmatrix} \right\} \tag{2.60}$$

leading to definitions of the *scattering vectors* (also called *target vectors*)

$$\boldsymbol{k}_{L4} = \frac{1}{2}\,\mathrm{trace}(\mathbf{S}\boldsymbol{\Psi}_L) = \begin{bmatrix} S_{hh} \\ S_{hv} \\ S_{vh} \\ S_{vv} \end{bmatrix}, \qquad \boldsymbol{k}_{P4} = \frac{1}{2}\,\mathrm{trace}(\mathbf{S}\boldsymbol{\Psi}_P) = \frac{1}{\sqrt{2}} \begin{bmatrix} S_{hh} + S_{vv} \\ S_{hh} - S_{vv} \\ S_{hv} + S_{vh} \\ i(S_{hv} - S_{vh}) \end{bmatrix} \tag{2.61}$$

Under the criterion of reciprocity, S_{hv} and S_{vh} are equal in the BSA convention so that the basis matrices are modified to obtain three element scattering vectors:

$$\boldsymbol{k}_{L3} = \begin{bmatrix} S_{hh} \\ \sqrt{2}S_{hv} \\ S_{vv} \end{bmatrix}, \qquad \boldsymbol{k}_{P3} = \frac{1}{\sqrt{2}} \begin{bmatrix} S_{hh} + S_{vv} \\ S_{hh} - S_{vv} \\ 2S_{hv} \end{bmatrix} \tag{2.62}$$

where the weighting factors of the cross polar terms are adjusted to keep the total scattered power in all scattering matrices and scattering vectors constant. The Pauli matrix basis

is particularly useful since it represents canonical scattering mechanisms with physical significance. The first component represents an ideal odd–bounce scattering mechanism, the second represents an even–bounce mechanism, and the third component represents a tilted 45°even–bounce mechanism.
The two scattering vector representations are related by a unitary transformation

$$\boldsymbol{k}_{P3} = \mathbf{D}\boldsymbol{k}_{L3} \iff \boldsymbol{k}_{L3} = \mathbf{D}^{\dagger}\boldsymbol{k}_{P3}, \qquad \text{where } \mathbf{D} = \frac{1}{\sqrt{2}}\begin{bmatrix} 1 & 0 & 1 \\ 1 & 0 & -1 \\ 0 & \sqrt{2} & 0 \end{bmatrix} \tag{2.63}$$

As has been shown in 2.4.3, the scattering of distributed targets consists of a coherent superposition of many elemental scattering matrices. These scattering mechanisms can be best represented using second–order statistics under the form of covariance and coherency matrices. A *covariance matrix* is defined as

$$\mathbf{C}_3 = \left\langle \boldsymbol{k}_{L3}\boldsymbol{k}_{L3}^{\dagger} \right\rangle = \begin{bmatrix} \left\langle |S_{hh}|^2 \right\rangle & \sqrt{2}\left\langle S_{hh}S_{hv}^{*} \right\rangle & \left\langle S_{hh}S_{vv}^{*} \right\rangle \\ \sqrt{2}\left\langle S_{hv}S_{hh}^{*} \right\rangle & 2\left\langle |S_{hv}|^2 \right\rangle & \sqrt{2}\left\langle S_{hv}S_{vv}^{*} \right\rangle \\ \left\langle S_{vv}S_{hh}^{*} \right\rangle & \sqrt{2}\left\langle S_{vv}S_{hv}^{*} \right\rangle & \left\langle |S_{vv}|^2 \right\rangle \end{bmatrix} \tag{2.64}$$

where $\langle\rangle$ denotes the expectation operation. The covariance matrix in the Pauli basis is called the *coherency matrix* and is given by

$$\mathbf{T}_3 = \left\langle \boldsymbol{k}_{P3}\boldsymbol{k}_{P3}^{\dagger} \right\rangle \tag{2.65}$$

$$= \frac{1}{2}\begin{bmatrix} \left\langle |S_{hh}+S_{vv}|^2 \right\rangle & \left\langle (S_{hh}+S_{vv})(S_{hh}-S_{vv})^{*} \right\rangle & 2\left\langle (S_{hh}+S_{vv})S_{hv}^{*} \right\rangle \\ \left\langle (S_{hh}-S_{vv})(S_{hh}+S_{vv})^{*} \right\rangle & \left\langle |S_{hh}-S_{vv}|^2 \right\rangle & 2\left\langle (S_{hh}-S_{vv})S_{hv}^{*} \right\rangle \\ 2\left\langle S_{hv}(S_{hh}+S_{vv})^{*} \right\rangle & 2\left\langle S_{hv}(S_{hh}-S_{vv})^{*} \right\rangle & 4\left\langle |S_{hv}|^2 \right\rangle \end{bmatrix} \tag{2.66}$$

The transformations between covariance and coherency matrices are given by

$$\mathbf{T}_3 = \mathbf{D}\mathbf{C}_3\mathbf{D}^{\dagger} \iff \mathbf{C}_3 = \mathbf{D}^{\dagger}\mathbf{T}_3\mathbf{D} \tag{2.67}$$

2.5.3 Polarization Synthesis

Wave Polarization Basis Transformation

From the formalism presented in 2.2, the polarization state vector of a wave can be synthesized from the orientation and the ellipticity angles, ψ, χ, as:

$$\hat{\boldsymbol{p}}(\psi,\chi) = \begin{bmatrix} \cos\psi & -\sin\psi \\ \sin\psi & \cos\psi \end{bmatrix}\begin{bmatrix} \cos\chi \\ i\sin\chi \end{bmatrix} \tag{2.68}$$

Given the whole scattering matrix, the backscattering coefficient for certain transmit and receive polarizations $\hat{\boldsymbol{p}}_t, \hat{\boldsymbol{p}}_r$ is given as

$$S_{rt} = \hat{\boldsymbol{p}}_r^{\mathrm{T}}\mathbf{S}\hat{\boldsymbol{p}}_t. \tag{2.69}$$

One can generalize this concept to the representation of a scattering matrix in arbitrary polarization basis using the special unitary transformation matrix $\mathbf{U}_2$ [83]:

$$\mathbf{S}_{AB} = \mathbf{U}_2^{\mathrm{T}}\mathbf{S}_{HV}\mathbf{U}_2, \qquad \mathbf{U}_2 = \begin{bmatrix} \hat{\boldsymbol{p}}_A & \hat{\boldsymbol{p}}_B \end{bmatrix} = \frac{1}{\sqrt{1+|\rho|^2}}\begin{bmatrix} 1 & -\rho^{*} \\ \rho & 1 \end{bmatrix}, \text{ with } \mathbf{U}_2\mathbf{U}_2^{\dagger} = \mathbf{I} \tag{2.70}$$

where the orthogonal unitary vectors $\hat{\boldsymbol{p}}_A, \hat{\boldsymbol{p}}_B$ expressed in the H-V basis determine the new polarization basis and ρ is the corresponding complex polarization ratio.

Eigenpolarizations of the Scattering Matrix

The concept of the eigenpolarizations of a scattering matrix is of special importance. Eigenpolarizations represent polarization states that are not modified by a scatterer, i.e. incident and scattered waves have the same polarizations [157, 105]. In case of reciprocal scattering, the eigenpolarizations are given by the con–eigenvectors of the scattering matrix, and the con–eigenvalues represent the associated backscattering coefficients [83]:

$$\begin{bmatrix} \lambda_1 & 0 \\ 0 & \lambda_2 \end{bmatrix} = \begin{bmatrix} \hat{\boldsymbol{p}}_{e1} & \hat{\boldsymbol{p}}_{e2} \end{bmatrix}^{\mathrm{T}} \mathbf{S} \begin{bmatrix} \hat{\boldsymbol{p}}_{e1} & \hat{\boldsymbol{p}}_{e2} \end{bmatrix} \tag{2.71}$$

$$\mathbf{S} = \begin{bmatrix} \hat{\boldsymbol{p}}_{e1} & \hat{\boldsymbol{p}}_{e2} \end{bmatrix}^{*} \begin{bmatrix} \lambda_1 & 0 \\ 0 & \lambda_2 \end{bmatrix} \begin{bmatrix} \hat{\boldsymbol{p}}_{e1} & \hat{\boldsymbol{p}}_{e2} \end{bmatrix}^{\dagger} \tag{2.72}$$

Furthermore, an effective homogeneous medium can be described by its eigenpolarizations and the corresponding con–eigenvalues which determine the propagation effects. The eigenpolarizations and the corresponding backscattering coefficients are sensitive to some of the scatterer characteristics such as its orientation and its shape. If the scatterer has a line of symmetry, the eigenpolarizations are linear and the vector elements are real. In this case the eigenpolarizations will be given by the axes of symmetry and can be characterized by a single parameter, the orientation angle which rotates the reference polarization basis into the eigenpolarizations.

Scattering Polarization Basis Transformation

Similarly to the extraction of a single–pol scattering coefficient from a scattering matrix using two projection vectors for transmit and receive polarizations in (2.69), one can extract a backscattering coefficient from the scattering vector using a single projection vector $\boldsymbol{\omega}$ (in lexicographic or Pauli basis):

$$S_{rt} = \boldsymbol{\omega}_{L/P}^{\dagger} \boldsymbol{k}_{L/P} \tag{2.73}$$

The vector $\boldsymbol{\omega}$ can be used to represent scattering mechanisms and it is determined by the receive and transmit polarizations:

$$\boldsymbol{\omega} := \boldsymbol{\omega}(\psi_r, \chi_r, \psi_t, \chi_t) = \boldsymbol{\omega}(\hat{\boldsymbol{p}}_r, \hat{\boldsymbol{p}}_t) \tag{2.74}$$

For quad–pol projection vectors in the lexicographic matrix basis $\boldsymbol{\omega}$ is given by

$$\boldsymbol{\omega}_L = \boldsymbol{p}_r \otimes \boldsymbol{p}_t = \begin{bmatrix} p_{r_1} p_{t_1} \\ p_{r_1} p_{t_2} \\ p_{r_2} p_{t_1} \\ p_{r_2} p_{t_2} \end{bmatrix}, \quad \text{where } \boldsymbol{p}_{r/t} = \begin{bmatrix} p_1 \\ p_2 \end{bmatrix} \tag{2.75}$$

where $\boldsymbol{p}_r, \boldsymbol{p}_t$ are determined by (2.68), and $\otimes$ represents the Kronecker product.
The transformations from the H–V to an A–B polarization basis are given by [15]

$$\boldsymbol{k}_{L_{AB}3} = \mathbf{U}_{L3} \boldsymbol{k}_{L_{HV}3}, \quad \boldsymbol{k}_{P_{AB}3} = \mathbf{U}_{P3} \boldsymbol{k}_{P_{HV}3} \tag{2.76}$$

$$\mathbf{C}_{3AB} = \mathbf{U}_{L3} \mathbf{C} \mathbf{U}_{L3}^{\dagger}, \qquad \mathbf{T}_{3AB} = \mathbf{U}_{P3} \mathbf{T} \mathbf{U}_{P3}^{\dagger} \tag{2.77}$$

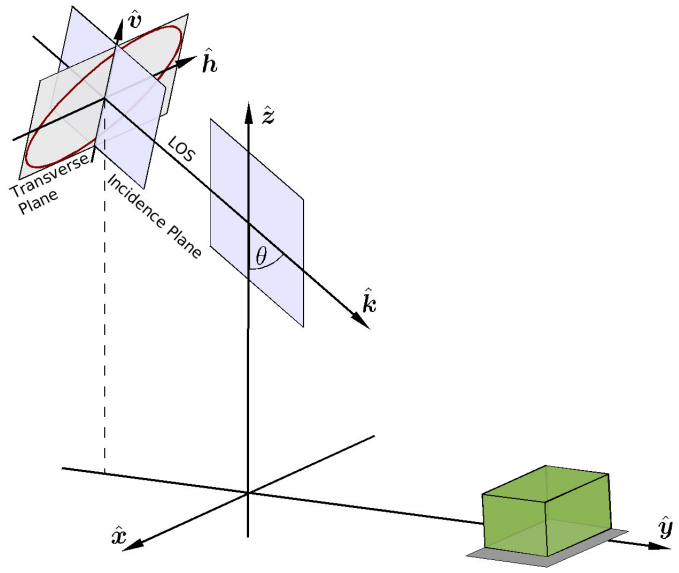

Figure 2.8: Geometry of the scene representing the polarization of the incidence electromagnetic wave and the illuminated medium.

where the unitary transformation matrix can be given in terms of the polarization ratio ρ or in terms of three orthogonal unitary projection vectors $\boldsymbol{\omega}_1, \boldsymbol{\omega}_2, \boldsymbol{\omega}_3$:

$$\mathbf{U}_{L3} = \frac{1}{1+\rho\rho^*}\begin{bmatrix} 1 & \sqrt{2}\rho & \rho^2 \\ -\sqrt{2}\rho^* & 1-\rho\rho^* & \sqrt{2}\rho \\ \rho^{*2} & -\sqrt{2}\rho^* & 1 \end{bmatrix} = \begin{bmatrix}\boldsymbol{\omega}_1 & \boldsymbol{\omega}_2 & \boldsymbol{\omega}_3\end{bmatrix}^\dagger, \ \mathbf{U}_{P3} = \mathbf{D}\mathbf{U}_{L3}\mathbf{D}^\dagger \tag{2.78}$$

For example, the circular polarization basis is characterized by polarization angles $\psi = \infty$, $\chi = \pm\frac{\pi}{2}$, and $\rho = \pm i$ and the covariance matrix is given by [74]

$$\mathbf{C}_{circ} = \left\langle \boldsymbol{k}_C \boldsymbol{k}_C^\dagger \right\rangle = \begin{bmatrix} \left\langle |S_{RR}|^2 \right\rangle & \sqrt{2}\left\langle S_{RR}S_{RL}^* \right\rangle & \left\langle S_{RR}S_{LL}^* \right\rangle \\ \sqrt{2}\left\langle S_{RL}S_{RR}^* \right\rangle & 2\left\langle |S_{RL}|^2 \right\rangle & \sqrt{2}\left\langle S_{RL}S_{LL}^* \right\rangle \\ \left\langle S_{LL}S_{RR}^* \right\rangle & \sqrt{2}\left\langle S_{LL}S_{RL}^* \right\rangle & \left\langle |S_{LL}|^2 \right\rangle \end{bmatrix} \tag{2.79}$$

where $\boldsymbol{k}_C$ is the circular scattering vector expressed in the H–V basis:

$$\boldsymbol{k}_C = \begin{bmatrix} S_{RR} \\ \sqrt{2}S_{RL} \\ S_{LL} \end{bmatrix} = \frac{1}{2}\begin{bmatrix} S_{hh} - S_{vv} + 2iS_{hv} \\ \sqrt{2}i(S_{hh} + S_{vv}) \\ S_{vv} - S_{hh} + 2iS_{hv} \end{bmatrix} \tag{2.80}$$

2.5.4 Scattering Symmetries

Considering bulk ensemble averages, many geophysical media possess symmetry properties with respect to a plane or axis. In [100], four basic symmetry groups were formulated and analyzed for remote sensing of geophysical media: the reflection, rotation, azimuthal, and centrical symmetries. But prior to discuss the symmetries and their effects one needs to define the reference geometry for the interaction of the wave with the scattering medium. Fig. 2.8 shows the geometry of the electromagnetic wave incident on a scattering medium

cell. The $(\hat{\boldsymbol{x}}, \hat{\boldsymbol{y}})$ plane defines the horizontal reference plane, containing also the horizontal wave vector $\hat{\boldsymbol{h}}$. $\hat{\boldsymbol{x}}$ is referred to as the azimuth direction, whereas $\hat{\boldsymbol{y}}$ represents the ground range direction. The plane $(\hat{\boldsymbol{v}}, \hat{\boldsymbol{k}})$ defines the *incidence plane* containing the *line of sight* (LOS) direction vector $\hat{\boldsymbol{k}}$. θ_0 is the *incidence angle* of the wave inside the incidence plane. The plane $(\hat{\boldsymbol{h}}, \hat{\boldsymbol{v}})$ is the *transverse plane* (also called the *polarization* plane) which contains the Jones vector $\mathbf{E}$.

Reflection symmetry occurs when the medium scattering exhibits mirror reflection about the incidence plane. This symmetry manifests itself in the covariance and coherency matrices by the total decorrelation of the co– and the cross–polarized components:

$$\left\langle S_{hh} {S_{hv}}^{\dagger} \right\rangle = \left\langle S_{vv} {S_{hv}}^{\dagger} \right\rangle = 0 \tag{2.81}$$

Thus, the covariance and the coherency matrices

$$\mathbf{C}_{\text{reflSym}} = a \begin{bmatrix} 1 & 0 & d+if \\ 0 & b & 0 \\ d-if & 0 & c \end{bmatrix}, \quad \mathbf{T}_{\text{reflSym}} = \alpha \begin{bmatrix} 1 & \delta+i\epsilon & 0 \\ \delta-i\epsilon & \beta & 0 \\ 0 & 0 & \gamma \end{bmatrix} \tag{2.82}$$

have 5 degrees of freedom: one for the reference intensity and four for the description of the polarization state.

Rotation symmetry occurs when the medium response is invariant under the rotation about the LOS axis $(\hat{\boldsymbol{k}})$. This implies that the rotation of the polarization orientation angle ψ in the polarization plane does not have any effect on the covariance and coherency matrices. This enforces strict constraints on the structure of the covariance and coherency matrices so that they can be parameterized using only three real valued terms [100, 24]:

$$\mathbf{C}_{\text{rotSym}} = a \begin{bmatrix} 1 & ig & 1-b \\ -ig & b & ig \\ 1-b & -ig & 1 \end{bmatrix}, \quad \mathbf{T}_{\text{rotSym}} = \alpha \begin{bmatrix} 1 & 0 & 0 \\ 0 & \beta & i\zeta \\ 0 & -i\zeta & \beta \end{bmatrix} \tag{2.83}$$

Azimuthal symmetry is the combination of both reflection and rotation symmetries. Under azimuthal symmetry the medium exhibits mirror reflection symmetry in any plane through the axis of rotation $\hat{\boldsymbol{k}}$. In this case only two degrees of freedom are needed:

$$\mathbf{C}_{\text{azSym}} = a \begin{bmatrix} 1 & 0 & 1-b \\ 0 & b & 0 \\ 1-b & 0 & 1 \end{bmatrix}, \quad \mathbf{T}_{\text{azSym}} = \alpha \begin{bmatrix} 1 & 0 & 0 \\ 0 & \beta & 0 \\ 0 & 0 & \beta \end{bmatrix} \tag{2.84}$$

Centrical symmetry is given when the medium is invariant to reflection about any plane containing the scattering cell and to rotation about any axis containing this cell. Therefore centrical symmetry can be considered as azimuthal symmetry for any incidence and azimuth angles, so that (2.84) is always valid independently of the wave incidence direction.

For example, forest canopy with completely randomly oriented particles (spherical orientation distribution) exhibits centrical symmetry. In presence of ground contribution or in case of preferred orientation effects inside the canopy, the centrical symmetry may not be verified. If the ground plane is parallel to the azimuth axis, the forest can be assumed to satisfy the reflection symmetry conditions.

Orientation Angle Estimation

Most natural media possess reflection symmetry with reference to a plane, which is not necessary the incidence plane of the electromagnetic wave. Examples include ocean waves with the wind direction vector laying not exactly in the incidence plane, or azimuth slopes of vegetated or non–vegetated terrains. If the plane of reflection symmetry can be obtained by rotating the incidence plane about the line of sight by an angle ψ, then one can transform the polarization basis of the covariance and coherency matrices into the reflection symmetric form by rotating the polarization ellipsis by the same angle.
For a single scatterer, if it has an axis of symmetry in the transverse plane, one can rotate the scattering matrix into the reflection symmetric form with a null cross–polarized scattering coefficient:

$$\mathbf{S}_{reflSym} = \begin{bmatrix} a & 0 \\ 0 & b \end{bmatrix} = \mathbf{R}^{\mathrm{T}}_{S(-\psi)} \mathbf{S}\, \mathbf{R}_{S(-\psi)}, \quad \mathbf{R}_{S(\psi)} = \begin{bmatrix} \cos\psi & -\sin\psi \\ \sin\psi & \cos\psi \end{bmatrix} \tag{2.85}$$

where $\mathbf{R}_{S(\psi)}$ is the polarization orientation rotation matrix. The rotation of the covariance and coherency matrices into the reflection symmetric form is given by

$$\mathbf{T}_{reflSym} = \mathbf{R}_{T(-2\psi)} \mathbf{T}\, \mathbf{R}^{\mathrm{T}}_{T(-2\psi)}, \quad \mathbf{R}_{T(2\psi)} = \begin{bmatrix} 1 & 0 & 0 \\ 0 & \cos 2\psi & \sin 2\psi \\ 0 & -\sin 2\psi & \cos 2\psi \end{bmatrix} \tag{2.86}$$

$$\mathbf{C}_{reflSym} = \mathbf{R}_{C(-2\psi)} \mathbf{C}\, \mathbf{R}^{\mathrm{T}}_{C(-2\psi)}, \quad \mathbf{R}_{C(2\psi)} = \mathbf{D}^{\dagger} \mathbf{R}_{T(2\psi)} \mathbf{D} \tag{2.87}$$

where $\mathbf{R}_{T(2\psi)}$ and $\mathbf{R}_{C(2\psi)}$ are rotation matrices for the polarization orientation angle of the coherency and covariance matrices and $\mathbf{D}$ is given in (2.63).
Several methods have been developed to estimate the polarization orientation angle of the scattering medium since it can be related to important geophysical parameters like the wind direction over the see or ocean, or the surface slopes which enables to reconstruct a *digital elevation model* (DEM) of the terrain. For example, the orientation angle for a sloped terrain is related to the azimuth and ground range terrain slopes $\upsilon_{az},\ \upsilon_{rg}$ via [75]

$$\tan\psi = \frac{\tan\upsilon_{az}}{-\tan\upsilon_{rg}\cos\theta_0 + \sin\theta_0} \tag{2.88}$$

There exist several approaches to estimate the main orientation angle from polarimetry: using polarization signatures [134, 163], using the phase difference between the circular polarizations [75], using the eigenvalue decomposition of the coherency matrix [24, 25], and using the Huynen decomposition [75]. Lee *et al.* [74] showed that the estimation of orientation angles from polarimetry based on circular polarizations is more robust in comparison to other approaches. Alternatively, terrain slopes can be obtained with the help of interferometry.

2.5.5 Separation of Distinctive Components by Means of Polarimetry: Target Decompositions

The objective of *target decompositions* is to express the scattering or covariance matrices as sums of contributions having distinctive physical meanings. In general, one

distinguishes between coherent and incoherent target decompositions. Coherent target decompositions are applied to the scattering matrix and are adapted to the study of deterministic responses. The most common coherent decompositions are the Pauli decomposition, the Krogager (sphere–diplane–helix) decomposition [67], the Cameron decomposition [14] and the symmetric scattering characterization method (SSCM) by Touzi and Charbonneau [149, 13]. Incoherent decompositions are adapted to the study of distributed environments and are applied to polarimetric second order representations. One may distinct model–based and analytical decomposition approaches. Model based decompositions, such as the Freeman–Durden decomposition [46, 45] or the Yamaguchi decomposition [169], decompose the covariance or coherency matrices into different scattering types, such as surface scattering, double bounce scattering, volume scattering, and helix scattering. Another approach relies on the eigendecomposition of the coherency matrix, namely the Cloude–Pottier decomposition [25,112] which enables to extract the physically meaningful parameters *entropy* (degree of polarization randomness), *alpha angle* (scattering mechanism type) and *anisotropy* (significance of secondary scattering mechanisms).

Entropy–Alpha–Anisotropy Decomposition

The Cloude and Pottier Entropy–Alpha–Anisotropy (H-α-A) decomposition [16, 15, 24, 25, 112] uses the eigendecomposition of the coherency matrix:

$$\mathbf{T}\boldsymbol{\omega}_i = \lambda_i \boldsymbol{\omega}_i \tag{2.89}$$

where $\lambda_i, \boldsymbol{\omega}_i$ ($i \in [1..3]$) are the eigenvalues and eigenvectors, respectively. The eigenvectors can be parameterized using the angles $\alpha, \beta, \gamma, \delta$, and ϕ:

$$\boldsymbol{\omega}_i = e^{i\phi_i} \begin{bmatrix} \cos\alpha_i \\ \sin\alpha_i \cos\beta_i e^{i\delta_i} \\ \sin\alpha_i \sin\beta_i e^{i\gamma_i} \end{bmatrix} \tag{2.90}$$

In dependence of the incidence angle and the dielectric properties, the $\alpha \in [0, \frac{1}{2}\pi]$ angle can be used to deduce the scattering mechanism type. Whereas $\beta \in [0, \pi]$ is related to orientations of the scatterers. $\delta, \gamma, \phi \in [-\pi, \pi]$ are the polarimetric phase difference angles. The polarization entropy is defined in the von Neumann sense by

$$H = -\sum_{i=1}^{3} p_i \log_3(p_i), \qquad p_i = \frac{\lambda_i}{\sum_{j=1}^{3} \lambda_j} \tag{2.91}$$

The mean alpha angle is the linear combination of the eigenvector alpha angles:

$$\alpha = \sum_{i=1}^{3} p_i \alpha_i \tag{2.92}$$

The anisotropy

$$A = \frac{\lambda_2 - \lambda_3}{\lambda_2 + \lambda_3} \tag{2.93}$$

is a difference measure of the second and third scattering mechanisms.

Freeman—Durden Decomposition

Assuming reflection symmetry, the Freeman–Durden model [46] attempts to decompose the covariance matrix into three components related to surface, volume, and double–bounce scattering:

$$\mathbf{C} = f_s\mathbf{C}_s + f_v\mathbf{C}_v + f_d\mathbf{C}_d \tag{2.94}$$

where the normalized covariance matrices represent the polarimetry of the different scattering types, and f_s, f_v, f_d represent the $|S_{hh}|^2$ intensities. The surface is modeled by first–order approximation of the small perturbation model from section 2.4.2

$$\mathbf{C}_s = \begin{bmatrix} 1 & 0 & \beta \\ 0 & 0 & 0 \\ \beta^* & 0 & |\beta|^2 \end{bmatrix}, \qquad \text{with } \arg(\beta) \approx 0 \tag{2.95}$$

The azimuthal symmetric volume component is represented by a collection of randomly oriented dipoles

$$\mathbf{C}_v = \begin{bmatrix} 1 & 0 & \frac{1}{3} \\ 0 & \frac{2}{3} & 0 \\ \frac{1}{3} & 0 & 1 \end{bmatrix} \tag{2.96}$$

And the double–bounce is given by

$$\mathbf{C}_d = \begin{bmatrix} 1 & 0 & \alpha \\ 0 & 0 & 0 \\ \alpha^* & 0 & |\alpha|^2 \end{bmatrix}, \qquad \text{with } \arg(\alpha) \approx \pm\pi \tag{2.97}$$

In 2007, the volume component model has been extended by Freeman [45] to consider different particle shapes inside the volume, represented by the parameter $\rho \in [\frac{1}{3}, 1]$:

$$\mathbf{C}_v = \begin{bmatrix} 1 & 0 & \rho \\ 0 & (1-\rho) & 0 \\ \rho^* & 0 & 1 \end{bmatrix} \tag{2.98}$$

Yamaguchi Decomposition

Yamaguchi *et al.* [169, 170] extended the Freeman–Durden model by allowing a certain degree of orientation inside the vegetation and introduced a helix component. The distribution of orientation angles is taken to follow a sine function and a set of covariance matrices is computed. The helicity is modeled by right and left helix covariance matrices

$$\mathbf{C}_h = \begin{bmatrix} 1 & \pm i\sqrt{2} & -1 \\ \mp i\sqrt{2} & 2 & \pm i\sqrt{2} \\ -1 & \mp i\sqrt{2} & 1 \end{bmatrix} \tag{2.99}$$

2.6 Conclusions

This chapter presented the basic theory of electromagnetic wave propagation, scattering and polarization, as well as the scattering processes in random media, and the basic concepts of polarimetry. The introduced basic notions and notations will be used throughout the whole thesis.
The next chapter will briefly introduce the functionality of synthetic aperture radar (SAR) imaging, together with the concepts of SAR Polarimetry and SAR Interferometry.

Chapter 3

Synthetic Aperture Radar Imaging

In the previous chapter, the general properties of electromagnetic wave propagation and scattering have been presented. In this chapter, instruments and techniques to acquire electromagnetic wave signals with the help of a synthetic aperture radar (SAR) are discussed. The principles of SAR raw data acquisition and processing are introduced, as well as SAR imaging modes including single–channel, polarimetric and interferometric modes.

3.1 SAR Geometry

SAR is an acronym for *Synthetic Aperture Radar*, where *Radar* is again an acronym for *RAdio Detection And Ranging*. Radar is in the meantime a common term and it refers to a device and a technique for detection and location of objects [137]. The radar emits electromagnetic signals (usually in microwave and radio frequencies) and detects the signal after its interaction with the medium. Radars are said to be *monostatic* if the transmitting and receiving antennas are the same and *bistatic* if the antennas are spatially separated. In the most basic form the radar consists of a microwave transmitter, a receiver, a circulator, and an antenna [137, 148, 158], as shown in Fig. 3.1.
The principle of the radar consists in emitting a wave and recording the received signal amplitude and possibly the phase as well as the time delay between transmission and reception. This time delay is proportional to the range distance d between the radar and

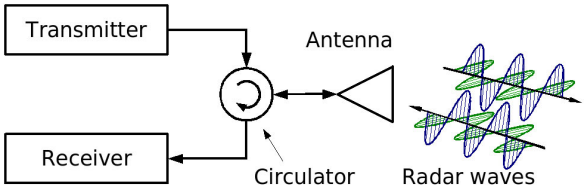

Figure 3.1: Basic monostatic radar system configuration consisting of a transmitter, receiver, circulator and an antenna.

the scattering medium:

$$\Delta t = \frac{2d}{c} \tag{3.1}$$

The received signal is a function of the scattering medium properties, the range distance, and the transmit and receive polarizations.
The technique to generate a two–dimensional image of the scattering medium is called *radar imaging*. The diversity required to build an image is provided by the movement of the radar system or the imaged object. Former radar systems, so called *real aperture radars* (RAR), were incoherent radars and did not acquire the phase information, requiring very large antennas for reasonable resolutions. The *synthetic aperture radar* (SAR) is able to use the phase information to construct a *synthetically large antenna*, which increases the resolution in the moving direction.
The acquisition geometry of an air–borne radar system is shown in Fig. 3.2. The radar is a side–looking device mounted on an air–plane. The air–plane is located at position $\boldsymbol{r}_1$ at height h and is moving along $\hat{\boldsymbol{v}}$ with a velocity $v = \|\boldsymbol{v}\|$. The radar emits short pulses of duration τ in the antenna beam direction with the *pulse repetition frequency* (PRF). When the emitted signal consists in a rectangular pulse, the slant range resolution δ_{sr} depends on the effective transmitted pulse length τ and is given by

$$\delta_{sr} = \frac{c\tau}{2} \tag{3.2}$$

To improve the resolution, one therefore needs to decrease the pulse length. However, it is technologically difficult to transmit a very short pulse with a sufficient level of energy. To overcome this limitation a long but *frequency modulated* (FM) pulse is transmitted. Usually, a linear frequency modulated pulse, known as *chirp*[(1)], is transmitted (with a bandwidth W_r) and leads to a range resolution of

$$\delta_{sr} = \frac{c}{2W_r}. \tag{3.3}$$

The ground range resolution depends on the incidence angle θ_0 and is given by

$$\delta_{gr} = \frac{\delta_{sr}}{\sin\theta_0} = \frac{c}{2W_r \sin\theta_0} \tag{3.4}$$

For an antenna width[(2)] L_x, the half–power beamwidth (3dB) in azimuth may be approximated as

$$\alpha_{az} = \frac{\lambda_0}{L_x} \tag{3.5}$$

where $\lambda_0 = \frac{c}{f_0}$ is the *carrier wavelength* and f_0 the *carrier frequency*. The spatial extent of the beam (radar footprint width) at range R in the far zone [148] can be given by

$$\delta_{az} = R\alpha_{az} = R\frac{\lambda}{L_x} \tag{3.6}$$

(1) This term comes from an audio signal or rising or falling frequency which is similar to a bird's chirp [66].
(2) The length of the antenna is called *aperture* [119].

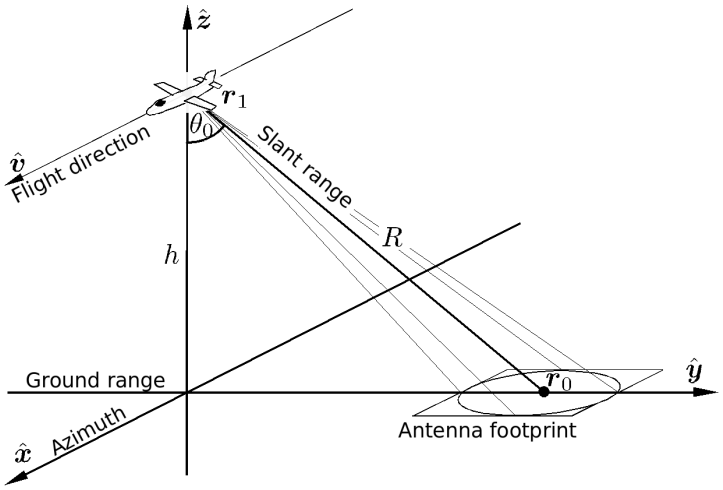

Figure 3.2: Air–Borne radar system geometry.

This is the azimuth resolution of a real aperture radar (RAR), which requires a large aperture for a fine resolution value.
In 1951, it has been noted by Carl Wiley that the motion of the sensor creates a modulation of the signal in the azimuth direction, similarly to the Doppler effect [148]. This effect can be used to generate a *synthetic aperture* L_{sa} that may be used to improve the azimuth resolution. The synthetic aperture is then determined by the length of the track over which a point of the scene is illuminated, in our case the radar footprint.

$$L_{sa} = \delta_{az} = R\frac{\lambda}{L_x} \tag{3.7}$$

The spatial resolution of the synthetic aperture considering an additional factor of 2 for the two–way path difference between synthetic aperture elements is then given by

$$\alpha_{sa} = \frac{\lambda}{2L_{sa}} = \frac{L_x}{2R}, \qquad \delta_{sa} = R\alpha_{sa} = \frac{1}{2}L_x \tag{3.8}$$

3.2 SAR Data Acquisition and Focusing

SAR Data Acquisition

Data acquisition can be described as the projection of illuminated objects from the ground into the collected raw data by a transfer function. The SAR imaging process deals with the reverse approach and aims to reconstruct the imaged area from the raw data.
The transmitted electromagnetic wave can be described by

$$\mathbf{E}_t(t) = \hat{\boldsymbol{p}}_t g_{rg}(t) e^{i\omega_0 t} \tag{3.9}$$

where $\hat{\boldsymbol{p}}_t$ represents the polarization of the transmitting antenna. The transmitted pulse starts at $t = t_0$ and continues for the pulse duration τ, so that the pulse frequency of the

chirp varies between $\omega_0 - W_r/2$ and $\omega_0 + W_r/2$. $g_{rg}(t)$ is the envelope of the transmitted signal, given by

$$g_{rg}(t') = e^{i\frac{\pi W_r}{\tau}t'^2}\Pi(\frac{t'}{\tau}) \tag{3.10}$$

In this function, t' represents the across–track time (also known as fast–time) [66], $\Pi()$ is the rectangular window function, taking into account the limited time duration of the impulse.
The received scattered wave from a single particle j coming back to the sensor position $\boldsymbol{r}_1$ is a replica of the transmitted wave modified by the backscattering amplitude matrix $\mathbf{F}_j$, decreased in magnitude (expressed by A_j) and delayed by Δt_j:

$$\mathbf{E}_{rj} = A_j \mathbf{F}_j \hat{\boldsymbol{p}}_t g_{rg}(t - \Delta t_j) e^{i\omega_0(t-\Delta t_j)} \tag{3.11}$$

The received signal is determined by the receiving antenna polarization $\hat{\boldsymbol{p}}_r$:

$$u'_{rj}(x,t) = \hat{\boldsymbol{p}}_r^{\mathrm{T}} \mathbf{E}_{rj}(x,t) \tag{3.12}$$

The time delay due to two–way range distance is given by

$$\Delta t_j = \frac{2d(\boldsymbol{r}_1, \boldsymbol{r}_j)}{c}. \tag{3.13}$$

where $d(\boldsymbol{r}_1, \boldsymbol{r}_j)$ is the distance between the sensor $\boldsymbol{r}_1$ and the scatterer $\boldsymbol{r}_j$. This distance varies with the sensor position along the azimuth axis, which is known as *range migration*. The function $d(\boldsymbol{r}_1, \boldsymbol{r}_j)$ describes a hyperbola during the acquisition, and using the first–order Taylor series expansion around $(x_1 - x_j)$ it can be approximated by a parabola:

$$d(\boldsymbol{r}_1, \boldsymbol{r}_j) = \sqrt{(x_1 - x_j)^2 + (y_1 - y_j)^2 + (z_1 - z_j)^2} \tag{3.14}$$

$$= \sqrt{(x_1 - x_j)^2 + R_j^2} \approx R_j + \frac{(x_1 - x_j)^2}{2R_j} \tag{3.15}$$

where

$$R_j = \sqrt{(y_1 - y_j)^2 + (z_1 - z_j)^2} \tag{3.16}$$

is the closest distance between the sensor and the scatterer, the so called *zero–Doppler* range.
Using the parabolic approximation, the received signal from a single scatterer can be expressed by

$$u'_{rj}(x,t) = A_j \hat{\boldsymbol{p}}_r^{\mathrm{T}} \mathbf{F}_j \hat{\boldsymbol{p}}_t g_{rg}(t - \Delta t_j) e^{i\omega_0 t} e^{-2i\frac{\omega_0}{c}(R_j + \frac{(x_1 - x_j)^2}{2R_j})} \tag{3.17}$$

At the receiver, the carrier frequency is removed by a coherent quadratic demodulation, eliminating the $e^{i\omega_0 t}$ exponential term in (3.17) [10]. Note that the quadratic term due to azimuth distance difference in the last exponential is a linear frequency modulation. This enables to introduce the azimuth chirp signal:

$$g_{az}(x; R_j) = e^{-2ik_0\frac{x^2}{R_j}}\Pi(\frac{x}{\delta_{sa}}) \tag{3.18}$$

where $k_0 = \frac{\omega_0}{c}$ is the carrier wavenumber and $\Pi(\frac{x}{\delta_{sa}})$ has been added to represent the limited extent of the antenna footprint.
Taking everything into account, the final received signal from a single scatterer can be represented by

$$u_{rj}(x,t) = A_j \hat{\boldsymbol{p}}_r^{\mathrm{T}} \mathbf{F}_j \hat{\boldsymbol{p}}_t g_{rg}(t - \Delta t_j) g_{az}(x_1 - x_j; R_j) e^{-2ik_0 R_j} \tag{3.19}$$

The last exponential term has a constant phase offset determined by the zero–Doppler range (minimum sensor–scatterer distance). It is essential for multi–channel imaging such as SAR interferometry.

SAR Image Formation Basics

The obtained raw data consists of information from the imaged scene which is spread over a certain region. The purpose of image formation is to extract this information by focusing the data. Three effects have to be accounted for:

- The signal envelope in form of a chirp which enables range compression and the improvement of range resolution.
- The spatial frequency diversity (so called Doppler spectrum) in the azimuth direction, which has the form of a chirp and enables the construction of the synthetic aperture and the improvement of the azimuth resolution.
- The presence of range cell migration, i.e. variation of $x_1 - x_j$ during the SAR acquisition, complicates the image formation and requires compensation techniques.

Due to range cell migration, range and azimuth coordinates are not independent anymore. Each scatterer response is located on a two–dimensional curve in the raw data. Additionally, the curvature depends on the range distance to the scatterer. There are several methods for raw data processing in both time– and frequency–domains. The most common methods are based on *matched filtering*. In the following the concept of a time–domain processor, the *backprojection algorithm*, will be used to illustrate SAR focusing.
The quantity of interest is the scattering amplitude $f_j = \hat{\boldsymbol{p}}_r^{\mathrm{T}} \mathbf{F}_j \hat{\boldsymbol{p}}_t$. In a first step, the received data can be focused in range without range migration compensation. For this, a matched filtering operation is performed at the receiver, which consists of correlating the received chirp signal with the complex conjugate of the replica of the transmitted signal. This provides the 1D range impulse response function

$$h_{rg}(R) = (g_{rg} * g_{rg}^*)(R) = \mathrm{sinc}\left(\frac{\pi R}{\delta_{sr}}\right) \tag{3.20}$$

where $\mathrm{sinc}(\cdot)$ is the mathematical sinus cardinal function $\mathrm{sinc}(x) = \frac{\sin(x)}{x}$.
Azimuth focusing requires the compensation of range migration effects. This step can be done by constructing a range–dependent two–dimensional reference function and the convolution of this function with the range–compressed data. The impulse response for azimuth compression can thus be represented by a two–dimensional convolution:

$$h_{az}(x,R) = (g_{az} * g_{az}^*)(x,R) \tag{3.21}$$

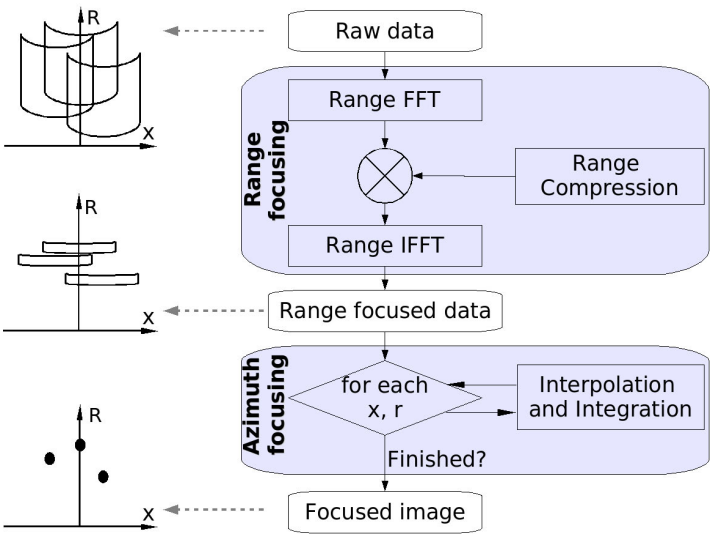

Figure 3.3: Flowchart of the time–domain backprojection algorithm. The images on the left represent the data regions of scattering echoes from 3 objects at different stages of the focusing procedure.

Fig. 3.3 shows a block diagram of the backprojection algorithm. The two–dimensional azimuth focusing in the time domain is computationally very intensive. Therefore, several alternative fast methods have been developed, all working in the frequency domain [30,31]. The earliest and simplest method is the *range doppler algorithm* [9]. The *chirp scaling algorithm* [116, 91] is more accurate. The $\omega - k$ *algorithm* [12] provides an exact solution to the problem of 2–D SAR focusing.
The complete focussing process can be described by the combined SAR impulse response function

$$h(x, R) = h_{rg}(R) h_{az}(x, R). \tag{3.22}$$

For the purpose of this thesis it is sufficient to approximate the SAR imaging process by decoupling the range and azimuth dependency separating the 2D focusing problem into two 1D problems. This results in the SAR impulse response function of the form [78, 10]

$$h(x, R) = \operatorname{sinc}\left(\frac{\pi x}{\delta_{az}}\right) \operatorname{sinc}\left(\frac{\pi R}{\delta_{sr}}\right) \tag{3.23}$$

SAR Image Model

Using the superposition principle and the Born approximation [10], the SAR image can finally be represented as the integration over an illuminated volume:

$$s(x, R) = \left[(u_r(x, t) + n_u) * * g_{rg}^*(t')\right] * * g_{az}^*(x, R) \tag{3.24}$$

$$= A \iiint \hat{\boldsymbol{p}}_r^{\mathrm{T}} \mathbf{F}(\boldsymbol{r}') \hat{\boldsymbol{p}}_t e^{-2ik_0 R'} h(x - x', R - R') dV' + n \tag{3.25}$$

where n_u and n represent the additional thermal noise of the radar system before and after focusing, respectively, and A accounts for amplitude modifications including the two–way energy loss due to wave propagation.
Under the plane wave approximation in the far field, the sensor–scatterer range distance can be expressed using the reference range to the resolution cell center R_0 [10, 105]:

$$R = R_0 + \Delta R \approx R_0 + \hat{\boldsymbol{k}} \cdot (\boldsymbol{r} - \boldsymbol{r}_0) \tag{3.26}$$

leading to

$$s(x, R) = Ae^{-2ik_0R_0} \iiint \hat{\boldsymbol{p}}_r^{\mathrm{T}} \mathbf{F}(\boldsymbol{r}') \hat{\boldsymbol{p}}_t e^{-2i\boldsymbol{k}\cdot(\boldsymbol{r}'-\boldsymbol{r}_0)} h(x - x', R - R') dV' + n \tag{3.27}$$

The focused complex $s(x, R)$ is sometimes referred to as *single–look complex* (SLC) data. It is often the end product of SAR processing of single–channel SAR imagery.

3.3 Polarimetric SAR Imaging

In the previous sections, SAR data acquisition and image formation were presented for a single channel, where only one element of the polarimetric scattering matrix could be acquired for given emitting and receiving polarizations. In order to reconstruct all elements of the scattering matrix it is required to emit and receive electromagnetic waves in two orthogonal polarization states (usually the horizontal H and the vertical V polarizations). In the simplest monostatic configuration, two antennas are used for alternating transmission and simultaneous reception. Fig. 3.4 shows a block diagram of such a polarimetric radar system [158].
A possible timing approach for acquiring all scattering matrix elements could be as follows: (1) transmit the pulse through the horizontally polarized antenna, (2) receive the scattered wave simultaneously on both antennas, (3) transmit the pulse through the vertically polarized antenna, (4) and receive simultaneously. This scheme is shown in Fig. 3.5.
An obvious disadvantage of using polarimetric imaging is the need to double the pulse repetition frequency (PRF) in comparison to single polarization radars. The processing of the raw data is similar to the processing of single–pol data and handles every channel separately.

3.3.1 Polarimetric Calibration

However, in order to reconstruct the scattering matrix correctly, an accurate polarimetric calibration of the relative amplitude and phase between the polarimetric channels is required. One distinguishes between internal calibration and external calibration. The internal calibration adjusts the system and sensor parameters, whereas the external calibration uses known target responses to calibrate the already available image [44]. In general, four criteria are used for polarimetric calibration: *symmetrization* of the cross–polar channels, *cross talk* correction, *channel imbalance* correction, and the *absolute calibration* of the radiometric calibration factor [44, 3, 158].
The final calibrated polarimetric scattering matrix image can be obtained by extending the single polarization model to full polarimetry:

$$\mathbf{S}(x, R) = Ae^{-2ik_0R_0} \iiint \mathbf{F}(\boldsymbol{r}') e^{-2i\boldsymbol{k}\cdot(\boldsymbol{r}'-\boldsymbol{r}_0)} h(x - x', R - R') dV' + \mathbf{N} \tag{3.28}$$

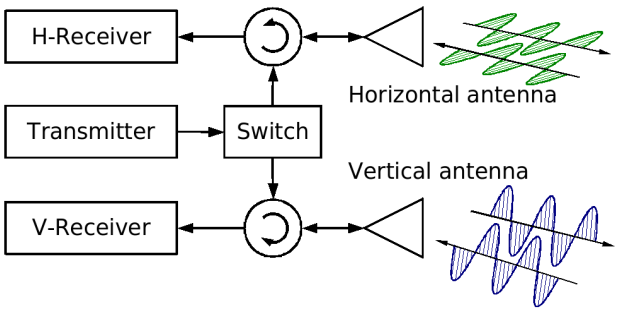

Figure 3.4: Polarimetric radar system configuration.

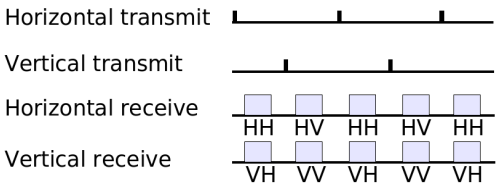

Figure 3.5: System timing for polarimetric data acquisition showing how all scattering matrix elements are acquired.

This model uses again the Born approximation neglecting propagation effects and assuming no system distortion and perfect calibration. The matrix $\mathbf{N}$ represents the independent noise contributions in the different channels.

3.3.2 Partial and Compact Polarimetric SAR Imaging

The reduction of the performance and the increase of the system complexity to acquire fully polarized scattering matrix elements may be incompatible with space–borne mission requirements. A compromise is to use so called *partial* and *compact* polarimetric modes. The sensor sends the signal only in one polarization but receives it simultaneously in two orthogonal polarizations using two antennas. With this technique one acquires two of the four elements of a transformed scattering matrix. A system model for the observables can be given by

$$\boldsymbol{k}_{L2}(x,R) = Ae^{-2ik_0R_0} \iiint \mathbf{U}_{L2}\mathbf{F}(\boldsymbol{r}')\hat{\boldsymbol{p}}_t e^{-2i\boldsymbol{k}\cdot(\boldsymbol{r}'-\boldsymbol{r}_0)} h(x-x', R-R')dV' + \mathbf{N} \quad (3.29)$$

where $\hat{\boldsymbol{p}}_t$ represents the transmit polarization, $\mathbf{U}_{L2}$ represents the transformation into the two receive polarizations, and $\boldsymbol{k}_{L2}$ represents a two element scattering vector in the lexicographic matrix basis of the system partial/compact polarizations. The two common partial polarimetric modes are the $HH - VH$ and the $VV - HV$ modes. Compact polarimetric modes include the $\frac{\pi}{4}$ mode [140], the dual circular mode, and circular transmit–linear receive mode (also called hybrid mode) [117].

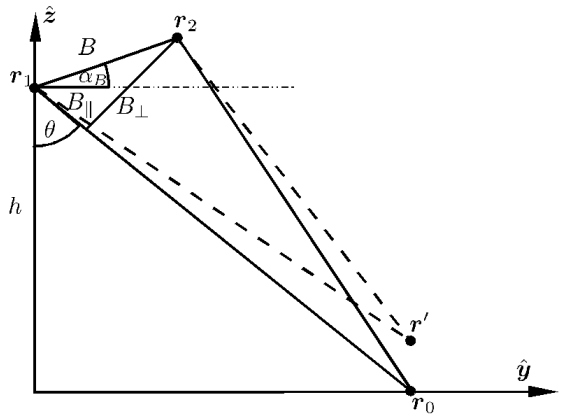

Figure 3.6: Interferometric SAR imaging geometry in the incidence plane.

3.4 Interferometric SAR Imaging

Due to the specific SAR geometry and processing, SAR imaging represents a projection of the 3D space (x, y, z) into the 2D cylindrical zero–Doppler coordinates (x, R). The information about one dimension is lost, and two different points with the same range distances but different heights will be imaged into the same resolution cell. Observing the scene from two slightly different incidence angles enables the reconstruction of the lost dimension up to a certain degree. SAR Interferometry (InSAR) uses the combination of two coherent SAR images acquired from slightly different incidence angles in order to reconstruct the height information from the phase difference.

3.4.1 Interferometric SAR Geometry

There are many approaches for interferometric data acquisition and application. In *across–track interferometry* two general modes are considered. In single–transmit mode, one antenna transmits the signal and both antennas receive the scattered signal simultaneously. In *alternate–transmit* mode, each antenna transmits and receives the signal, see Fig. 3.7. Whereas the single–transmit mode is only possible for single–pass interferometry, the alternate–transmit mode is possible in single–pass and in repeat–pass acquisitions.
For all across–track interferometric modes, the geometry is represented in Fig. 3.6. The two sensors $\boldsymbol{r}_1, \boldsymbol{r}_2$ are separated by the baseline $B = \|\boldsymbol{b}\|$ in the incidence plane perpendicular to the along–track direction:

$$\boldsymbol{b} = \boldsymbol{r}_2 - \boldsymbol{r}_1 = B \begin{bmatrix} 0 \\ \cos\alpha_B \\ \sin\alpha_B \end{bmatrix} = B_h \begin{bmatrix} 0 \\ 1 \\ 0 \end{bmatrix} + B_v \begin{bmatrix} 0 \\ 0 \\ 1 \end{bmatrix} \tag{3.30}$$

where α_B is the baseline inclination angle. The baseline can be separated into the perpendicular part $B_\perp$ (also called *effective baseline*) and the parallel part $B_\parallel$

$$B_\perp = B\cos(\theta_1 - \alpha_B), \qquad B_\parallel = B\sin(\theta_1 - \alpha_B) \tag{3.31}$$

where θ_1 is the incidence angle from the first sensor.

Given a point scatterer at position $\boldsymbol{r}$, the range distances from the two sensors are given by $R_1 = |\boldsymbol{r}_1 - \boldsymbol{r}|$ and $R_2 = |\boldsymbol{r}_2 - \boldsymbol{r}| = R_1 + \Delta R$. For two received signals at the baseline ends

$$s_1(x,R) = |s_1(x,R)|e^{i\phi_1(x,R)}, \qquad s_2(x,R) = |s_2(x,R)|e^{i\phi_2(x,R)} \tag{3.32}$$

the *complex interferogram* is given by

$$v(x,R) = s_1(x,R)s_2^*(x,R) = |s_1(x,R)||s_2(x,R)|e^{i\phi(x,R)} \tag{3.33}$$

where $\phi = \phi_1 - \phi_2$ is the interferometric phase. For a point scatterer, the signal phase is composed of the range delay and the object phase induced by scattering:

$$\phi_1 = -2k_0R_{j1} + \phi_{obj}, \qquad \phi_2 = -2k_0(R_{j1} + \Delta R) + \phi_{obj}. \tag{3.34}$$

where the factor of 2 corresponds to the alternate–transmit mode, due to the two–way range distance difference. Taking the difference, the interferometric phase is therefore given by

$$\phi = \phi_1 - \phi_2 = 2k_0\Delta R = 2k_0(R_2 - R_1) \tag{3.35}$$

Using the cosine law, R_2 and ΔR can be expressed by

$$R_2^2 = R_1^2 + B^2 - 2R_1B\cos(\frac{\pi}{2} - (\theta_1 - \alpha_B)) = R_1^2 + B^2 - 2R_1B\sin(\theta_1 - \alpha_B) \tag{3.36}$$

$$\Delta R = R_2 - R_1 = -B\sin(\theta_1 - \alpha_B) + \frac{B^2}{2R_1} - \frac{\Delta R^2}{2R_1} \tag{3.37}$$

Since the baseline B and the range difference ΔR are very small in comparison to R_1, the last two terms of the last equation can be neglected. This leads to the plane wave approximation in the far–field (sometimes also called *parallel ray approximation*):

$$\Delta R \approx -B\sin(\theta_1 - \alpha_B) = -B_{\parallel} \tag{3.38}$$

The interferometric phase is then proportional to the parallel component of the baseline. Noting that

$$\cos\theta_0 = \frac{h - z}{R} \tag{3.39}$$

where z and R are the coordinates of a scatterer in the incidence plane and h is the height of the sensor, one can derive the partial derivatives of (3.35) with reference to local coordinates R, z and x.

Locally, in the surrounding of the resolution cell center, the phase dependence on range and height coordinates (R, z) (defining range and height sensitivities of the interferometric phase) can be obtained by a first–order Taylor expansion of the phase difference [127,153] using (3.38) and (3.39):

$$k_r \approx \left.\frac{\partial\phi}{\partial R}\right|_{\boldsymbol{r}=\boldsymbol{r}_0} = 2k_0\left.\frac{\partial\Delta R}{\partial R}\right|_{\boldsymbol{r}=\boldsymbol{r}_0} = 2k_0\frac{B_{\perp}}{R_0\tan\theta_0} \tag{3.40}$$

$$k_z \approx \left.\frac{\partial\phi}{\partial z}\right|_{\boldsymbol{r}=\boldsymbol{r}_0} = 2k_0\left.\frac{\partial\Delta R}{\partial z}\right|_{\boldsymbol{r}=\boldsymbol{r}_0} = 2k_0\frac{B_{\perp}}{R_0\sin\theta_0} \tag{3.41}$$

$$k_x \approx \left.\frac{\partial\phi}{\partial x}\right|_{\boldsymbol{r}=\boldsymbol{r}_0} = 2k_0\left.\frac{\partial\Delta R}{\partial x}\right|_{\boldsymbol{r}=\boldsymbol{r}_0} = 0 \tag{3.42}$$

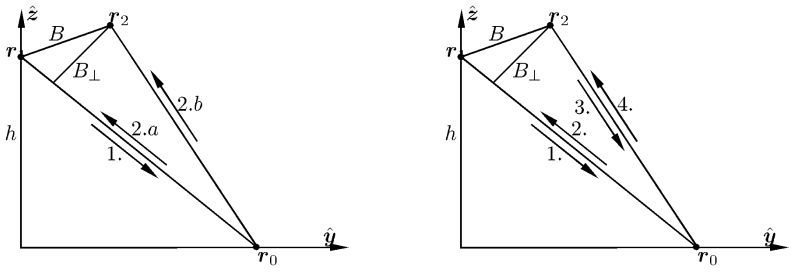

Figure 3.7: Interferometric single–transmit (left) and alternate–transmit (right) modes.

where $\theta_0 = \frac{\theta_1+\theta_2}{2}$ and $R_0 = \frac{R_1+R_2}{2}$ are the average incidence angle and the average range distance.
k_z is often referred to as the *vertical wavenumber*. Alternatively, the 2π height ambiguity $z_{2\pi}$ expresses the height difference leading to an interferometric phase change of 2π:

$$z_{2\pi} = \frac{2\pi}{k_z} \tag{3.43}$$

The major observable of SAR interferometry, next to the interferometric phase, is the complex coherence

$$\gamma = |\gamma| e^{i\phi} = \frac{\langle s_1 s_2^* \rangle}{\sqrt{\langle s_1 s_1^* \rangle \langle s_2 s_2^* \rangle}} \tag{3.44}$$

The absolute value of γ is the degree of interferometric coherence and it ranges between zero and one. It is also an indicator of the phase information quality.
The slightly different sensor positions cause the sampling of two slightly different spectral slices. As shown in Fig. 3.8 for the ground range and height, the spectra slices will have one common part which is shifted, and non–correlated parts. The system bandwidth W_r limits the maximal possible perpendicular baseline, called the *critical baseline*, given by

$$B_{\perp,crit} = \frac{W_r \lambda R}{c} \tan\theta_0 \tag{3.45}$$

The degree of range decorrelation is determined by the non–overlapping parts in the spectra. If only surface scattering is present, this decorrelation can be reduced by *wavenumber shift* filtering [49]. However, the presence of a vertical distribution of scatterers will cause volume decorrelation which cannot be compensated in the data.

3.4.2 Interferometric Model for One Homogeneous Layer

The model for an interferometric SAR image pair, after perfect calibration and coregistration and under the Born approximation is given by [54, 10]

$$s_1(x, R_1) = A \iiint f(\boldsymbol{r}') e^{-2ik_0 R_1'} h(x - x', R_1 - R_1') dV' + n_1 \tag{3.46}$$

$$s_2(x, R_2) = A \iiint f(\boldsymbol{r}') e^{-2ik_0 R_2'} h(x - x', R_2 - R_2') dV' + n_2 \tag{3.47}$$

$$\tag{3.48}$$

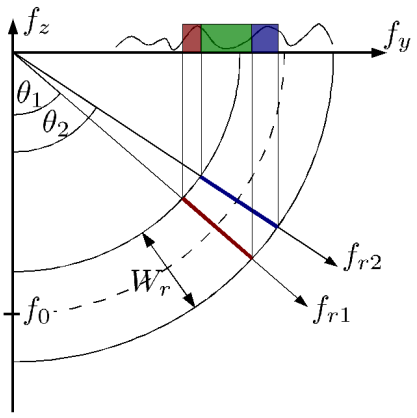

Figure 3.8: The reflectivity spectral slices of a pair of InSAR images. f_y and f_z represent the ground and the height spectra, while f_{r1}, f_{r2} are the slant range spectra of two SAR images in dependence of the incidence angle. The green region of the ground spectrum is the overlapping correlated part, and the red and blue are non–overlapping uncorrelated parts of image spectra.

where we have assumed that the amplitude variations are negligible ($A_1 = A_2 = A$) and where R_i, R_i' are given by $|\boldsymbol{r}_i - \boldsymbol{r}|, |\boldsymbol{r}_i - \boldsymbol{r}'|$ and $f(\boldsymbol{r}') = \hat{\boldsymbol{p}}_r^{\mathrm{T}} \mathbf{F} \hat{\boldsymbol{p}}_t$. The scattering amplitudes are assumed to follow independent circular complex Gaussian distributions, as discussed in appendix A, so that

$$\left\langle f_1(\boldsymbol{r}) f_1^*(\boldsymbol{r}') \right\rangle = \left\langle f_2(\boldsymbol{r}) f_2^*(\boldsymbol{r}') \right\rangle = \sigma_v(\boldsymbol{r}') \delta(\boldsymbol{r} - \boldsymbol{r}') \tag{3.49}$$

$$\left\langle f_1(\boldsymbol{r}) f_2^*(\boldsymbol{r}') \right\rangle = \sigma_{ve}(\boldsymbol{r}') \delta(\boldsymbol{r} - \boldsymbol{r}') \tag{3.50}$$

where σ_v is the backscattering coefficient and σ_{ve} is the temporally stable backscattering coefficient (also called the effective backscattering coefficient).
Assuming perfect coregistration, the interferometric cross–correlation is given by

$$\langle s_1 s_2^* \rangle = A^2 \iiint \sigma_{ve}(\boldsymbol{r}') |h(...)|^2 e^{2ik_0(R_2' - R_1')} dV' \tag{3.51}$$

Using the first–order Taylor expansion of the phase term (3.35) from (3.40)–(3.42) [153]

$$2ik_0(R_2 - R_1) \approx 2ik_0(R_{20} - R_{10}) + ik_r(R - R_0) + ik_z(z - z_0) \tag{3.52}$$

$$= i\phi_0 + ik_r(R - R_0) + ik_z(z - z_0) \tag{3.53}$$

the cross–correlation becomes

$$\langle s_1 s_2^* \rangle = A^2 e^{i\phi_0} \iiint \sigma_{ve}(\boldsymbol{r}') |h(...)|^2 e^{ik_r(R' - R_0)} e^{ik_z(z' - z_0)} dV' \tag{3.54}$$

where $\phi_0 = 2k_0(R_{20} - R_{10})$ is the reference phase.
Let σ_{ve} and σ_v be homogeneous along the horizontal plane and let them be dependent only on height:

$$\sigma_{ve}(\boldsymbol{r}') = \sigma_{ve}^0 \rho(z'), \quad \sigma_v(\boldsymbol{r}') = \sigma_v^0 \rho(z') \tag{3.55}$$

where $\sigma_v^0, \sigma_{ve}^0$ are the average backscattering coefficients and $\rho(z)$ is the normalized distribution of the scatterers with $\int \rho(z')dz' = 1$. Then one can separate the integral (3.54) into

$$\langle s_1 s_2^* \rangle = A^2 e^{i\phi_0} \sigma_{ve}^0 \iint |h(...)|^2 e^{ik_r(R'-R_0)} dR' dx' \int \rho(z') e^{ik_z(z'-z_0)} dz' \tag{3.56}$$

$$= A^2 e^{i\phi_0} \sigma_{ve}^0 I_{rx} I_z \tag{3.57}$$

where I_{rx} and I_z represent the corresponding integrals over the range and azimuth, and over the height dimensions, respectively.
The autocorrelation of the received signal is given by [54, 153, 5, 10]

$$\langle s_i s_i^* \rangle = A^2 \iiint \sigma_v |h(...)|^2 dV' + \sigma_n = A^2 \sigma_v^0 \iint |h(...)|^2 dR' dx' \int \rho(z') dz' + \sigma_n \tag{3.58}$$

$$= A^2 \sigma_v^0 I_{rx}^0 I_z^0 + \sigma_n \tag{3.59}$$

where $\sigma_n = \left\langle |n|^2 \right\rangle$ is the noise variance.
The complex coherence for this layer can thus be given by

$$\gamma = \frac{\langle s_1 s_2^* \rangle}{\sqrt{\langle |s_1|^2 \rangle \langle |s_2|^2 \rangle}} = e^{i\phi_0} \frac{\sigma_{ve}^0}{\sigma_v^0} \frac{I_{rx}}{I_{rx}^0} \frac{I_z}{I_z^0} \frac{\sigma_0}{\sigma_0 + \sigma_n}, \quad \text{where } \sigma_0 = A^2 \sigma_v^0 I_{rx}^0 I_z^0 \tag{3.60}$$

$$= e^{i\phi_0} \gamma_{temp} \gamma_r \gamma_z \gamma_{therm} \tag{3.61}$$

This simple model enables to split the coherence into several physically meaningful components: the temporal decorrelation, the range decorrelation, the volume decorrelation, and the thermal decorrelation. The interferometric phase is determined by the ground reference phase ϕ_0 and a possible offset due to the present volume, $\arg(\gamma_z)$. Additionally it is possible to include into this model decorrelation effects due to coregistration, calibration, temporal coherent and incoherent changes, multiple layers, attenuation, refraction, inhomogeneities, topography variations, Doppler centroid, atmosphere propagation, etc. (see e.g. [78, 171, 127, 10, 86, 128, 57, 126, 92]).

3.4.3 Separation of Independent Layers by Means of Interferometry

As presented in the previous section, one can decompose the coherence term into a product of several meaningful decorrelation sources. In this section we demonstrate the separability of medium induced decorrelation sources (temporal and volume coherences), either from a vertical structure of the layers, or due to the fact that layers have uncorrelated scattering mechanism components.

Spatially Separated Layers

Let consider the case of two spatially separated layers l_1, l_2. Let these layers be homogeneous in the horizontal direction and let the backscattering structure be given by

$$\sigma_{ve}(\boldsymbol{r}') = \begin{cases} \sigma_{ve1}^0 \rho_1(z') & z_{1b} \le z' < z_{1t} \\ \sigma_{ve2}^0 \rho_2(z') & z_{2b} \le z' < z_{2t} \end{cases} \tag{3.62}$$

and

$$\sigma_v(\boldsymbol{r}') = \begin{cases} \sigma^0_{v1}\rho_1(z') & z_{1b} \leq z' < z_{1t} \\ \sigma^0_{v2}\rho_2(z') & z_{2b} \leq z' < z_{2t} \end{cases} \tag{3.63}$$

where z_{ib}, z_{it} are bottom and top heights of these layers. The backscattering coefficients can be equal ($\sigma^0_{ve1} = \sigma^0_{ve2}$, $\sigma^0_{v1} = \sigma^0_{v2}$), but the layers are assumed to be non–overlapping, so that $z_{1t} \leq z_{2b}$. Then we can rewrite the cross–correlation and the autocorrelation from equations (3.56) and (3.58) to

$$\langle s_1 s_2^* \rangle = A^2 e^{i\phi_0} \iint |h(...)|^2 e^{ik_r(R'-R_0)} dR' dx' \times \tag{3.64}$$

$$\left(\sigma^0_{ve1} \int \rho_1(z') e^{ik_z(z'-z_0)} dz' + \sigma^0_{ve2} \int \rho_2(z') e^{ik_z(z'-z_0)} dz' \right) \tag{3.65}$$

$$= A^2 e^{i\phi_0} I_{rx} (\sigma^0_{ve1} I_{z1} + \sigma^0_{ve2} I_{z2}) \tag{3.66}$$

$$\langle s_i s_i^* \rangle = A^2 \iint |h(...)|^2 dR' dx' \left(\sigma^0_{v1} \int \rho_1(z') dz' + \sigma^0_{v2} \int \rho_2(z') dz' \right) + \sigma_n \tag{3.67}$$

$$= A^2 I^0_{rx} (\sigma^0_{v1} I^0_{z1} + \sigma^0_{v2} I^0_{z2}) + \sigma_n \tag{3.68}$$

The complex coherence for this two–layer structure can thus be given in analogy to (3.60) by

$$\gamma = \frac{\langle s_1 s_2^* \rangle}{\sqrt{\langle |s_1|^2 \rangle \langle |s_2|^2 \rangle}} = e^{i\phi_0} \frac{I_{rx}}{I^0_{rx}} \left(\frac{\sigma^0_{ve1} I_{z1} + \sigma^0_{ve2} I_{z2}}{\sigma^0_{v1} I^0_{z1} + \sigma^0_{v2} I^0_{z2}} \right) \frac{\sigma_0}{\sigma_0 + \sigma_n} \tag{3.69}$$

where

$$\sigma_0 = A^2 I^0_{rx} (\sigma^0_{v1} I^0_{z1} + \sigma^0_{v2} I^0_{z2}) \tag{3.70}$$

The inner fraction containing the sums represents the temporal and the volume decorrelation sources of the two layers. There are two ways to represent them as independent coherences. One involves the *intensity ratio* of the two layers

$$\Delta = \frac{\sigma^0_{v1} I^0_{z1}}{\sigma^0_{v2} I^0_{z2}} \tag{3.71}$$

and the other involves the *intensity weightings* of the layers

$$c_1 = \frac{\sigma^0_{v1} I^0_{z1}}{\sigma^0_{v1} I^0_{z1} + \sigma^0_{v2} I^0_{z2}} = \frac{\Delta}{\Delta + 1}, \qquad c_2 = \frac{\sigma^0_{v2} I^0_{z2}}{\sigma^0_{v1} I^0_{z1} + \sigma^0_{v2} I^0_{z2}} = \frac{1}{\Delta + 1} = 1 - c_1 \tag{3.72}$$

with $c_1 + c_2 = 1$.
Using these definitions, one can decompose the layer decorrelation sources so that (3.69) becomes

$$\gamma = e^{i\phi_0} \gamma_r \left(\frac{\Delta \gamma_{temp1} \gamma_{z1} + \gamma_{temp2} \gamma_{z2}}{\Delta + 1} \right) \gamma_{therm} \tag{3.73}$$

$$= e^{i\phi_0} \gamma_r (c_1 \gamma_{temp1} \gamma_{z1} + c_2 \gamma_{temp2} \gamma_{z2}) \gamma_{therm} \tag{3.74}$$

This two layer structure can be generalized to multiple layers:

$$\gamma = e^{i\phi_0}\gamma_r \left(\frac{\sum_{i=1}^{N} \Delta_i^1 \gamma_{temp,i}\gamma_{z,i}}{\sum_{i=1}^{N} \Delta_i^1} \right) \gamma_{therm} \tag{3.75}$$

$$= e^{i\phi_0}\gamma_r \left(\sum_{i=1}^{N} c_i \gamma_{temp,i}\gamma_{z,i} \right) \gamma_{therm} \tag{3.76}$$

where Δ_i^1 is the intensity ratio of layer 1 to layer i, and c_i is the normalized intensity of layer i ($\sum c_i = 1$).

Uncorrelated Layers

In equivalence to (3.62) and (3.63) one can express the backscattering coefficients as a sum of two uncorrelated scattering components

$$\sigma_{ve}(\boldsymbol{r}') = \sigma_{ve1}^0 \rho_1(z') + \sigma_{ve2}^0 \rho_2(z') \tag{3.77}$$

$$\sigma_v(\boldsymbol{r}') = \sigma_{v1}^0 \rho_1(z') + \sigma_{v2}^0 \rho_2(z') \tag{3.78}$$

without any restrictions on ρ_1, ρ_2. Inserting these definitions into (3.56) and (3.58) one obtains the same formulations for cross–correlation, autocorrelation and complex coherence functions as in the previous derivations (3.64)–(3.76).
An often used two–layers structure consists of a ground layer $l_1 = l_g$ and the vegetation volume layer $l_2 = l_v$. In this case, Δ is called the ground–to–volume ratio and $|\gamma_{z1}| = 1$ [154, 106]. In [154], the volumetric coherence expressions for surface, random (and oriented) volume, and double–bounce scattering components were derived and the surface–volume and double–bounce–volume coherence combinations were presented for the random volume case. The double–bounce–volume coherence combination for the oriented volume case has been explicitly computed in [7]. All these approaches assume single–pass interferometric data acquisition and neglect temporal decorrelation.

3.5 Conclusions

In this chapter, the principles of synthetic aperture radar data acquisition and processing were presented. Single–channel, polarimetric and interferometric SAR imaging modes have been examined. In particular, an interferometric coherence model has been derived and the decomposition of the coherence into independent decorrelation sources and independent media structures has been demonstrated.

Chapter 4

PolInSAR Coherence Set Characteristics

Polarimetric SAR interferometry (PolInSAR) is a relatively new technique with ongoing research activities. Based on the previous works on PolInSAR, this chapter will present our studies on fundamental PolInSAR data properties, its generic information content and restrictions. The aim is to present common PolInSAR properties, independently of the scattering medium under consideration.
At the beginning of this chapter, PolInSAR data representations are presented as introduced by Cloude and Papathanassiou [22, 105], together with the whitened form and the coherency contraction [22, 105, 84], as well as the concept of polarimetric stationarity in SAR interferometry, recently formulated by Ferro–Famil and Neumann [39]. The concept of PolInSAR coherence set, which relies on the works of Tabb and Flynn [142, 143, 42] and Colin [29], is extended by us to retrieve information on coherence set geometry, density, and distribution. The last topic of this chapter deals with PolInSAR coherence optimization. We re-examine the coherence optimization problem in order to improve the interpretation of the optimal coherences and optimal scattering mechanisms. Then, we introduce methods which extend single–baseline coherence optimization to the multiple baseline case.

4.1 Polarimetric SAR Interferometry

A PolInSAR image is a coherent combination of two polarimetric images by means of interferometry:

$$\boldsymbol{k}_P = \begin{bmatrix} \boldsymbol{k}_{P1} \\ \boldsymbol{k}_{P2} \end{bmatrix}, \qquad \mathbf{T} = \left\langle \boldsymbol{k}_P \boldsymbol{k}_P^\dagger \right\rangle = \begin{bmatrix} \mathbf{T}_{11} & \boldsymbol{\Omega}_{12} \\ \boldsymbol{\Omega}_{12}^\dagger & \mathbf{T}_{22} \end{bmatrix} \tag{4.1}$$

$$\boldsymbol{k}_L = \begin{bmatrix} \boldsymbol{k}_{L1} \\ \boldsymbol{k}_{L2} \end{bmatrix}, \qquad \mathbf{C} = \left\langle \boldsymbol{k}_L \boldsymbol{k}_L^\dagger \right\rangle = \begin{bmatrix} \mathbf{C}_{11} & \mathbf{Q}_{12} \\ \mathbf{Q}_{12}^\dagger & \mathbf{C}_{22} \end{bmatrix} \tag{4.2}$$

where $\mathbf{C}_{ii}, \mathbf{T}_{ii}$ are the common polarimetric covariance and coherency matrices corresponding to polarimetric scattering vectors $\boldsymbol{k}_{Li}, \boldsymbol{k}_{Pi}$ and $\mathbf{Q}_{12}, \boldsymbol{\Omega}_{12}$ are the cross–correlation matrices describing the polarimetric and interferometric relationship between the two images. PolInSAR covariance matrix dimensions is 8×8 in the case of the general quad–pol

data, 6×6 in case of reciprocity, and 4×4 in case of partial or compact polarimetry. In the following, for the sake of compactness, we will use only the coherency matrix form in the Pauli basis assuming reciprocity, if not otherwise stated.
In order to obtain usual scalar interferometric coherences and phases one can use the unitary projection vectors $\boldsymbol{\omega}_1 = \boldsymbol{\omega}_{pq}, \boldsymbol{\omega}_2 = \boldsymbol{\omega}_{ab}$ where the indices $_{pq}$, $_{ab}$ represent certain transmit and receive polarizations, as presented in section 2.5.3. Scalar scattering coefficients can thus be obtained by

$$\mu_1 = \boldsymbol{\omega}_1^\dagger \boldsymbol{k}_{P1}, \qquad \mu_2 = \boldsymbol{\omega}_2^\dagger \boldsymbol{k}_{P2} \tag{4.3}$$

The common polarimetric intensities and interferometric cross–correlations are obtained using equal projection vectors ($\boldsymbol{\omega}_1 = \boldsymbol{\omega}_2 = \boldsymbol{\omega}$)

$$\left\langle \mu_i \mu_i^\dagger \right\rangle = \left\langle \boldsymbol{\omega}^\dagger \boldsymbol{k}_{Pi} \boldsymbol{k}_{Pi}^\dagger \boldsymbol{\omega} \right\rangle = \boldsymbol{\omega}^\dagger \left\langle \boldsymbol{k}_{Pi} \boldsymbol{k}_{Pi}^\dagger \right\rangle \boldsymbol{\omega} = \boldsymbol{\omega}^\dagger \mathbf{T}_{ii} \boldsymbol{\omega} \quad i \in \{1, 2\} \tag{4.4}$$

$$\left\langle \mu_1 \mu_2^\dagger \right\rangle = \left\langle \boldsymbol{\omega}^\dagger \boldsymbol{k}_{P1} \boldsymbol{k}_{P2}^\dagger \boldsymbol{\omega} \right\rangle = \boldsymbol{\omega}^\dagger \left\langle \boldsymbol{k}_{P1} \boldsymbol{k}_{P2}^\dagger \right\rangle \boldsymbol{\omega} = \boldsymbol{\omega}^\dagger \boldsymbol{\Omega}_{12} \boldsymbol{\omega} \tag{4.5}$$

Using non–equal projection vectors one can obtain polarimetric correlations, as well as combined polarimetric and interferometric cross–correlations. Similarly, the concept of the scalar interferometric coherence can be generalized to the vector expression for the complex PolInSAR coherence [22, 105]

$$\gamma = |\gamma| e^{i\phi} = \gamma_{(\boldsymbol{\omega}_1, \boldsymbol{\omega}_2)} = \frac{\boldsymbol{\omega}_1^\dagger \boldsymbol{\Omega}_{12} \boldsymbol{\omega}_2}{\sqrt{\boldsymbol{\omega}_1^\dagger \mathbf{T}_{11} \boldsymbol{\omega}_1 \boldsymbol{\omega}_2^\dagger \mathbf{T}_{22} \boldsymbol{\omega}_2}} \tag{4.6}$$

It is usually assumed that the projection vectors do not introduce phase offsets, i.e. $\arg(\boldsymbol{\omega}_1^\dagger \boldsymbol{\omega}_2) = 0$. If this is not the case, the PolInSAR coherence phase is disturbed by the additional phase offset.
In general, using the projection vectors one aims to estimate the interferometric phase or the degree of coherence for the same object or scattering mechanism as observed from two different times and/or positions. It is reasonable to use equal projection vectors assuming equal polarization signatures of the object in the two data sets. However, there are also several possible causes to use non–equal projection vectors for the coherence estimation: temporal changes (e.g. [86, 126]), atmosphere propagation effects (e.g. Faraday rotation [125, 167, 47]), processing and calibration distortions, radio frequency interferences [120], and effects due to slightly different incidence angles.
It is convenient to visualize the coherences in the complex coherence plane, as shown on an example in Fig. 4.1. The axes represent the real and imaginary parts of the coherences. All coherences are located inside the unitary circle. A glance at the locations of the individual coherences enables an easy interpretation: the closer the locations are to the origin, the more decorrelated the signal at the given polarization. Phase difference for two polarizations represents the separation of the scattering responses.

PolInSAR Basis Transformation

Any polarimetric scattering vector or polarimetric coherency matrix can be transformed from the given form into another polarization or matrix basis, as shown in section 2.5.3:

$$\boldsymbol{k}_{Pi}' = \mathbf{U}_i \boldsymbol{k}_{Pi} \quad \rightarrow \qquad \mathbf{T}_{ii}' = \mathbf{U}_i \mathbf{T}_{ii} \mathbf{U}_i^\dagger, \quad \boldsymbol{\Omega}_{ij}' = \mathbf{U}_i \boldsymbol{\Omega}_{ij}' \mathbf{U}_j^\dagger \tag{4.7}$$

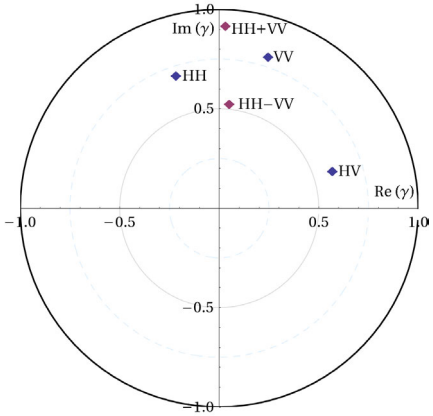

Figure 4.1: Examples of PolInSAR coherences in the complex coherence plane.

To transform the whole PolInSAR coherency matrix, one can construct the generalized PolInSAR transformation matrix $\mathbf{U}$:

$$\mathbf{U} = \begin{bmatrix} \mathbf{U}_1 & \mathbf{0} \\ \mathbf{0} & \mathbf{U}_2 \end{bmatrix} \tag{4.8}$$

so that

$$\mathbf{T}' = \mathbf{U}\mathbf{T}\mathbf{U}^\dagger. \tag{4.9}$$

If $\mathbf{U}_1 \neq \mathbf{U}_2$ then the two data sets are transformed into two individual bases. This can be useful for instance for calibration purposes.

Whitened PolInSAR Representations

One can isolate the coherence information of the coherency matrix using the *whitened* PolInSAR representation [105]

$$\widetilde{\mathbf{T}}_6 = \begin{bmatrix} \mathbf{I} & \mathbf{\Pi} \\ \mathbf{\Pi}^\dagger & \mathbf{I} \end{bmatrix} = \mathbf{R}\mathbf{T}_6\mathbf{R}, \quad \mathbf{R} = \begin{bmatrix} \mathbf{T}_{11}^{-1/2} & \mathbf{0} \\ \mathbf{0} & \mathbf{T}_{22}^{-1/2} \end{bmatrix} \tag{4.10}$$

where

$$\mathbf{\Pi} = \mathbf{T}_{11}^{-1/2}\mathbf{\Omega}_{12}\mathbf{T}_{22}^{-1/2} \tag{4.11}$$

is a *coherency contraction* matrix [59, 84, 26], since by definition $\sigma_{max}(\mathbf{\Pi}) \leq 1$ where σ_{max} is the largest singular value of $\mathbf{\Pi}$.
With substitutions

$$\boldsymbol{v}_i = \frac{\sqrt{\mathbf{T}_{ii}}\boldsymbol{\omega}_i}{\boldsymbol{\omega}_i^\dagger\sqrt{\mathbf{T}_{ii}}\boldsymbol{\omega}_i}, \qquad \boldsymbol{\omega}_i = \frac{\mathbf{T}_{ii}^{-1/2}\boldsymbol{v}_i}{\boldsymbol{v}_i^\dagger\mathbf{T}_{ii}^{-1/2}\boldsymbol{v}_i} \tag{4.12}$$

the coherence equation (4.6) becomes:

$$\gamma = \gamma_{(\boldsymbol{v}_1,\boldsymbol{v}_2)} = \boldsymbol{v}_1^\dagger\mathbf{\Pi}\boldsymbol{v}_2, \quad \text{with } \boldsymbol{v}_i^\dagger\boldsymbol{v}_i = 1 \tag{4.13}$$

Polarization basis transformation applies to the coherency contraction in the same way as to the full PolInSAR coherency matrix since

$$\mathbf{T}' = \mathbf{U}\mathbf{T}\mathbf{U}^\dagger \;\rightarrow\; \mathbf{\Pi}' = \mathbf{U}_1\mathbf{\Pi}\mathbf{U}_2^\dagger \tag{4.14}$$

Hadamard Coherence Formulation

In [83], the PolInSAR information is represented using the Hadamard products of scattering vectors:

$$\boldsymbol{z} = \boldsymbol{k}_{P1} \circ \boldsymbol{k}_{P2} = \begin{bmatrix} s_1^1 s_1^2 \\ s_2^1 s_2^2 \\ s_3^1 s_3^2 \end{bmatrix}, \quad \mathbf{C}_H = \left\langle \boldsymbol{z}\boldsymbol{z}^\dagger \right\rangle \tag{4.15}$$

Assuming a lack of correlation between $\boldsymbol{k}_{P1}$ and $\boldsymbol{k}_{P2}$, it follows

$$\mathbf{C}_{H0} := \left\langle \boldsymbol{k}_{P1}\boldsymbol{k}_{P1}^\dagger \right\rangle \circ \left\langle \boldsymbol{k}_{P2}\boldsymbol{k}_{P2}^\dagger \right\rangle \tag{4.16}$$

If on the contrary the scattering vectors are fully correlated, one obtains

$$\mathbf{C}_{H\infty} := \left\langle z_\infty z_\infty^\dagger \right\rangle, \quad \boldsymbol{z}_\infty = \boldsymbol{k}_{P1} \circ \boldsymbol{k}_{P1} \propto \boldsymbol{k}_{P2} \circ \boldsymbol{k}_{P2} \tag{4.17}$$

This allows to define the Hadamard coherency indicator γ_H using largest singular values:

$$\gamma_H = \frac{\sigma_1(C_H) - \sigma_1(C_{H0})}{\sigma_1(C_{H\infty}) - \sigma_1(C_{H0})} \tag{4.18}$$

We note this PolInSAR coherency indicator for completeness, but it has been hardly used up to now.

4.2 Multi–Baseline Polarimetric SAR Interferometry

Single–baseline (SB) PolInSAR data analysis can be readily generalized to multi–baseline (MB) PolInSAR by scaling the data space and the processing techniques. Multi–baseline data with n acquisitions consists of $\frac{1}{2}n(n-1)$ direct baselines. Assuming no zero–baselines, the number of spatially distinct baselines is between $n-1$ and $\frac{1}{2}n(n-1)$ in dependence of the regularity of the tracks, where the limits are given for the cases of all tracks being regularly and irregularly spaced, respectively. The MB coherency matrix is thus given by

$$\mathbf{T}_{MB} = \left\langle \boldsymbol{k}_P \boldsymbol{k}_P^\dagger \right\rangle = \begin{bmatrix} \mathbf{T}_{11} & \dots & \boldsymbol{\Omega}_{1n} \\ \vdots & \ddots & \vdots \\ \boldsymbol{\Omega}_{1n}^\dagger & \dots & \mathbf{T}_{nn} \end{bmatrix}, \quad \text{with } \boldsymbol{k}_P = \begin{bmatrix} \boldsymbol{k}_{P1} \\ \vdots \\ \boldsymbol{k}_{Pn} \end{bmatrix} \tag{4.19}$$

and the whitened MB coherency matrix is

$$\widetilde{\mathbf{T}}_{MB} = \left\langle \boldsymbol{k}_P \boldsymbol{k}_P^\dagger \right\rangle = \begin{bmatrix} \mathbf{I} & \boldsymbol{\Pi}_{12} & \dots & \boldsymbol{\Pi}_{1n} \\ \boldsymbol{\Pi}_{12}^\dagger & \mathbf{I} & \dots & \boldsymbol{\Pi}_{2n} \\ \vdots & \vdots & \ddots & \vdots \\ \boldsymbol{\Pi}_{1n}^\dagger & \boldsymbol{\Pi}_{2n}^\dagger & \dots & \mathbf{I} \end{bmatrix} = \mathbf{R}_{MB}\mathbf{T}_{MB}\mathbf{R}_{MB} \tag{4.20}$$

where

$$\mathbf{R}_{MB} = \begin{bmatrix} \mathbf{T}_{11}^{-1/2} & \dots & \mathbf{0} \\ \vdots & \ddots & \vdots \\ \mathbf{0} & \dots & \mathbf{T}_{nn}^{-1/2} \end{bmatrix} \tag{4.21}$$

Basis transformation can also be generalized to

$$\mathbf{T}'_{MB} = \mathbf{U}_{MB}\mathbf{T}\mathbf{U}_{MB}^{\dagger}, \quad \mathbf{U}_{MB} = \begin{bmatrix} \mathbf{U}_1 & \dots & \mathbf{0} \\ \vdots & \ddots & \vdots \\ \mathbf{0} & \dots & \mathbf{U}_n \end{bmatrix} \tag{4.22}$$

The interferometric coherence between two data sets i and j is given in analogy to (4.6) and (4.13) by

$$\gamma_{ij} = \frac{\boldsymbol{\omega}_i^{\dagger}\boldsymbol{\Omega}_{ij}\boldsymbol{\omega}_j}{\sqrt{\boldsymbol{\omega}_i^{\dagger}\mathbf{T}_{ii}\boldsymbol{\omega}_i\boldsymbol{\omega}_j^{\dagger}\mathbf{T}_{jj}\boldsymbol{\omega}_j}} = \boldsymbol{v}_i^{\dagger}\boldsymbol{\Pi}_{ij}\boldsymbol{v}_j, \qquad i,j \in [1,n],\ i \neq j \tag{4.23}$$

To quantify the overall degree of correlation of all data sets for one given set of projection vectors $\boldsymbol{\omega}_1, ..., \boldsymbol{\omega}_n$ one can use for instance the geometrical coherence mean

$$\rho_{geom(\boldsymbol{\omega}_{MB})} = \left[\prod_{i=1}^{n}\prod_{j=i+1}^{n} |\gamma_{ij}(\boldsymbol{\omega}_i, \boldsymbol{\omega}_j)|\right]^{\frac{2}{n(n-1)}} \qquad \boldsymbol{\omega}_{MB} = \begin{bmatrix} \boldsymbol{\omega}_1 \\ \vdots \\ \boldsymbol{\omega}_n \end{bmatrix} \tag{4.24}$$

where $\boldsymbol{\omega}_{MB}$ represents the *multi–baseline projection vector* containing the individual projection vectors. Alternatively, the arithmetical coherence mean can be used:

$$\rho_{arithm(\boldsymbol{\omega}_{MB})} = \frac{2}{n(n-1)}\sum_{i=1}^{n}\sum_{j=i+1}^{n} |\gamma_{ij}(\boldsymbol{\omega}_i, \boldsymbol{\omega}_j)| \tag{4.25}$$

The relationship between these multi–baseline coherence indicators is given by

$$0 \leq \rho_{geom(\boldsymbol{\omega}_{MB})} \leq \rho_{arithm(\boldsymbol{\omega}_{MB})} \leq 1 \quad \forall\ \boldsymbol{\omega}_{MB} \tag{4.26}$$

While in general one can use individual projection vectors $\boldsymbol{\omega}_i$ for every track, often a single projection vector is used ($\boldsymbol{\omega}_i = \boldsymbol{\omega}_j = \boldsymbol{\omega}$).

4.3 Polarimetric Stationarity Conditions

One often used assumption of interferometry is the stationarity of the scattering mechanisms: in the absolute scattering mechanism amplitude and phase as well as the relative polarization. This assumption, also known as *polarimetric stationarity hypothesis* [39,40], can usually be expected to hold in case of distributed media, but it does not apply in case of significant temporal changes and for certain scattering media (e.g. urban areas or few strong point scatterers) with large incidence angle differences.
First and foremost, *polarimetric stationarity* (PS) expresses itself in equal polarimetric coherency matrix expectations:

$$E[\mathbf{T}_{11}] = E[\mathbf{T}_{22}] \tag{4.27}$$

Ferro-Famil proposed in [39] the normalized maximum likelihood (ML) ratio test for PS:

$$\Lambda_{PS} = \frac{\sqrt{|\mathbf{T}_{11}|}\sqrt{|\mathbf{T}_{22}|}}{|\hat{\mathbf{T}}_3|}, \qquad \text{with } \hat{\mathbf{T}}_3 = \frac{\mathbf{T}_{11} + \mathbf{T}_{22}}{2} \tag{4.28}$$

where $\hat{\mathbf{T}}_3$ is the ML estimate of $E[\mathbf{T}_{11}] = E[\mathbf{T}_{22}]$.
Thus, the coherence can be computed by

$$\gamma_{PS(\boldsymbol{\omega}_1,\boldsymbol{\omega}_2)} = \frac{\boldsymbol{\omega}_1^\dagger \boldsymbol{\Omega}_{12} \boldsymbol{\omega}_2}{\sqrt{\boldsymbol{\omega}_1^\dagger \hat{\mathbf{T}}_3 \boldsymbol{\omega}_1 \boldsymbol{\omega}_2^\dagger \hat{\mathbf{T}}_3 \boldsymbol{\omega}_2}} \quad \Longleftrightarrow \quad \gamma_{PS(\boldsymbol{v}_1,\boldsymbol{v}_2)} = \boldsymbol{v}_1^\dagger \widetilde{\boldsymbol{\Pi}} \boldsymbol{v}_2 \tag{4.29}$$

where $\widetilde{\boldsymbol{\Pi}} = \hat{\mathbf{T}}_3^{-1/2} \boldsymbol{\Omega}_{12} \hat{\mathbf{T}}_3^{-1/2}$.
For equal projection vectors, $\boldsymbol{\omega}_1 = \boldsymbol{\omega}_2 = \boldsymbol{\omega}$, (4.29) can be reduced to

$$\gamma_{PS(\boldsymbol{\omega},\boldsymbol{\omega})} = \frac{\boldsymbol{\omega}^\dagger \boldsymbol{\Omega}_{12} \boldsymbol{\omega}}{\boldsymbol{\omega}^\dagger \hat{\mathbf{T}}_3 \boldsymbol{\omega}} \quad \Longleftrightarrow \quad \gamma_{PS(\boldsymbol{v},\boldsymbol{v})} = \boldsymbol{v}^\dagger \widetilde{\boldsymbol{\Pi}} \boldsymbol{v} \tag{4.30}$$

so that

$$|\gamma_{PS(\boldsymbol{\omega},\boldsymbol{\omega})}| \leq |\gamma_{(\boldsymbol{\omega},\boldsymbol{\omega})}| \qquad \text{and} \qquad \arg \gamma_{PS(\boldsymbol{\omega},\boldsymbol{\omega})} = \arg \gamma_{(\boldsymbol{\omega},\boldsymbol{\omega})} \tag{4.31}$$

since the numerators of $\gamma(\boldsymbol{\omega},\boldsymbol{\omega})$ and $\gamma_{PS}(\boldsymbol{\omega},\boldsymbol{\omega})$ are the same while the denominators differ, and since the geometrical mean is less or equal to the arithmetical mean:

$$\sqrt[2]{(\boldsymbol{\omega}^\dagger \mathbf{T}_{11} \boldsymbol{\omega})(\boldsymbol{\omega}^\dagger \mathbf{T}_{22} \boldsymbol{\omega})} \leq \frac{(\boldsymbol{\omega}^\dagger \mathbf{T}_{11} \boldsymbol{\omega}) + (\boldsymbol{\omega}^\dagger \mathbf{T}_{22} \boldsymbol{\omega})}{2} = \boldsymbol{\omega}^\dagger \hat{\mathbf{T}}_3 \boldsymbol{\omega} \tag{4.32}$$

One useful property of this assumption is the equality of the scattering mechanism projection vectors for both the general coherency matrix and the coherency contraction (cf. (4.12)):

$$\text{PS} \quad \rightarrow \quad (\boldsymbol{\omega}_1 = \boldsymbol{\omega}_2 \iff \boldsymbol{v}_1 = \boldsymbol{v}_2) \tag{4.33}$$

This means that if the projection vectors of the PolInSAR coherency matrix are equal, the projection vectors of the coherency contraction are equal too. Otherwise it is possible that although $\boldsymbol{\omega}_1 = \boldsymbol{\omega}_2$, the contraction matrix projection vectors are not equal, $\boldsymbol{v}_i \neq \boldsymbol{v}_j$, and vice versa.
However, the constraint (4.27) does not simplify the form of $\boldsymbol{\Omega}$. Even more, under the PS condition (4.27) the degree of coherence depends on the ordering of projection vectors, i.e. the polarization projection vectors at the two images might not commute under the degree of coherence generation function:

$$|\gamma_{PS(\boldsymbol{\omega}_i,\boldsymbol{\omega}_j)}| \neq |\gamma_{PS(\boldsymbol{\omega}_j,\boldsymbol{\omega}_i)}|, \qquad \text{where } \|\boldsymbol{\omega}_i\| = \|\boldsymbol{\omega}_j\| = 1,\ \arg(\boldsymbol{\omega}_i^\dagger \boldsymbol{\omega}_j) = 0 \tag{4.34}$$

This means that despite of the equality of polarimetric signatures of the two images, the coherence magnitude will be in general different if one exchanges the polarizations in the two images. This is to a certain degree counter–intuitive and needs further examination.
Let the *interferometrically polarimetric stationarity* (IPS) condition be given by

$$E[\gamma_{PS(\boldsymbol{\omega}_1,\boldsymbol{\omega}_2)}] = E[\gamma_{PS(\boldsymbol{\omega}_2,\boldsymbol{\omega}_1)}] \tag{4.35}$$

which can be reduced to

$$\boldsymbol{\omega}_1^\dagger E[\boldsymbol{\Omega}_{12}] \boldsymbol{\omega}_2 = \boldsymbol{\omega}_2^\dagger E[\boldsymbol{\Omega}_{12}] \boldsymbol{\omega}_2, \qquad \arg(\boldsymbol{\omega}_1^\dagger \boldsymbol{\omega}_2) = 0 \tag{4.36}$$

Condition	$\mathbf{T}_{11} = \mathbf{T}_{22}$	$\lvert\gamma_{(\boldsymbol{\omega}_1,\boldsymbol{\omega}_2)}\rvert = \lvert\gamma_{(\boldsymbol{\omega}_2,\boldsymbol{\omega}_1)}\rvert$
General case	-	-
Polarimetric Stationarity (PS)	✓	-
Not relevant	-	✓
Interf. Pol. Stationarity (IPS)	✓	✓

Table 4.1: Polarimetric stationarity conditions.

Using the singular value decomposition

$$E[\boldsymbol{\Omega}_{12}] = \mathbf{U}\boldsymbol{\Lambda}\mathbf{V}^\dagger, \quad \mathbf{U}\mathbf{U}^\dagger = \mathbf{V}\mathbf{V}^\dagger = \mathbf{I},\ \boldsymbol{\Lambda} = \mathrm{diag}(\lambda_i) \tag{4.37}$$

one can show that (4.35) is valid if and only if

$$\mathbf{U}\mathbf{V}^\dagger = \mathbf{I} \tag{4.38}$$

so that

$$E[\boldsymbol{\Omega}_{12}]E[\boldsymbol{\Omega}_{12}^\dagger] = E[\boldsymbol{\Omega}_{12}^\dagger]\mathbf{E}[\boldsymbol{\Omega}_{12}] \tag{4.39}$$

This shows that for IPS to be valid, the expectation of $\boldsymbol{\Omega}_{12}$ needs to be a normal matrix. Similarly one can show that the expectation of $\boldsymbol{\Pi}$ also needs to be a normal matrix for IPS.
The normalized ML ratio test for IPS is given by [39]

$$\Lambda_{IPS} = \Lambda_{PS}\frac{|\mathbf{I} - \hat{\mathbf{P}}|}{|\mathbf{I} - \widetilde{\boldsymbol{\Pi}}\widetilde{\boldsymbol{\Pi}}^\dagger|}, \qquad \text{with } \widetilde{\boldsymbol{\Pi}} = \mathbf{T}_3^{-1/2}\boldsymbol{\Omega}\mathbf{T}_3^{-1/2}, \hat{\mathbf{P}} = \frac{\widetilde{\boldsymbol{\Pi}}\widetilde{\boldsymbol{\Pi}}^\dagger + \widetilde{\boldsymbol{\Pi}}^\dagger\widetilde{\boldsymbol{\Pi}}}{2} \tag{4.40}$$

The proper examination of the implications of IPS requires the introduction of coherence sets and coherence optimization methods, which are presented in the following sections. To summarize the common configuration of PolInSAR data, Table 4.1 presents the permutations of polarimetric stationarity conditions and their denotations.

4.3.1 Media Symmetries in PolInSAR Data

Polarimetric reciprocity and scattering symmetries are often taken for granted to focus on the most valuable information in the data. In this thesis, the media of interest will be considered to fulfil the reciprocity and the reflection symmetry conditions (after calibration and transformation into the reflection symmetric form). A single PolSAR coherency matrix has therefore the expectation matrix

$$E[\mathbf{T}_3] = \begin{bmatrix} A & D + iE & \\ D - iE & B & 0 \\ 0 & 0 & C \end{bmatrix} \tag{4.41}$$

A PolInSAR coherency matrix under such conditions has 20 degrees of freedom and the expectation matrices [89]

$$E[\mathbf{T}_{11}] = \begin{bmatrix} A_1 & D_1 + iE_1 & 0 \\ D_1 - iE_1 & B_1 & 0 \\ 0 & 0 & C_1 \end{bmatrix},\ E[\mathbf{T}_{22}] = \begin{bmatrix} A_2 & D_2 + iE_2 & 0 \\ D_2 - iE_2 & B_2 & 0 \\ 0 & 0 & C_2 \end{bmatrix}, \tag{4.42}$$

$$E[\mathbf{\Omega}_{12}] = \begin{bmatrix} F+iG & L+iM & 0 \\ N+iO & H+iI & 0 \\ 0 & 0 & J+iK \end{bmatrix} \tag{4.43}$$

Naturally, under the PS, reciprocity and reflection symmetry conditions, the number of degrees of freedom of $E[\mathbf{T}]$ is reduced to 15.

4.4 Coherence Set Theory

InSAR provides the possibility to measure a single scalar complex coherence value depending on the system acquisition geometry and the transmit and receive polarizations. PolInSAR provides the possibility to measure the coherence value for any polarization combination. Up to now we have considered PolInSAR coherences as scalar values in dependence of polarization. The continuous polarization space enables us to use the polarization diversity and to consider the set of all coherences as a continuous entity. We will refer to the set of all coherences in the following as the *coherence set*. It has been identified that the coherence set is directly connected with the mathematical concept of the *numerical range* (also known as *field of values*) of the contraction matrix.
This section aims to present some theoretical aspects of the PolInSAR coherence set. The first part of this section deals with the different definitions of the numerical range. The second and third parts present principles to extract information about the coherence set geometry and density in the complex coherence plane.

4.4.1 The Numerical Range

In a series of conference proceedings papers, Tabb and Flynn presented techniques for analyzing and processing PolInSAR data based on the numerical range of the contraction matrix. They presented methods to extract the shape of the coherence region in the complex plane [42], a decomposition based on interferometric phase diversity [143], a decomposition of the shape into principal sub–shapes [142], and the reduction of SNR decorrelation in the coherence shape [142]. Colin analyzed the numerical range for deterministic targets and high resolution imagery [29, 28]. The numerical radius has been used to optimize the coherence magnitude [29, 95]. Approaches have also been developed to extract from coherence sets and coherence shapes parameters related to physical properties of scattering media [97, 96, 81].
All of these methods assumed at least the polarimetric stationarity. However, the theoretical aspects behind these methods were often presented in an insufficient form. To fill this gap, mathematical basics of the numerical range in relation to the PolInSAR coherence set have been independently presented at the same time by Colin [27] and Neumann *et al.* [98].
Based on the conditions of coherence computation, one can distinguish the following coherence set definitions.

Two Scattering Mechanisms (2SM) Coherence Sets

The set of all coherences for all possible polarization projection vectors $\boldsymbol{\omega}_1, \boldsymbol{\omega}_2$ is given by

$$\Gamma = \{\gamma_{(\boldsymbol{\omega}_1, \boldsymbol{\omega}_2)} : \boldsymbol{\omega}_1, \boldsymbol{\omega}_2 \in \mathbb{C}^3, \boldsymbol{\omega}_1^\dagger \boldsymbol{\omega}_1 = \boldsymbol{\omega}_2^\dagger \boldsymbol{\omega}_2 = 1\}$$

$$= \{\boldsymbol{v}_1^\dagger \boldsymbol{\Pi} \boldsymbol{v}_2 : \boldsymbol{v}_1, \boldsymbol{v}_2 \in \mathbb{C}^3, \boldsymbol{v}_1^\dagger \boldsymbol{v}_1 = \boldsymbol{v}_2^\dagger \boldsymbol{v}_2 = 1\} \tag{4.44}$$

This is the most general coherence set formulation without any mathematical constraints. Its equivalent in mathematics is a union of *q–numerical ranges* [98]:

$$\Gamma = \bigcup_{q \in \mathbb{C}, |q| \leq 1} \mathcal{W}_q(\boldsymbol{\Pi}) \tag{4.45}$$

where $\mathcal{W}_q(\mathbf{A})$ is the q–numerical range of a matrix $\mathbf{A}$ [59]:

$$\mathcal{W}_q(\mathbf{A}) = \{\boldsymbol{y}^\dagger \mathbf{A} \boldsymbol{x} : \boldsymbol{x}, \boldsymbol{y} \in \mathbb{C}^n, \boldsymbol{y}^\dagger \boldsymbol{y} = \boldsymbol{x}^\dagger \boldsymbol{x} = 1, \boldsymbol{y}^\dagger \boldsymbol{x} = q\} \tag{4.46}$$

As it can be seen, (4.44) and (4.45) are equivalent (substitute $\boldsymbol{x}, \boldsymbol{y}$ with $\boldsymbol{v}_1, \boldsymbol{v}_2$ and $\mathbf{A}$ with $\boldsymbol{\Pi}$). This set is represented by a filled disk in the complex coherence plane, as shown in Fig. 4.2.a). This implies that we loose the interferometric phase sensitivity since it is possible to introduce an arbitrary phase shift θ between the projection vectors: $\arg q = \arg \boldsymbol{v}_1^\dagger \boldsymbol{v}_2 = \theta$. This problem has also been recognized in [22]. In order to break the phase ambiguity the constraint $\arg(\boldsymbol{v}_1, \boldsymbol{v}_2) = 0$ was introduced. This corresponds to the restriction of q to the non–negative real space.
Introducing into the coherence computation (4.13) the constraint $\arg \boldsymbol{v}_1^\dagger \boldsymbol{v}_2 \in \mathbb{R}^{\geq 0}$ one can define the *most general phase ambiguity free* coherence set Γ_{2SM}. The subscript expresses the usage of two scattering mechanisms (SM) for coherence computation.

$$\Gamma_{2SM} = \bigcup_{q \in \mathbb{R}, 0 \leq q \leq 1} \mathcal{W}_q(\boldsymbol{\Pi}) = \{\boldsymbol{v}_1^\dagger \boldsymbol{\Pi} \boldsymbol{v}_2 : \boldsymbol{v}_1, \boldsymbol{v}_2 \in \mathbb{C}^3, q \in [0,1], \boldsymbol{v}_1^\dagger \boldsymbol{v}_1 = \boldsymbol{v}_2^\dagger \boldsymbol{v}_2 = 1, \boldsymbol{v}_1^\dagger \boldsymbol{v}_2 = q\} \tag{4.47}$$

Although this given coherence set is phase ambiguity free, it is still not the best representation of the PolInSAR data set. For instance, this coherence set always includes the zero–coherence point independently of the contraction matrix $\boldsymbol{\Pi}$. This is due to the fact that for every vector $\boldsymbol{v}_2$ one can always find a vector $\boldsymbol{v}_1$ so that $\boldsymbol{v}_1$ is orthogonal to the vector $\boldsymbol{\Pi} \boldsymbol{v}_2$ leading to $\boldsymbol{v}_1^\dagger \boldsymbol{\Pi} \boldsymbol{v}_2 = 0$.

One Scattering Mechanism (1SM) Coherence Sets

2SM coherence sets contain not only meaningful information but also irrelevant coherence set regions (coherences at zero and around). In addition, coherence sets with 2 projection vectors are more complex to handle and to interpret. Therefore, usually the projection vectors are forced to be equal ($\boldsymbol{\omega}_1 = \boldsymbol{\omega}_2$), to obtain a single *scattering mechanism* (1SM) coherence set. In the general case, using equal projection vectors, the 1SM coherence is given by

$$\gamma_{1SM(\boldsymbol{\omega})} = \frac{\boldsymbol{\omega}^\dagger \boldsymbol{\Omega}_{12} \boldsymbol{\omega}}{\sqrt{\boldsymbol{\omega}^\dagger \mathbf{T}_{11} \boldsymbol{\omega} \boldsymbol{\omega}^\dagger \mathbf{T}_{22} \boldsymbol{\omega}}}, \quad \boldsymbol{\omega}^\dagger \boldsymbol{\omega} = 1 \tag{4.48}$$

Setting $\boldsymbol{v} = \frac{\sqrt{\mathbf{T}_{22}} \boldsymbol{\omega}}{\sqrt[4]{\boldsymbol{\omega}^\dagger \mathbf{T}_{11} \boldsymbol{\omega} \boldsymbol{\omega}^\dagger \mathbf{T}_{22} \boldsymbol{\omega}}}$ and $\mathbf{H} = \mathbf{T}_{22}^{-\frac{1}{2}} \mathbf{T}_{11}^{\frac{1}{2}}$, (4.48) can be reformed into:

$$\gamma_{1SM(\boldsymbol{v})} = \boldsymbol{v}^\dagger \mathbf{H} \boldsymbol{\Pi} \boldsymbol{v}, \quad |\boldsymbol{v}^\dagger \mathbf{H} \boldsymbol{v}| = 1 \tag{4.49}$$

(4.48) and (4.49) are general coherence definitions restricting the parameter space to equal projection vectors $\boldsymbol{\omega}$ and $\boldsymbol{v}$. No approximations are involved up to now. In numerical range

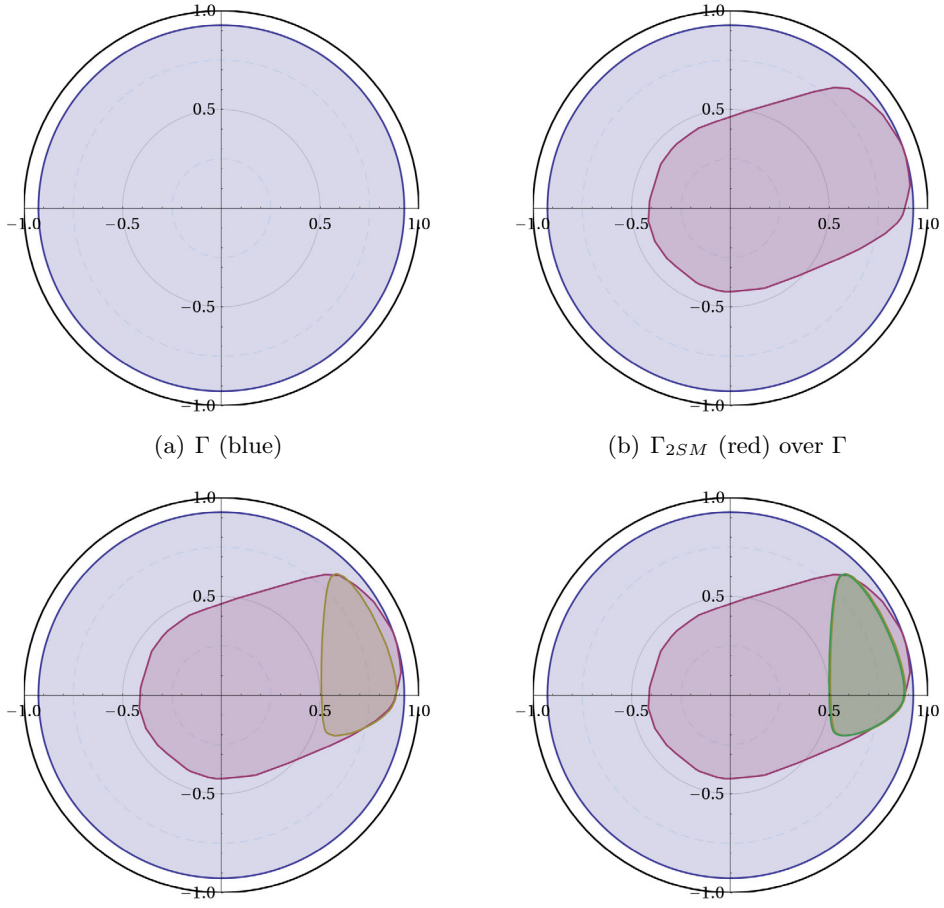

(a) Γ (blue)

(b) Γ_{2SM} (red) over Γ

(c) Γ_{1SM} (brown) over Γ_{2SM} and Γ

(d) Γ_{PS} (green) over Γ_{1SM}, Γ_{2SM} and Γ

Figure 4.2: Coherence sets according to different definitions: (a) general phase-ambiguous 2SM coherence set Γ (blue), (b) phase–ambiguity free 2SM coherence set Γ_{2SM} (red), (c) 1SM coherence set Γ_{1SM} (brown), (d) 1SM coherence set under PS assumption Γ_{PS} (green). Γ_{PS} perfectly overlaps Γ_{1SM} showing that the PS assumption is valid for this data point.

theory, the coherence set Γ_{1SM} of all γ_{1SM} can be represented by the *generalized inner product numerical range*

$$\mathcal{W}_H(\mathbf{A}) = \{\boldsymbol{x}^\dagger \mathbf{H}\mathbf{A}\boldsymbol{x} : \boldsymbol{x} \in \mathbb{C}^n, |\boldsymbol{x}^\dagger \mathbf{H}\boldsymbol{x}| = 1\} \tag{4.50}$$

so that

$$\Gamma_{1SM} = \{\boldsymbol{v}^\dagger \mathbf{H}\boldsymbol{\Pi}\boldsymbol{v} : \boldsymbol{v} \in \mathbb{C}^3, |\boldsymbol{v}^\dagger \mathbf{H}\boldsymbol{v}| = 1\} = \mathcal{W}_H(\boldsymbol{\Pi}) \tag{4.51}$$

Note that $\mathbf{H}$ is in general neither Hermitian nor positive definite. However, $\mathbf{T}_{11}$ and $\mathbf{T}_{22}$ are both positive definite after the appropriate multi–looking and have over natural environments very similar eigenvectors. Hence, $\mathbf{H}$ is in practice positive definite ($\min(\mathrm{Re}\,\lambda_i) > 0$). Even more, $\mathbf{H}$ is very close to Hermitian since the eigenvalues $\lambda_i (i \in \{1,2,3\})$ of $\mathbf{H}$ fulfil $|\mathrm{Re}\,\lambda_i| \gg |\mathrm{Im}\,\lambda_i|$.
In case of polarimetric stationarity ($E[\mathbf{T}_{11}] = E[\mathbf{T}_{22}]$) the matrix $\mathbf{H}$ tends towards the identity matrix and the condition (4.33) is valid. The coherence set

$$\Gamma_{PS} = \{\gamma_{PS(\boldsymbol{v})} : \boldsymbol{v} \in \mathbb{C}^3, \|\boldsymbol{v}\| = 1\} = \mathcal{W}(\boldsymbol{\Pi}) \tag{4.52}$$

is then equivalent to the standard *numerical range* $\mathcal{W}(\mathbf{A})$, defined as

$$\mathcal{W}(\mathbf{A}) = \{\boldsymbol{x}^\dagger \mathbf{A}\boldsymbol{x} : \boldsymbol{x} \in \mathbb{C}^n, \boldsymbol{x}^\dagger \boldsymbol{x} = 1\} \tag{4.53}$$

The standard numerical range (in the following it will be just called *numerical range*) of a matrix is a well developed concept in matrix analysis [59], where methods exist to interrelate properties of a matrix and its numerical range. Therefore, in the next sections only coherence sets consisting of the numerical range of a polarimetrically stationary (PS) PolInSAR coherency matrices will be presented.
One may note that if the PS condition is not fulfilled, the matrix $\boldsymbol{\Pi}$ can be slightly modified in order to use numerical range analysis techniques. The coherence set is then given by

$$\Gamma_{1SM} = \mathcal{W}_{\mathbf{H}}(\boldsymbol{\Pi}) \approx \mathcal{W}(\widetilde{\boldsymbol{\Pi}}), \qquad \text{with } \widetilde{\boldsymbol{\Pi}} = \mathbf{S}\boldsymbol{\Pi}\mathbf{S}^{-1} \tag{4.54}$$

where $\mathbf{S}$ is obtained from [98]

$$\frac{1}{2}(\mathbf{H} + \mathbf{H}^\dagger) = \mathbf{S}^\dagger \mathbf{S} \tag{4.55}$$

The potential additional validity of IPS does not require the modification of coherence set definitions. The IPS condition does influence the form of $\boldsymbol{\Pi}$ and the resulting coherence set, but not the definition.

4.4.2 Coherence Set Geometry

The PolInSAR coherence set can be understood as the projection of the PolInSAR coherency contraction onto the complex coherence plane. Based on the properties of $\boldsymbol{\Pi}$ and its numerical range, the geometrical properties of the coherence set region in the complex coherence plane can be predicted.
Two important characteristics of the numerical range of a matrix $\mathbf{A}$ are the *numerical radius*

$$r_{\mathcal{W}}(\mathbf{A}) = \max\{|z| : z \in \mathcal{W}(\mathbf{A})\} \tag{4.56}$$

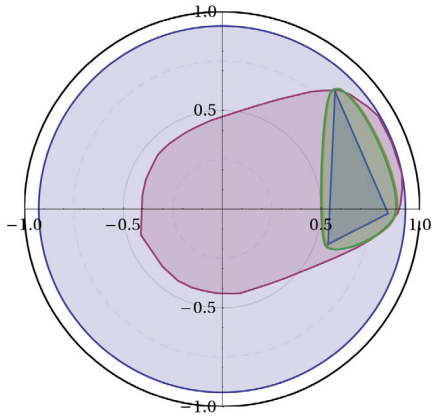

Figure 4.3: Coherence set Γ_{IPS} under the IPS condition over Γ_{PS}, Γ_{1SM}, Γ_{2SM}, Γ with reference to Fig. 4.2.

and the minimal distance to the origin denoted by

$$\widetilde{r}_{\mathcal{W}}(\mathbf{A}) = \min\{|z| : z \in \mathcal{W}(\mathbf{A})\} \tag{4.57}$$

Numerical algorithms exist to compute $r_{\mathcal{W}}(\mathbf{A})$ and $\widetilde{r}_{\mathcal{W}}(\mathbf{A})$ (e.g. [165, 87]). Within a coherence set, the numerical radius is the maximal possible degree of coherence, and methods based on numerical radii have been developed to obtain optimal polarizations and coherences [29, 95].
The numerical range has always a convex filled shape and is always continuous, except in the trivial case of one discrete point. Numerical approaches for the computation of the numerical range boundary $\boldsymbol{\mathcal{S}}(\mathbf{A})$ [59] have also been applied to PolInSAR data to obtain the coherence set shape and region [42]. This method computes a predefined number of points on the outer border of the coherence region.
The phase diversity method [143] is connected with the *angular numerical range*:

$$\mathcal{W}'(\mathbf{A}) = \{\boldsymbol{x}^{\dagger}\mathbf{A}\boldsymbol{x} : \boldsymbol{x} \in \mathbb{C}^n, \boldsymbol{x} \neq \mathbf{0}\} \tag{4.58}$$

In the complex plane, this set has an unbounded cone–shaped form with the vertex in the origin. The aim of phase diversity is to compute the phase extremes and the corresponding polarizations. These phases, $\phi_{\mathcal{W}_1}$ and $\phi_{\mathcal{W}_2}$, define the border rays of the angular numerical range.
The numerical range radii and phase extrema are real valued quantities. With the knowledge of the related projection vectors one can compute the complex coherence values of these quantities and their locations in the complex coherence plane $\gamma_{r_{\mathcal{W}}}, \gamma_{\widetilde{r}_{\mathcal{W}}}, \gamma_{\phi_{\mathcal{W}_1}}, \gamma_{\phi_{\mathcal{W}_2}}$.
Using the *Schur* decomposition of $\mathbf{A}$, the numerical range can be decomposed into basic ellipsoid structures [142]. However, this decomposition into ellipses depends on the polarization basis of the matrix: although the ellipse foci are invariant to polarization basis transformations, the ellipticities are polarization basis dependent. All ellipse foci represent the set of eigenvalues of $\mathbf{A}$.
Some further numerical range properties help to relate the PolInSAR coherency matrix structure to the coherence set shape:

- The numerical range of a matrix includes the numerical ranges of principal sub–matrices.
- The numerical range of a direct sum of matrices is the convex hull of these matrices.
- The numerical range of a complex 2×2 matrix has always the shape of an ellipse (possibly degenerated into a line segment or a point). Ellipse characteristics like its position, orientation and ellipticity can be directly read out from the matrices.
- After Schur decomposition, the foci of the 2×2 principal matrix ellipses are equal to the pair–wise eigenvalues of $\mathbf{\Pi}$, determining the orientation of the ellipses. Since the Schur decomposition is not invariant to polarization, the ellipticities of these ellipses depend on the polarization basis.
- Any vertices on the outer boundary of the numerical range shape correspond to normal eigenvalues of the matrix.
- The numerical range shape of a normal matrix is given by the convex hull of its eigenvalues. For matrices with up to four dimensions, this relationship can be reversed. Note that a scalar can also be interpreted as a normal matrix. For instance, to obtain a line structured coherence set requires therefore a normal $\mathbf{\Pi}$ matrix.
- The numerical range is invariant to unitary basis transformations.

Based on these properties one can reason about the coherence set geometry of the PolInSAR coherency matrix. Fig. 4.4 shows all possible coherence set shapes using equal projection vectors and assuming polarimetric stationarity (Γ_{PS}). This figure shows the outer coherence shapes $\boldsymbol{\mathcal{S}}(\mathbf{\Pi})$, as well as the inner coherence set shapes of 2×2 principal sub–matrix ellipses after the Schur decomposition and the eigenvalues of $\mathbf{\Pi}$ which are at the same time the foci of the ellipses. 6 classes of coherence shapes are identified:

- Type A: general case
- Type B: $\mathbf{\Pi}$ has one normal eigenvalue, leading to a vertex at the border. This means the matrix $\mathbf{\Pi}$ can be brought into block–sum form consisting of a 2×2 matrix and a scalar. These two blocks are related to orthogonal polarization spaces and the coherences of these blocks do not correlate with each other.
- Type C: $\mathbf{\Pi}$ is a normal matrix which is diagonalizable by a unitary transformation. The coherences are uncorrelated for the given orthogonal eigenpolarizations.
- Type D: The outer shape is an ellipse of a 2×2 sub–matrix. The third eigenvalue is located inside the ellipse and it can be a normal or a non–normal eigenvalue. This shape is a special case of both Type A and Type B shapes.
- Type E: $\mathbf{\Pi}$ is a normal matrix with co–linear normal eigenvalues. This means that all interferometric coherences are linear combinations of two coherence locations, in dependence of the polarization.
- Type F: The coherence shape degenerates to a single point, implying that the interferometric coherence is independent of polarization.

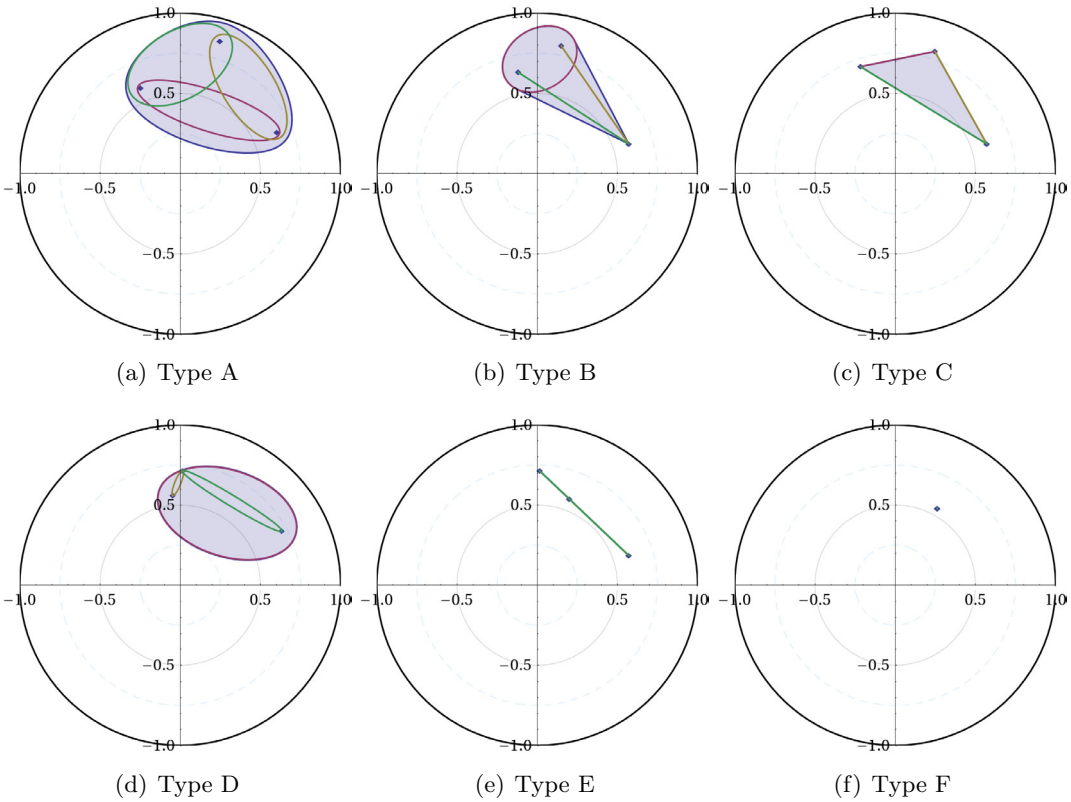

(a) Type A (b) Type B (c) Type C

(d) Type D (e) Type E (f) Type F

Figure 4.4: Possible coherence set shapes $\boldsymbol{\mathcal{S}}(\mathbf{\Pi})$ in the complex coherence plane.

Assumption	Possible Coherence Shapes
Reflection symmetry	B, C, D, E, F
Rotation symmetry	B, C, D, E, F
Azimuthal symmetry	C, E, F
Centrical symmetry	C, E, F
PS	A, B, C, D, E, F
IPS	C, E, F

Table 4.2: Relations between coherence shape types and PolInSAR approximations.

Under the common assumptions of reciprocity and reflection symmetry the coherency contraction is given by

$$E[\mathbf{\Pi}] = \begin{bmatrix} \gamma_{11} & \rho_{12} & 0 \\ \rho_{21} & \gamma_{22} & 0 \\ 0 & 0 & \gamma_{33} \end{bmatrix} = \boldsymbol{\mathcal{E}} \oplus x \tag{4.59}$$

where $\boldsymbol{\mathcal{E}}$ is the 2×2 linearly co–polarized coherency ellipse matrix, x the cross–polarized coherence, and $\tilde{\gamma} = \frac{1}{3}\,\mathrm{trace}\, E[\mathbf{\Pi}]$ the center of the coherence set. The whole coherence set shape is formed as the convex hull over $\boldsymbol{\mathcal{E}}$ and x, as shown on an example in Fig. 4.5. The eigenvalues of $\boldsymbol{\mathcal{E}}$ provide the foci f_1, f_2 of the ellipse, and the spectrum (set of eigenvalues) of $E[\mathbf{\Pi}]$ is given by $\{f_1, f_2, x\}$.

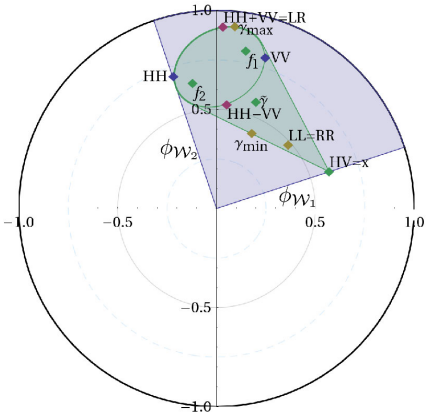

Figure 4.5: An example of a general coherence set geometry for a monostatic acquisition with reflection symmetry. The angular numerical range is shown in blue with the phase extrema $\phi_{\mathcal{W}_1}, \phi_{\mathcal{W}_2}$, the coherence set shape in green.

Under the IPS condition the coherency contraction is a normal matrix. Therefore, it is unitary equivalent to a diagonal matrix which can be obtained by polarization basis transformation:

$$\mathbf{U}E[\mathbf{\Pi}_{IPS}]\mathbf{U}^{\dagger} = \begin{bmatrix} \gamma_{11} & 0 & 0 \\ 0 & \gamma_{22} & 0 \\ 0 & 0 & \gamma_{33} \end{bmatrix} \tag{4.60}$$

The diagonal elements are the eigenvalues of $E[\mathbf{\Pi}_{IPS}]$ and span the coherence set in the complex coherence plane. Therefore, the coherence set under IPS is given in the general form by a triangle (possibly degenerated to a line or a point), where the vertices are given by the eigenvalues of $\mathbf{\Pi}$. For the example from Fig. 4.2, the coherence set under the IPS condition is shown in Fig. 4.3.
Summarizing, Table 4.2 presents the possible coherence set shape types for different media symmetries and polarimetric stationarity conditions.
To quantify the coherence set region shape using a few values, we proposed in [97] to approximate the coherence shape by an ellipsis in order to extract the important shape parameters, namely *pseudo–ellipticity*, *radial/tangential standard deviation relationship*, and *outward tendency*. Other parameter sets are possible.
However, despite the strong mathematical background of the numerical range properties of the PolInSAR coherence set geometry, interpretations of its properties might lead to unreliable conclusions and should be applied with precautions to physical problems. The extension of the coherence set region is more influenced by coherences with high noise (low backscattering energy, high phase noise, large coherence set region) than by coherences with low noise (high backscattering energy, low phase noise, compact coherence set region). Especially $\widetilde{r}_{\mathcal{W}}$, but also $\phi_{\mathcal{W}_1}, \phi_{\mathcal{W}_2}$ can be distorted by coherences for polarizations with high degree of noise. Therefore, it is important to consider instead the coherence set density with respect to both polarization and energy.

4.4.3 Coherence Set Density

Coherence set density is defined with respect to a frequency function. One approach is to consider the density of coherences in dependence of polarization density. It is the inverse of the coherence signature concept, as named by Sagués [130,129], which images the coherence value over the polarization angles. However, the interpretation of the coherence signature is less intuitive.
The polarization coherence set density is the imaging of the coherence density in the complex coherence circle in dependence of the polarization density. Given the polarization density $f_{\boldsymbol{\Psi}}(\boldsymbol{\omega})$ which is defined over the scattering polarization space $\boldsymbol{\Psi}$ and is independent of the scattering medium, the coherence polarization density is thus

$$f_{\gamma_{\boldsymbol{\Psi}}}(\gamma) = \int_{\boldsymbol{\omega}} \delta_{(\gamma-\gamma(\boldsymbol{\omega}))} f_{\boldsymbol{\Psi}(\boldsymbol{\omega})} d\boldsymbol{\Psi} \tag{4.61}$$

where $\delta_{(\gamma-\gamma(\boldsymbol{\omega}))}$ represents the delta function.
More reasonable is to consider coherence set density with respect to the backscattered energy. This approach can be related to the imaging of polarization signatures. Polarization signature, as introduced by van Zyl *et al.* in [163], image backscattered energy over the polarization angles. Coherence set densities image the backscattered energy (or polarization density) over the complex coherence plane. This imaging technique makes it possible to obtain a qualitative, visual interpretation of the constituents of the resolution cell: the spatial locations of dominant scattering centers and their polarization states. The formal definition of the coherence energy density can be given by

$$f_{\gamma_\sigma}(\gamma) = \int_{\boldsymbol{\omega}} \delta_{(\gamma-\gamma(\boldsymbol{\omega}))} \frac{\sigma_{(\boldsymbol{\omega})}}{\sigma_{tot}} f_{\boldsymbol{\Psi}(\boldsymbol{\omega})} d\boldsymbol{\Psi} \tag{4.62}$$

where

$$\sigma_{(\boldsymbol{\omega})} = \boldsymbol{\omega}^\dagger \mathbf{T}_3 \boldsymbol{\omega} \tag{4.63}$$

is the scattered energy at given polarization and

$$\sigma_{tot} = \int_{\boldsymbol{\omega}} \sigma_{(\boldsymbol{\omega})} f_{\boldsymbol{\Psi}(\boldsymbol{\omega})} d\boldsymbol{\Psi} = \operatorname{trace} \mathbf{T}_3 \tag{4.64}$$

represents the total scattered energy or the span of the resolution cell. $\frac{\sigma_{(\omega)}}{\sigma_{tot}}$ represents the normalized polarization signature [163] if the scattering polarization space $\boldsymbol{\Psi}$ is given in terms of the polarization angles.
In practice, due to unavailability of closed form expressions for $f_{\gamma_{\boldsymbol{\Psi}}}(\gamma)$ and $f_{\gamma_\sigma}(\gamma)$, these functions need to be computed numerically in form of histograms of complex coherences over the defined parameter space.
However, the observed PolInSAR coherence set is only one realization of the true coherence set and needs further statistical assessment in order to evaluate the confidence in the coherences. Based on the SAR statistics in appendix A, we have derived a numerical approach for statistical coherence set analysis with respect to the polarization density which is presented in section A.2 [96]. As of now, the computation of coherence set densities and coherence set probability distributions (a–priori or a–posteriori) is prohibitively expensive and is, therefore, presented only briefly. To note is an alternative approach by

O. Stebler [141], where a rough region of confidence is drawn based on the amplitude and phase statistics of a few extrema coherences.
In summary, Fig. 4.6 shows different imaging possibilities of polarimetric and interferometric information of a single coherency matrix: (a) the polarization signature, (b) the coherence magnitude signature, (c) the coherence phase signature, (d) the coherence set geometry, (e) the coherence energy density, (f) the coherence set probability density function for 50 looks, (g) and the corresponding confidence regions corresponding to confidence levels $\alpha_i = 1 - \mathrm{erf}(i/\sqrt{2})$, for $i \in \{1, 2, 3, 4\}$, where erf() is the error function (i.e. $1 - \alpha_i \in \{68.27\%, 95.45\%, 99.73\%, 99.994\%\}$).

4.5 Coherence Optimization

By varying the transmission and reception polarization states, optimal scattering mechanisms with the highest interferometric coherence can be obtained. Optimizing the coherence provides the possibility to reduce the uncertainty in the interferometric phase estimation. Polarimetric coherence optimization can also be applied to vertically structured media to resolve the dominant scattering centers, as e.g. done for vegetation in [168] and for urban areas in [29]. Further on, coherence optimization techniques have been applied for phase unwrapping [101], DEM generation [129], forest mapping and classification [37], and polarimetric differential SAR interferometry [122, 123].
An optimization problem consists of three components:

- The *object function* $f(\boldsymbol{x})$, which has to be optimized (maximized or minimized).
- A set of unknown *variables* $\boldsymbol{x} = \{x_1, ..., x_n\}$ which represents the degrees of freedom of the object function.
- A set of *constraints* $g(\boldsymbol{x}) = \{g_1(\boldsymbol{x}), ..., g_m(\boldsymbol{x})\}$ which restricts the range of the variables (search space), enforcing reasonable (in our case physically possible) solutions. Constrained problems can often be transformed into unconstrained problems (modifying f and $\boldsymbol{x}$, while setting $g(\boldsymbol{x}) = \{\}$) with the help of Lagrange multipliers.

In these notations, a maximization problem can thus be given by

$$\underset{\boldsymbol{x}}{\mathrm{maximize}} \{ f(\boldsymbol{x}) : g_1(\boldsymbol{x}), ..., g_m(\boldsymbol{x}) \} \tag{4.65}$$

Different methods exist for solving optimization problems. One distinguishes between constrained vs. unconstrained optimization, global vs. local, analytical vs. iterative, linear vs. non–linear, continuous vs. discrete, etc. The goal is to find/develop an *effective* optimization method which suits the application needs. In case of SAR remote sensing data, the foremost priority is the optimization speed, as the optimization has to be applied for every pixel independently. In this section, we will at first review available coherence optimization methods, and later we will introduce and evaluate two new methods for multi–baseline coherence optimization.

4.5.1 Single–baseline Coherence Optimization

Most of the current airborne and spaceborne PolInSAR systems acquire data with spatial and temporal baseline separations. Two main coherence optimization criteria can be identified, depending on the baseline properties.

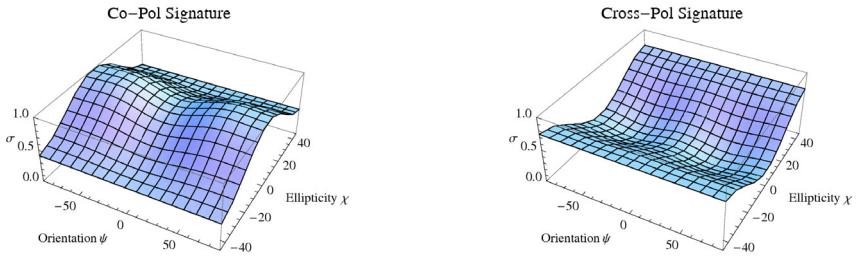

(a) Polarization signature

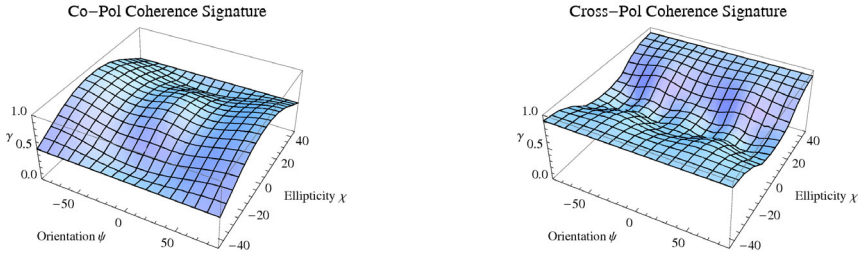

(b) Coherence magnitude signature

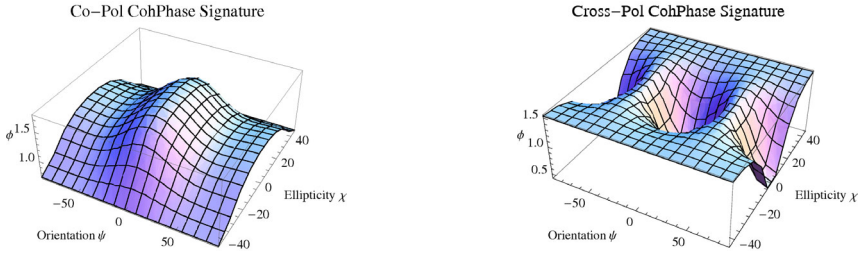

(c) Coherence phase signature

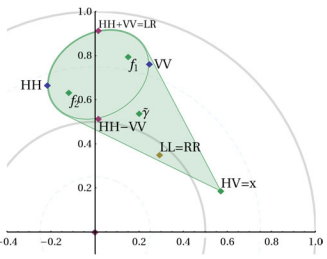

(d) Coherence set geometry

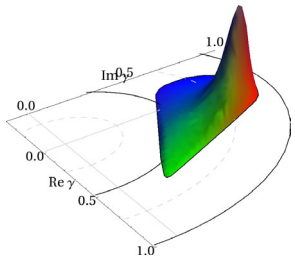

(e) Coherence energy density

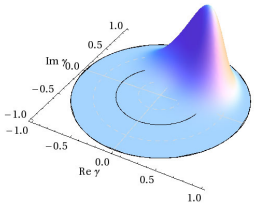

(f) A–priori probability distribution

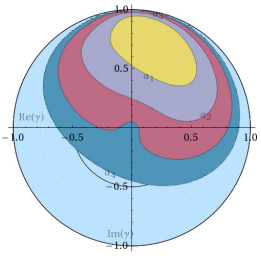

(g) Confidence regions

Figure 4.6: Imaging of polarimetric and interferometric information of one single data set: (a) the polarization signature, (b) the coherence magnitude signature, (c) the coherence phase signature, (d) the coherence set geometry, (e) the coherence energy density, (f) the coherence set probability density function for 50 looks, (g) and the corresponding confidence regions.

Optimization Criterion	Single Baseline (SB)	Multi Baseline (MB)
MSM	section 4.5.1, [21, 22]	section 4.5.2 [95]
ESM	section 4.5.1 [29]	section 4.5.2 [95]

Table 4.3: Table of Polarimetric Interferometric Coherence Optimization Techniques.

In certain cases it is meaningful to use slightly different polarizations (multiple scattering mechanisms, MSM) for different tracks to estimate the coherence of the dominant scattering centers. As an example, changes in the scattering behavior, caused by meteorological influences or vegetation growth between the acquisition times, will induce different polarization signatures for the same scattering structures. Also, a change of the incidence angle can slightly change the polarization of the optimal scattering mechanism. The optimization problem with a distinctive projection vector for every track is given by

$$\text{MSM: } \underset{\boldsymbol{\omega}_1,\boldsymbol{\omega}_2}{\text{maximize}} \{|\gamma(\boldsymbol{\omega}_1,\boldsymbol{\omega}_2)| : \boldsymbol{\omega}_1,\boldsymbol{\omega}_2 \in \mathbb{C}^3, \boldsymbol{\omega}_1^\dagger\boldsymbol{\omega}_1 = \boldsymbol{\omega}_2^\dagger\boldsymbol{\omega}_2 = 1, \arg\boldsymbol{\omega}_1^\dagger\boldsymbol{\omega}_2 = 0\} \quad (4.66)$$

Therefore, the search range space is given by the Γ_{2SM} coherence set, as presented in section 4.4.1 and shown for an example in Fig. 4.2.(b).
With more proximate baseline properties (insignificant changes in incidence angles and temporal variations with respect to media polarization properties) polarimetric stationarity of the medium can be assumed. Therefore, the induced polarization differences between the data sets are assumed to be only due to the thermal noise. To reduce the sensitivity of the optimization procedure to this noise, it is reasonable to use equal scattering mechanisms (ESM) for the coherence optimization. In this case the optimization problem is given by

$$\text{ESM: } \underset{\boldsymbol{\omega}}{\text{maximize}} \{|\gamma(\boldsymbol{\omega})| : \boldsymbol{\omega} \in \mathbb{C}^3, \boldsymbol{\omega}^\dagger\boldsymbol{\omega} = 1\} \quad (4.67)$$

The search range space of this optimization is restricted to the region of the Γ_{PS} coherence set, as presented in section 4.4.1 and in Fig. 4.2.(d).
Another reason to use a single projection vector for the optimization problem is a common desire to concentrate only on a minimal set of parameters with highest significance.
With the introduction of PolInSAR, an analytical method for MSM coherence optimization was presented by Cloude and Papathanassiou [21]. Since then, several other methods [130, 51, 115] have been proposed to solve the ESM coherence optimization problem. However, these methods deliver sub–optimal solutions. Finally, Colin *et al.* [29] presented a general iterative optimization routine for the ESM problem which computed the numerical radius of the coherency contraction matrix under the polarimetric stationarity assumption.

SB–MSM Optimization 1: Complex Lagrangian Approach

The first single–baseline PolInSAR coherence optimization procedure has been introduced by Cloude and Papathanassiou [21, 22, 105]. It optimizes the modulus of the covariance $\boldsymbol{\omega}_1^\dagger\boldsymbol{\Omega}_{12}\boldsymbol{\omega}_2$ for two datasets, while keeping the variances $\boldsymbol{\omega}_1^\dagger\mathbf{T}_{11}\boldsymbol{\omega}_1$ and $\boldsymbol{\omega}_2^\dagger\mathbf{T}_{22}\boldsymbol{\omega}_2$ constant. In [21], the modulus of the complex Lagrangian L is maximized by introducing the real valued multipliers λ_1, λ_2:

$$L = \boldsymbol{\omega}_i^\dagger\boldsymbol{\Omega}_{12}\boldsymbol{\omega}_2 - \lambda_1(\boldsymbol{\omega}_1^\dagger\mathbf{T}_{11}\boldsymbol{\omega}_1 - 1) - \lambda_2(\boldsymbol{\omega}_2^\dagger\mathbf{T}_{22}\boldsymbol{\omega}_2 - 1) \quad (4.68)$$

As it has been shown, the solution can be obtained by setting the partial derivatives of L with respect to variables $\lambda_1, \lambda_2, \boldsymbol{\omega}_1, \boldsymbol{\omega}_2$ to zero:

$$\frac{\partial L}{\partial \lambda_1} = \boldsymbol{\omega}_1^\dagger \mathbf{T}_{11} \boldsymbol{\omega}_1 - 1 = 0 \tag{4.69}$$

$$\frac{\partial L}{\partial \lambda_2} = \boldsymbol{\omega}_2^\dagger \mathbf{T}_{22} \boldsymbol{\omega}_2 - 1 = 0 \tag{4.70}$$

$$\frac{\partial L}{\partial \boldsymbol{\omega}_1^\dagger} = \boldsymbol{\Omega}_{12} \boldsymbol{\omega}_2 - \lambda_1 \mathbf{T}_{11} \boldsymbol{\omega}_1 = 0 \tag{4.71}$$

$$\frac{\partial L^\dagger}{\partial \boldsymbol{\omega}_2^\dagger} = \boldsymbol{\Omega}_{12}^\dagger \boldsymbol{\omega}_1 - \lambda_2^* \mathbf{T}_{22} \boldsymbol{\omega}_2 = 0 \tag{4.72}$$

Optimal SMs and the corresponding coherences are obtained from the resulting eigenvalue problems:

$$\mathbf{T}_{22}^{-1} \boldsymbol{\Omega}_{12}^\dagger \mathbf{T}_{11}^{-1} \boldsymbol{\Omega}_{12} \boldsymbol{\omega}_2 = \nu \boldsymbol{\omega}_2 \tag{4.73}$$

$$\mathbf{T}_{11}^{-1} \boldsymbol{\Omega}_{12} \mathbf{T}_{22}^{-1} \boldsymbol{\Omega}_{12}^\dagger \boldsymbol{\omega}_1 = \nu \boldsymbol{\omega}_1 \tag{4.74}$$

where $\nu = \lambda_1 \lambda_2^*$. Since $\mathbf{T}_{11}$ and $\mathbf{T}_{22}$ are non–singular, the inverses of these matrices exist. One can show that $\lambda_1 = \lambda_2 = \lambda$ by left multiplying (4.71) and (4.72) with $\boldsymbol{\omega}_1^\dagger$ and $\boldsymbol{\omega}_2^\dagger$, and using (4.69), (4.70). The eigenanalysis of (4.73) and (4.74) provides three positive real–valued eigenvalues ν_i which are related to pairs of eigenvectors $\boldsymbol{\omega}_{1_i}, \boldsymbol{\omega}_{2_i}$. The square roots of the eigenvalues is equal to the optimized coherence moduli:

$$|\gamma_{opt_i}| = \sqrt{\nu_i} \tag{4.75}$$

After phase ambiguity removal, the eigenvectors can be used to obtain the optimized complex coherences and the optimal phases.
In the following, two additional coherence optimization approaches will be presented. Method 2 reformulates the optimization problem to maximize the square of the coherence magnitude. Method 3 uses the phase ambiguity between the projection vectors to reduce the optimization problem of complex L in (4.68) to a real valued problem. All three optimization approaches lead to the same results.

SB–MSM Optimization 2: Cauchy–Schwartz Approach

Ferro-Famil *et al.* [38] presented an alternative derivation of the SB–MSM coherence optimization problem based on the Cauchy–Schwarz inequality. This derivation uses the coherency contraction matrix. The optimization of the coherence magnitude is equivalent to the optimization of the square of the coherence magnitude:

$$\underset{\boldsymbol{v}_1, \boldsymbol{v}_2}{\operatorname{argmax}}(|\gamma_{(\boldsymbol{v}_1, \boldsymbol{v}_2)}|) = \underset{\boldsymbol{v}_1, \boldsymbol{v}_2}{\operatorname{argmax}}(|\gamma_{(\boldsymbol{v}_1, \boldsymbol{v}_2)}|^2) \tag{4.76}$$

Note that $\boldsymbol{v}_i$ are directly related to $\boldsymbol{\omega}_i$ via (4.12) and the optimization in $\boldsymbol{v}$ is equivalent to optimization in $\boldsymbol{\omega}$ vectors. This optimization problem is related to the singular value decomposition (SVD) of the contraction:

$$\text{SVD:} \quad \boldsymbol{\Pi} = \mathbf{W}_1 \boldsymbol{\Sigma}^{1/2} \mathbf{W}_2^\dagger, \quad \boldsymbol{\Sigma} = \begin{bmatrix} \nu_1 & 0 & 0 \\ 0 & \nu_2 & 0 \\ 0 & 0 & \nu_3 \end{bmatrix} \tag{4.77}$$

where $\mathbf{W}_1, \mathbf{W}_2$ are unitary and contain the left and right eigenvectors of $\mathbf{\Pi}$ and $\mathbf{\Sigma}$ contains the non–negative real–valued singular values of $\mathbf{\Pi}$, i.e. the eigenvalues of $\mathbf{\Pi\Pi}^\dagger$ and $\mathbf{\Pi}^\dagger\mathbf{\Pi}$. Using the coherency contraction matrix the square of the coherence magnitude is given by

$$\nu = |\gamma_{(\boldsymbol{\omega}_1,\boldsymbol{\omega}_2)}|^2 = \gamma_{(\boldsymbol{\omega}_1,\boldsymbol{\omega}_2)}\gamma^\dagger_{(\boldsymbol{\omega}_1,\boldsymbol{\omega}_2)} = \boldsymbol{v}_1^\dagger\mathbf{\Pi}\boldsymbol{v}_2\boldsymbol{v}_2^\dagger\mathbf{\Pi}^\dagger\boldsymbol{v}_1 \leq \boldsymbol{v}_1^\dagger\mathbf{\Pi\Pi}^\dagger\boldsymbol{v}_1 \tag{4.78}$$

$$= \gamma^\dagger_{(\boldsymbol{\omega}_1,\boldsymbol{\omega}_2)}\gamma_{(\boldsymbol{\omega}_1,\boldsymbol{\omega}_2)} = \boldsymbol{v}_2^\dagger\mathbf{\Pi}^\dagger\boldsymbol{v}_1\boldsymbol{v}_1^\dagger\mathbf{\Pi}\boldsymbol{v}_2 \leq \boldsymbol{v}_2^\dagger\mathbf{\Pi}^\dagger\mathbf{\Pi}\boldsymbol{v}_2 \tag{4.79}$$

where the inequality is due to the *Cauchy–Schwarz inequality* [58,39]. Equality is achieved when the inner vector $\boldsymbol{v}_2$ is equal to one of the right eigenvectors of $\mathbf{\Pi}$, $\boldsymbol{w}_{2_i}$, or if $\boldsymbol{v}_1$ is equal to one of the left eigenvectors of $\mathbf{\Pi}$, $\boldsymbol{w}_{1_i}$. This leads to two eigenvalue problems

$$\mathbf{\Pi\Pi}^\dagger\boldsymbol{v}_1 = \nu\boldsymbol{v}_1 \tag{4.80}$$

$$\mathbf{\Pi}^\dagger\mathbf{\Pi}\boldsymbol{v}_2 = \nu\boldsymbol{v}_2 \tag{4.81}$$

where $\boldsymbol{v}_1, \boldsymbol{v}_2$ are the left and right eigenvectors of $\mathbf{\Pi}$ and ν is the singular value of $\mathbf{\Pi\Pi}^\dagger$. The optimal complex coherences are computed using the eigenvectors.

SB–MSM Optimization 3: Canonical Correlation Analysis (CCA) Approach

An alternative interpretation of the SB–MSM optimization has been presented by us [93, 95] which is based on the canonical correlation analysis (CCA) [61]. The complex Lagrange function (4.68) can be represented using a real valued function:

$$L_2 = \sum_{i=1}^{2}\sum_{j=1\neq i}^{2}\boldsymbol{\omega}_i^\dagger\mathbf{\Omega}_{ij}\boldsymbol{\omega}_j - \lambda\sum_{i=1}^{2}(\boldsymbol{\omega}_i^\dagger\mathbf{T}_{ii}\boldsymbol{\omega}_i - 1) \tag{4.82}$$

This function is real valued due to the fact that the first term of L stands for the sum of $\mathrm{Re}(\boldsymbol{\omega}_i^\dagger\mathbf{\Omega}_{ij}\boldsymbol{\omega}_j)$ for all $i \neq j$, since $\boldsymbol{\omega}_i^\dagger\mathbf{\Omega}_{ij}\boldsymbol{\omega}_j = (\boldsymbol{\omega}_j^\dagger\mathbf{\Omega}_{ji}\boldsymbol{\omega}_i)^\dagger$. This modification uses the phase ambiguity between $\boldsymbol{\omega}_i$ and $\boldsymbol{\omega}_j$, $\arg(\boldsymbol{\omega}_i^\dagger\boldsymbol{\omega}_j)$, to cause a shift of coherence phases towards zero. The second term in (4.82) is real valued since it contains quadratic forms of Hermitian matrices.
Setting the partial derivatives of (4.82) to zero leads to a generalized eigenvalue problem (4.83) that optimizes a linear combination of coherences ($i = \{1, 2\}$).

$$\sum_{j=1\neq i}^{2}\mathbf{\Omega}_{ij}\boldsymbol{\omega}_j = \lambda\mathbf{T}_{ii}\boldsymbol{\omega}_i \iff \begin{bmatrix}\mathbf{0} & \mathbf{\Omega}_{12}\\ \mathbf{\Omega}_{12}^\dagger & \mathbf{0}\end{bmatrix}\begin{bmatrix}\boldsymbol{\omega}_1\\ \boldsymbol{\omega}_2\end{bmatrix} = \lambda\begin{bmatrix}\mathbf{T}_{11} & \mathbf{0}\\ \mathbf{0} & \mathbf{T}_{22}\end{bmatrix}\begin{bmatrix}\boldsymbol{\omega}_1\\ \boldsymbol{\omega}_2\end{bmatrix} \tag{4.83}$$

The optimized coherence modulus is equal to the largest eigenvalue in (4.83) and the square root of the largest eigenvalues in (4.73) and (4.74). Furthermore, the phase of the single–baseline optimized coherence is equal to $-\arg(\boldsymbol{\omega}_1^\dagger\boldsymbol{\omega}_2)$ $(= \arg(\boldsymbol{\omega}_2^\dagger\boldsymbol{\omega}_1))$ from (4.83), since (4.82) automatically deals with the phase ambiguity issue:

$$\gamma_{opt1} = \lambda_1 e^{-i\arg(\boldsymbol{\omega}_{1_1}^\dagger\boldsymbol{\omega}_{2_1})} \tag{4.84}$$

SB–ESM Optimization: Polarimetric Stationarity

Assuming stationary polarimetric behavior in the data sets and requiring equal scattering mechanism vectors $\boldsymbol{\omega}_1 = \boldsymbol{\omega}_2$, the coherence optimization problem is equivalent to the problem of computing the numerical radius of the matrix $\mathbf{\Pi}$, as shown by Colin *et al.* [29, 26]. Because no analytical methods exist for the solution of the general numerical radius problem, an iterative method is presented. It is based on the fact that [77]

$$\max_{\boldsymbol{v}}|\gamma(\boldsymbol{v})| = r(\mathbf{\Pi}) = \max_{\theta}\{\lambda_{max}\left(\mathbf{H}(\mathbf{\Pi}e^{-i\theta})\right) : \theta \in [0, 2\pi]\} \tag{4.85}$$

where $\lambda_{max}(\mathbf{A})$ represents the largest eigenvalue of $\mathbf{A}$ and $\mathbf{H}(\mathbf{A}) = \frac{1}{2}(\mathbf{A} + \mathbf{A}^{\dagger})$ is the Hermitian part of the matrix $\mathbf{A}$. This means that the optimal coherence is given by the numerical radius which is equal to the largest eigenvalue of the Hermitian part of the phase shifted matrix $\mathbf{\Pi}$. The phase angle θ which leads to the numerical radius is the phase of the optimal coherence, and the eigenvector of the involved eigenproblem is the optimal projection vector.
In [29], an iterative gradient ascend optimization algorithm for this problem is presented. The process flow consists of simultaneous search for the optimized coherence phase and the corresponding optimal projection vector [165]. After asymptotic convergence, the optimal coherence is given by

$$\gamma_{opt} = \lambda_{max}e^{i\theta} \tag{4.86}$$

This method converges towards a local maximum which might be not the global maxima. To avoid sub–optimal maxima, one can perform several optimizations with different initial phase shifts. Another approach is an effective strategy for initialization. Since the coherence set describes a simple, convex filled region in the unitary complex coherence plane, the phase shift angles θ can be initialized with the trace phase of $\mathbf{\Pi}$. Such an initialization significantly improves the optimization performance with respect to the number of iterations and to the robustness.

4.5.2 Multi–baseline Coherence Optimization

The extension of single–baseline PolInSAR to multiple baselines increases the observation space. Analyzing a series of coherent polarimetric datasets enables more advanced and more accurate applications. The range varies from polarimetric differential interferometry (PolDInSAR) to parameter inversion techniques with more complex physical models. It is also of importance to identify the most coherent scattering center in all datasets, thus minimizing phase uncertainty.
Given a multi–baseline dataset, coherences can be optimized independently for every baseline. This reproduces the results of the SB case, and leads to different dominant scattering centers depending on the chosen pair of images. A better approach to find the most coherent and dominant scattering center is a simultaneous optimization of all multi–baseline coherences. This approach generally leads to lower coherence magnitudes, but the corresponding scattering mechanisms and their interferometric phases are estimated on the basis of all available information and thus more accurately. And, most important, the interferometric phases and the degrees of coherence from the different baselines are related to each other as they represent the same scattering structure.

We have developed two methods for the MB PolInSAR coherence optimization problem, one general and one adapted to the polarimetric stationarity assumption.
The methods aim to optimize the sum of the coherence magnitudes over all direct baselines:

$$\text{MB–MSM:} \quad \underset{\boldsymbol{\omega}_1,\ldots\boldsymbol{\omega}_n}{\text{maximize}} \{\sum_{i=1}^{n}\sum_{j=1\neq i}^{n} |\gamma_{ij}(\boldsymbol{\omega}_i,\boldsymbol{\omega}_j)| : \forall i,j\ \boldsymbol{\omega}_i \in \mathbb{C}^3, \boldsymbol{\omega}_i^\dagger\boldsymbol{\omega}_i = 1, \arg\boldsymbol{\omega}_i^\dagger\boldsymbol{\omega}_j = 0\} \tag{4.87}$$

$$\text{MB–ESM:} \quad \underset{\boldsymbol{\omega}}{\text{maximize}} \{\sum_{i=1}^{n}\sum_{j=1\neq i}^{n} |\gamma_{ij}(\boldsymbol{\omega})| : \boldsymbol{\omega} \in \mathbb{C}^3, \boldsymbol{\omega}^\dagger\boldsymbol{\omega} = 1\} \tag{4.88}$$

MB–MSM Optimization: Multiset Canonical Correlation Analysis (MCCA) Approach

The general multi–baseline multiple scattering mechanisms (MB–MSM) method assigns a distinct scattering mechanism to each track. This approach permits to optimize the coherence for SMs that might have different polarimetric signatures in different datasets. This optimization problem is related to the multiset canonical correlation analysis (MCCA) problem [60, 65, 102]. As it is well known from MCCA theory, there is no exact analytical method applicable for the simple optimization problem presented in (4.87). However, one algorithm will be presented that achieves a similar goal, namely the *weighted* optimization, by solving a single eigenvalue problem.
Scaling the single–baseline Lagrangian optimization function (4.82) to multiple baselines leads to

$$L = \sum_{i=1}^{n}\sum_{j=1\neq i}^{n} \boldsymbol{\omega}_i^\dagger\boldsymbol{\Omega}_{ij}\boldsymbol{\omega}_j - \lambda\sum_{i=1}^{n}(\boldsymbol{\omega}_i^\dagger\mathbf{T}_{ii}\boldsymbol{\omega}_i - 1) \tag{4.89}$$

This function is real valued due to the fact that the first term of L stands for the sum of $\mathrm{Re}(\boldsymbol{\omega}_i^\dagger\boldsymbol{\Omega}_{ij}\boldsymbol{\omega}_j)$ for all $i \neq j$, since $\boldsymbol{\omega}_i^\dagger\boldsymbol{\Omega}_{ij}\boldsymbol{\omega}_j = (\boldsymbol{\omega}_j^\dagger\boldsymbol{\Omega}_{ji}\boldsymbol{\omega}_i)^\dagger$. This modification uses the phase ambiguity between $\boldsymbol{\omega}_i$ and $\boldsymbol{\omega}_j$, $\arg(\boldsymbol{\omega}_i^\dagger\boldsymbol{\omega}_j)$, to cause a shift of coherence phases towards zero. The second term in (4.89) is real valued since it contains quadratic forms of Hermitian matrices.
Equation (4.89) can be interpreted as a weighted optimization of coherences, since it refers to optimizing the sum of covariances $\boldsymbol{\omega}_i^\dagger\boldsymbol{\Omega}_{ij}\boldsymbol{\omega}_j$, while keeping the sum of variances $\boldsymbol{\omega}_i^\dagger\mathbf{T}_{ii}\boldsymbol{\omega}_i$ constant. It is a standard optimization problem in MCCA theory, called *SUMCOR* for the optimization of the sum of correlations. Setting the partial derivatives of (4.89) to zero leads to the generalized eigenvalue problem (4.90) that optimizes a linear combination of coherences ($i \in [1,\ldots,n]$).

$$\mathbf{A}\boldsymbol{\omega}_{MB} = \lambda\mathbf{B}\boldsymbol{\omega}_{MB} \tag{4.90}$$

$$\Longleftrightarrow \qquad \sum_{j=1\neq i}^{n} \boldsymbol{\Omega}_{ij}\boldsymbol{\omega}_j = \lambda\mathbf{T}_{ii}\boldsymbol{\omega}_i \tag{4.91}$$

$$\Longleftrightarrow \qquad \begin{bmatrix} \mathbf{0} & \boldsymbol{\Omega}_{12} & \ldots & \boldsymbol{\Omega}_{1n} \\ \boldsymbol{\Omega}_{21} & \mathbf{0} & \ldots & \boldsymbol{\Omega}_{2n} \\ \vdots & \vdots & \ddots & \vdots \\ \boldsymbol{\Omega}_{n1} & \boldsymbol{\Omega}_{n2} & \ldots & \mathbf{0} \end{bmatrix} \begin{bmatrix} \boldsymbol{\omega}_1 \\ \boldsymbol{\omega}_2 \\ \vdots \\ \boldsymbol{\omega}_n \end{bmatrix} = \lambda \begin{bmatrix} \mathbf{T}_{11} & \mathbf{0} & \ldots & \mathbf{0} \\ \mathbf{0} & \mathbf{T}_{22} & \ldots & \mathbf{0} \\ \vdots & \vdots & \ddots & \vdots \\ \mathbf{0} & \mathbf{0} & \ldots & \mathbf{T}_{nn} \end{bmatrix} \begin{bmatrix} \boldsymbol{\omega}_1 \\ \boldsymbol{\omega}_2 \\ \vdots \\ \boldsymbol{\omega}_n \end{bmatrix} \tag{4.92}$$

Note that in contrary to the single–baseline case, the largest eigenvalue of (4.90) does not correspond to the optimized coherence modulus any longer, but rather to the weighted sum of the optimized coherence moduli. The weights are included in the norms of individual projection vectors $\boldsymbol{\omega}_i$ from the eigenvector $\boldsymbol{\omega}_{MB}$.
MB–MSM coherence optimization can be summarized by the following algorithm:

1. Obtain eigenvectors from the generalized eigenvalue problem (4.90):
   $\mathbf{A}\boldsymbol{\omega}_{MB} = \lambda\mathbf{B}\boldsymbol{\omega}_{MB}$, where $\mathbf{A} = \mathbf{T} - \mathbf{B}$, $\mathbf{B} = \bigoplus_{i=1}^{n} \mathbf{T}_{ii}$, and $\bigoplus$ is the direct sum operator.
2. Normalize the projection vectors from $\boldsymbol{\omega}_{MB} = [\boldsymbol{\omega}_1, \ldots, \boldsymbol{\omega}_n]^T$ so that for all $i \in [1, n] : \boldsymbol{\omega}_i^\dagger \boldsymbol{\omega}_i = 1$.
3. Remove the phase shift from these vectors with respect to an arbitrary track $m \in [1, n]$, so that for all $i \in [1, n] : \arg(\boldsymbol{\omega}_m^\dagger \boldsymbol{\omega}_i) = 0$.

MB–ESM Optimization: Joint Numerical Radius Approach

The method for single–baseline coherence optimization under polarimetric stationarity can be extended to multiple baselines. Instead of a single phase shift angle θ for single–baseline ESM, we have to introduce $\frac{n(n-1)}{2}$ phase shifts θ_{ij} (with $\theta_{ji} = -\theta_{ij}$), one for every direct baseline. Using the optimization problem formulation (4.88), one can show that

$$\max_{\boldsymbol{v}} \sum_{i=1}^{n} \sum_{j=1 \neq i}^{n} |\widetilde{\gamma}_{ij(\boldsymbol{v})}| \geq \max_{\boldsymbol{v}} \sum_{i=1}^{n} \sum_{j=1 \neq i}^{n} \widetilde{\gamma}_{ij(\boldsymbol{v})} e^{-i\theta_{ij}} \tag{4.93}$$

The maximum of the left side depends on the given set of phase shift variables $\{\theta_{ij}\}$, while the maximum on the right side is constant. Equality is achieved when phase shifts are equal to the phases of optimal coherences, so that the real parts of the phase shifted optimal coherences are equal to the coherence moduli. Therefore, the optimization process consists in the simultaneous search for the optimized coherence phases and the corresponding optimal scattering mechanism. An efficient iterative optimization method that converges in a few (i.e. 2–5) iterations is presented in Fig. 4.7.
An estimate for the optimal scattering mechanism can be obtained from the eigenvector associated with the largest eigenvalue of the Hermitian matrix $\mathbf{H}$ in

$$\mathbf{H}\boldsymbol{v} = \lambda\boldsymbol{v}, \quad \text{where } \mathbf{H} = \sum_{i=1}^{n} \sum_{j=1 \neq i}^{n} \boldsymbol{\Pi}_{ij} e^{-i\theta_{ij}} \tag{4.94}$$

Estimates for optimal phase shifts are in turn obtained from

$$\theta_{ij} = \arg(\boldsymbol{v}^\dagger \boldsymbol{\Pi}_{ij} \boldsymbol{v}) \tag{4.95}$$

Phase shifts can then be reintroduced to (4.94) to obtain an improved estimate of the optimal vector $\boldsymbol{v}$. By iteratively adjusting the phase shifts θ_{ij} one obtains progressively better estimates of $\boldsymbol{v}$. Optimal coherences can then be computed with the converged vector $\boldsymbol{v}$ and (4.6).
This method may lead to a sub–optimal local maximum. To avoid this, one can perform several optimizations with different initial phase shifts. Another approach is an effective

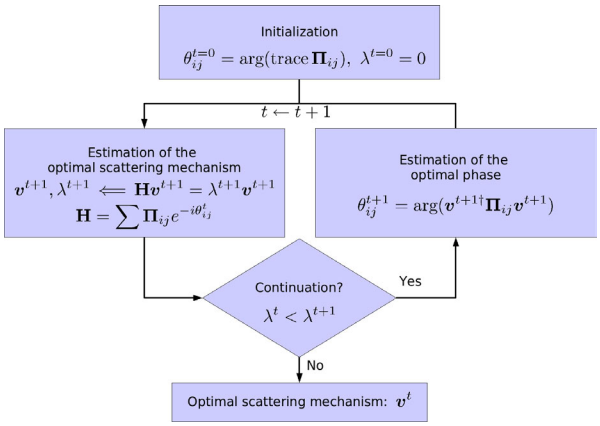

Figure 4.7: Iterative MB–ESM coherence optimization algorithm.

strategy for initialization. Since the polarimetric coherence sets of every matrix $\mathbf{\Pi}_{ij}$ describe simple, convex filled regions in the unitary complex coherence plane, phase shift angles θ_{ij} can be initialized with the trace phases of $\mathbf{\Pi}_{ij}$. Such an initialization significantly improves the optimization performance with respect to the number of iterations and to the robustness.
It should be noted that when the PolSAR matrices $\mathbf{T}_{ii}$ differ significantly, the ESM coherence optimization might fail to converge on the global optimum. In such cases, the MSM coherence optimization method should be preferred.
Finally, the steps involved in the proposed MB–ESM coherence optimization algorithm are given by:

1. Initialization: $\theta_{ij} = \arg(\mathrm{trace}\,\mathbf{\Pi}_{ij})$; $\hat{\lambda} = 0$
2. Computation of $\mathbf{H}$ and $\boldsymbol{v}$ from (4.94) with current estimates of optimal phase shifts θ_{ij}. $\boldsymbol{v}$ is the eigenvector corresponding to the highest eigenvalue λ_{max}.
3. Improved estimation of θ_{ij} using computed $\boldsymbol{v}$ via (4.95).
4. Termination criterion: $\lambda_{max} - \hat{\lambda} \leq \varepsilon$, where ε is an arbitrary small constant. If the criterion is not met, then $\hat{\lambda} = \lambda_{max}$ and go to step 2).
5. The optimal SM vector $\boldsymbol{\omega}$ and corresponding optimal coherences are calculated from $\boldsymbol{v}$ using (4.6) and 4.12.

4.6 Experimental Results: Multi–Baseline Coherence Optimization

For the experimental evaluation of single–baseline and multi–baseline PolInSAR coherence optimization methods, a multi–temporal airborne data set at L–band has been used. The fully–polarimetric 4 tracks data were acquired by the German Aerospace Center's (DLR) E–SAR sensor in 2000 and 2001 over the test–site Oberpfaffenhofen. Tracks 1 and 2 were both acquired on the 27th August, 2001, with a temporal baseline of 12 minutes. Track 3

#	Tracks	B_t	$B_\perp$
1	1×2	12 min	2.4–17.5 m
2	1×3	438 days	-1.4–13.9 m
3	2×3	438 days	—
4	1×4	346 days	0.2–5.9 m
5	2×4	346 days	—
6	3×4	92 days	-1.7–11.4 m

Table 4.4: Baseline characteristics. For the 3rd and 5th baselines, the exact range of perpendicular baselines is not available, but it is as well in the range of 0–15 meters.

was acquired on the 15th June, 2000, and track 4 on the 4th September, 2000 [124, 123]. Fig. 4.9 shows color–coded intensity images of the test–site, together with 5 defined regions of interest (ROI). The ROI are: (1) low and sparse vegetation, (2) forest of medium hight and density, (3) agricultural field, (4) bare surface (pasture/meadow and runway), (5) urban area.
The combination of the four tracks enables us to construct a 12×12 MB–PolInSAR coherency matrix $\mathbf{T}_{MB}$. $\mathbf{T}_{MB}$ has 6 direct baselines with temporal baselines (B_t) between 12 minutes and 438 days, nominal spatial baselines of 0 meters and real spatial perpendicular baselines ($B_\perp$) between 0 and 17 meters, with a mean below 10 meters [124], as summarized in Table 4.4.
A pre–processing step including flat–earth removal and range spectral filtering is applied prior to coherence optimization. After the construction of the coherency matrix image, the image was shrunk by a factor of 3 in range and 8 in azimuth to obtain averaged coherency matrices and to reduce the image size, obtaining an image size of 482×2048 pixels (range × azimuth) and 24 looks per pixel. The choice of $3 \times 8 = 24$ looks is caused by the recommendation of a minimum number of looks of an $N \times N$ covariance matrix equal to $2N$ [118], which in our case is $2 * 12 = 3 * 8 = 24$. In order to evaluate the coherence optimization performance using two different numbers of looks, two images were generated: the first is the original high–resolution image with 24 spatial looks, and the second image has been extensively speckle filtered using the Simulated Annealing[(1)] filter [133] which creates very homogeneous areas with an equivalent number of looks larger than 500. Due to the large differences in the filtering approaches and the numbers of looks, we denote the first image as "non–filtered" and the second as "filtered". These two choices represent extreme cases of a high–resolution image with a low number of looks versus a widely smoothed one with a large number of looks. One might assume that intermediate multi–looking strategies will lead to results lying between these extreme cases.

4.6.1 Qualitative Observations

Figures 4.10–4.13 present the color–compositions of lexicographic coherences and optimized coherences using SB–MSM, SB–ESM, MB–MSM, and MB–ESM methods for the first (1×2, B_t : 12min) and the second (1×3, B_t: $>$ 1year) baselines.

[(1)] To note is, the Simulated Annealing filtering criterion was based only on the intensities and did not consider interferometric correlations.

Figure 4.8: Optical image of the Oberpfaffenhofen test site (Source: googleearth).

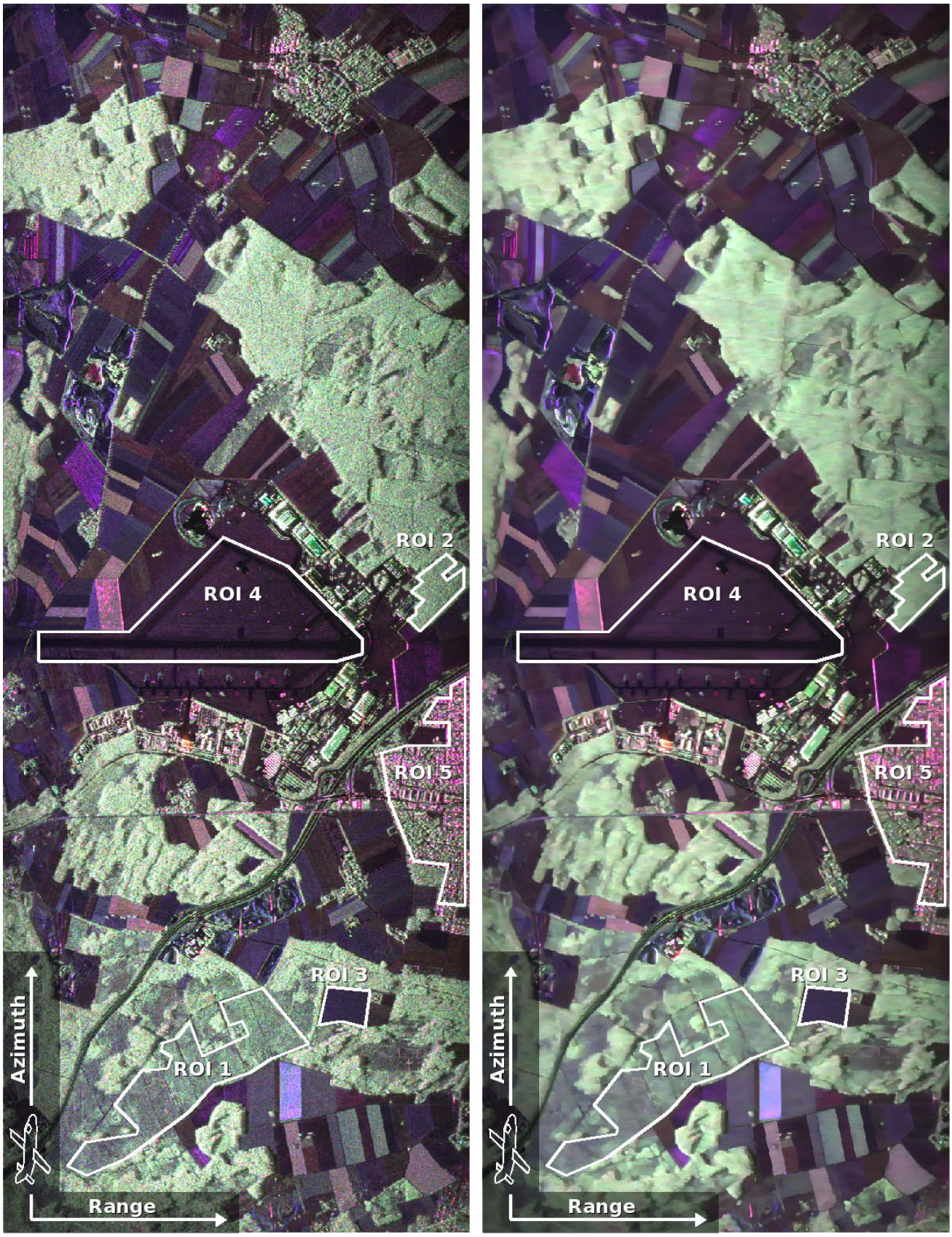

Figure 4.9: Intensity images of the first track. Left: non–filtered; Right: filtered.

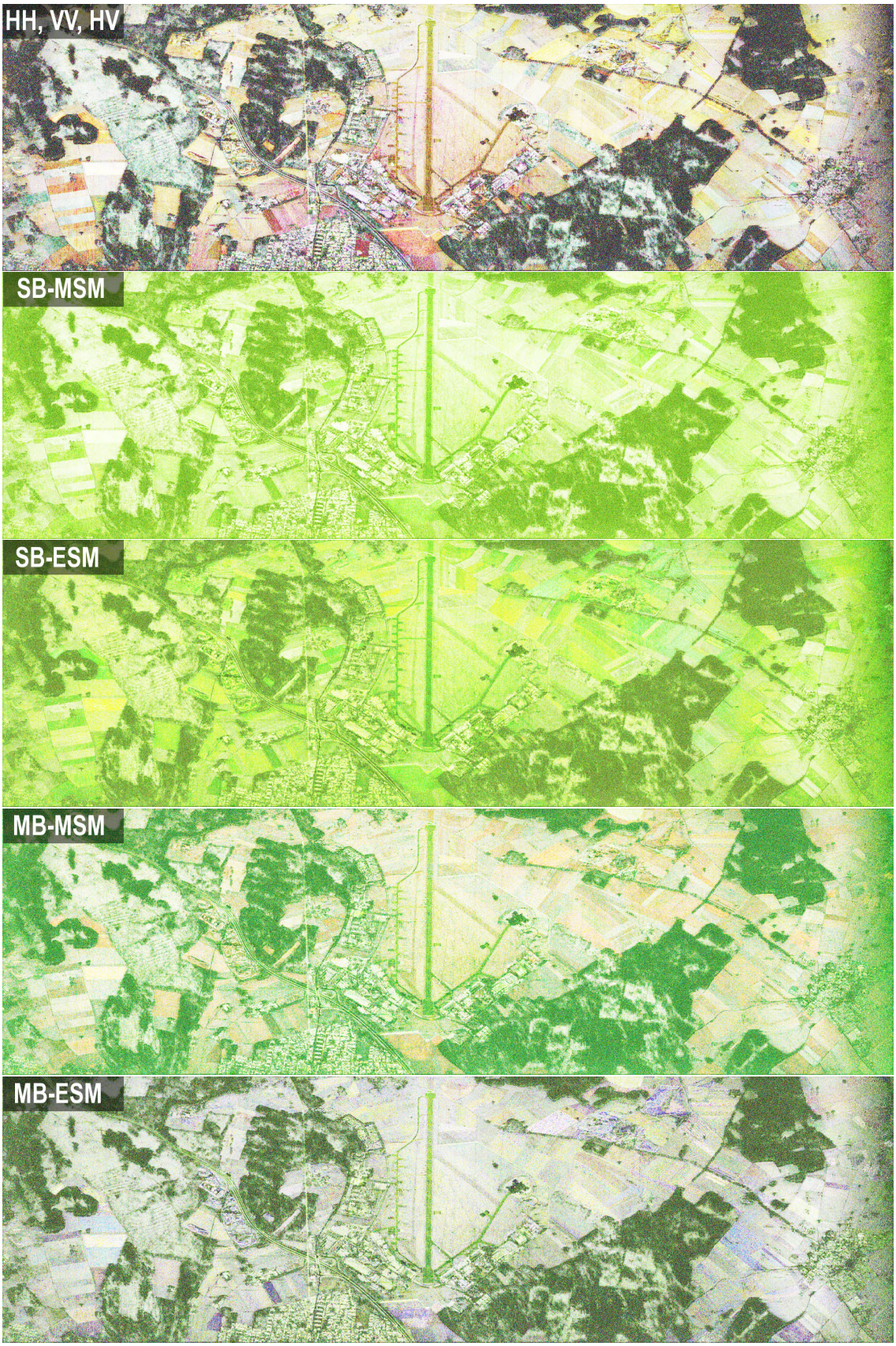

Figure 4.10: Non–filtered data: Coherence over the first baseline (1×2, B_t=12 minutes). From top to bottom: Lexicographic basis (RGB: [HH, VV, HV]), SB–MSM, SB–ESM, MB–MSM, MB–ESM (RGB: [γ_{opt2}, γ_{opt1}, γ_{opt3}]).

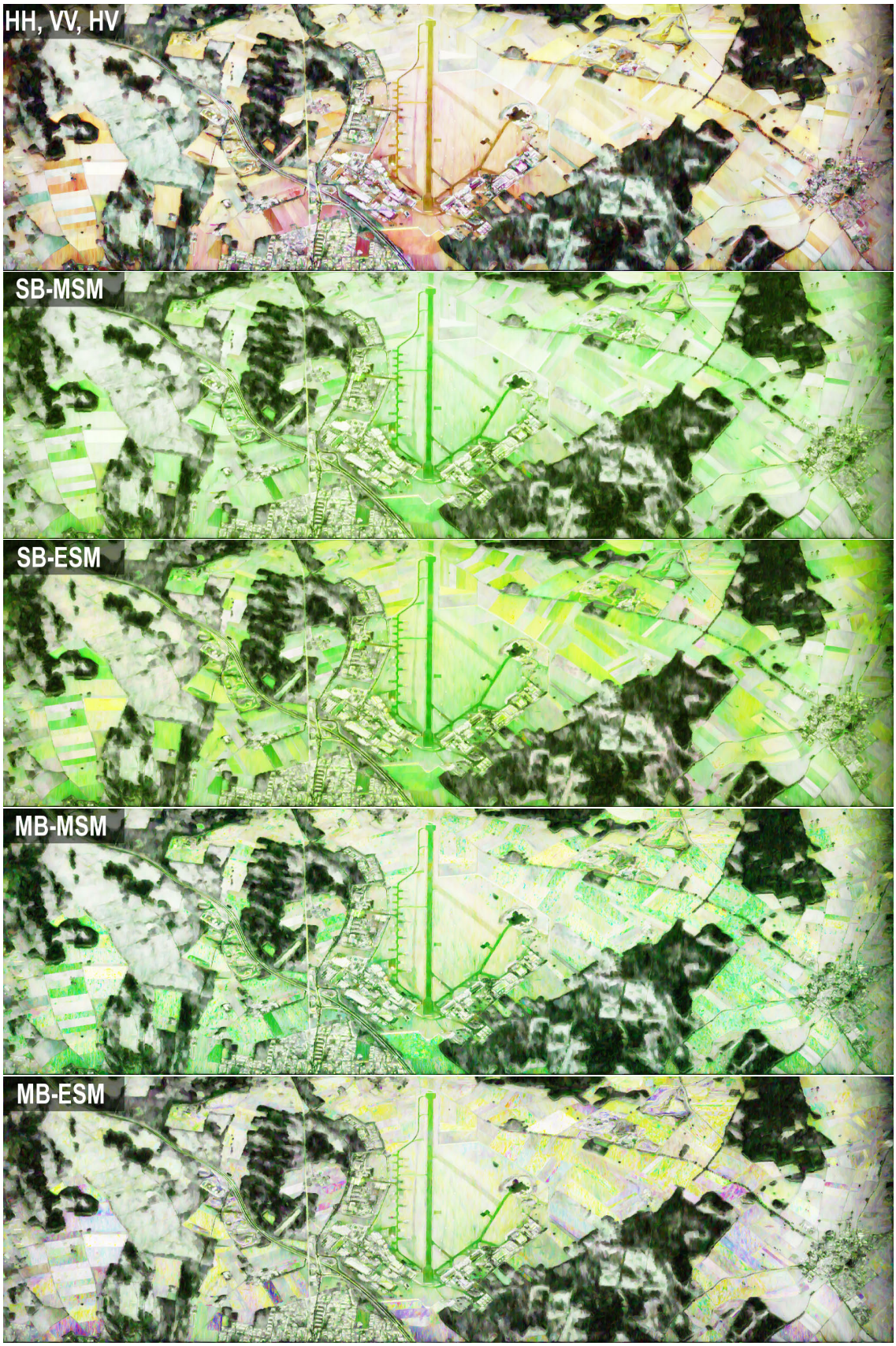

Figure 4.11: Filtered data: Coherence over the first baseline (1×2, B_t=12 minutes). From top to bottom: Lexicographic basis (RGB: [HH, VV, HV]), SB–MSM, SB–ESM, MB–MSM, MB–ESM (RGB: $[\gamma_{opt2}, \gamma_{opt1}, \gamma_{opt3}]$).

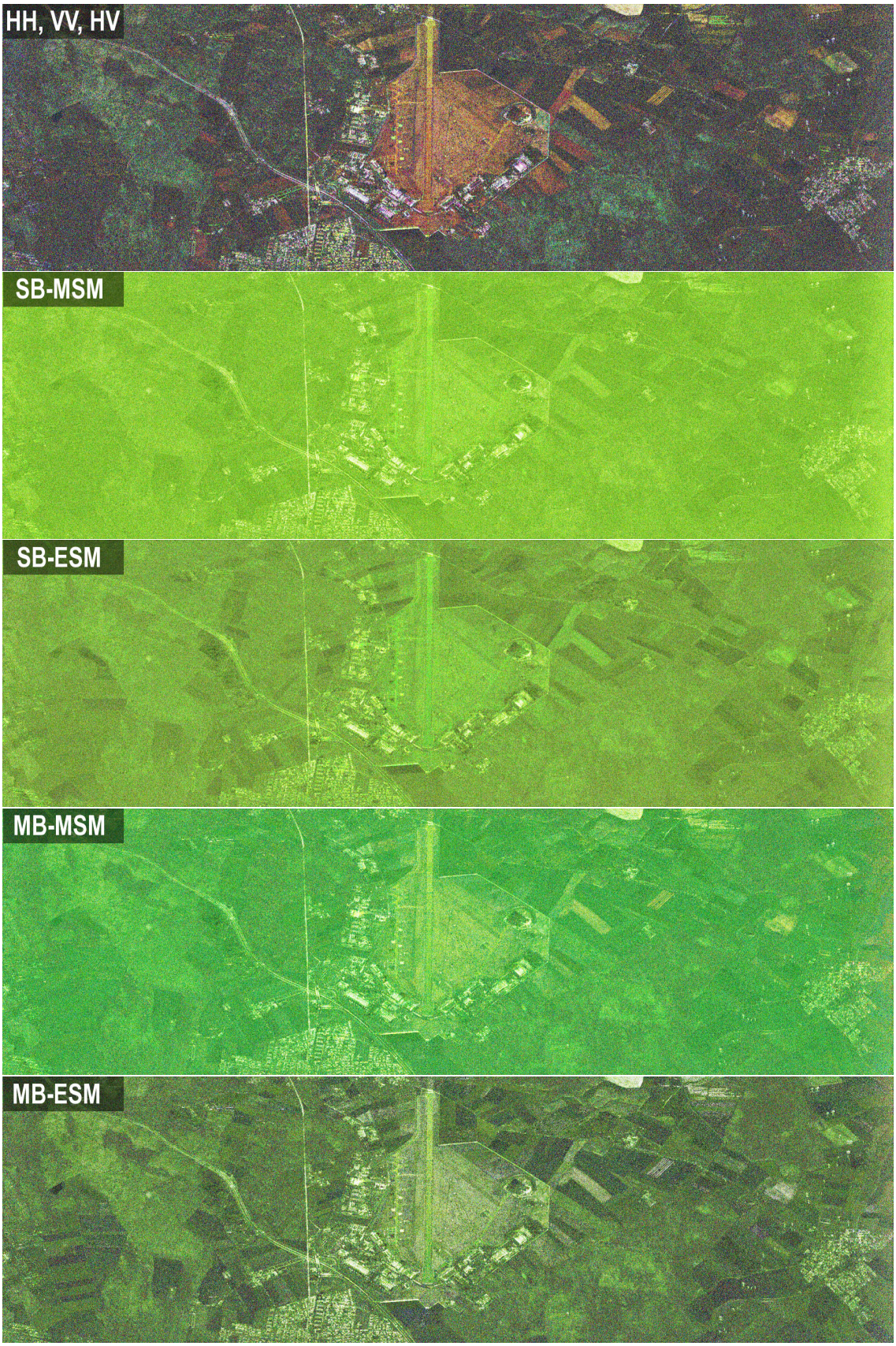

Figure 4.12: Non–filtered data: Coherence over the second baseline (1×3, B_t=438 days). From top to bottom: Lexicographic basis, SB–MSM, SB–ESM, MB–MSM, MB–ESM.

Figure 4.13: Filtered data: Coherence over the second baseline (1×3, B_t=438 days). From top to bottom: Lexicographic basis, SB–MSM, SB–ESM, MB–MSM, MB–ESM.

From the lexicographic basis coherences one can for example observe the incidence angle dependency of the coherences and of the polarizability of the coherences, as it is clearly visible from the change of color along the runway. This effect is due to thermal decorrelation, since the reflectivity of bare surfaces decreases with larger incidence angles, also in dependence of polarization.
Within the first baseline (shortest temporal baseline of 12 minutes), the surfaces and agricultural fields have very high coherence, especially in the near range. High forests decorrelate significantly, partly due to volume decorrelation, and, to a big extent, due to temporal decorrelation caused mostly by wind. In the second baseline (longest temporal baseline of 438 days), we can observe that the coherence is preserved over the artificial structures (such as the highway, the railroad, and the urban areas, especially some large building structures) and bare surfaces (such as the runway, the pastures and the meadows). Over the low and high forest a certain degree of coherence is preserved as well, even over this large time span. A complete loss of coherence is observed over cultivated agricultural fields.
The visual qualitative interpretation of the optimized coherences indicates the main properties of the optimization methods. SB–MSM optimization maximizes the coherences for a single baseline independently of other baselines and achieves the maximal possible coherence. The pre–dominant light green color indicates a very high optimal coherence and a large distance to the second and third optimal coherences. Almost white colors indicate that all three coherences are very high, whereas very dark colors indicate that all coherences are low.
SB–ESM method enforces equal scattering mechanisms in both tracks. The obtained optimal coherences are lower in comparison to SB–MSM. The additional constraint of equal scattering mechanisms caused several agricultural fields to become more yellowish, indicating that the first and the second optimal coherences are both relatively high in comparison to the third one.
The MB methods optimize the coherences considering all baselines. Therefore, these methods are much more constrained and achieve smaller coherence values as compared to the SB methods. Since the optimal projection vectors are found from all baselines, the computed coherences corresponding to the first optimal projection vector at an individual baseline might be not optimal, as the red and blue colored areas indicate. The optimization criterion is the *sum* of coherences from all baselines, and therefore, only $\sum|\gamma_{opt_1}| \geq \sum|\gamma_{opt_2}| \geq \sum|\gamma_{opt_3}|$ is guaranteed, but not $|\gamma_{opt_1}| \geq |\gamma_{opt_2}| \geq |\gamma_{opt_3}|$.
It can be observed that using MB vs. SB optimization methods as well as ESM vs. MSM methods improves the contrast of the optimal coherences. This can be best seen over the images with a low number of looks (see the coherence images of the non–filtered data set in the appendix).

4.6.2 Quantitative Observations

For quantitative analysis of the optimization methods, several performance indicators have been developed and applied to the data over different regions of interest. The results are presented and discussed below.

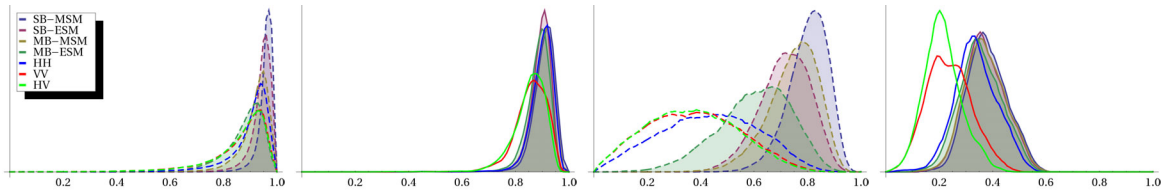

(a) ROI 1: Low and sparse vegetation

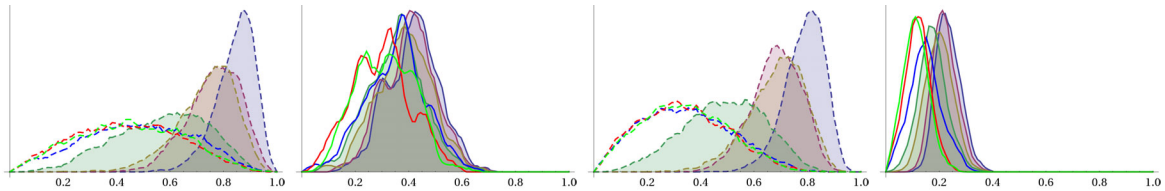

(b) ROI 2: High forest

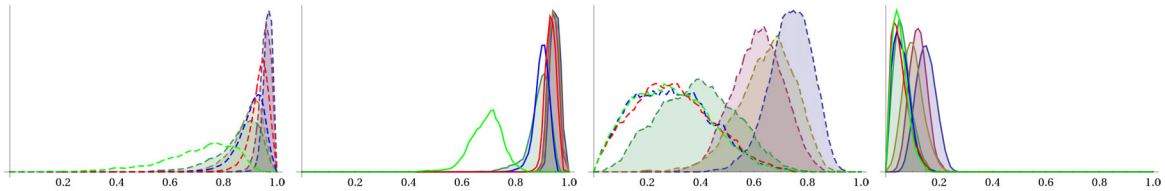

(c) ROI 3: Agricultural field

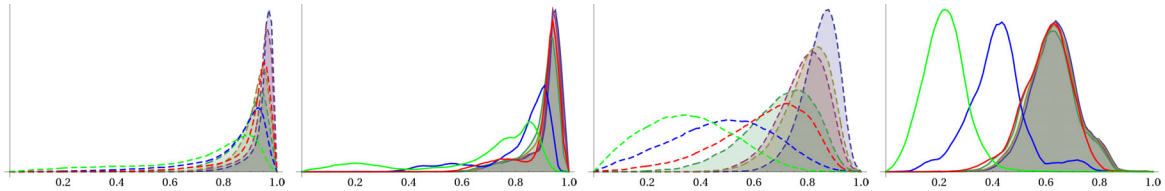

(d) ROI 4: Bare surface: pasture and runway

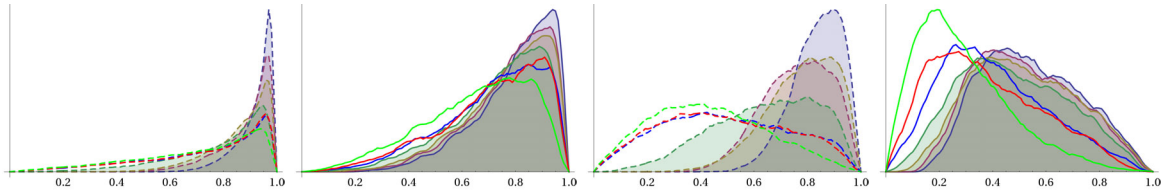

(e) ROI 5: Urban area

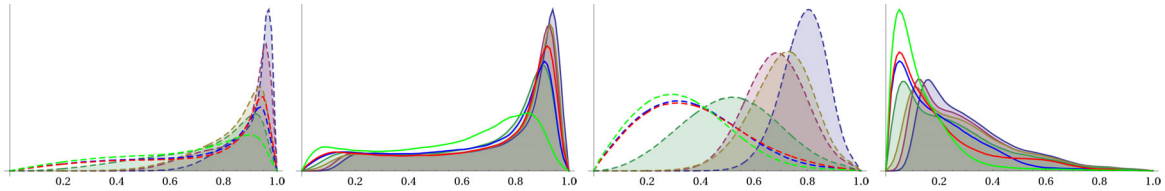

(f) Whole image

Figure 4.14: Histograms of coherence moduli for the first (left two graphs) and the second (right two graphs) baselines. For each case, the first graph is for the 16 looks data, and the second graph is for the speckle filtered (Simulated Annealing) data. Presented are the coherence distribution histograms for all regions of interest as well as for the whole image, representing the coherences in the lexicographic basis ($\gamma_{HH}, \gamma_{VV}, \gamma_{HV}$), and the maximal coherences for the different optimization methods ($\gamma_{opt_1}^{SB-MSM}$, $\gamma_{opt_1}^{SB-ESM}$, $\gamma_{opt_1}^{MB-MSM}$, $\gamma_{opt_1}^{MB-ESM}$).

Optimized Coherence Histograms

Comparing non-filtered and filtered data, we see that after Simulated Annealing filtering, the coherence distribution histograms, as shown in Fig. 4.14, do not anymore correspond to the theoretical coherence distribution, due to the adaptive nature of the filtering approach, which filters different positions in the data with different number of looks in dependence of the local homogeneity.
The histograms show that in all cases the optimized coherences are higher than the lexicographic coherences. For most cases, the following coherence magnitude order can be observed:

$$|\gamma_{opt_1}^{MB-xxx}| \leq |\gamma_{opt_1}^{SB-xxx}| \qquad \text{and} \qquad |\gamma_{opt_1}^{xx-ESM}| \leq |\gamma_{opt_1}^{xx-MSM}| \tag{4.96}$$

Observations:

- Non–filtered coherences are too high, since they have been generated using a low number of looks, and, therefore are biased. It is important to note, that no coherence bias removal techniques [150] have been applied to the data. It is not of importance for the filtered coherences as they are estimated from data with a very high number of looks (ENL $\geq$ 500). However, the bias might be severe for the non–filtered data, which have only a spatial averaging using 24 looks, and the ENL for the whole image has been estimated around 8.

  In the second baseline, as an example, the agricultural field (ROI 3) should be completely decorrelated (see Fig. 4.14.c.3). Lexicographic coherences have low values, and after coherence bias removal they will be even much lower, but the optimized coherence histograms wrongly depict a relatively highly coherent region. This indicates that the coherence optimization is performed in this case over noise.

- The potential for coherence optimization is higher for images with a lower number of looks. This is related to the previous point.

- For some regions, the optimal coherences have similar distributions as obtained for lexicographic polarizations. For example, over bare surfaces (ROI 4), the optimal coherences (filtered data) have a very similar distribution as the VV coherences, for both baselines (Figs. 4.14.d.2 and 4.14.d.4). This behavior agrees with the theoretically higher backscattering (and with it lower thermal decorrelation) over bare surfaces for the VV polarization than for HH and HV polarizations. A similar effect is observed over low forestry vegetation (ROI 1), where optimal coherences are only slightly higher than for the HH polarization (Figs. 4.14.a.2 and 4.14.a.4). For more complex environments, such as the urban area (ROI 5), coherence optimization identifies the most coherent scattering mechanism, which can hardly be guessed from standard coherences.

Optimized Phase Correlation

SB and the MB optimization methods show significantly different behavior. Since single–baseline methods optimize coherences independently, they reach higher coherence values, but the corresponding phases and scattering mechanisms are different, relating to different dominant scattering centers. Such an effect can be examined in relation to interferometric

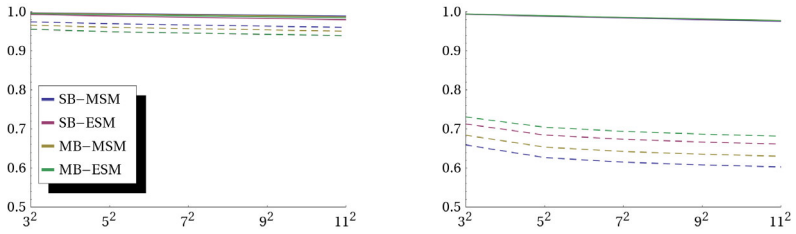

(a) ROI 1: Low and sparse vegetation

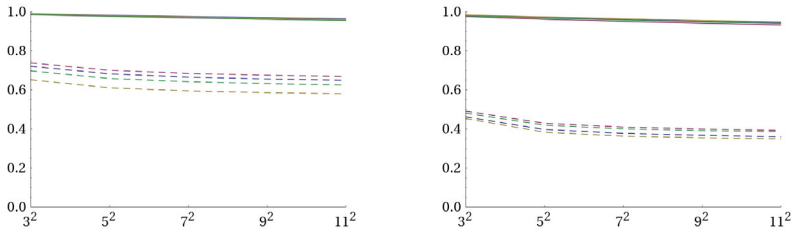

(b) ROI 2: High forest

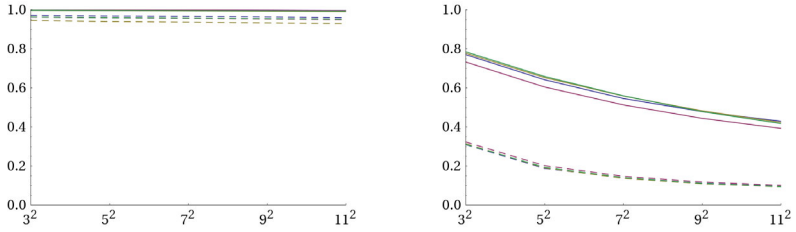

(c) ROI 3: Agricultural field

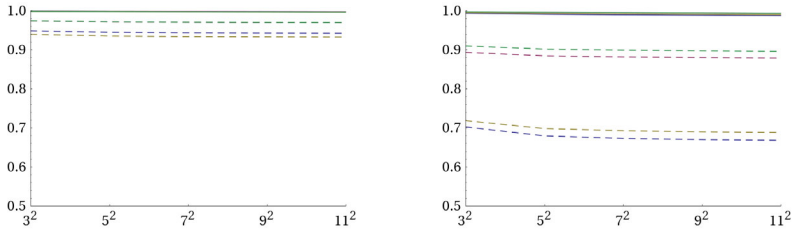

(d) ROI 4: Bare surface: pasture and runway

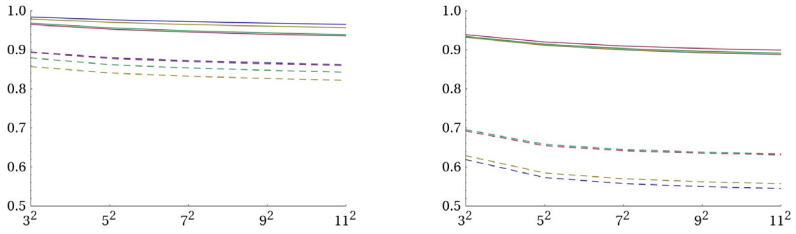

(e) ROI 5: Urban area

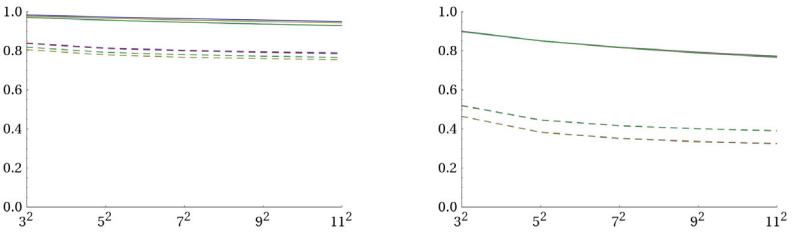

(f) Whole image

Figure 4.15: Correlation of the optimized interferometric phase over the spatial averaging window: on the left for the first baseline (12 minutes), and on the right for the second baseline (438 days) (solid lines: filtered; dashed lines: non–filtered).

phases of optimized coherences and their spatial variance. The examination of the local phase correlation over homogeneous areas reveals the improvement of the phase stability with a higher number of baselines. The correlation of optimized phases ρ_ϕ is computed from the already optimized coherence phases over a local window of N pixels around the pixel i:

$$\rho_{\phi(i)} = |\left\langle e^{i\phi} \right\rangle| = |\frac{1}{N}\sum_{j=1}^{N} e^{i\phi_{(j)}}|, \quad \text{where } \phi_{(j)} = \arg\gamma_{opt_1(j)} \tag{4.97}$$

Fig. 4.15 presents ρ_ϕ over different number of looks for the first and the second baselines. The spatial averaging of the optimized phases ranges from $N = 3^2 = 9$ to $N = 11^2 = 121$. Observations:

- The phase stability indicator for filtered data is quite stable, and similar for all optimization methods. This has been expected since data have been largely spatially smoothed prior to coherence optimization.
- Over the bare surface area (ROI 4, Fig. 4.15.d), which is the most coherent and homogeneous region along all baselines, one can observe two main properties of the phase stability indicator: (1) MB optimized coherence phases are locally more stable than SB optimized ones and (2) ESM optimized phases are more stable too, compared with the MSM ones. (1) can be related to the fact, that the data over which one optimizes has more looks in the MB case as in the SB case, i.e. we have additionally a kind of interferometric multi–looking operation. (2) can be reasoned to be due to additional constraints on ESM optimization, avoiding the void optimization over the noise subspace.
- For other ROIs the result interpretation is less straightforward, partly since the regions are less homogeneous and partly due to the large temporal decorrelation.

Scattering Mechanisms Correlation

In a similar way to the optimized phase stability, the local variation of the optimal scattering mechanism vectors is examined. The local scattering mechanisms similarity indicator can be computed via

$$\rho_{\boldsymbol{\omega}(i)} = \frac{1}{N}\sum_{j=1}^{N} |\boldsymbol{\omega}^{\dagger}_{opt_1(i)}\boldsymbol{\omega}_{opt_1(j)}| \tag{4.98}$$

where the index j runs over a local neighborhood of N pixels. However, since all optimization methods but the MB–ESM, deliver several optimal scattering mechanisms, this metric needs to adapted to all optimization methods. The numbers of obtained optimal scattering mechanism vectors for the general case and for the experimental data set with 4 tracks are presented in Table 4.5.
Comparing only the corresponding scattering mechanism vectors, and not their similarity between each other leads to

$$\rho_{\boldsymbol{\omega}(i)} = \frac{1}{N\, n_{\boldsymbol{\omega}}}\sum_{j=1}^{N}\sum_{k=1}^{n_{\boldsymbol{\omega}}} |\boldsymbol{\omega}^{k\dagger}_{opt_1(i)}\boldsymbol{\omega}^{k}_{opt_1(j)}| \tag{4.99}$$

where $n_{\boldsymbol{\omega}}$ is given in Table 4.5 in dependence of the optimization method.

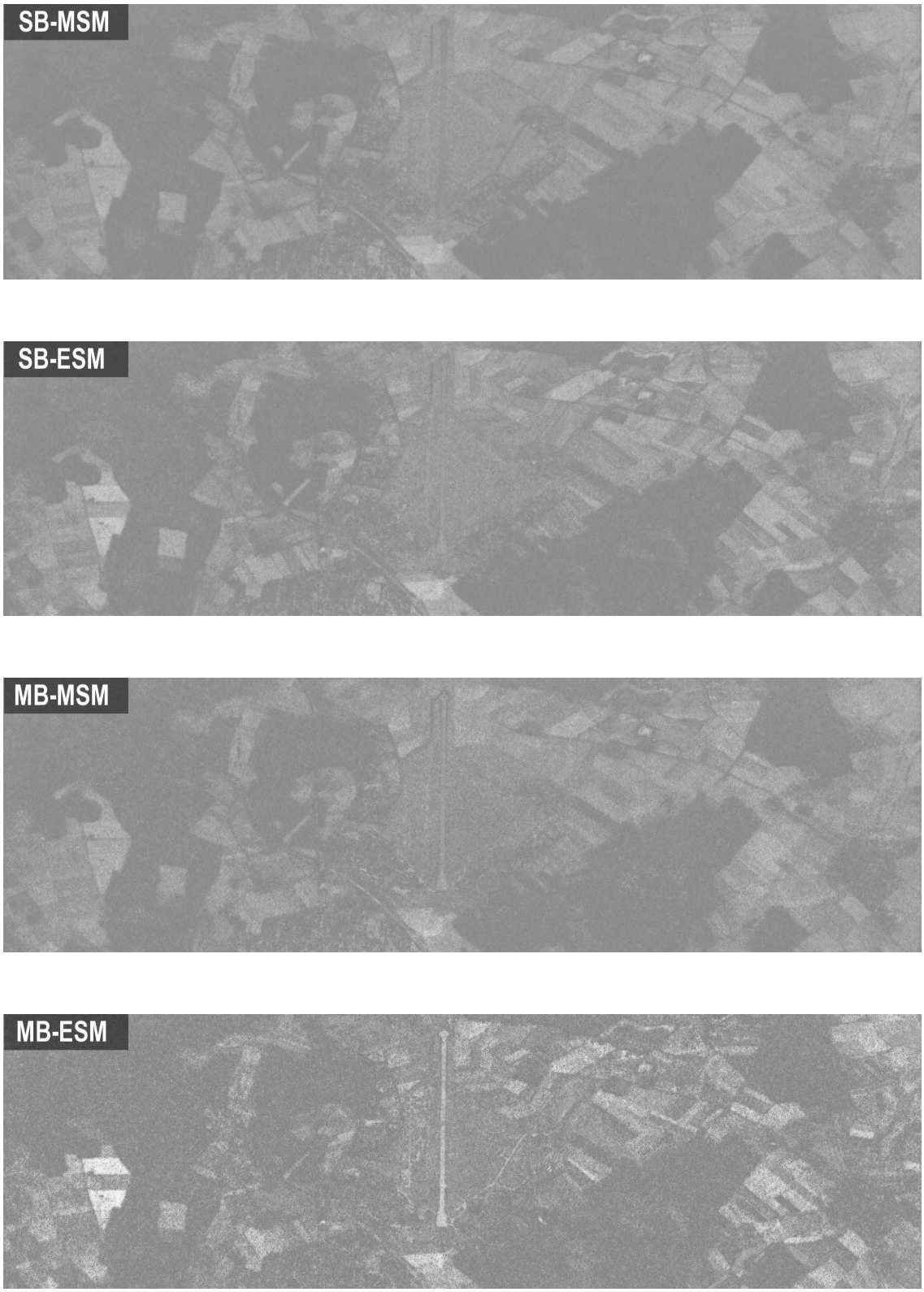

Figure 4.16: Non–filtered data: Local scattering mechanisms correlation $\rho_{\boldsymbol{\omega}}$ images for $N = 7^2$. From top to bottom: SB–MSM, SB–ESM, MB–MSM, MB–ESM.

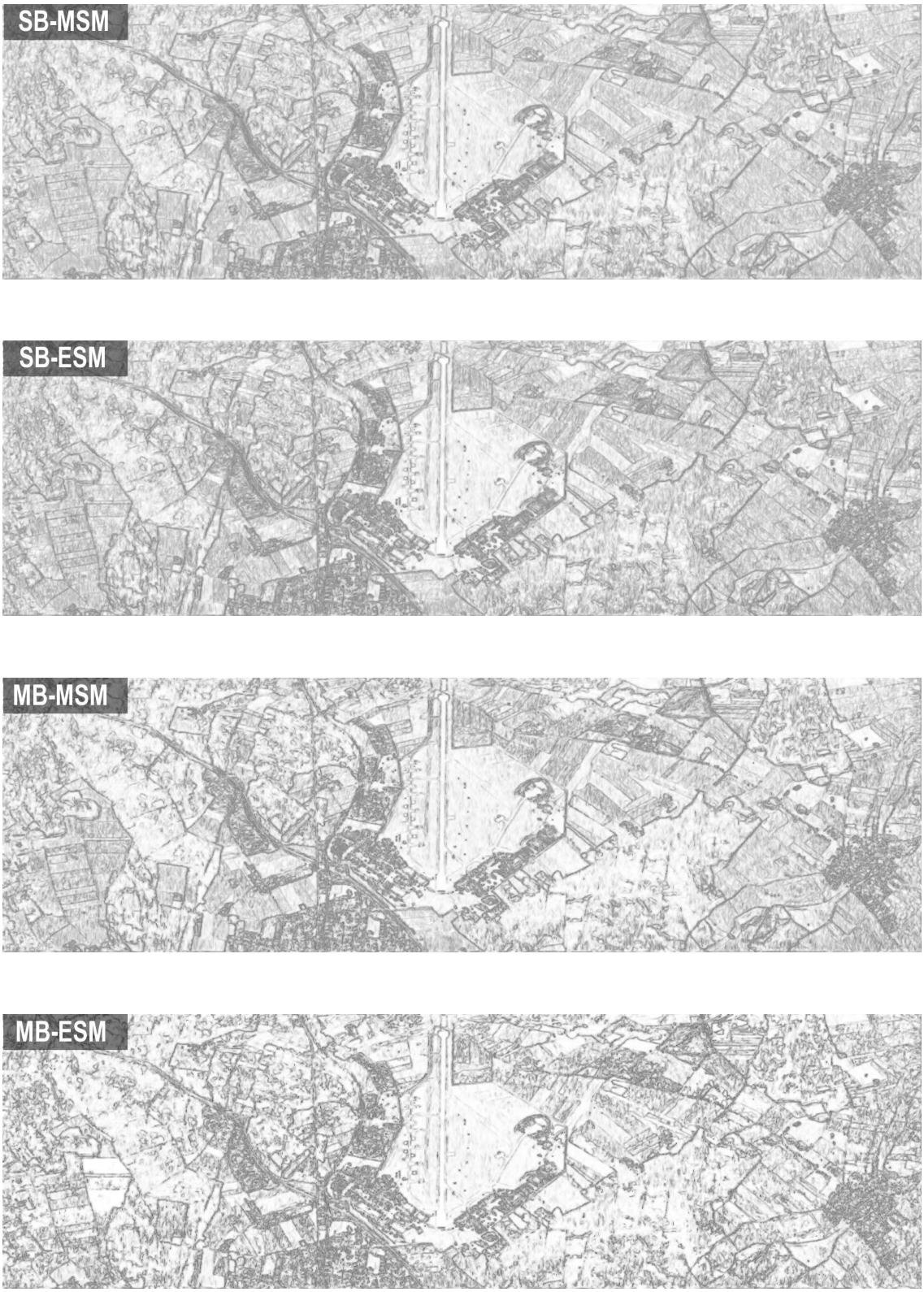

Figure 4.17: Filtered data: Local scattering mechanisms correlation $\rho_{\boldsymbol{\omega}}$ images for $N = 7^2$. From top to bottom: SB–MSM, SB–ESM, MB–MSM, MB–ESM.

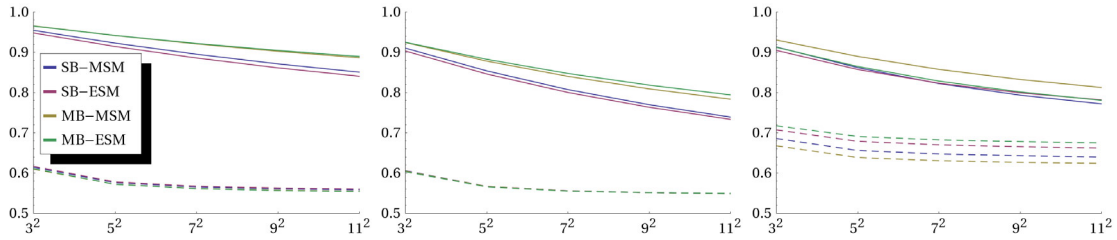

(a) ROI 1: Low and sparse vegetation (b) ROI 2: High forest (c) ROI 3: Agricultural field

(d) ROI 4: Bare surface: pasture and runway (e) ROI 5: Urban area (f) Whole image

Figure 4.18: Local scattering mechanisms correlation $\rho_{\boldsymbol{\omega}}$ over the spatial averaging window size N. Solid lines correspond to filtered data, while dashed lines correspond to non–filtered data.

Method	$n_{\boldsymbol{\omega}}$: Number of $\boldsymbol{\omega}_{opt1}$ vectors	Example with 4 tracks
SB–MSM	2 per baseline	12
SB–ESM	1 per baseline	6
MB–MSM	1 per track	4
MB–ESM	1	1

Table 4.5: Number of optimized scattering mechanism vectors $n_{\boldsymbol{\omega}}$ for different optimization methods.

Similarly to ρ_ϕ, $\rho_{\boldsymbol{\omega}} \in [0,1]$. The results for $N = 7^2 = 49$ for the different optimization methods is shown in Figs. 4.16 and 4.17. A qualitative examination of the images shows significant differences between the optimization methods, which can also be quantitatively validated, by computing the average $\rho_{\boldsymbol{\omega}}$ over the regions of interest and using different N, as shown in Fig. 4.18.
Observations:

- In comparison to ρ_ϕ, $\rho_{\boldsymbol{\omega}}$ is much more sensitive to the averaging window size N and to the optimization method.
- As expected, the filtered data delivers much higher correlation of the scattering mechanism vectors than the non–filtered data because of the previous smoothing operation.
- Over most ROI one can observe that $\rho_{\boldsymbol{\omega}}$ is higher for MB optimization methods and for ESM optimization methods. This re-confirms the observations and the interpretations of the ρ_ϕ indicator.

4.6.3 Summary and Discussion

It has been observed that enforcing simultaneous MB coherence optimization, it is still possible to achieve very high coherences close to SB optimized ones. It has been shown that the utilization of multiple baselines for the optimization of coherences has certain advantages over SB optimization with regard to accuracy improvement in the estimation of dominant phase centers, scattering mechanism vectors, and coherence contrast improvement, which may be related to the optimal coherence bias reduction.
The following conclusions can be formulated about the properties of different coherence optimization methods

- By definition, single–baseline optimized coherences are always higher than multi–baseline optimized coherences

$$|\gamma_{opt_1}^{MB-xxx}| \leq |\gamma_{opt_1}^{SB-xxx}| \tag{4.100}$$

  due to additional constraints for MB optimization.

- For the same reason, MSM optimized coherences are higher than ESM optimized coherences:

$$|\gamma_{opt_1}^{xx-ESM}| \leq |\gamma_{opt_1}^{xx-MSM}| \tag{4.101}$$

- The optimized phases and scattering mechanism vectors are locally more stable after MB optimization (in comparison to SB optimization), partly due to the increased number of observables.
- The optimized phases and scattering mechanism vectors are locally more stable after ESM optimization (in comparison to MSM optimization), partly due to the additional constraints and reduced search space (which comprises also the void noise subspace).

- The filtering approach and the number of looks is important. If not enough looks are used for the estimation of the PolInSAR coherency matrix, the optimization is partly performed over the noise subspace, delivering highly biased coherences. This is especially an issue for MSM optimization. Using ESM and/or multi–baseline optimization reduces this effect.
- The potential of coherence optimization is higher for images with a lower number of looks.
- In the absence of both changes between polarimetric responses and noise, MSM and ESM methods should deliver the same results. Therefore, non–similarity of the results indicates either noise contributions, or changes in the scattering mechanisms, or both.
- Only multi–baseline optimization methods can be used meaningful for multi–image data sets , as e.g. for differential SAR interferometry, multi–temporal change monitoring.

To simplify the choice of one of the optimization methods we propose the following guidelines:

- Sort out completely decorrelated images.
- If multiple baselines are available, use all data for coherence optimization.
- If computational speed is an issue, MSM methods should be preferred.
- In presence of significant changes of polarimetric signatures (responses), MSM methods ought to be preferred to the ESM methods.
- In other cases, if possible, ESM optimization should be used due to the reduced parameterization space with easier physical interpretation, and the reduced search space which suppresses the void optimization over noise significantly.

The extension of polarimetric optimization to the MB case has potential practical uses in various areas. The presented methods provide coherence optimization techniques to applications with more than one baseline for the first time. New application fields are, for instance, PolDInSAR, permanent scatterer determination, classification, or change monitoring and detection over multi–temporal and multi–baseline data sets. Furthermore, utilizing more than two data sets, if available, will improve the robustness in determining the most coherent SMs and is useful even for SB applications, such as digital elevation model extraction or parameter inversion.

4.7 Conclusions

In this chapter we have presented our own works on the theory of PolInSAR. These studies are largely based on the theoretical framework of polarimetric SAR interferometry, as developed by S. Cloude and K. Papathanassiou [22, 105]. In addition, the works on coherence set theory and optimization were built on the contributions by M. Tabb and T. Flynn *et al.* [42, 143, 142], and E. Colin *et al.* [29].

Based on the named contributions, we have analyzed the concepts of polarimetric stationarity, as initially proposed by L. Ferro–Famil and M. Neumann [39].
The mathematical concept of the numerical range of a matrix is related to the PolInSAR coherence set. We have presented its most important properties and analyzed the relationships between the properties of the PolInSAR contraction matrices and the shapes of the coherence sets in the complex coherence plane. All possible coherence set shapes have been classified and related to possible media symmetries and polarimetric stationarity conditions. We have also presented a numerical framework for the density examination and the statistical analysis of the coherence sets, with respect to both the polarization density and the backscattered energy density. Some of the results on coherence set theory were presented by us also as in [98, 96, 97].
Finally, PolInSAR coherence optimization techniques have been investigated. Based on the analysis of the developed single–baseline coherence optimization methods we have developed and presented PolInSAR coherence optimization methods for multiple baselines. Two most reasonable optimization criteria were considered: (1) coherence optimization using multiple scattering mechanism vectors (MSM), and (2) optimization using equal scattering mechanism vectors (ESM). The methods have been evaluated on real SAR data, and the properties of the optimization methods and obtained optimized coherences, phases and scattering mechanism vectors were evaluated for different scattering media types.
The initial results on coherence optimization performance were already reported by us in [95]. The multi–baseline coherence optimization methods are expected to have an impact on multi–temporal and multi–baseline PolInSAR change monitoring, persistent scatterers identification, and polarimetric differential interferometry (PolDInSAR). A. Reigber *et al.* [122, 123] used the multi–baseline coherence optimization methods for polarimetric differential SAR interferometry (PolDInSAR) applications to obtain and to analyze differential phases over vegetated areas.
Also, it is to expect, that these methods will be very useful for dual– and full–polarization space–borne SAR data. Given the long repeat pass cycles and the resulting temporal decorrelation, coherence optimization will be able to enhance time–series analyses. Since in dual–pol mode the physical interpretation is less important, the use of coherence optimization to reduce phase noise for any kind of application which uses second–order statistics will become very reasonable.

Chapter 5

Polarimetric Interferometric Vegetation Scattering Model

In this chapter we present a polarimetric interferometric scattering model for agricultural and forest vegetation. The presented model is kept as simple as possible to facilitate its inversion, but still contains important parameters for the characterization of vegetation structures which can be discriminated by radar polarimetry and interferometry: vegetation particles characteristics, orientation distribution, ground characteristics, and the vertical structure of the vegetation. At first, a polarimetric model for first–order scattering components is presented. We explicitly consider the modeled parameters under both Born and distorted Born (Born+EFA) approximations. Complementarily, an interferometric coherence model for the same components is presented enabling the construction of a PolInSAR model. Both single–transmit and alternate–transmit interferometric acquisition modes are analyzed. Based on the synergy of polarimetry and interferometry, it is recognized that a hybrid mode (alternate–transmit simultaneous–receive) will improve the distinction between surface scattering and the double–bounce scattering based on the interferometric coherence.
In this chapter, individual elements of the model will be considered in general. As a specific example, a model which will be used in the next chapter for forest parameter retrieval consists of ground, trunk, and canopy layers, as shown in Fig. 5.1.
Table 5.1 presents an overview of the parameters for the volume and ground layers incorporated in the modeling approach. Explicitly denoted is either these parameters affect the polarimetric or interferometric properties. These parameters will be explained in more detail in the course of this chapter.

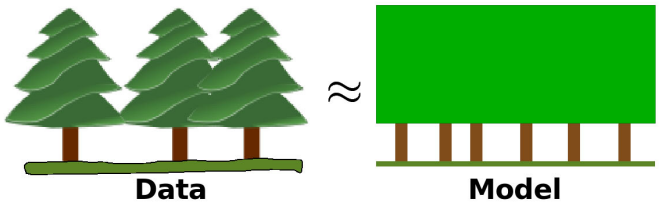

Figure 5.1: Three layer model for forests: ground, trunks, and canopy.

Volume layer		Pol	In
$\widetilde{\psi}$	Main orientation of vegetation particles	*	
τ	Orientation randomness	*	
δ	Particle scattering anisotropy (backscattering)	*	
δ'	Bi–static particle scattering anisotropy	*	
σ	Extinction [dB/m]		*
$\Delta\sigma$	Difference in extinction	*	*
$\Delta\chi$	Difference in refractivity	*	*
h_v	Vegetation layer depth		*
z_{v0}	Layer bottom height		*
r_h	Canopy–fill–factor		*
Ground layer		**Pol**	**In**
v_{az}	Terrain azimuth slope	*	
v_{rg}	Terrain ground range slope	*	
z_0	Ground topography height		*
$\beta, \beta_{\frac{vv}{hh}}, \beta_{\frac{hv}{hh}}$	Surface backscattering parameters	*	
η	Fresnel reflection coefficients ratio	*	
$\mathrm{Re}\,\epsilon_r$	Surface permittivity under SPM approximation	*	
α	Double–bounce parameter (replaces η, δ')	*	

Table 5.1: Model parameters for a single volumetric layer over the ground (some of them are complex and some are derivable from others).

5.1 Vegetation Structure

Vegetated areas like forests or agricultural fields can be modeled in a simple way by a set of possibly overlapping volume layers over the ground, where every layer has its own distinguishing characteristics. In the most simple case a single volume layer over the ground is considered. The electromagnetic scattering from the volume might be modeled by considering an equivalent continuous medium or a medium consisting of discrete scatterers. In the continuous case, the medium is characterized by a fluctuating permittivity function $\epsilon(\boldsymbol{r})$ [62, 157]. In the discrete case, the medium consists of a collection of randomly distributed scatterers [69]. The response of discrete media can be modeled using the incoherent radiative transfer theory or the coherent wave theory. Radiative transfer deals with the transport of intensity through the scattering medium. The wave theory, also called the multiple scattering theory, starting from Maxwell's equations, derives the solution for a single scatterer, and then considers multiple scattering effects, as presented in chapter 2 and especially in section 2.4. In this study, the vegetation medium is modeled by a coherent discrete scatterer approach using the distorted Born approximation.

5.1.1 Particle Scattering Anisotropy

The direct backscattering from a simplified volumetric vegetation layer can be characterized by a collection of discrete scatterers whose electromagnetic properties are governed by the probability density functions (pdf) of their positions, shapes, sizes, dielectric constants, and orientations. The polarimetric coherency matrix for the volume can be represented

by

$$\mathbf{T} = \iiint \hat{\mathbf{T}}_{(\boldsymbol{r},\Xi,D,\epsilon_r,\nu,\psi)}\, p_{(\boldsymbol{r},\Xi,D,\epsilon_r,\nu,\psi)}\, d\boldsymbol{r}\, d\Xi\, dD\, d\epsilon_r\, d\nu\, d\psi \tag{5.1}$$

where $\hat{\mathbf{T}}$ is the coherency matrix of a single scatterer and $p_{(\boldsymbol{r},\Xi,D,\epsilon_r,\nu,\psi)}$ represents the joint pdf of scatterer positions $\boldsymbol{r}$, shapes Ξ, sizes D, permittivities ϵ_r, and tilt ν and orientation ψ angles with respect to the polarization plane.
Inside of the homogeneous layer, the scatterers are assumed to be randomly distributed, with a uniform pdf of positions ($p_{\boldsymbol{r}}(\boldsymbol{r}) = const$) having a density of n_0 scatterers per unit volume.
Furthermore, assuming the independence of the scatterers orientations from other characteristics allows to write

$$\mathbf{T} = \int \left[\iiint \hat{\mathbf{T}}_{(\boldsymbol{r},\Xi,D,\epsilon_r,\nu,\psi)}\, p_{(\Xi,D,\epsilon_r,\nu)}\, d\Xi\, dD\, d\epsilon_r\, d\nu\, p_{(\boldsymbol{r})}\, d\boldsymbol{r} \right] p_{(\psi)}\, d\psi \tag{5.2}$$

$$= \int \mathbf{R}_{T(2\psi)} \left[\iiint \hat{\mathbf{T}}_{(\boldsymbol{r},\Xi,D,\epsilon_r,\nu)}\, p_{(\Xi,D,\epsilon_r,\nu)}\, d\Xi\, dD\, d\epsilon_r\, d\nu\, p_{(\boldsymbol{r})}\, d\boldsymbol{r} \right] \mathbf{R}^{\mathrm{T}}_{T(2\psi)} p_{(\psi)}\, d\psi \tag{5.3}$$

$$= \int \mathbf{R}_{T(2\psi)} \left[\hat{P} \hat{\mathbf{T}}_{\delta} \right] \mathbf{R}^{\mathrm{T}}_{T(2\psi)} p_{(\psi)}\, d\psi \tag{5.4}$$

$$\tag{5.5}$$

where $\mathbf{R}_{T(2\psi)}$ is the orientation angle rotation matrix, $\hat{P}$ is the normalization factor for the scattered power, and $\hat{\mathbf{T}}_{\delta}$ is the normalized coherency matrix describing the scattering properties in the polarization plane independently from the particle orientation. $\hat{\mathbf{T}}_{\delta}$ has the form

$$\begin{bmatrix} 1 & \delta & 0 \\ \delta^* & |\delta|^2 & 0 \\ 0 & 0 & 0 \end{bmatrix} \tag{5.6}$$

where δ is the *effective particle scattering anisotropy*, determined by the average scattering properties of the particles (shapes, sizes, permittivities, and the tilt angles).
δ represents simple scatterers, assuming the existence of an axis of symmetry. One may represent the backscattering matrix of the effective (average) particle in the BSA convention in the eigenpolarizations $\hat{\boldsymbol{p}}_a, \hat{\boldsymbol{p}}_b$ by

$$\mathbf{S} = \begin{bmatrix} S_{aa} & 0 \\ 0 & S_{bb} \end{bmatrix} \tag{5.7}$$

The particle scattering anisotropy is therefore determined from the backscattering coefficients independently of orientation and scattered power via

$$\delta = \left(\frac{S_{aa} - S_{bb}}{S_{aa} + S_{bb}} \right)^* \tag{5.8}$$

Using δ, the backscattering matrix can also be expressed by

$$\mathbf{S} = \frac{S_{aa} + S_{bb}}{2} \begin{bmatrix} 1 + \delta^* & 0 \\ 0 & 1 - \delta^* \end{bmatrix} \tag{5.9}$$

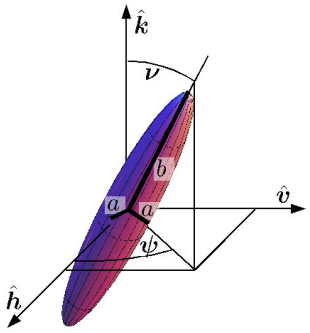

Figure 5.2: Spheroidal particle extension and orientation in the global coordinate system $\hat{\boldsymbol{k}}$, $\hat{\boldsymbol{h}}$, $\hat{\boldsymbol{v}}$.

The particle scattering anisotropy is a characteristic of the effective shape of an average particle and depends on the particle and background permittivities. If the particle permittivity is similar to the background (i.e. air) permittivity, $\epsilon_r \approx 1$, the particle scattering anisotropy tends towards 0 independently of the real shape of the particle [157, 20], and the scattering effectively vanishes. In the other case ($\epsilon_r \gg 1$), assuming simple ellipsoid particles, one can make the following predictions about the effective particle shapes: as $|\delta| \to 0$, the average effective particle shape approaches an isotropic sphere/disk, whereas for $|\delta| \to 1$ the effective shape of the scattering particle in the polarization plane tends towards a dipole. In the line of sight direction of the wave, the particles axis of symmetry tends to be horizontal if $\mathrm{Re}\,\delta > 0$ and vertical if $\mathrm{Re}\,\delta < 0$, with respect to the polarization basis of the particle scattering amplitude matrix.

5.1.2 Spheroidal Particles

The particle scattering anisotropy is a measure of the *effective shape* of the particle, as observed in the polarization plane. Using the spheroid particle model from [162, 82, 20, 1], one can relate δ to real physical characteristics, assuming the model corresponds to the illuminated particle.
Let the spheroid particle be characterized by the half–axes a and b and the polar angles (Euler angles) ψ and ν which describe orientation and tilt of the particle with respect to the line of sight (LOS) and the incidence plane, as shown in Fig. 5.2. For such an ellipsoid particle, the abstract shape and size indicators Ξ and D become the concrete dimensions $a \times a \times b$. The polarizabilities along the main axes are given by [162]

$$\alpha_a = \frac{V}{4\pi(L_a + 1/(\epsilon_r - 1))}, \quad \alpha_b = \frac{V}{4\pi(L_b + 1/(\epsilon_r - 1))} \tag{5.10}$$

where V is the particle volume, ϵ_r is the permittivity, and L_a, L_b are given by

$$L_a = \int_0^\infty \frac{ab^2}{2(s+a^2)^{3/2}(s+b^2)} ds \tag{5.11}$$

$$L_b = \int_0^\infty \frac{ab^2}{2(s+a^2)^{1/2}(s+b^2)^2} ds \tag{5.12}$$

L_a, L_b are related to the particle dimensions via

$$\frac{L_a}{L_b} \approx \frac{b}{a}, \text{ and } L_a + 2L_b = 1 \tag{5.13}$$

$$\Longrightarrow L_b = \frac{a}{2a+b}, \; L_a = \frac{b}{2a+b} \tag{5.14}$$

The backscattering matrix elements can be given in terms of the particle polarizabilities and orientation angles by [162, 20]

$$S_{hh} = \alpha_a \sin^2\nu\cos^2\psi + \alpha_b(\sin^2\psi + \cos^2\nu\cos^2\psi) \tag{5.15}$$

$$S_{vv} = \alpha_a \sin^2\nu\sin^2\psi + \alpha_b(\cos^2\psi + \cos^2\nu\sin^2\psi) \tag{5.16}$$

$$S_{hv} = (\alpha_a + \alpha_b)\sin^2\nu\sin\psi\cos\psi \tag{5.17}$$

After rotation of the polarization basis $\hat{\boldsymbol{p}}_h, \hat{\boldsymbol{p}}_v$ into the eigenbasis $\hat{\boldsymbol{p}}_a, \hat{\boldsymbol{p}}_b$ of the particle ($\psi \to 0$), one obtains

$$\mathbf{S}_{\hat{\boldsymbol{p}}_a\hat{\boldsymbol{p}}_b} = \mathbf{R}^{\mathrm{T}}_{S(\psi)}\mathbf{S}_{\hat{\boldsymbol{p}}_h\hat{\boldsymbol{p}}_v}\mathbf{R}_{S(\psi)} \tag{5.18}$$

$$S_{aa} = \alpha_a \sin^2\nu + \alpha_b\cos^2\nu \tag{5.19}$$

$$S_{bb} = \alpha_b \tag{5.20}$$

$$S_{ab} = 0 \tag{5.21}$$

Using the shape indicators [20, 17]

$$m = \frac{b}{a} \propto \frac{L_a}{L_b} \quad \begin{cases} m < 1 & \textit{prolate} \\ m = 1 & \textit{spherical} \\ m > 1 & \textit{oblate} \end{cases} \tag{5.22}$$

$$B = \frac{\alpha_b}{\alpha_a} = \frac{L_a + 1/(\epsilon_r - 1)}{L_b + 1/(\epsilon_r - 1)} = \frac{L_a(\epsilon_r - 1) + 1}{L_b(\epsilon_r - 1) + 1} \tag{5.23}$$

$$= \frac{m\epsilon_r + 2}{m + \epsilon_r + 1} \tag{5.24}$$

the particle scattering anisotropy for a spheroid is given by

$$\delta^* = \frac{S_{aa} - S_{bb}}{S_{aa} + S_{bb}} = \frac{1 - B}{1 + B + 2B\cot^2\nu} \tag{5.25}$$

The equation (5.25) provides the relationship between the particle scattering anisotropy and the particle characteristics. Whereas the forward model is simple, the inversion is not straightforward due to the non–linearity and the abundance of parameters.

5.1.3 Volume Layer

For the distribution of orientation angles in the polarization plane, a circular unimodal probability density function is assumed. Thus, this function can be characterized by two parameters: the mean orientation of the particles $\widetilde{\psi}$, and the degree of orientation randomness τ. It is assumed that the orientation of vegetation particles is independent

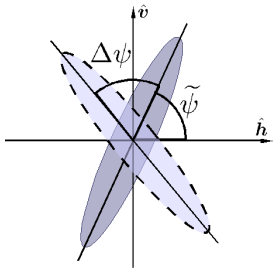

Figure 5.3: Orientation of a particle in the polarization plane, showing the mean orientation $\widetilde{\psi}$, and the individual departure of a single particle from the average $\Delta\psi$.

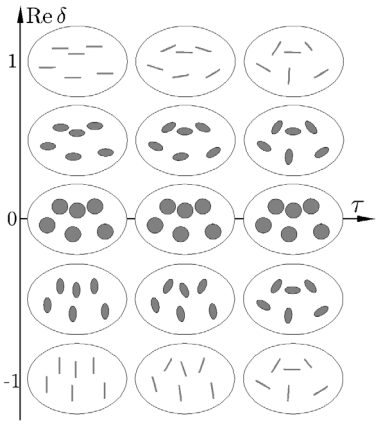

Figure 5.4: Schematic representation of effective shapes and orientations of particles in the line of sight (LOS) for different degrees of particle scattering anisotropy δ and orientation randomness τ.

of other particle characteristics. The mean orientation $\widetilde{\psi} \in [-\frac{\pi}{2}, \frac{\pi}{2}[$ is defined as the average orientation angle of the major axis of the particle in the polarization plane with respect to the horizontal axis, as shown in Fig. 5.3. The major axis corresponds to the eigenpolarization axis with the highest scattering coefficient ($\max\{|a|, |b|\}$). $p(\psi - \widetilde{\psi})$ is defined over $[-\frac{\pi}{2}, \frac{\pi}{2}[$ and is in general a circular probability density function. The degree of orientation randomness τ is defined in the range from zero to one. As $\tau \to 0$ the volume becomes strongly aligned in the preferred orientation direction, whereas for $\tau \to 1$ the particle orientations become completely random. Fig. 5.4 visualizes volume particles in the direction of the line of sight (LOS) in dependence of the degrees of particle scattering anisotropy and orientation randomness. Note that the degree of orientation randomness becomes meaningless for (effectively) isotropic scatterers ($\delta = 0$).

Distribution of Orientation Angles

In the past, the volume orientation has been modeled either as completely random (e.g. [46, 106]), or by a few discrete states [169] or has been given in an integral form (e.g. [134, 20]. However, it has been recognized that orientation effects in the vegetation can often be significant. Therefore, in this study the orientation properties of vegetation are

examined and closed form solutions are presented for the covariance and coherency matrix elements.
Under the central limit theorem condition, given a large number of scatterers, the orientations of these scatterers in the polarization plane are normally distributed [108], and follow the *von Mises* distribution (also known as the circular normal distribution) [2] which is the circular analogue of the Gaussian distribution[(1)]:

$$p_\psi(\psi) = p_C(\psi|\widetilde{\psi},\kappa) = \frac{e^{\kappa\cos(2(\psi-\widetilde{\psi}))}}{\pi I_0(\kappa)} \tag{5.27}$$

where κ is the degree of concentration (analogous of the inverse of the standard deviation), and $I_0(\kappa)$ is the modified Bessel function of order 0.
For completeness, orientation distributions based on truncated Gaussian and truncated uniform pdf's will be presented, as these distributions have been considered previously and might represent an approximation to the von Mises distribution. A close approximation of the von Mises distribution is the truncated Gaussian distribution

$$p_\psi(\psi) = p_{\overline{G}(\psi|\widetilde{\psi},\sigma)} = \begin{cases} \frac{p_{G(\psi|\widetilde{\psi},\sigma)}}{\int_{-\pi/2}^{\pi/2} p_{G(\psi'|\widetilde{\psi},\sigma)}d\psi'} & -\frac{\pi}{2} \le \psi \le \frac{\pi}{2} \\ 0 & \text{otherwise} \end{cases} \tag{5.28}$$

where

$$p_{G(\psi|\widetilde{\psi},\sigma)} = \frac{e^{-\frac{(\psi-\widetilde{\psi})^2}{2\sigma^2}}}{\sigma\sqrt{2\pi}} \tag{5.29}$$

is the non–truncated centered Gaussian probability density, and σ is the variance of the non–truncated Gaussian distribution.
The most simple approximation is the truncated uniform distribution as proposed in [20]

$$p_\psi(\psi) = p_{\overline{U}(\psi|\widetilde{\psi},\Psi)} = \begin{cases} \frac{1}{\Psi} & |2(\psi-\widetilde{\psi})| \le \Psi \\ 0 & \text{otherwise} \end{cases} \tag{5.30}$$

with the parameter Ψ determining the width of orientation angle distribution.
The degree of orientation randomness τ is defined independently of the orientation angle pdf as the area under $p(\psi-\widetilde{\psi})$ divided by the area of the smallest enclosing box in the range $\psi \in [-\frac{\pi}{2},\frac{\pi}{2}[$. Since the integral over the probability density function equals 1, and the maximum of $p(\psi)$ is at $\widetilde{\psi}$, one obtains:

$$\tau = \frac{\int p_\psi(\psi-\widetilde{\psi})d\psi}{\pi\max p_\psi(\psi)} = \frac{1}{\pi p_\psi(\widetilde{\psi})} \tag{5.31}$$

This definition is chosen because it normalizes the degree of orientation randomness to the range $[0,1]$ and because it provides a simple geometrical interpretation.

(1) The common definition for the von Mises distribution is

$$p_C(x|\mu,\kappa) = \frac{e^{\kappa\cos(x-\mu)}}{2\pi I_0(\kappa)} \tag{5.26}$$

which is circular over 2π. We have modified it in (5.27) to be circular over 1π.

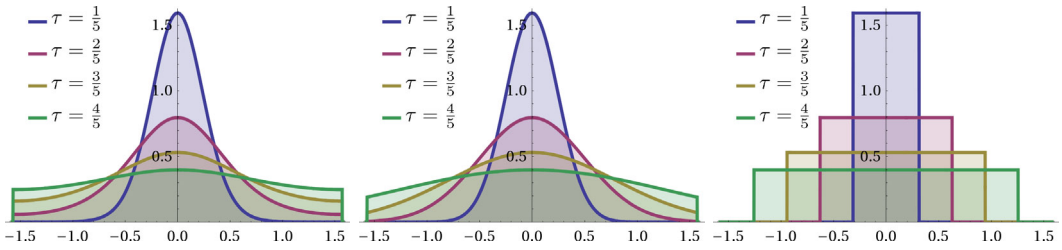

(a) von Mises PDF $p_C(\psi - \widetilde{\psi})$ (b) Truncated Gaussian PDF $p_{\overline{G}}(\psi - \widetilde{\psi})$ (c) Truncated Uniform PDF $p_{\overline{U}}(\psi - \widetilde{\psi})$

Figure 5.5: The orientation angle probability density functions $p_C(\psi)$, $p_{\overline{G}}(\psi)$, $p_{\overline{U}}(\psi)$ for different degrees of orientation randomness ($\tau = \{\frac{1}{5}, \frac{2}{5}, \frac{3}{5}, \frac{4}{5}\}$). For $\tau = 1$, the orientation angles are uniformly distributed over the whole range $[-\frac{\pi}{2}, \frac{\pi}{2}]$, whereas for $\tau = 0$, the distribution resembles a delta impulse at $\psi = \widetilde{\psi}$.

The degrees of orientation randomness for the analyzed distributions can thus be given by:

$$\tau_C = I_0(\kappa)e^{-\kappa}, \qquad \tau_{\overline{G}} = \sqrt{\frac{2\sigma^2}{\pi}}\,\mathrm{erf}\left(\frac{\pi}{\sqrt{8}\sigma}\right), \qquad \tau_{\overline{U}} = \frac{\Psi}{\pi} \tag{5.32}$$

where $\mathrm{erf}(\cdot)$ is the error function.
Examples for these distributions for different degrees of orientation randomness are shown in Fig. 5.5. As it can be seen, only the von Mises distribution is truly continuous circular. The truncated Gaussian pdf has a discontinuity at $\psi = \widetilde{\psi} \pm \frac{\pi}{2}$ and the truncated uniform has two discontinuities at $\psi = \widetilde{\psi} \pm \frac{\Psi}{2}$.

5.1.4 Complete Vegetation Structure

Further assumptions for the presented model are

- **Ground**: The direct surface backscattering is not constrained excepted for the assumed reflection symmetry about the incidence plane. For the double– and triple–bounce scattering components, the specular surface scattering is modeled using a first–order approximation.

- **Volume layer**: The vegetation volume is assumed to be homogeneous, using the Foldy–Lax approximation for the computation of the extinction σ and refractivity χ, as presented in section 2.4.3. The distorted Born approximation is used, representing single scattering in an effective field. The layer is assumed to be sparse: with negligible multiple–scattering, and no correlations between particle scattering fields.

- **Layer structure**: The normal vector of the ground terrain is assumed to be in the plane of the volume eigenpolarizations, so that both surface and volume share a common eigenpolarization basis (same azimuthal orientation). Terrain slopes can be accounted for. For simplicity, we will assume that the polarimetric second–order

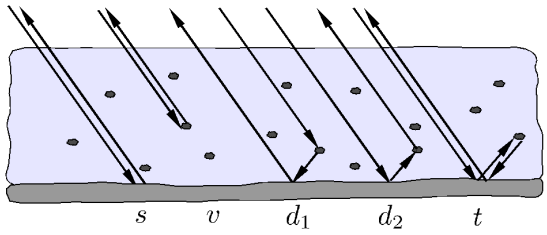

Figure 5.6: Zeroth and first order scattering components for a volume layer over the ground: surface (s), volume (v), double–bounce (d), and triple–bounce (t).

matrices can be transformed into the reflection symmetric form (cf. sections 2.5.4). The different layer components are assumed to be independent between each other.

- **Resolution cell**: The dimensions of the resolution cell are large, so that the coherent phase summation is uniformly distributed.

5.2 Polarimetric First–Order Model Components

The main zeroth and first order scattering contributions for a volumetric layer over a surface are presented in Fig. 5.6. These contributions include the direct surface scattering, the direct volume scattering, the double–bounce (volume–ground and ground–volume) scattering, and the triple–bounce (ground–volume–ground) scattering. Since these contributions are statistically independent, the covariance matrix can be decomposed into four components

$$\mathbf{C} = f_s\mathbf{C}_s + f_v\mathbf{C}_v + f_d\mathbf{C}_d + f_t\mathbf{C}_t \tag{5.33}$$

where covariance matrices are normalized with respect to the $\langle S_{hh}S_{hh}^*\rangle$ terms, and f_s, f_v, f_d, f_t represent the individual $\langle S_{hh}S_{hh}^*\rangle$ terms. The indices $_{s,\,v,\,d,\,t}$ stand for surface, volume, double bounce, and triple bounce scattering components.
The individual components are presented in the following. It will prove beneficial to use covariance matrix as well as coherency matrix representations due to the fact that different scattering and propagation effects may be better represented in one of the two forms.

5.2.1 Attenuation–Free Medium (Born Approximation)

Surface Scattering Contribution

The normalized direct ground scattering contribution can be represented for a horizontal surface using the following parametric form:

$$\mathbf{C}_s = \begin{bmatrix} 1 & 0 & \beta \\ 0 & \beta_{\frac{hv}{hh}} & 0 \\ \beta^* & 0 & \beta_{\frac{vv}{hh}} \end{bmatrix} \tag{5.34}$$

where $\beta_{\frac{hv}{hh}}$ and $\beta_{\frac{vv}{hh}}$ are real–valued whereas β is complex.

In order to reduce the complexity of this scattering component, the surface response might be modeled using the first–order small perturbation method (SPM, see section 2.4.2), which is applicable over slightly rough surfaces. The covariance matrix elements for this model are given by (2.41), so that the normalized covariance matrix becomes

$$\mathbf{C}_s = \begin{bmatrix} 1 & 0 & \beta \\ 0 & 0 & 0 \\ \beta^* & 0 & |\beta|^2 \end{bmatrix}, \quad \text{with } \beta = \left(\frac{\alpha_{vv}}{\alpha_{hh}}\right)^* \tag{5.35}$$

where α_{hh}, α_{vv} are defined in (2.42) and depend on both the incidence angle and the dielectric constant ϵ_r of the soil. As proposed in [154, 90], the imaginary part of ϵ_r can be made dependent on the real part: $\operatorname{Im}\epsilon_r = 0.15 \operatorname{Re}\epsilon_r$. This would reduce the parameterization of surface scattering polarimetry to only one real–valued coefficient.

Volume Scattering Contribution

The polarimetric scattering and coherency matrices of a single simple scatterer with backscattering anisotropy $\delta = \left(\frac{a-b}{a+b}\right)^*$ and orientation angle ψ are proportional to

$$\mathbf{S}_v \propto \mathbf{R}_{S(\psi)}^{\mathrm{T}} \begin{bmatrix} a & 0 \\ 0 & b \end{bmatrix} \mathbf{R}_{S(\psi)}, \quad \mathbf{R}_{S(\psi)} = \begin{bmatrix} \cos\psi & \sin\psi \\ -\sin\psi & \cos\psi \end{bmatrix} \tag{5.36}$$

$$\hat{\mathbf{T}}_v(\psi) \propto \mathbf{R}_{T(2\psi)} \begin{bmatrix} 1 & \delta & 0 \\ \delta^* & |\delta|^2 & 0 \\ 0 & 0 & 0 \end{bmatrix} \mathbf{R}_{T(2\psi)}^{\mathrm{T}}, \; \mathbf{R}_{T(2\psi)} = \begin{bmatrix} 1 & 0 & 0 \\ 0 & \cos 2\psi & \sin 2\psi \\ 0 & -\sin 2\psi & \cos 2\psi \end{bmatrix} \tag{5.37}$$

where $\mathbf{R}_{S(\psi)}$ and $\mathbf{R}_{T(2\psi)}$ are rotation matrices for the polarization orientation angle of the scattering and coherency matrices. Given the orientation angle distribution $p_\psi(\psi)$ one can obtain the ensemble averaged coherency matrix after integration over the orientation angles:

$$\mathbf{T}_v = \int_{-\pi/2}^{\pi/2} p_\psi(\psi) \hat{\mathbf{T}}_v(\psi) d\psi \tag{5.38}$$

$$= \int_{-\pi/2}^{\pi/2} p_\psi(\psi) \begin{bmatrix} 1 & \delta\cos 2\psi & -\delta\sin 2\psi \\ \delta^*\cos 2\psi & |\delta|^2\cos^2 2\psi & -|\delta|^2\cos 2\psi\sin 2\psi \\ -\delta^*\sin 2\psi & -|\delta|^2\cos 2\psi\sin 2\psi & |\delta|^2\sin^2 2\psi \end{bmatrix} d\psi. \tag{5.39}$$

where the integration is performed element-wise. The solution is in general non reflection symmetric. However, since $p_\psi(\psi)$ is a circular pdf, symmetric around the mean vegetation orientation $\widetilde{\psi}$, one can rotate the polarization orientation angle by $\widetilde{\psi}$ to obtain a reflection symmetric form.
Using trigonometric identities and the functions

$$g = \int_{-\pi/2}^{\pi/2} p_\psi(\psi) \cos 4\psi \; d\psi \tag{5.40}$$

$$g_c = \int_{-\pi/2}^{\pi/2} p_\psi(\psi) \cos 2\psi \; d\psi \tag{5.41}$$

equation (5.38) can be integrated over all elements to obtain the coherency matrix for a volumetric vegetation layer under reflection symmetry

$$\mathbf{T}_v = \mathbf{R}_{T(2\widetilde{\psi})} \begin{bmatrix} 1 & g_c\delta & 0 \\ g_c\delta^* & \frac{(1+g)}{2}|\delta|^2 & 0 \\ 0 & 0 & \frac{(1-g)}{2}|\delta|^2 \end{bmatrix} \mathbf{R}^{\mathrm{T}}_{T(2\widetilde{\psi})} \tag{5.42}$$

The final values for g and g_c are determined by the orientation angle pdf.
Integrating over the von Mises distribution, one obtains

$$g = \frac{I_2(\kappa)}{I_0(\kappa)}, \quad g_c = \frac{I_1(\kappa)}{I_0(\kappa)} \tag{5.43}$$

where I_n are the modified Bessel functions of n–th order. This result is obtained using [2] (p. 376, def. 9.6.19)

$$I_n(\kappa) = \frac{1}{\pi}\int_0^{\pi} e^{\kappa\cos(2\psi)}\cos(n2\psi)d\psi = \frac{1}{\pi}\int_{-\frac{\pi}{2}}^{\frac{\pi}{2}} e^{\kappa\cos(2\psi)}\cos(n2\psi)d\psi \tag{5.44}$$

with $n = 2, 1$ for g and g_c.
Using the truncated Gaussian distribution (5.28), the integrals in (5.41), (5.40) can be reformulated (with $n = 2$ for g_c and $n = 4$ for g) into

$$g_c/g = \left(\int_{-\pi/2}^{\pi/2} e^{-\frac{\psi^2}{2\sigma^2}+in\psi}d\psi + \int_{-\pi/2}^{\pi/2} e^{-\frac{\psi^2}{2\sigma^2}-in\psi}d\psi\right)\left[\int_{-\pi/2}^{\pi/2} e^{-\frac{\psi'^2}{2\sigma^2}}d\psi'\right]^{-1} \tag{5.45}$$

Using the substitutions $u' = \frac{1}{\sqrt{2}\sigma}\psi'$ for the denominator integral, $u_1 = \frac{1}{\sqrt{2}\sigma}(\psi - in)$ for the first summand integral, and $u_2 = \frac{1}{\sqrt{2}\sigma}(\psi + in)$ for the second, one can obtain the solution

$$g = \frac{e^{-8\sigma^2}\left[\mathrm{erf}(\frac{\pi-8i\sigma^2}{\sigma\sqrt{8}}) + \mathrm{erf}(\frac{\pi+8i\sigma^2}{\sigma\sqrt{8}})\right]}{2\,\mathrm{erf}(\frac{\pi}{\sigma\sqrt{8}})} \quad g_c = \frac{e^{-2\sigma^2}\left[\mathrm{erf}(\frac{\pi-4i\sigma^2}{\sigma\sqrt{8}}) + \mathrm{erf}(\frac{\pi+4i\sigma^2}{\sigma\sqrt{8}})\right]}{2\,\mathrm{erf}(\frac{\pi}{\sigma\sqrt{8}})} \tag{5.46}$$

where $\mathrm{erf}(\cdot)$ is the Gauss error function

$$\mathrm{erf}(x) = \frac{2}{\sqrt{\pi}}\int_0^x e^{-t^2}dt. \tag{5.47}$$

For the truncated uniform distribution (5.30) the solution is given by

$$g = \mathrm{sinc}(2\pi\tau), \quad g_c = \mathrm{sinc}(\pi\tau). \tag{5.48}$$

Since in the following it will prove more useful to work in the lexicographic matrix basis, one can obtain the normalized covariance matrix for the volume scattering using (2.67):

$$\mathbf{C}_v = \begin{bmatrix} 1 & 0 & v_c \\ 0 & v_x & 0 \\ v_c^* & 0 & v_o \end{bmatrix}, \qquad \text{with} \begin{cases} v_x = \frac{2(1-g)|\delta|^2}{2+(1+g)|\delta|^2+4g_c\,\mathrm{Re}\,\delta} \\ v_o = \frac{2+(1+g)|\delta|^2-4g_c\,\mathrm{Re}\,\delta}{2+(1+g)|\delta|^2+4g_c\,\mathrm{Re}\,\delta} \\ v_c = \frac{2-(1+g)|\delta|^2-4ig_c\,\mathrm{Im}\,\delta}{2+(1+g)|\delta|^2+4g_c\,\mathrm{Re}\,\delta} \end{cases} \tag{5.49}$$

where the indices in v_o, v_x, v_c stand for the normalized co–polar variance, cross–polar variance, and the co–polar correlation.

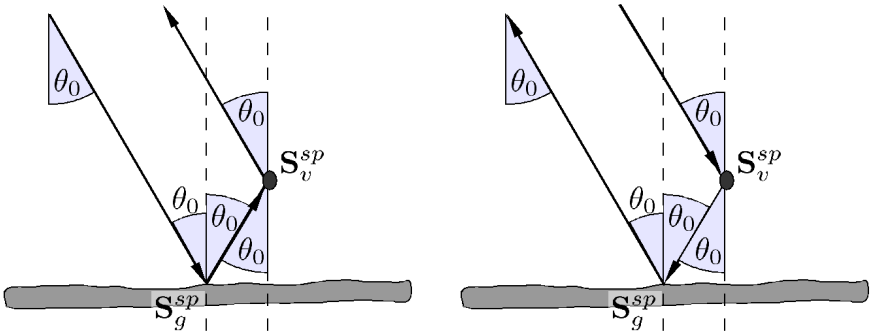

Figure 5.7: Geometry of double bounce scattering.

Double–Bounce Contribution

The double–bounce component is characterized by the specular reflection at the ground and a bistatic scattering at the volume particles [34, 32]. To derive the polarimetric covariance matrix of the double–bounce component one needs to coherently combine two scattering contributions: one path consisting of a specular reflection on the ground and another specular reflection on a volume particle, and the other path in the other direction, as shown in Fig. 5.7.
Coherently combining both scattering paths and accounting for the particle orientation leads to the following formulation in the BSA coordinates:

$$\mathbf{S}_d = \begin{bmatrix} R_h & 0 \\ 0 & R_v \end{bmatrix} \mathbf{R}_{S(\psi)} \begin{bmatrix} a' & 0 \\ 0 & b' \end{bmatrix} \mathbf{R}_{S(\psi)}^{\mathrm{T}} + \mathbf{R}_{S(\psi)} \begin{bmatrix} a' & 0 \\ 0 & b' \end{bmatrix} \mathbf{R}_{S(\psi)}^{\mathrm{T}} \begin{bmatrix} R_h & 0 \\ 0 & R_v \end{bmatrix} \tag{5.50}$$

where R_h, R_v are the Fresnel reflection coefficients. This matrix can be separated into volume and ground factor matrices

$$\mathbf{S}_d = \left(\mathbf{R}_{S(\psi)} \begin{bmatrix} a' & 0 \\ 0 & b' \end{bmatrix} \mathbf{R}_{S(\psi)}^{\mathrm{T}} \right) \circ \begin{bmatrix} 2R_h & R_h + R_v \\ R_h + R_v & 2R_v \end{bmatrix} \tag{5.51}$$

where $\circ$ represents element–wise matrix multiplication (Hadamard product). For simplicity, we will again characterize the scattering processes by complex scalar values, the ground reflection coefficients ratio

$$\eta = \left(\frac{R_v}{R_h} \right)^* \tag{5.52}$$

and the bistatic particle scattering anisotropy

$$\delta' = \left(\frac{a' - b'}{a' + b'} \right)^* \tag{5.53}$$

Since the volume and the ground characteristics are uncorrelated, the polarimetric covariance matrix can be obtained by integrating over the volume orientation independently of the specular ground contribution. Since the main orientation of the particles is assumed to be either perpendicular or parallel to the surface, the orientation statistics for

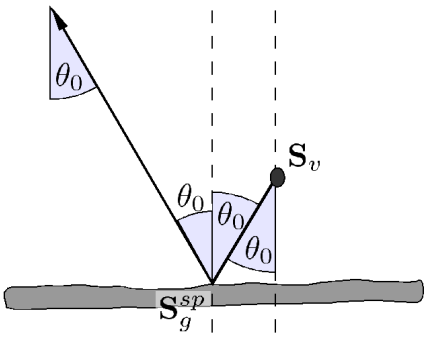

Figure 5.8: Geometry of triple bounce scattering.

the bistatic volume are the same as for the direct volume component leading to the same degree of orientation randomness ($\tau' = \tau$). Therefore, the volume part can be integrated over the orientation angle probability density as presented in the previous section. In the lexicographic matrix basis, the resulting double bounce covariance matrix has the form

$$\mathbf{C}_d = \begin{bmatrix} 1 & 0 & \eta v_c' \\ 0 & |\frac{1+\eta}{2}|^2 v_x' & 0 \\ (\eta v_c')^* & 0 & |\eta|^2 v_o' \end{bmatrix} \tag{5.54}$$

where the v_i' coefficients can be related to the v_i coefficients by replacing the backscattering particle scattering anisotropy δ by the bistatic particle scattering anisotropy δ'.
The Freeman and Durden model for the double bounce scattering can be obtained with perfectly aligned scatterers ($\tau = 0$), leading to

$$\mathbf{C}_d = \begin{bmatrix} 1 & 0 & \alpha \\ 0 & 0 & 0 \\ \alpha^* & 0 & |\alpha|^2 \end{bmatrix} \tag{5.55}$$

where α is a product of specular reflection coefficients of the ground and the volume particles ($\alpha = \eta(\frac{b'}{a'})^*$) [46]. For anisotropic and vertically aligned scatterers the bistatic particle scattering becomes actually a specular reflection. If in addition the surface is relatively smooth with high soil moisture content leading to strong reflection and low attenuation in the volume, the double bounce contribution can dominate over all other contributions.

Triple–Bounce Contribution

The triple–bounce component is characterized by two specular ground reflections and backscattering towards the ground at the volume particles. Since the volume particle characteristics are symmetrical with reference to the horizontal plane, the backscattering in the ground direction is in average equal to the backscattering in the radar direction (same δ and τ). The scattering matrix can thus be represented by

$$\mathbf{S}_t = \begin{bmatrix} R_h & 0 \\ 0 & R_v \end{bmatrix} \mathbf{R}_{S(\psi)}^{\mathrm{T}} \begin{bmatrix} a & 0 \\ 0 & b \end{bmatrix} \mathbf{R}_{S(\psi)} \begin{bmatrix} R_h & 0 \\ 0 & R_v \end{bmatrix} \tag{5.56}$$

$$= \left(\mathbf{R}_{S(\psi)}^{\mathrm{T}} \begin{bmatrix} a & 0 \\ 0 & b \end{bmatrix} \mathbf{R}_{S(\psi)} \right) \circ \begin{bmatrix} R_h^2 & R_h R_v \\ R_h R_v & R_v^2 \end{bmatrix} \tag{5.57}$$

The reflection coefficients ratio, η, determined by the Fresnel reflection coefficients of the surface, is the same as for the double–bounce component. Also, due to horizontal plane reflection symmetry of the scattering matrix, the backscattering coefficient is the same as for the volume component.
Similarly to the previous cases, the integration over the orientation angles leads to the normalized triple–bounce covariance matrix whose form is given by

$$\mathbf{C}_t = \begin{bmatrix} 1 & 0 & \eta^2 v_c \\ 0 & |\eta|^2 v_x & 0 \\ (\eta^2 v_c)^* & 0 & |\eta|^4 v_o \end{bmatrix} \tag{5.58}$$

The triple bounce component does not introduce any new parameters with respect to the volume and the double–bounce components, except of the intensity weighting. It becomes important in case of low extinction and very flat reflective ground, and in the limit it approaches the volume scattering component.

5.2.2 Attenuating and Refracting Medium (Distorted Born Approximation)

In this section, attenuation and refractivity effects on the covariance matrices and interferometric coherences are derived. During the propagation of the wave through the vegetation, it gets attenuated and refracted due to absorption and scattering. Up to now, extinction and refractivity of the vegetation have been assumed to be equal for all polarizations, and were included in the power coefficients. However, in case of orientation preference of vegetation particles ($\tau < 1$), extinction and refractivity might be different for the different polarizations.
As discussed in sections 2.1, 2.4, and 2.5.3, the wave propagation along one of the eigenpolarizations of the effective medium, $\hat{\boldsymbol{p}}_a, \hat{\boldsymbol{p}}_b$, is characterized by the effective propagation constant $k_{a/b} = k_0 + \kappa_{a/b} = k_0 + (k_0 \chi_{a/b} + i\frac{\sigma_{a/b}}{2})$, where χ is the real part of the complex index of refraction minus one [153], and σ is the two–way extinction. If the effective medium is not isotropic, as it is the case for oriented volumes, the propagation constants are not equal. In this case, of importance for polarimetry and interferometry are the mean extinction σ, and the differences in extinction and refractivity $\Delta\sigma$, $\Delta\chi$:

$$\sigma = \frac{\sigma_a + \sigma_b}{2}, \quad \Delta\sigma = \frac{\sigma_a - \sigma_b}{2}, \quad \Delta\chi = \chi_a - \chi_b, \quad \xi = -\Delta\sigma + ik_0\Delta\chi \tag{5.59}$$

where the indices a, b refer to the eigenpolarizations of the medium.
It will prove useful to introduce the function $f_\diamond(s)$ ($\diamond \in [a, b, c, 0]$)

$$f_\diamond(s) = \frac{e^{(-2\sigma+2x)s}}{\int_0^{\frac{h_v}{\cos\theta_0}} e^{-2\sigma s'} ds'}, \quad x = \begin{cases} 0 & \text{for } \diamond = 0 \\ -\Delta\sigma & \text{for } \diamond = a \\ +\Delta\sigma & \text{for } \diamond = b \\ ik_0\Delta\chi & \text{for } \diamond = c \end{cases} \tag{5.60}$$

which represents the normalized effective density (with respect to a medium with mean extinction σ) of the volume as seen by the radar at a certain polarization state. f_0

($\diamond = 0$) is the effective density for the random volume case which represents an isotropic medium with equal extinction and refractivity values at all polarizations. f_a, f_b, and f_c ($\diamond = a, b, c$) represent the normalized effective density accounting for differences in extinction and refractivity at the eigenpolarizations.
The covariance and coherency matrices accounting for the differences in the propagation constants for forth and back propagation of a distance s in a homogeneous medium can be represented by

$$\mathbf{C}' = e^{-2\sigma s}\mathbf{P}_{L(s)}\mathbf{C}\mathbf{P}^{\dagger}_{L(s)}, \qquad \mathbf{T}' = e^{-2\sigma s}\mathbf{P}_{P(s)}\mathbf{T}\mathbf{P}^{\dagger}_{P(s)} \tag{5.61}$$

where the matrices $\mathbf{P}_L$ and $\mathbf{P}_P$ [152] represent the effects due to different propagation constants at the eigenpolarizations

$$\mathbf{P}_{L(s)} = \begin{bmatrix} e^{\xi s} & 0 & 0 \\ 0 & 1 & 0 \\ 0 & 0 & e^{-\xi s} \end{bmatrix}, \quad \mathbf{P}_{P(s)} = \begin{bmatrix} \cosh\xi s & \sinh\xi s & 0 \\ \sinh\xi s & \cosh\xi s & 0 \\ 0 & 0 & 1 \end{bmatrix} \tag{5.62}$$

Therefore, the attenuation in the volume for the direct ground and the double bounce components can be readily accounted for using (5.61). After normalization, the correction factors can be represented using the element–wise matrix multiplication (Hadamard product):

$$\mathbf{C}_{s/d} \leftarrow \mathbf{C}_{s/d} \circ \begin{bmatrix} 1 & 0 & \zeta \\ 0 & |\zeta| & 0 \\ \zeta^* & 0 & |\zeta|^2 \end{bmatrix} \tag{5.63}$$

where $\zeta = e^{2\xi s}$, and $s = h_v/\cos\theta_0$ for a volume layer of depth h_v.
For the volume term one needs to integrate over the whole propagation path to obtain the polarization change induced by different propagation constants. One obtains

$$\mathbf{C}_v \leftarrow \int_0^{\frac{h_v}{cos\theta_0}} e^{-2\sigma s}\mathbf{P}_{L(s)}\mathbf{C}_v\mathbf{P}^{\dagger}_{L(s)}ds \propto \mathbf{C}_v \circ \begin{bmatrix} q_a & 0 & q_\chi \\ 0 & 1 & 0 \\ q^*_\chi & 0 & q_b \end{bmatrix} \tag{5.64}$$

where $\circ$ is the element–wise multiplication and the q factors express the normalized change due to extinction and refractivity:

$$q_{a/b/\chi/0} = \int_0^{\frac{h_v}{\cos\theta_0}} f_\diamond(s)ds \tag{5.65}$$

Note that the co–polar variances depend only on the extinction difference, whereas the co–polar correlation depends only on the refractivity difference. Naturally, if one of the differences approaches zero, one obtains unity for the corresponding correction factors.
The attenuation and refractivity of the triple–bounce component is twofold, since it gets attenuated due to wave propagation till the ground plus the additional wave propagation from the ground into the volume, resulting in

$$\mathbf{C}_t \leftarrow \mathbf{C}_t \circ \begin{bmatrix} 1 & 0 & \frac{q_c}{q_a}\zeta \\ 0 & \frac{1}{q_a}|\zeta| & 0 \\ (\frac{q_c}{q_a}\zeta)^* & 0 & \frac{q_b}{q_a}|\zeta|^2 \end{bmatrix} \tag{5.66}$$

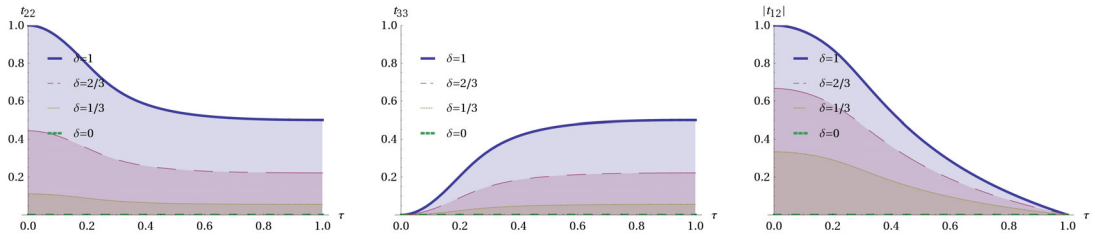

Figure 5.9: Normalized coherency matrix elements as functions of τ for different $|\delta|$. Von Mises distribution of orientation angles.

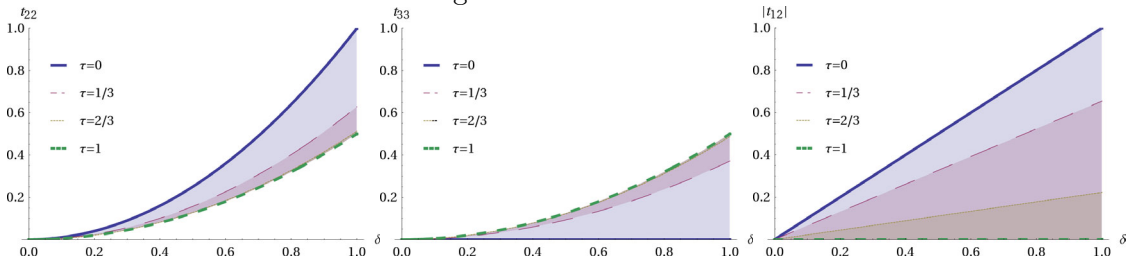

Figure 5.10: Normalized coherency matrix elements as functions of $|\delta|$ for different τ. Von Mises distribution of orientation angles.

In summary, the covariance matrices for the four basic scattering components considering orientation and attenuation effects can be represented by

$$\mathbf{C}_g = \begin{bmatrix} 1 & 0 & \beta\zeta \\ 0 & 0 & 0 \\ (\beta\zeta)^* & 0 & |\beta\zeta|^2 \end{bmatrix}, \qquad \mathbf{C}_v = \begin{bmatrix} 1 & 0 & \frac{q_c}{q_a}v_c \\ 0 & \frac{1}{q_a}v_x & 0 \\ (\frac{q_c}{q_a}v_c)^* & 0 & \frac{q_o}{q_a}v_0 \end{bmatrix} \tag{5.67}$$

$$\mathbf{C}_d = \begin{bmatrix} 1 & 0 & \eta\zeta v_c' \\ 0 & |\frac{1+\eta}{2}|^2|\zeta|v_x' & 0 \\ (\eta\zeta v_c')^* & 0 & |\eta\zeta|^2 v_o' \end{bmatrix}, \quad \mathbf{C}_t = \begin{bmatrix} 1 & 0 & \eta^2\frac{q_c}{q_a}\zeta v_c \\ 0 & |\eta|^2\frac{1}{q_a}|\zeta|v_x & 0 \\ (\eta^2\frac{q_c}{q_a}\zeta v_c)^* & 0 & |\eta|^4\frac{q_b}{q_a}|\zeta|^2 v_o \end{bmatrix} \tag{5.68}$$

5.3 Interpretation of the δ/τ Model

The coherency matrix form (5.42), as derived in section 5.2.1, deserves further inspection. The coherency and covariance matrix elements as a function of particle scattering anisotropy and the degree of orientation randomness are shown in Figs. 5.9–5.12. Figs. 5.9 and 5.10 present the normalized coherency matrix elements $t_{v22} = \frac{\langle|S_{hh}-S_{vv}|^2\rangle}{\langle|S_{hh}+S_{vv}|^2\rangle}$, $t_{v33} = \frac{2\langle|S_{hv}|^2\rangle}{\langle|S_{hh}+S_{vv}|^2\rangle}$, and $|t_{v12}| = |\frac{\langle(S_{hh}+S_{vv})(S_{hh}-S_{vv})^*\rangle}{\langle|S_{hh}+S_{vv}|^2\rangle}|$ with circular normal distribution of orientation angles. Figs. 5.11 and 5.12 show the normalized covariance matrix elements $c_{v33} = \frac{\langle|S_{vv}|^2\rangle}{\langle|S_{hh}|^2\rangle}$, $c_{v22} = \frac{2\langle|S_{hv}|^2\rangle}{\langle|S_{hh}|^2\rangle}$ and $|c_{v13}| = |\frac{\langle S_{hh}S_{vv}^*\rangle}{\langle|S_{hh}|^2\rangle}|$ in dependence of τ and δ. Note that the elements corresponding to the cross–polar terms (c_{22}, t_{33}) are not equal since the normalization factors ($|HH|^2$, $|HH+VV|^2$) are not the same. Figs. 5.13 and 5.14 show a 3-D view of the same parameters using the whole $(\tau, |\delta|)$ space. For comparison, the

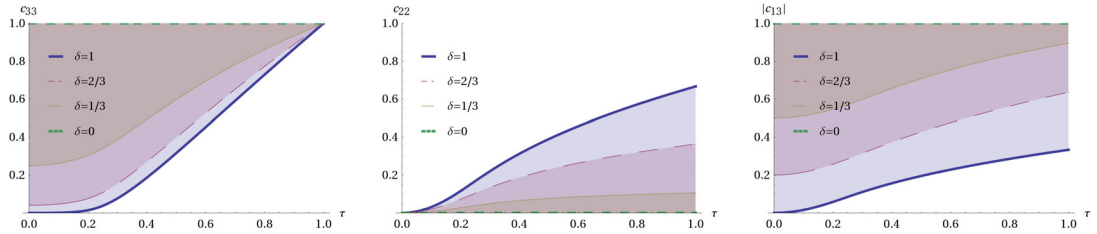

Figure 5.11: Normalized covariance matrix elements as functions of τ for different $|\delta|$. Von Mises distribution of orientation angles.

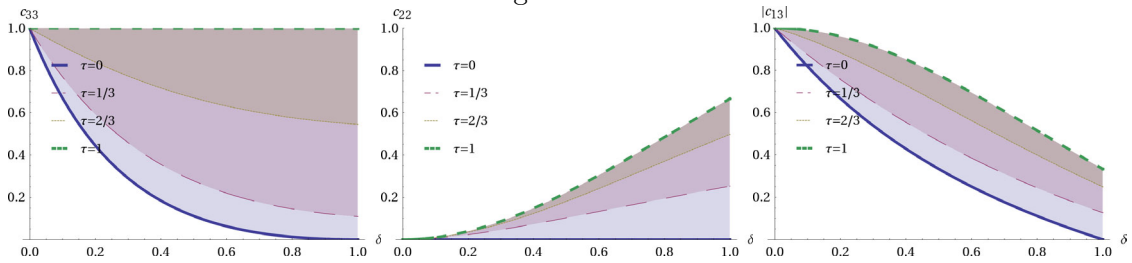

Figure 5.12: Normalized covariance matrix elements as functions of $|\delta|$ for different τ. Von Mises distribution of orientation angles.

parameter space and the range of the Freeman–Durden decomposition [46] is presented by the blue circle, and that of the Freeman II decomposition by the red curve.
The orientation effects in the volume have been derived from the formulations in [46], assuming a non–uniform orientation angle distribution. As it has been identified afterwards, similar derivation approaches have been previously undertaken by Cloude *et al.* [20] and Schuler *et al.* [135]. Cloude *et al.* [20] (1999) presented the integral form (5.38) and used the truncated uniform orientation angle distribution for data analysis. Schuler *et al.* [135] (2002) extended this approach and obtained a form similar to (5.42) but having 3 real and 1 complex variables (reducible to 2 real and 1 complex variables as in our case), using a Gaussian pdf for the orientations (not the *truncated* Gaussian distribution) to represent surface slopes. Yamaguchi *et al.* [169, 170] (2005, 2006) used a sine function to represent the orientation angle distribution and computed a discrete set of oriented coherency matrices to enhance the decomposition of the data into main scattering components. Recently, Freeman extended in 2007 [45] the Freeman–Durden decomposition [46] to account for different particle shapes using the parameter ρ which is the related to the particle scattering anisotropy $|\delta|$. In comparison to these approaches, we have derived the general form of the volume coherency matrix making the dependence of the polarimetry on the main physical parameters (particle scattering anisotropy δ and orientation randomness τ) explicit and identifying the von Mises circular normal distribution as the most probable unimodal distribution of orientation angles under the central limit theorem.

Scattering Mechanism

The δ/τ model decomposition of the polarimetric coherency matrix was originally intended for volumetric distributed targets in terms of second order statistics for a large number of

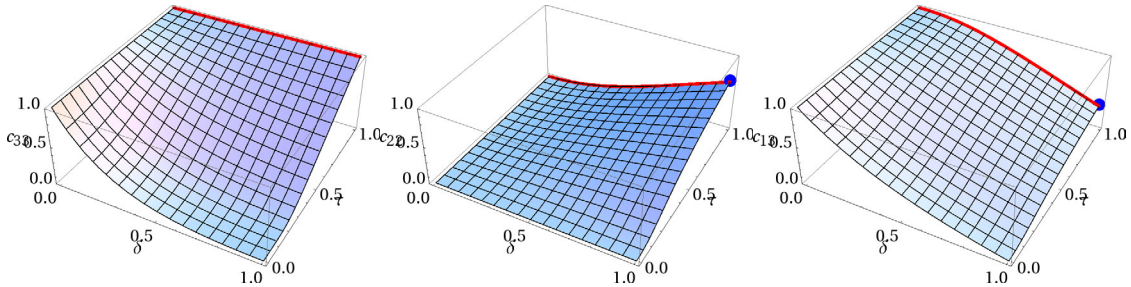

(a) $c_{33} = \frac{\langle |S_{vv}|^2 \rangle}{\langle |S_{hh}|^2 \rangle}$ (b) $c_{22} = \frac{\langle |S_{hv}|^2 \rangle}{\langle |S_{hh}|^2 \rangle}$ (c) $|c_{13}| = \frac{|\langle S_{hh} S_{vv}^* \rangle|}{\langle |S_{hh}|^2 \rangle}$

Figure 5.13: Normalized covariance matrix elements $(c_{33}, c_{22}, |c_{13}|)$ over τ and $|\delta|$. Von Mises distribution of orientation angles. The blue point and the red line correspond to the parameter space of the Freeman–Durden and the Freeman II models, respectively.

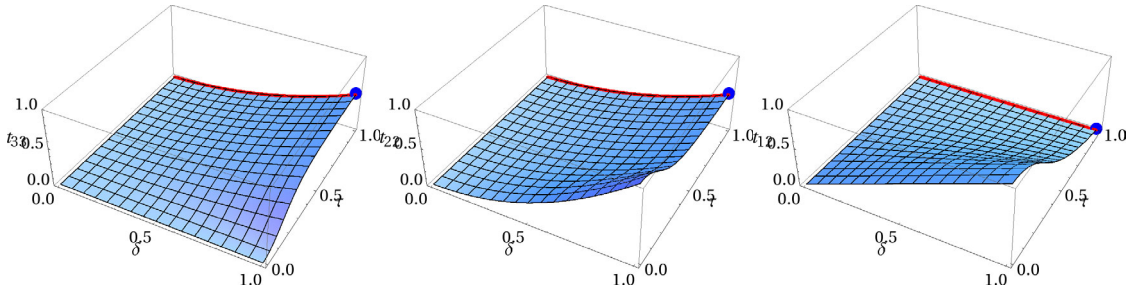

(a) $t_{33} = \frac{\langle |S_{hv}|^2 \rangle}{\langle |S_{hh}+S_{vv}|^2 \rangle}$ (b) $t_{22} = \frac{\langle |S_{hh}-S_{vv}|^2 \rangle}{\langle |S_{hh}+S_{vv}|^2 \rangle}$ (c) $|t_{12}| = \frac{|\langle (S_{hh}+S_{vv})(S_{hh}-S_{vv})^* \rangle|}{\langle |S_{hh}+S_{vv}|^2 \rangle}$

Figure 5.14: Normalized coherency matrix elements $(t_{33}, t_{22}, |t_{12}|)$ over $\tau \in [0, 1]$ and $|\delta| \in [0, 1]$. Von Mises distribution of orientation angles. The blue point and the red line correspond to the parameter space of the Freeman–Durden and the Freeman II models of the volume component, respectively.

scatterers under the Born approximation. Closer inspection shows that this decomposition scheme can be related to other models and scattering mechanism types.
In particular, the particle scattering anisotropy magnitude $|\delta|$ is directly related to *Cloude's* α angle [25]:

$$|\delta| = \tan\alpha \tag{5.69}$$

Also, it can be expressed using *Freeman's* shape parameter ρ [45]:

$$|\delta| = 2\frac{1-\rho}{1+\rho} \tag{5.70}$$

Considering now $|\delta|$ as a general scattering mechanism indicator, and not only as an effective particle scattering anisotropy, one can extend the range of $|\delta|$ to $[0, \infty]$.
The common ideal canonical scattering mechanism types can therefore be represented by

	sphere/surface	dipole	dihedral/helix
$\|\delta\|$	0	1	∞
α	0	$\frac{1}{4}\pi$	$\frac{1}{2}\pi$
ρ	1	$\frac{1}{3}$	0

In all cases, the tilt angle distribution is already integrated into these parameters. In order to obtain indicators related to the real particle shape, permittivity, and tilt distribution characteristics, one needs to have additional a–priori information.
Under the assumptions of reciprocity, reflection symmetry, and independence of scattering mechanism types from orientation angles in the polarization plane, the general coherency matrix form is therefore given by

$$\mathbf{T} = \begin{bmatrix} 1 & g_c\delta & 0 \\ g_c\delta^* & \frac{(1+g)}{2}|\delta|^2 & 0 \\ 0 & 0 & \frac{(1-g)}{2}|\delta|^2 \end{bmatrix} \tag{5.71}$$

where, under the Central Limit Theorem, g and g_c are given by (5.40) and (5.41).
With reference to surface scattering, this model is related to the X–Bragg model [55, 56, 135] assuming truncated uniform or Gaussian orientation angles distributions.

Linear Approximation of Orientation Randomness

Fig. 5.15 shows g and g_c as functions of the degree of orientation randomness for the different orientation distribution functions. A simple approximation for g and g_c can be deduced from this figure since g and g_c appear to be almost linearly related to τ in the range $\tau \in [0, 0.5]$ and $\tau \in [0, 1]$, respectively. This suggests a very simple *linear* approximation of these functions (compare Fig. 5.16)

$$g_{(\tau)} = \begin{cases} 1-2\tau & \tau \le \frac{1}{2} \\ 0 & \tau > \frac{1}{2} \end{cases}, \qquad g_{c(\tau)} = 1-\tau \tag{5.72}$$

which can be readily inverted. This linear approximation can be used to obtain coarse estimates of the orientation randomness, since it represents the dynamic range of the

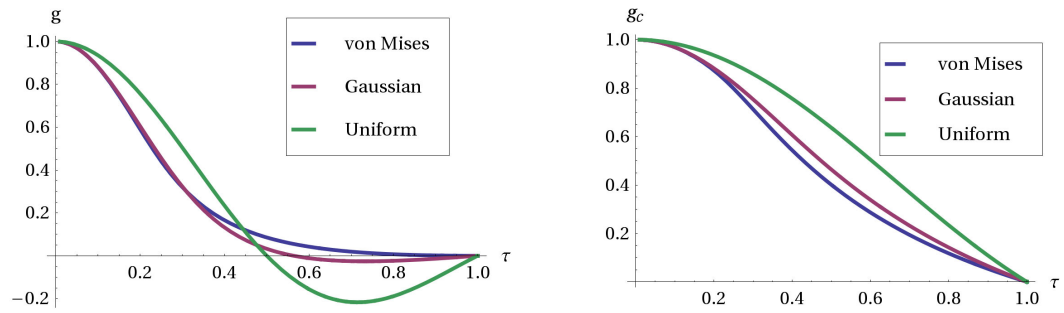

Figure 5.15: Graphs of g, g_c for von Mises, Gaussian, and uniform distributions.

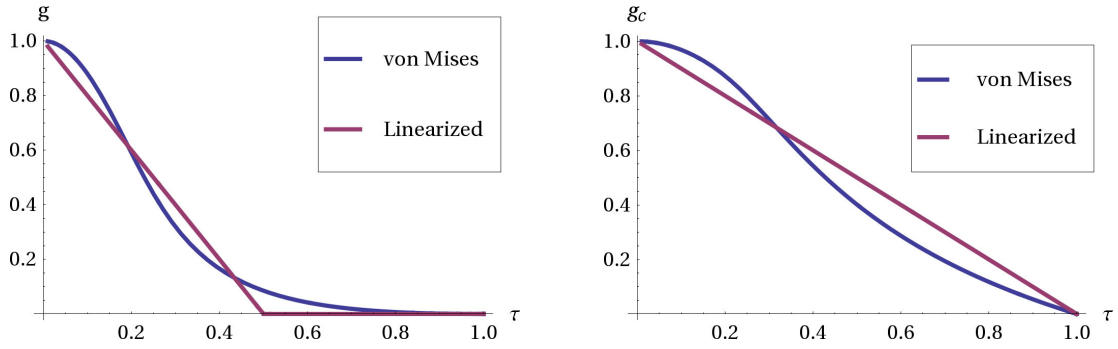

Figure 5.16: Graphs of g, g_c for the von Mises distribution and the linear approximation.

degree of orientation randomness. If more accurate results are required, e.g. for forward–modeling, then the von Mises distribution results should be preferred.
Using the linear approximation for the orientation distribution, one obtains two linear models for the coherency matrix form:

$$\mathbf{T} = \begin{cases} \begin{bmatrix} 1 & (1-\tau)\delta & 0 \\ (1-\tau)\delta^* & (1-\tau)|\delta|^2 & 0 \\ 0 & 0 & \tau|\delta|^2 \end{bmatrix} & \tau \leq \frac{1}{2} \\ \begin{bmatrix} 1 & (1-\tau)\delta & 0 \\ (1-\tau)\delta^* & \frac{1}{2}|\delta|^2 & 0 \\ 0 & 0 & \frac{1}{2}|\delta|^2 \end{bmatrix} & \tau > \frac{1}{2} \end{cases} \tag{5.73}$$

For low degree of orientation randomness ($\tau \leq \frac{1}{2}$), one observes a trade–off between the co–polar terms and the cross–polar HV component. For no orientation randomness ($\tau = 0$), a common first–order coherency matrix form is obtained.
For high degree of orientation randomness ($\tau > \frac{1}{2}$), which is the case for most vegetation types at large ranges of incidence angles, the diagonal elements appear to be saturated, and one observes sensitivity to the orientation randomness only in the off–diagonal correlation $(S_{hh} + S_{vv})(S_{hh} - S_{vv})^*$.

Inversion

Once the volume response has been separated from the other contributions, and after transformation to the coherency matrix form and normalization, the magnitude and the phase of the particle scattering anisotropy δ can be obtained independently of the degree of orientation randomness via

$$|\delta| = \sqrt{t_{v22} + t_{v33}} = \sqrt{\frac{\langle|S_{hh} - S_{vv}|^2\rangle + 4\langle|S_{hv}|^2\rangle}{\langle|S_{hh} + S_{vv}|^2\rangle}} \tag{5.74}$$

$$\arg\delta = \arg(t_{v12}) = \arg(\langle(S_{hh} + S_{vv})(S_{hh} - S_{vv})^*\rangle) \tag{5.75}$$

g and g_c are computed using δ. From g and g_c it is possible to obtain the degree of orientation randomness by inverting (5.43) or (5.72). For the linear approximation, the degree of orientation randomness can be more easily retrieved from the co–polar correlation

$$\tau = 1 - \frac{|t_{v12}|}{|\delta|} = 1 - \frac{1}{|\delta|}\frac{|\langle(S_{hh} + S_{vv})(S_{hh} - S_{vv})^*\rangle|}{\langle|S_{hh} + S_{vv}|^2\rangle} \tag{5.76}$$

Alternatively, for relatively aligned particles the diagonal elements of the coherency matrix can be used for an estimation of τ. The equations (5.74) and (5.76) offer two basic and easy indicators for particle scattering anisotropy (scattering mechanism type) and orientation randomness if the coherency matrix is dominated by volume scattering. Using appropriate models (e.g. [20]) one is able to invert more physical parameters, if a–priori knowledge about the permittivity, the shape and the tilt angles distribution of the particles is available.

5.4 Interferometric First–Order Model Components

In analogy to the polarimetric model of $\mathbf{C}$ in (5.33), the interferometric behavior of the main scattering contributions from a layer of random volume vegetation over the ground can be modeled by a linear combination of polarimetric interferometric cross–correlation matrices.

$$\mathbf{Q} = \mathbf{Q}_s + \mathbf{Q}_v + \mathbf{Q}_d + \mathbf{Q}_t \tag{5.77}$$

If the attenuation inside the vegetation is independent of the polarization, the volume decorrelation terms become polarization independent, too. If in addition the decorrelation is caused only due to the volumetric structure of the vegetation, then (5.77) can be expressed by

$$\mathbf{Q} = f_s\mathbf{C}_s\gamma_s + f_v\mathbf{C}_v\gamma_v + f_d\mathbf{C}_d\gamma_d + f_t\mathbf{C}_t\gamma_t \tag{5.78}$$

where $\gamma_s, \gamma_v, \gamma_d, \gamma_t$ are the volume coherence terms for the given scattering mechanism types.
Alternatively, (5.78) can be analogously represented by a coherence model:

$$\gamma_{(\boldsymbol{\omega})} = c_{s(\boldsymbol{\omega})}\gamma_s + c_{v(\boldsymbol{\omega})}\gamma_v + c_{d(\boldsymbol{\omega})}\gamma_d + c_{t(\boldsymbol{\omega})}\gamma_t \tag{5.79}$$

where the c_i coefficients are the normalized polarimetric power coefficients:

$$c_{i(\boldsymbol{\omega})} = f_i \frac{\boldsymbol{\omega}^\dagger \mathbf{C}_i \boldsymbol{\omega}}{\boldsymbol{\omega}^\dagger \mathbf{C} \boldsymbol{\omega}}, \quad i \in \{s, v, d, t\}, \quad \forall\, \boldsymbol{\omega} : \sum_i c_{i(\boldsymbol{\omega})} = 1 \tag{5.80}$$

In the next section, the constituents of this model are presented assuming constant extinctions and refractivities over all polarizations. Later on, the case of polarization dependent extinctions and refractivities will be considered.

5.4.1 Volume Coherences: Polarization Independent Attenuation

Single–Pass Alternate–Transmit Mode or Repeat–Pass

In section 3.4.3, we have shown that the interferometric coherence can be decomposed into a product of constituents induced by acquisition system and scattering medium. The medium induced constituents can be further decomposed into a weighted linear combination of coherences which correspond either to spatially separated layers or components with uncorrelated scattering characteristics. In the following we present the main, zeroth– and first–order, scattering contributions from a random volume over ground. Assuming single–pass acquisition with no temporal decorrelation ($\gamma_{temp,i} = 1$), the volume coherence for any polarization $\boldsymbol{\omega}$ can be decomposed into uncorrelated coherence components due to surface, volume, double–bounce, and triple–bounce scattering components which were presented in section 2.4.3:

$$\gamma_z = c_s \gamma_{z,s} + c_v \gamma_{z,v} + c_d \gamma_{z,d} + c_t \gamma_{z,t} \tag{5.81}$$

The modified van Cittert-Zernike theorem states that the volume coherence can be obtained as the Fourier transform of the spatial distribution of the scatterers [127, 52]. This theorem validates the volume coherence expression derived in (3.60), where the spatial distribution is represented by $\rho(z)$ in dependence of height z. Thus, the volume coherence γ_z for any component $i \in \{s, v, d, t\}$ can be computed by (see (3.60))

$$\gamma_{z,i} = \frac{I_{z,i}}{I^0_{z,i}} = \frac{\int \rho_i(z') e^{ik_z(z'-z_0)} dz'}{\int \rho_i(z') dz'}, \qquad i \in \{s, v, d, t\} \tag{5.82}$$

Since, by definition, $\rho(z')$ is normalized to unity, the volume coherence can be given by

$$\gamma_{z,i} = \frac{I_{z,i}}{I^0_{z,i}} = \int \rho_i(z') e^{ik_z(z'-z_0)} dz' \tag{5.83}$$

Note that the reference phase is not included in these formulations.
It is of importance to understand the meaning of $\rho(z')$. It represents the *effective* normalized backscattering strength of the given scattering type component. Here, effective implies two aspects. One includes the attenuation effects, so that for the same density of scatterers, in the presence of extinction the backscattering strength from the lower layer will be weaker than from the upper layer ($\rho(z_1) \leq \rho(z_2)$ for $z_1 < z_2$). The other implies that z has to be regarded not as the true height coordinate of the scatterer, but the *apparent* height, relating the range delay to a straight ray without reflections at the ground. This concept is visualized in Fig. 5.17, showing the true wave paths (in black)

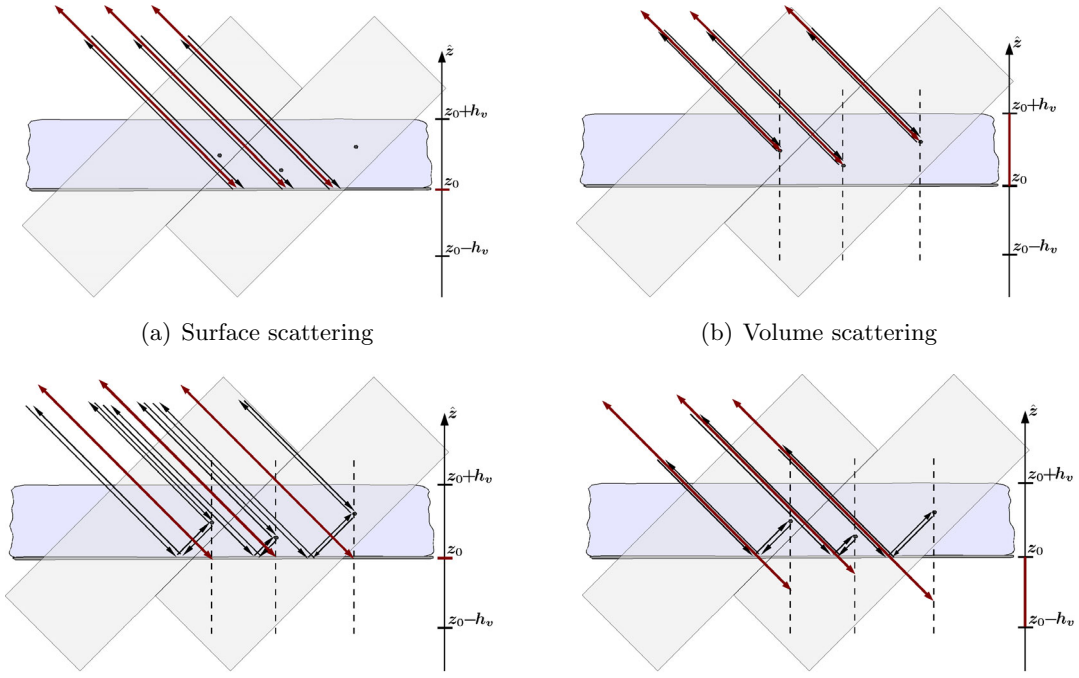

(a) Surface scattering (b) Volume scattering

(c) Double–bounce scattering (d) Triple–bounce scattering

Figure 5.17: Zeroth and first–order scattering components as seen by the radar in the repeat–pass acquisition (or in the alternate transmit mode of single pass acquisition) . The wave propagation paths are represented in black arrows. The effective paths, i.e. the assumed paths based on the range delay, are represented in red. The $\hat{z}$–axis is marked red for the height range of integration for the given scattering components. Two range resolution cells are denoted.

and the *effective* paths (in red) for the different component types. The *apparent* effective range of heights, as it will be visible to a repeat–pass interferometer, is denoted in red along the $\hat{\boldsymbol{z}}$–axis. As it can be seen, for the surface and volume components the apparent heights correspond to the true scatterer heights, whereas for the double–bounce and the triple–bounce components the apparent heights are located either at the ground level or underneath, due to the specular reflections at the ground. The effective relative backscattering strength functions depend on height and are given by

$$\rho_s(z) = \begin{cases} 1 & z = z_0 \\ 0 & \text{else} \end{cases} \qquad \rho_v(z) = \begin{cases} \dfrac{e^{\frac{2\sigma}{\cos\theta_0}(z_0+h_v-z)}}{\int_{z_0}^{z_0+h_v} e^{\frac{2\sigma}{\cos\theta_0}(z_0+h_v-z')}dz'} & z \in [z_0, z_0+h_v] \\ 0 & \text{else} \end{cases} \tag{5.84}$$

$$\rho_d(z) = \begin{cases} 1 & z = z_0 \\ 0 & \text{else} \end{cases} \qquad \rho_t(z) = \begin{cases} \dfrac{e^{\frac{2\sigma}{\cos\theta_0}(z_0-z)}}{\int_{z_0-h_v}^{z_0} e^{\frac{2\sigma}{\cos\theta_0}(z_0-z')}dz'} & z \in [z_0-h_v, z_0] \\ 0 & \text{else} \end{cases} \tag{5.85}$$

where the Foldy–Lax approximation for the effective medium has been applied to include the height dependence on the extinction. Inserting $\rho_i(z)$ into the volumetric coherence

function, one obtains the following decorrelation sources

$$\gamma_s = \rho_s(z)e^{ik_z(z-z_0)} = 1 \tag{5.86}$$

$$\gamma_v = \int_{z_0}^{z_0+h_v} \rho_v(z)e^{ik_z(z-z_0)}dz = \int_0^{h_v} f_0(\tfrac{z}{\cos\theta_0})e^{ik_z z}dz, \quad \text{where } f_0(s) = \frac{e^{2\sigma s}}{\int e^{2\sigma s'}ds'} \tag{5.87}$$

$$\gamma_d = 1 \tag{5.88}$$

$$\gamma_t = \int_{z_0-h_v}^{z_0} \rho_t(z)e^{ik_z(z-z_0)}dz = \int_0^{h_v} f_0^*(\tfrac{z}{\cos\theta_0})e^{-ik_z z}dz \tag{5.89}$$

where in the volume and the triple–bounce coherence terms, the spatial scatterer distribution function (height dependent) $\rho_i(z)$ has been replaced by the travel distance dependent function $f_0(s)$ from (5.60). $f_0^*(s)$ is the complex conjugate of $f_0(s)$. For completeness, all these coherence terms need to be multiplied with the $e^{i\phi_0}$ which represents the baseline dependent ground reference phase.
Note that, if the range resolution is much smaller than the height of the volume, the first order scattering contributions from the same scatterers will fall into different resolution cells. This is for example the case for L–band remote sensing of forests, or S, C, and X–bands for agricultural vegetation.

Single–Pass Single–Transmit Mode

In the single–transmit mode the acquisition geometry is different causing modified volume coherence values. At first, sending at one antenna and receiving at another is already a bistatic configuration. However, the difference in positions of the two antennas in comparison to the range distance is quite small for the considered applications, so that this aspect has no effects on backscattering coefficients and polarimetry of the response, except of the phase. Second, the interferometric phase difference is effectively halved (but not always, since it can only be assumed for direct scattering contributions) because the two–way range difference is only half of the two–way range difference of a repeat–pass acquisition mode. Thus, the vertical wavenumber k_z needs to be computed accordingly (compare with k_z in repeat pass mode in equation (3.41)):

$$\text{Single–transmit mode:} \quad k_z = k_0 \frac{B_\perp}{R_0 \sin\theta_0} \tag{5.90}$$

In particular, it has been pointed out by Treuhaft and Siqueira [154], that the vertical wavenumber for the double–bounce contribution needs to be computed in rectangular coordinates. This results in the following term for the double–bounce coherence (combining the two propagation paths):

$$\gamma_d = \frac{1}{2h_v}\left[\int_0^{h_v} e^{i\sin^2(\theta_0)k_z z}dz + \int_0^{h_v} e^{-i\sin^2(\theta_0)k_z z}dz\right] = \text{sinc}(\sin^2(\theta_0)k_z h_v) \tag{5.91}$$

and is independent of the extinction since the scattering center is still located at the ground. The term $\sin^2(\theta_0)k_z$ represents the vertical wavenumber with respect to the rectangular coordinate system, contrary to the cylindrical coordinate system, as required for the double bounce phase difference computation [154].

In summary, the volume coherence terms for the single–transmit acquisition mode are given by

$$\gamma_s = \rho_s(z)e^{ik_z(z-z_0)} = 1 \tag{5.92}$$

$$\gamma_v = \int_0^{h_v} f_0(\tfrac{z}{\cos\theta_0})e^{ik_z z}dz \tag{5.93}$$

$$\gamma_d = \mathrm{sinc}(\sin^2(\theta_0)k_z h_v) \tag{5.94}$$

$$\gamma_t = \int_0^{h_v} f_0^*(\tfrac{z}{\cos\theta_0})e^{-ik_z z}dz \tag{5.95}$$

5.4.2 Polarization Dependent Attenuation and Refractivity

Oriented volume with extinction or refractivity differences will have different effective densities of the same volume at different polarizations. The interferometric surface and double–bounce coherences are hardly affected by extinction magnitude and difference because the propagation path distance in the vegetation is the same and the phase center is always located at the ground level independent of the extinction. Only the phase can slightly vary given perceptible difference in indices of refractivity, which might also cause a minor degradation of coherence magnitude. On the contrary, the volume scattering and the triple–scattering coherence terms become polarization dependent and require further modifications for accurate modeling and estimation.
The polarization dependent volume coherence can be obtained as a linear combination of the coherences corresponding to the eigenpolarizations:

$$\gamma_{v(\boldsymbol{\omega})} = c_{a(\boldsymbol{\omega})}\gamma_{va} + c_{b(\boldsymbol{\omega})}\gamma_{vb} + c_{c(\boldsymbol{\omega})}\gamma_{vc}, \quad \forall\boldsymbol{\omega} : c_{va(\boldsymbol{\omega})} + c_{vb(\boldsymbol{\omega})} + c_{vc(\boldsymbol{\omega})} = 1 \tag{5.96}$$

where $\gamma_{va}, \gamma_{vb}, \gamma_{vc}$ represent the volume scattering coherences with the adjusted effective density functions f_a, f_b, f_c, instead of f_0 for the random volume case (see equation 5.60). The indices $_{a,b}$ indicate the co–polarized eigenpolarizations, while $_c$ indicates the cross–polarized eigenpolarization. The triple–bounce coherence is modified in the same way:

$$\gamma_{t(\boldsymbol{\omega})} = c_{a(\boldsymbol{\omega})}\gamma_{ta} + c_{b(\boldsymbol{\omega})}\gamma_{tb} + c_{c(\boldsymbol{\omega})}\gamma_{tc} \tag{5.97}$$

One can obtain the expressions for $c_{a/b/c(\boldsymbol{\omega})}$ in terms of eigenvalues and eigenvectors of $\mathbf{C}_v$. These eigenvectors can be obtained after eigendecomposition of the direct volume covariance matrix:

$$\mathbf{C}_{va} = \lambda_a\frac{\boldsymbol{v}_a\boldsymbol{v}_a^\dagger}{\boldsymbol{v}_a^\dagger\boldsymbol{v}_a},\ \mathbf{C}_{vb} = \lambda_b\frac{\boldsymbol{v}_b\boldsymbol{v}_b^\dagger}{\boldsymbol{v}_b^\dagger\boldsymbol{v}_b},\ \mathbf{C}_{vc} = \lambda_c\frac{\boldsymbol{v}_c\boldsymbol{v}_c^\dagger}{\boldsymbol{v}_c^\dagger\boldsymbol{v}_c},\ \text{with } \mathbf{C}_{va}+\mathbf{C}_{vb}+\mathbf{C}_{vc} = \mathbf{C}_v \tag{5.98}$$

$$\lambda_{a/b} = \frac{1}{2}\left[v_{11}+v_{33} \pm \sqrt{4|v_{13}|^2+(v_{11}-v_{33})^2}\right], \tag{5.99}$$

$$\boldsymbol{v}_{a/b} = [v_{11}-v_{33} \pm \sqrt{4|v_{13}|^2+(v_{11}-v_{33})^2},\ 0,\ 1]^T \tag{5.100}$$

$$\lambda_c = v_{22},\ \boldsymbol{v}_c = [0,\ 1,\ 0]^T \tag{5.101}$$

where the v_{ij} are the elements of the volume covariance matrix $\mathbf{C}_v$.
Since the eigenpolarizations of the ground and the volume are assumed to be collinear, one can use for the eigendecomposition also the whole polarimetric covariance matrix $\mathbf{C}$.

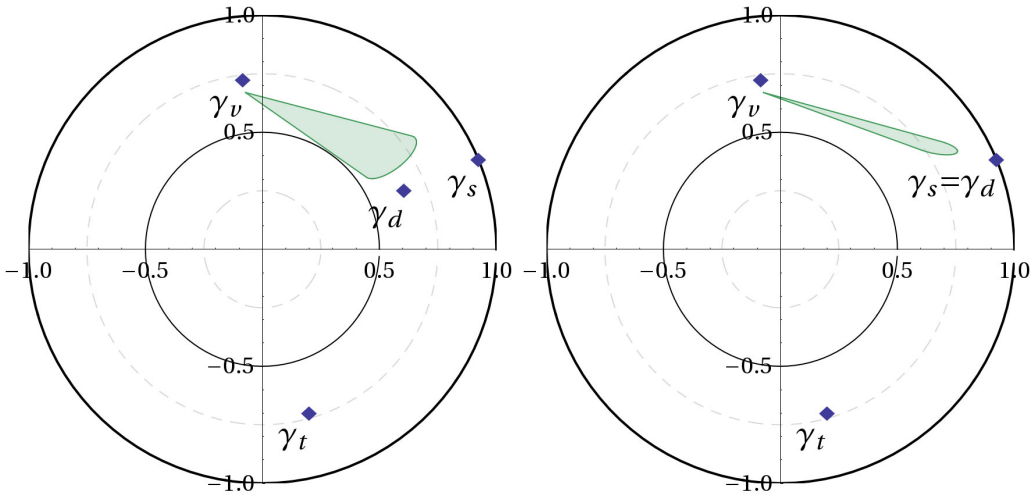

Figure 5.18: Schematic representations of the coherence plane with the locations of the dominant coherence centers for the single transmit mode (left) and the alternate transmit mode (right).

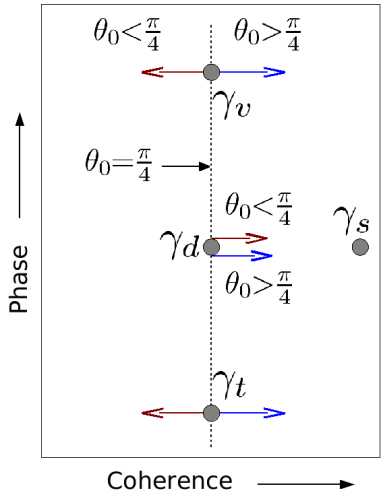

Figure 5.19: Schematic representation of the variance of the coherence components in the single–transmit mode with coherence magnitude, phase, and incidence angle.

5.4.3 Combining the Coherence Contributions

Interferometry provides additional means (with respect to polarimetry) to separate the different scattering contributions, increasing the number of observables and their sensitivity to vegetation parameters. However, the degree of separability depends on the acquisition system geometry, and needs careful performance analysis and a selective choice of the baseline.
Fig. 5.18 shows an example of the coherence components in the complex coherence plane, together with an example of the coherence set region, representing the linear combina-

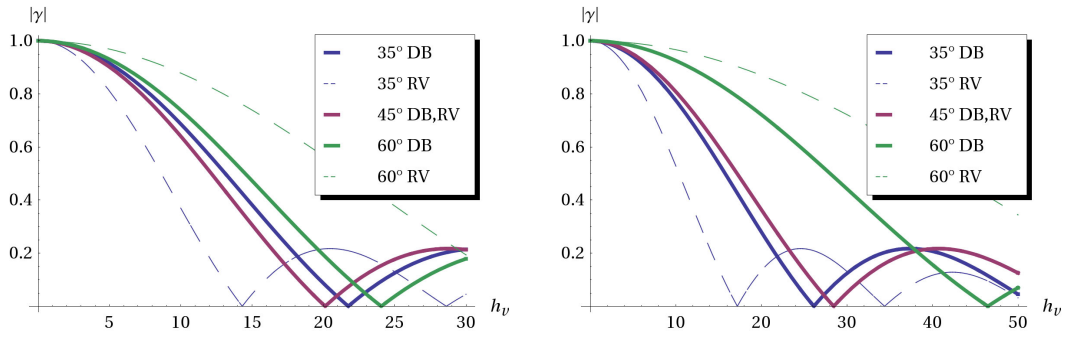

(a) $\alpha_B = 45°$ (b) $\alpha_B = 0°$

Figure 5.20: Random volume and double bounce coherence magnitudes (single transmit mode) in dependence of vegetation height and incidence angles. Vegetation extinction $\sigma = 0dB$, wavelength $\lambda = 23cm$, platform attitude $H = 3.5km$, baseline $B = 20m$. The vertical wavenumber is modified with the change of the incidence angle. Left: baseline inclination angle $\alpha_B = 45°$, right: $\alpha_B = 0°$. Note the h_v range change between the two images.

tions of coherences for different polarizations. For several vegetation scenarios the single–transmit mode is of special importance, since it is able to separate all major scattering contributions, either by the interferometric phase, or by the degree of coherence, or both. That is, the volume and the triple–bounce contributions have the same degree of coherence but different phases, whereas the surface scattering and the double–bounce contributions have the same phase but different coherence magnitudes. In general it can be assumed that for vegetation the first three components will be the dominant ones. Designing the system geometry parameters in a way that the ground and the double–bounce coherences are maximally separated allows to separate these three major components and to estimate the vegetation and surface parameters. The triple–bounce component, although not strong, can still be of influence as seen in Fig. 5.18. For example in the repeat–pass mode, in absence of γ_t all coherences would lie on a line between the ground and the volume coherence as assumed in the RVoG model, but in presence of the triple–bounce contribution the line structure gets distorted.
Comparing the double–bounce coherence magnitudes to volume coherence magnitude for the zero extinction case (see Fig. 5.19), one can see that the coherence degrees are equal in case the incidence angle is equal to $45°(\sin^2(\theta_i) = 1/2)$. For incidence angles $< 45°$, the pure volume decorrelates more than the double–bounce term, for incidence angle $> 45°$, the double bounce term is more decorrelated. With increasing extinction, the pure volume term tends to be less decorrelated, while the double–bounce coherence is independent of the extinction. The maximum DB decorrelation is given at an incidence angle of 45°, which provides the optimal separation between the double–bounce and the ground coherence. With the change of incidence angle the perpendicular baseline also changes and with it the vertical wavenumber. This can cause significant variance of volume coherence over one image for the same vegetation height. However, as shown exemplary in Fig. 5.20, which compares the degree of double–bounce coherence with volume coherence as a function of the vegetation height and the incidence angle (keeping

the perpendicular baseline constant), the double–bounce coherence is much less sensitive to incidence angle change as the volume coherence.
The combination of single–transmit and alternate–transmit modes could be of special interest. It would provide the advantages of both modes, enabling a more accurate separation of the main scattering contributions.

5.5 Conclusions

In this chapter we derived the expressions for polarimetric and interferometric components and presented a new polarimetric model which takes into account orientation effects inside of the volume and extends with it the Freeman II model. Providing simple volume coherence expressions as derived by Treuhaft and Siqueira we have identified the potential of a single–pass hybrid mode PolInSAR system to improve the separation of the surface scattering from the double–bounce scattering, which would enable us to improve the accuracy of soil moisture and surface roughness estimation. The modeled vegetation parameters include the effective particle scattering anisotropy, the vegetation orientation, the degree of orientation randomness, the vegetation height, extinction, refractivity, and the ground topography. This model has been kept as simple as possible but still contains the most import geophysical parameters needed to describe the vegetation layers in order to be invertible. This model is not restricted to the vegetation (agriculture and forests), and can be applied to a number of various geophysical random volumetric media (if the distorted Born approximation is valid), such as snow, ice and dry soil, in dependence of the frequency. If the volume component significantly dominates over the others, then several characteristic parameters could be directly extracted from the polarimetric coherency matrix. These parameters are of importance for identification, characterization and classification of the vegetation and random volumes.
In the following chapter, the presented model is used for vegetation parameter retrieval.

Chapter 6

Vegetation Parameter Retrieval

In the previous chapter, a model for polarimetric interferometric vegetation scattering components has been presented. It is related to the *forward problem* (or *direct model*) which aims to model electromagnetic data from geophysical parameters, in contrast to the *inverse problem* which aims to estimate model parameters from data observables. The inverse problem theory is an interdisciplinary research field with strong roots in mathematics, geophysics, remote sensing, medical imaging and many others [139,138,144]. The general principle is outlined in Fig. 6.1. There, G, representing the forward problem, is an abstract operator which aims to predict a set of data observables $\boldsymbol{d} = \{...\}$ on the basis of a set of model parameters $\boldsymbol{m} = \{...\}$. The inverse problem is represented by the operator G^{-1} which estimates the model parameters on the basis of data observables.
In this chapter, the *inverse problem* for *vegetation parameter retrieval* is discussed. The model that has been developed in the last chapter is used to estimate some physical parameters based on the observed data. The vegetation parameter retrieval problem is analyzed and four acquisition mode scenarios and two vegetation type scenarios are determined for further evaluation. Experimental results are presented using three data sources: simulations based on the presented forward model perturbed by Gaussian noise, PolInSAR imagery simulations of forest stands by the PolSARPro simulator, and real SAR data at L–band. As the results indicate, several modeled vegetation parameters can be reliably retrieved from the data.

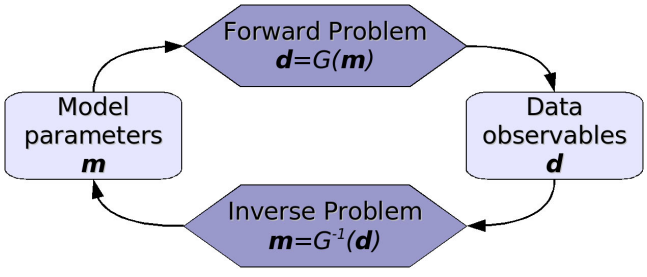

Figure 6.1: General framework of a forward and an inverse problem.

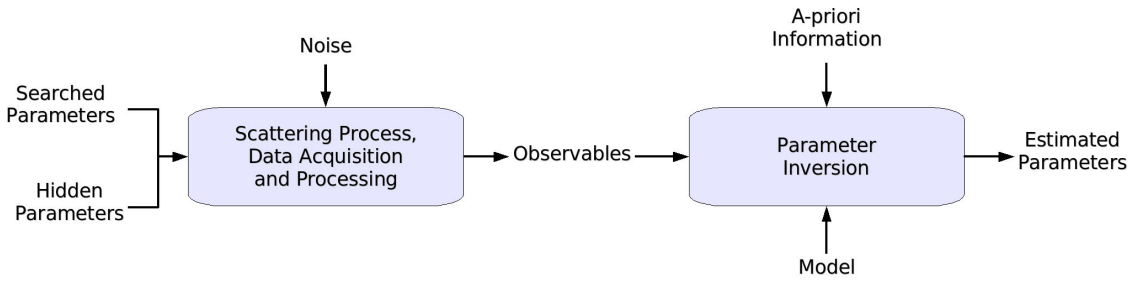

Figure 6.2: Parameter estimation problem.

6.1 Parameter Retrieval Goals

Fig. 6.2 outlines the general parameter inversion problem. In abstract terms, data acquisition and processing combine searched (modeled) and hidden parameters with the noise to deliver the observables. Based on forward modeling and additional a–priori information the searched parameters are estimated.
The model aims to relate some fundamentally important vegetation parameters to the observables. It is not intended and cannot represent exactly the true scattering process which is usually too complex. Approximations have to be taken into account, and the modeling process can be considered as a low–pass filter of the information, accounting for the most influential parameters and neglecting small and rapidly varying parameters. The quality of parameter estimation is mainly driven by the accuracy, relevance and representativity of the forward model.
This section examines the dimensionality, i.e. the number of degrees of freedom, of the forward and the inverse problems for different PolInSAR data acquisition modes and for two different types of vegetation, forests and agricultural fields.

Data Dimensionality

In the previous chapter, a general model has been developed for direct ground and all first–order scattering contributions from a volume layer above the ground. While a general model consisting of all contributions can be set up, it is not very promising due to the profusion of variables, related to the different physical processes involved. It is more auspicious to adjust the model to the vegetation type under consideration. For instance, due to its low associated intensity, the triple–bounce contribution is often neglected. The double–bounce contribution, on the other hand, is very strong for straight vertical trunks, but may be neglected for the canopy layer, especially in strongly attenuating vegetation. As discussed in section 4.3, under reciprocity, reflection symmetry and polarimetric stationarity conditions generally assumed for distributed media, the covariance matrix has the following form:

$$\mathbf{C}_6 = \begin{bmatrix} \mathbf{C} & \mathbf{Q} \\ \mathbf{Q}^\dagger & \mathbf{C} \end{bmatrix}, \quad \mathbf{C} = \begin{bmatrix} A & 0 & D+iE \\ 0 & B & 0 \\ D-iE & 0 & C \end{bmatrix}, \quad \mathbf{Q} = \begin{bmatrix} F+iG & 0 & L+iM \\ 0 & H+iI & 0 \\ N+iO & 0 & J+iK \end{bmatrix} \tag{6.1}$$

and can be parameterized using 15 real–valued coefficients[1]. *A,B,C,D,E* are the polarimetric parameters, where only four of them determine the polarization state, and one represents the total power. F, G, H, I, J, K, L, M, N, O are the interferometric parameters obtained through polarization diversity. Therefore, the set of independent observables for a single–baseline PolInSAR covariance matrix under reciprocity, reflection symmetry and polarimetric stationarity consist in the general case of 1 for the total power, 4 describing the normalized polarimetric information, and 10 for the response related to interferometry. The same considerations apply to both, single–transmit and alternate transmit acquisition modes. Under the same assumptions, a multi–baseline dataset with n_B distinctive baselines will have $10n_B$ distinctive data observables for polarimetric interferometry in addition to the polarimetric parameters. In terms of Fig. 6.1, the set of all these data observables is represented by $\boldsymbol{d}$.
Four characteristic acquisition mode scenarios are examined:

1. AT: Single–baseline alternate–transmit (ping–pong) mode (in single–pass or repeat–pass): 15 observables.
2. ST: Single–baseline single–transmit (standard) mode (single–pass): 15 observables.
3. HY: Dual–baseline alternate–transmit simultaneous–receive (hybrid) mode (single–pass): 25 observables.
4. MB: Multi–baseline mode in repeat–pass. The number of distinctive baselines n_B is between $n-1$ and $\frac{1}{2}n(n-1)$ for n acquisition tracks, where the limits are given for all tracks being completely regularly or completely irregularly spaced, respectively. The resulting dimensionality is $5{+}10n_B$ observables for n_B distinctive baselines.

In addition, one can consider multiple baselines in the single–transmit mode, as it is a possible configuration for instance in the cart–wheel satellite scenario. The dual–baseline hybrid mode can also be extended to a repeat–pass multi–baseline configuration.

Model Dimensionality

The complete characterization of a single volume layer over the ground in reflection symmetric form, according to the forward model presented in the last chapter, consists of 21 real valued parameters:

$$\begin{aligned}\boldsymbol{m} = \{&\tau, \operatorname{Re}\delta, \operatorname{Im}\delta, \operatorname{Re}\delta', \operatorname{Im}\delta', \sigma, \Delta\sigma, \Delta\chi, h_v, r_h, z_0,\\ &\operatorname{Re}\beta, \operatorname{Im}\beta, \beta_{vv}, \beta_{hv}, \operatorname{Re}\eta, \operatorname{Im}\eta, f_s, f_v, f_d, f_t\}\end{aligned}$$

For completeness, the individual backscattering power components can be computed by

$$P_s = \operatorname{trace}(f_s\mathbf{C}_s),\ P_v = \operatorname{trace}(f_v\mathbf{C}_v),\ P_d = \operatorname{trace}(f_d\mathbf{C}_d),\ P_t = \operatorname{trace}(f_t\mathbf{C}_t) \qquad (6.2)$$

$$P_g = \operatorname{trace}(f_g\mathbf{C}_g) = P_s + P_d$$

In order to reduce the dimensionality of the model, further assumptions can be made:

[1] One degree of freedom has to be additionally accounted for the rotation of the polarization basis into the reflection symmetric form.

- The triple–bounce component (f_t) may be neglected: for vegetated areas it is usually negligibly small and becomes more important for man–made structures.
- Difference in refractivity ($\Delta\chi$) may be neglected: whether the difference in refractivity is of importance for vegetation parameter estimation and whether it can be retrieved from PolInSAR data has to be examined.
- The surface scattering coefficients may be simplified ($\mathrm{Re}\,\beta$, $\mathrm{Im}\,\beta$, β_{vv}, $\beta_{hv} \rightarrow \mathrm{Re}\,\beta$, $\mathrm{Im}\,\beta \rightarrow \mathrm{Re}\,\epsilon_r$): if appropriate, using a first–order SPM approximation for relatively flat surfaces can reduce the number of surface parameters to 2. Further on, in [154] it has been pointed out that an approximate linear relationship for soils ($\mathrm{Im}\,\epsilon_r \approx 0.15\,\mathrm{Re}\,\epsilon_r$) might be used, so that the permittivity and the whole surface scattering contribution can be effectively described by a single real–valued parameter. However, the validity constraints for SPM are almost never met for the surface scattering under forests and agriculture (except perhaps over rice fields or wetlands which are flooded with water), and its usage would introduce erroneous estimates.
- The double–bounce component might be simplified ($\mathrm{Re}\,\delta'$, $\mathrm{Im}\,\delta'$, $\mathrm{Re}\,\eta$, $\mathrm{Im}\,\eta \rightarrow \mathrm{Re}\,\alpha$, $\mathrm{Im}\,\alpha$): The double–bounce component can be modeled by a first–order solution (as e.g. in the Freeman–Durden model) using only the complex parameter α.
- Combination of surface and double–bounce component in the alternate–transmit mode ($\beta, \alpha \rightarrow \beta'$, β, β_{hv}, β_{vv}, η, $\delta' \rightarrow \beta'$, β'_{hv}, β'_{vv}): In the alternate–transmit mode, the interferometric coherences are not distinguishable for surface and double bounce scattering components. This enables us to combine these two components and to further reduce the modeled degrees of freedom.
- Extinction difference ($\Delta\sigma$) might be neglected in some cases; for instance, in media with a high degree of orientation randomness or where the overall extinction is already very low. This condition may apply to many forests at L–band.

These have been general considerations about the number of observables and the degree of freedom of the model. In dependence of the acquisition geometry and the vegetation scenario, the model has to be adapted to the observations. However, there is no one–to–one correspondence between the degrees of freedom of the observables and the model. Some modeled parameters are ambiguous to a certain extent leading to the same observables, and some observables (especially in the MB–case) might be redundant.

6.2 Vegetation Models

The main characteristics of two considered vegetation types are given below. These models represent basic examples and more complex structured media models can be constructed.

Forest Scenario

The forest is modeled by two layers over the ground (Fig. 6.3.a). The canopy consists of partly oriented branches which are often more horizontally oriented for coniferous trees and more vertically aligned for deciduous trees. This statement is of course very coarse and cannot be applied to all tree species. The trunk layer might overlap with the canopy

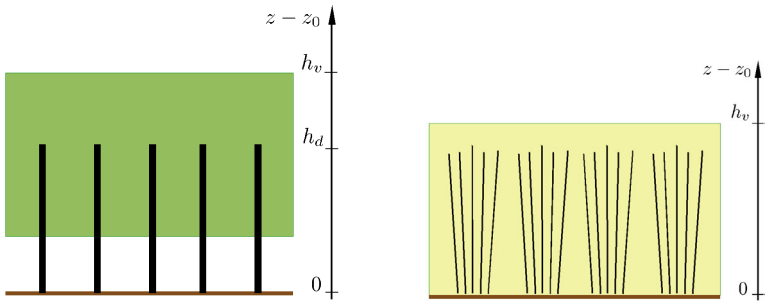

(a) Forest model. (b) Agriculture model.

Figure 6.3: Simplified forest and agricultural field vertical structures.

layer. The canopy layer is assumed to be responsible only for the volume contribution, whereas the trunk layer is responsible only for the double–bounce contribution.
The ground is characterized by the topography height z_0 and the backscattering parameters $\beta, \beta_{vv}, \beta_{hv}$. The trunk layer is assumed to be strictly aligned ($\tau = 0$), with a given height of h_d and specular bistatic scattering anisotropy δ'. The canopy layer is characterized by the particle scattering anisotropy δ, the degree of orientation randomness τ, the extinction σ, the bottom height of the layer z_{v0} (not necessary equal to $z_0 + h_d$), the total vegetation height h_v, and the canopy–fill–factor ratio $r_h \in [0, 1]$, which can be expressed as

$$r_h = \frac{h_v - (z_{v0} - z_0)}{h_v} \tag{6.3}$$

The general forward model $G_{(\boldsymbol{m})}$ can be represented by the models of the polarimetric covariance matrix $\mathbf{C}$, the cross–correlation matrix $\mathbf{Q}$ and the coherences γ. For the single–transmit mode the forward model is given by

$$G^{ST}_{(\boldsymbol{m})}: \quad \begin{cases} \mathbf{C} & = f_s \mathbf{C}_s(\beta, \beta_{vv}, \beta_{hv}) + f_v \mathbf{C}_v(\delta, \tau) + f_d \mathbf{C}_d(\delta', \eta, \tau) \\ \mathbf{Q} & = f_s \mathbf{C}_s(\beta, \beta_{vv}, \beta_{hv}) \gamma_s(\phi_{0s}) + f_v \mathbf{C}_v(\delta, \tau) \gamma_v(\phi_{0s}, h_v, r_h, \sigma) \\ & \quad + f_d \mathbf{C}_d(\delta', \eta, \tau) \gamma_d(\phi_{0s}, h_d) \\ \gamma_{(\boldsymbol{\omega})} & = c_s(\boldsymbol{\omega}; \beta, \beta_{vv}, \beta_{hv}, f_s) \gamma_s(\phi_{0s}) + c_v(\boldsymbol{\omega}; \delta, \tau, f_v) \gamma_v(\phi_{0s}, h_v, r_h, \sigma) \\ & \quad + c_d(\boldsymbol{\omega}; \delta', \eta, \tau, f_d) \gamma_d(\phi_{0s}, h_d) \end{cases} \tag{6.4}$$

For the alternate–transmit mode, the surface scattering and the double–bounce scattering components are combined which leads to

$$G^{AT}_{(\boldsymbol{m})}: \quad \begin{cases} \mathbf{C} & = f_g \mathbf{C}_g(\beta', \beta'_{vv}, \beta'_{hv}) + f_v \mathbf{C}_v(\delta, \tau) \\ \mathbf{Q} & = f_g \mathbf{C}_g(\beta', \beta'_{vv}, \beta'_{hv}) \gamma_g(\phi_{0a}) + f_v \mathbf{C}_v(\delta, \tau) \gamma_v(\phi_{0a}, h_v, r_h, \sigma) \\ \gamma_{(\boldsymbol{\omega})} & = c_g(\boldsymbol{\omega}; \beta', \beta'_{vv}, \beta'_{hv}, f_g) \gamma_g(\phi_{0a}) + c_v(\boldsymbol{\omega}; \delta, \tau, f_v) \gamma_v(\phi_{0a}, h_v, r_h, \sigma) \end{cases} \tag{6.5}$$

The hybrid alternate–transmit simultaneous–receive mode contains both G^{ST} and G^{AT}:

$$G^{HY}_{(\boldsymbol{m})} = \begin{cases} G^{ST}_{(\boldsymbol{m})} \\ G^{AT}_{(\boldsymbol{m})} \end{cases} \tag{6.6}$$

Agricultural Vegetation Scenario

The agricultural field model (Fig. 6.3.b) is characterized by a single layer of relatively oriented particles. The double–bounce contribution can be significant, as well as the surface and the volume contributions. The radar frequency is expected to be S– or C–band. The canopy fill factor is 1, i.e. the volume layer extends till the ground. The orientation effects can be significant in dependence of the crop type, with preference in the vertical direction, most pronounced in far range and less in near range. For agricultural fields flooded with water one might be able to use the SPM model for the surface scattering component.
The forward models can again be represented using the G operator:

$$G^{ST}_{(\boldsymbol{m})}: \quad \begin{cases} \mathbf{C} & = f_s\mathbf{C}_s(\beta,\beta_{vv},\beta_{hv}) + f_v\mathbf{C}_v(\delta,\tau) + f_d\mathbf{C}_d(\delta',\eta,\tau) \\ \mathbf{Q} & = f_s\mathbf{C}_s(\beta,\beta_{vv},\beta_{hv})\gamma_s(\phi_{0s}) + f_v\mathbf{C}_v(\delta,\tau)\gamma_v(\phi_{0s},h_v,r_h,\sigma) \\ & \quad + f_d\mathbf{C}_d(\delta',\eta,\tau)\gamma_d(\phi_{0s},h_d) \\ \gamma_{(\boldsymbol{\omega})} & = c_s(\boldsymbol{\omega};\beta,\beta_{vv},\beta_{hv},f_s)\gamma_s(\phi_{0s}) + c_v(\boldsymbol{\omega};\delta,\tau,f_v)\gamma_v(\phi_{0s},h_v,r_h,\sigma) \\ & \quad + c_d(\boldsymbol{\omega};\delta',\eta,\tau,f_d)\gamma_d(\phi_{0s},h_d) \end{cases} \tag{6.7}$$

$$G^{AT}_{(\boldsymbol{m})}: \quad \begin{cases} \mathbf{C} & = f_g\mathbf{C}_g(\beta',\beta'_{vv},\beta'_{hv}) + f_v\mathbf{C}_v(\delta,\tau) \\ \mathbf{Q} & = f_g\mathbf{C}_g(\beta',\beta'_{vv},\beta'_{hv})\gamma_g(\phi_{0a}) + f_v\mathbf{C}_v(\delta,\tau)\gamma_v(\phi_{0a},h_v,r_h,\sigma) \\ \gamma_{(\boldsymbol{\omega})} & = c_g(\boldsymbol{\omega};\beta',\beta'_{vv},\beta'_{hv},f_g)\gamma_g(\phi_{0a}) + c_v(\boldsymbol{\omega};\delta,\tau,f_v)\gamma_v(\phi_{0a},h_v,r_h,\sigma) \end{cases} \tag{6.8}$$

6.3 Parameter Inversion Framework

Due to the higher complexity and non–linear effects, a linear method, like for instance presented in [46,23,169] cannot be applied in the given inverse problem. An iterative non–linear parameter estimation method is required. The goal is to estimate model parameters $\boldsymbol{m}$ which minimize the distance between the data observables $\boldsymbol{d}$ and the predicted observables based on the forward model $G_{(\boldsymbol{m})}$. Therefore, the inverse problem operator $G^{-1}_{(\boldsymbol{d})}$ can be represented by

$$G^{-1}_{(\boldsymbol{d})}: \quad \underset{\boldsymbol{m}}{\text{minimize}} \, \|\boldsymbol{d} - G_{(\boldsymbol{m})}\| \tag{6.9}$$

which closes the circle in Fig. 6.1.
We use the Nelder–Mead simplex method [114] for the minimization/optimization task, which does not guarantee the optimal solution, but which, even with repeated trials, is computationally effective. The usage of a more sophisticated optimization method, like simulated annealing or genetic algorithms, would provide better results but the computation cost will be enormous in this case. The implementation includes hard and soft constraints: hard for physically possible solutions, and soft for initial regions.
The optimization function $\|\cdot\|$ is chosen to be the L_2 vector norm (root mean square error) of a set of covariance matrix and scalar coherence elements.
Simulated and real SAR data have been used to evaluate and validate the presented model and the parameter retrieval technique. Two types of simulated data were generated. In a first series of experiments, the validity of the parameter inversion method is examined. Assuming the best case scenario, data has been simulated by the Monte Carlo method

	true	ST	AT	HY	SUM
δ	2/3	0.7 (0.1)	0.66 (0.05)	0.67 (0.07)	0.68 (0.05)
τ	0.9	0.9 (0.08)	0.88 (0.09)	0.9 (0.08)	0.89 (0.07)
$\widetilde{\psi}$	H	H	H	H	H
h_d [m]	14	10.52 (6.66)	-	11.45 (7.01)	
r_h	2/3	0.67 (0.08)	0.66 (0.036)	0.66 (0.04)	0.66 (0.04)
h_v [m]	18	18.2 (0.77)	17.92 (0.46)	17.9 (0.42)	18 (0.4)
RMSE(h_v) [m]		0.79	0.47	0.43	0.58
σ [dB/m]	0.1	0.1	0.1	0.1	0.1
P_v/P_{total}	0.48	0.48	0.49	0.48	0.48

Table 6.1: Parameter estimation performance for the trees scenario, using a–priori extinction coefficients.

according to the presented forward models for forest and for agricultural vegetation, and parameter inversion has been carried out.
In the second series of experiments, electromagnetic simulations of the SAR imagery of tree and forest structures have been generated with the PolSARPro simulator [166]. In this case, data can be simulated only for the forest model in the alternate–transmit mode, but for two different tree species: pine trees, and deciduous trees. The goal of this second series of tests is to evaluate in a controlled manner, either the presented model is able to capture the structure of complex trees and either it is possible to invert parameters related to tree morphology. Parameter inversion performance tests have been carried out with respect to the different forest types, the number of looks, the incidence angle, and the baseline length.
The real data set consists of a multi–baseline multi–temporal air–borne acquisition at L–band over the Traunstein test site. Because it is a repeat–pass acquisition, a parameter retrieval method has been developed which is robust against temporal decorrelation, as will be presented in section 6.6.1.

6.4 Parameter Retrieval from Forward Model Simulations

The first scenario consists of a distribution of idealized trees corresponding to the model 1 in Fig. 6.3, with a layer of vertical trunks extending from z_0 to $z_0 + h_d$, and a canopy layer with depth $r_h h_v$ and minimum height z_{v0}. The total vegetation height is, therefore, h_v. The vegetation is characterized by a very wide distribution of orientation angles, with a slight preference for the horizontal direction.
This scenario is realized at L–band, assuming a strong volume component from the canopy, a strong double–bounce component from the trunks, and a medium strength surface scattering component.
The second scenario represents agricultural crops (maize) corresponding to the configuration depicted in model 2 in Fig. 6.3, with a single layer of strongly vertically oriented stems. The degree or orientation randomness is low. This model is realized at C–band, with the crops layer having similarly strong volume and double–bounce contributions as the surface scattering.

	true	ST	AT	HY	SUM
δ	2/3	0.68 (0.09)	0.67 (0.04)	0.68 (0.5)	0.68 (0.05)
τ	0.9	0.89 (0.08)	0.9 (0.08)	0.9 (0.08)	0.9 (0.06)
$\widetilde{\psi}$	H	H	H	H	H
h_d [m]	14	10.43 (6.45)	-	9.19 (7.39)	-
r_h	2/3	0.65 (0.06)	0.67 (0.04)	0.69 (0.05)	0.67 (0.03)
h_v [m]	18	18.15 (0.86)	18.05 (0.58)	18.08 (0.83)	18.10 (0.57)
RMSE(h_v) [m]		0.85	0.57	0.82	0.76
σ [dB/m]	0.1	0.07 (0.1)	0.09 (0.07)	0.12 (0.13)	0.09 (0.06)
P_v/P_{total}		0.5	0.48	0.49	0.49

Table 6.2: Parameter estimation performance for the trees scenario.

For simplicity, the surface and double–bounce responses are realized using only first–order approximation terms β and α, and the imaginary parts of β, α, δ have been neglected. Monte Carlo simulations were conducted using the Cholesky decomposition to generate correlated data samples according to the model. For final experiments, covariance matrices with 100 looks were used.

Tables 6.1–6.4 show the parameter retrieval performance for the vegetation parameters. Two tables (6.1 and 6.3) depict the results using a–priori knowledge about the extinction coefficient, whereas the other tables (6.2 and 6.4) show results with no a–priori knowledge. For both cases, the performance for the single–transmit (ST), alternate–transmit (AT), hybrid (HY), and the combination of all three modes (SUM). The last mode assumes data acquisition in HY mode, but the parameter retrieval is carried out for all three modes independently and are averaged afterwards. Per mode, 100 parameter inversion trials have been conducted on independently simulated samples, in order to show the average of the estimated parameters and their standard deviation (SDEV) in the parentheses.

From top to bottom, the tables represent the true and the estimated values for canopy particles anisotropy δ, degree of orientation randomness τ, preferred orientation (horizontal H or vertical V), trunk layer height h_d (where applicable), canopy–fill-factor r_h (where applicable), vegetation height h_v, root mean square vegetation height estimation error RMSE(h_v), extinction coefficient σ, and the normalized volume backscattering power. The main orientation direction $\widetilde{\psi}$ is estimated from the particle scattering anisotropy δ, with $\widetilde{\psi} = H$ for $\delta > 0$, and $\widetilde{\psi} = V$ for $\delta < 0$. Further parameters related to the surface and the double–bounce scattering are estimated but are not presented here because of the emphasis on vegetation parameters.

In all cases the polarimetric vegetation characteristics (degree of randomness, particle scattering anisotropy, preferred orientation, volume backscattering power) could be reliably estimated.

The total vegetation height h_v could also be accurately estimated in all acquisition modes independently of the estimation of the extinction and the trunk layer height.

For the forest scenario, the canopy–fill–factor r_h was reliably estimated, too.

The estimation of the extinction coefficients was noisy, with high standard deviation. As of now, the problem of extinction estimation is insufficiently solved and needs further analysis.

	true	ST	AT	HY	SUM
δ	-0.5	-0.5 (0.07)	-0.5 (0.02)	-0.5 (0.05)	-0.5 (0.04)
τ	0.25	0.25 (0.05)	0.24 (0.04)	0.25 (0.06)	0.25 (0.03)
$\widetilde{\psi}$	V	V	V	V	V
h_v [m]	2	2.02 (0.08)	2.05 (0.33)	2.01 (0.10)	2.03 (0.13)
RMSE(h_v) [m]		0.08	0.33	0.10	0.21
σ [dB/m]	0.3	0.3	0.3	0.3	0.3
P_v/P_{total}		0.35	0.34	0.34	0.34

Table 6.3: Parameter estimation performance for the crops scenario, using a–priori extinction coefficients.

	true	ST	AT	HY	SUM
δ	-0.5	-0.51 (0.08)	-0.49 (0.1)	-0.5 (0.05)	-0.5 (0.05)
τ	0.25	0.26 (0.04)	0.26 (0.04)	0.28 (0.06)	0.26 (0.04)
$\widetilde{\psi}$	V	V	V	V	V
h_v [m]	2	2.03 (0.08)	1.94 (0.14)	2.01 (0.11)	1.99 (0.07)
RMSE(h_v) [m]		0.09	0.15	0.11	0.12
σ [dB/m]	0.3	0.24 (0.11)	0.18 (0.11)	0.38 (0.25)	0.27 (0.12)
P_v/P_{total}		0.35	0.34	0.34	0.34

Table 6.4: Parameter estimation performance for the crops scenario.

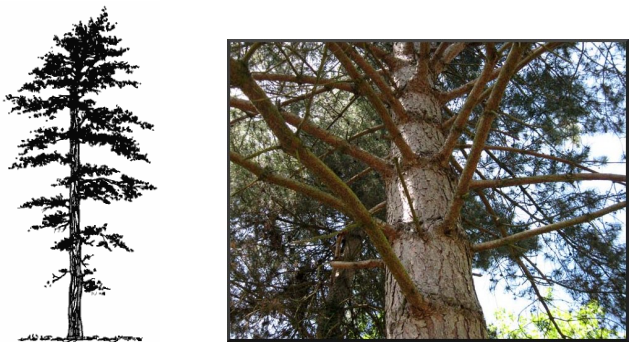

Figure 6.4: Structure of simulated coniferuous trees.

The depth of the trunk layer has also been estimated with high standard deviation, but approaching the correct values with an underestimation of 2 to 5 meters.

6.5 Parameter Retrieval from Structural Forest Simulations

For the next experiments, forest stand simulations have been used [166]. The surface and the trees structure and scattering properties are based on observed distributions of real trees. Every tree has an individual structure consisting of a trunk, and several levels of branches. The simulation of wave propagation and scattering is based on the discrete scatterer approach with the Foldy–Lax approximation.

Figure 6.5: Structure of simulated deciduous trees.

Pine Forest Simulations

The pine trees are characterized by very straight stems with branches usually radiating perpendicular from the stem (compare Fig. 6.4). The simulated forest stand with pine trees has a relatively smooth ground with medium soil moisture. The forest stand is dense with about 300 trees per hectare. The total height of the forest is about 18 meters, and the interferometric ground phase is at about 0 degree.
The deciduous trees have a much larger canopy volume per tree and therefore a relatively sparse forest stand is generated with only 30 trees per hectare. This results in non–homogeneous spatial distribution of trees with many gaps between the trees with unattenuated surface scattering and many layover and shadow effects. The stems of the deciduous trees are often slightly tilted and the angles of the branches are more varying (compare Fig. 6.5).
To estimate the main vegetation parameters, the presented forest model in the alternate–transmit mode is used. The parameter inversion process consists in optimizing the error function and estimating the physical parameters $\delta, \tau, z_0, z_{v0}, h_v, \sigma, f_v, f_g, \beta, \beta_{vv}$, and β_{hv}. Since in the presence of noise the vertical structure parameters $\boldsymbol{z}_{v0}, h_v, \sigma$ cannot be determined ambiguity–free from single–baseline data, a constraint has been introduced to reduce the variance: the canopy layer depth is set to $\frac{2}{3}$ of the total vegetation height. This constraint restricts the beginning of the canopy layer above the ground to the given height. The final PolInSAR coherence model for this scenario can be given by

$$\gamma_{(\boldsymbol{\omega})} = c_{g(\boldsymbol{\omega};\beta,\beta_{vv},\beta_{hv},f_g)}\gamma_{g(z_0)} + c_{v(\boldsymbol{\omega};\delta,\tau,f_v)}\gamma_{v(z_0,h_v,\sigma)} \tag{6.10}$$

Fig. 6.6 presents the parameter inversion performance for the pine forest stand over the effective number of looks L. The acquisition is done in L–band. One look corresponds to one sample pixel, which has a slant range resolution of about 1 meter and an azimuth resolution of 1.5 meters. The incidence angle is 45 degrees and the height of the aperture is 3km above the ground. The height sensitivity is given by the vertical wavenumber which is about 0.16. This corresponds to 2π height ambiguity of about 40 meters. In the experiments, for any given L, 100 independent samples have been generated and the graphs show the mean value and the standard deviation of the estimated parameters.
The results indicate that in average the canopy particles can be described as prolonged ellipsoids ($|\delta| \approx 0.7$), the orientation randomness is high ($\tau \approx 0.75$), the preferred orientation direction is horizontal ($\mathrm{Re}\,\delta > 0$), extinction is around 0.02dB/m, the total

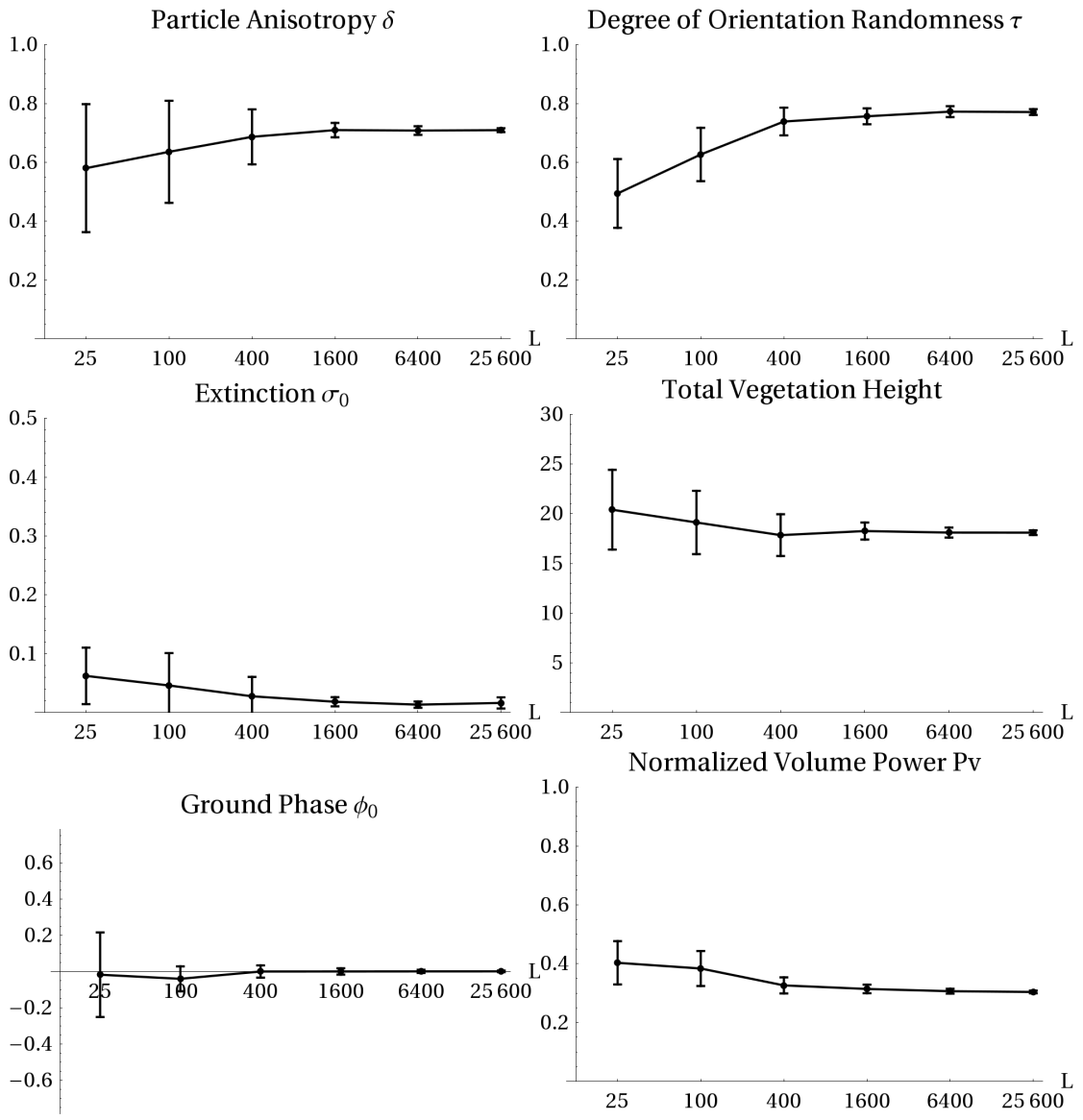

Figure 6.6: Parameter estimation for the pine forest scenario. The experiments consisted in parameter inversion for different number of looks L. For every L, 100 samples have been generated.

vegetation height is around 18 meters, the ground phase is around 0 radians, and the canopy backscattering power is about 0.35 of the total power.

Deciduous Trees Forest Simulations

Fig. 6.7 shows in comparison the parameter inversion results for another type of forest structure, the deciduous trees. Due to the less homogeneous structure, the variance of estimated parameters increases. In the limit of large number of looks, the particle scattering anisotropy tends towards -0.8 indicating in average more thinner particles than in the

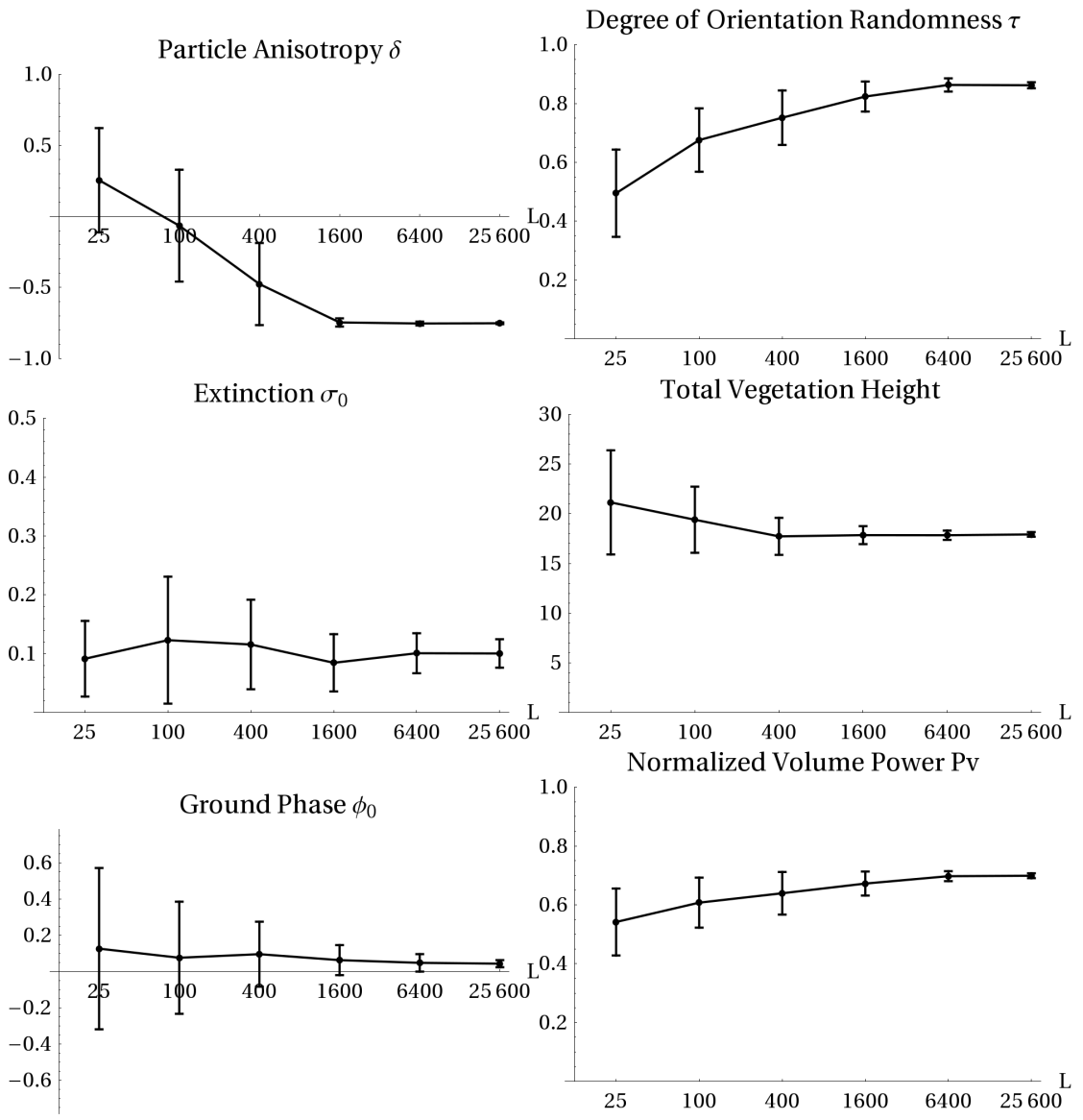

Figure 6.7: Parameter estimation for the deciduous forest scenario. The experiments consisted in parameter inversion for different number of looks L. For every L, 100 samples have been generated.

pine forest, and a preference for slightly vertical direction. The orientation randomness is with 0.85 also a bit higher. The tree height is estimated to be around 18 meters and the ground phase around 0 radians. Extinction is higher for the deciduous trees, too, as well as the normalized volume power. This can be explained with the stronger double–bounce component in case of the pine forest stand. Since the stems of the deciduous trees are less straight, they contribute less locally focused double bounce scattering. Also, a single deciduous tree has in general a much richer canopy with many more branches than the pine trees.
It can be observed that most parameters are biased with reference to the number of looks.

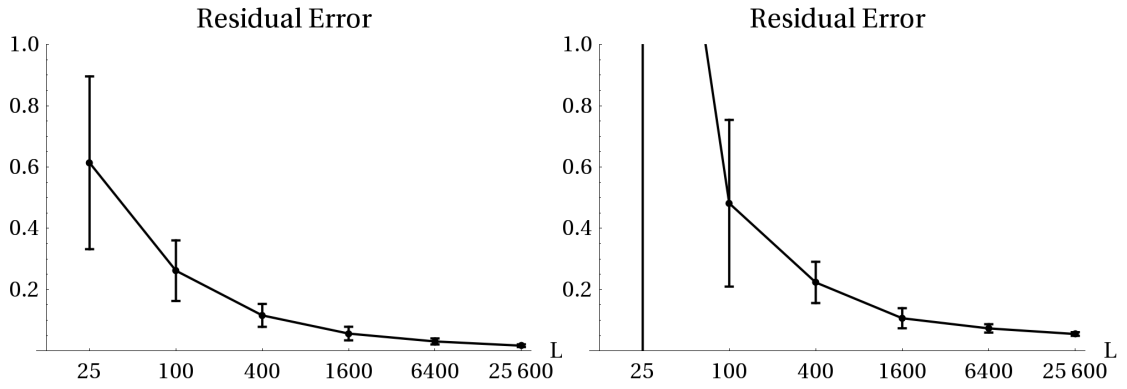

Figure 6.8: Residual errors for the pine (left) and deciduous (right) forest scenarios.

The estimation of the degree of orientation randomness requires an adequate number of looks. The particle scattering anisotropy is very unstable for the deciduous trees scenario due to a spatially highly non–homogeneous stand. In general, with low number of looks the results exhibit strong variance, and only with 400 or better 1600 looks does one obtains relatively stable estimates. Therefore, the following tests are carried out with 1600 looks. Fig. 6.8 shows in addition the residual errors and their variances for the different number of looks for both forest stands. As it can be seen, in the limit of a large number of looks the residual errors approach very low values. This probably indicates that the model is able to represent the structure of the forest.

Multiple Incidence Angles Simulations

Fig. 6.9 presents the results of parameter inversion for different incidence angles ($30, 45, 60$ degrees) while keeping all other parameters constant, including the vertical wavenumber. As the results show, the variance of estimated parameters and the residual error are improved for steeper incidence angles. The degree of orientation randomness gets higher with steeper incidence angles, as expected for volumes with preferred horizontal particles. At nadir incidence, the orientation randomness should be equal to 1. The estimation of extinction and vegetation height is constant, with a slight improvement of variance with steeper incidence angles. The ground phase is overestimated in the near range. The relative volume contribution to the power decreases with larger incidence angles. This can to some extent be explained with the orientation of the scatterers. The backscattering for more horizontally aligned scatterers is stronger for steeper incidence angles, while for more vertically aligned scatterers the backscattering would be stronger at larger incidence angles.

Multiple Baselines Simulations

Fig. 6.10 presents the results of parameter inversion for different baselines. The 2π height ambiguities are 30, 40 and 50 meters, which correspond to vertical wavenumbers of $\frac{\pi}{25}$, $\frac{\pi}{20}$ and $\frac{\pi}{15}$, and perpendicular baselines of 16.3, 12.2 and 9.78 meters, respectively. In general, the estimated parameters keep constant over the different baselines. To point out is the

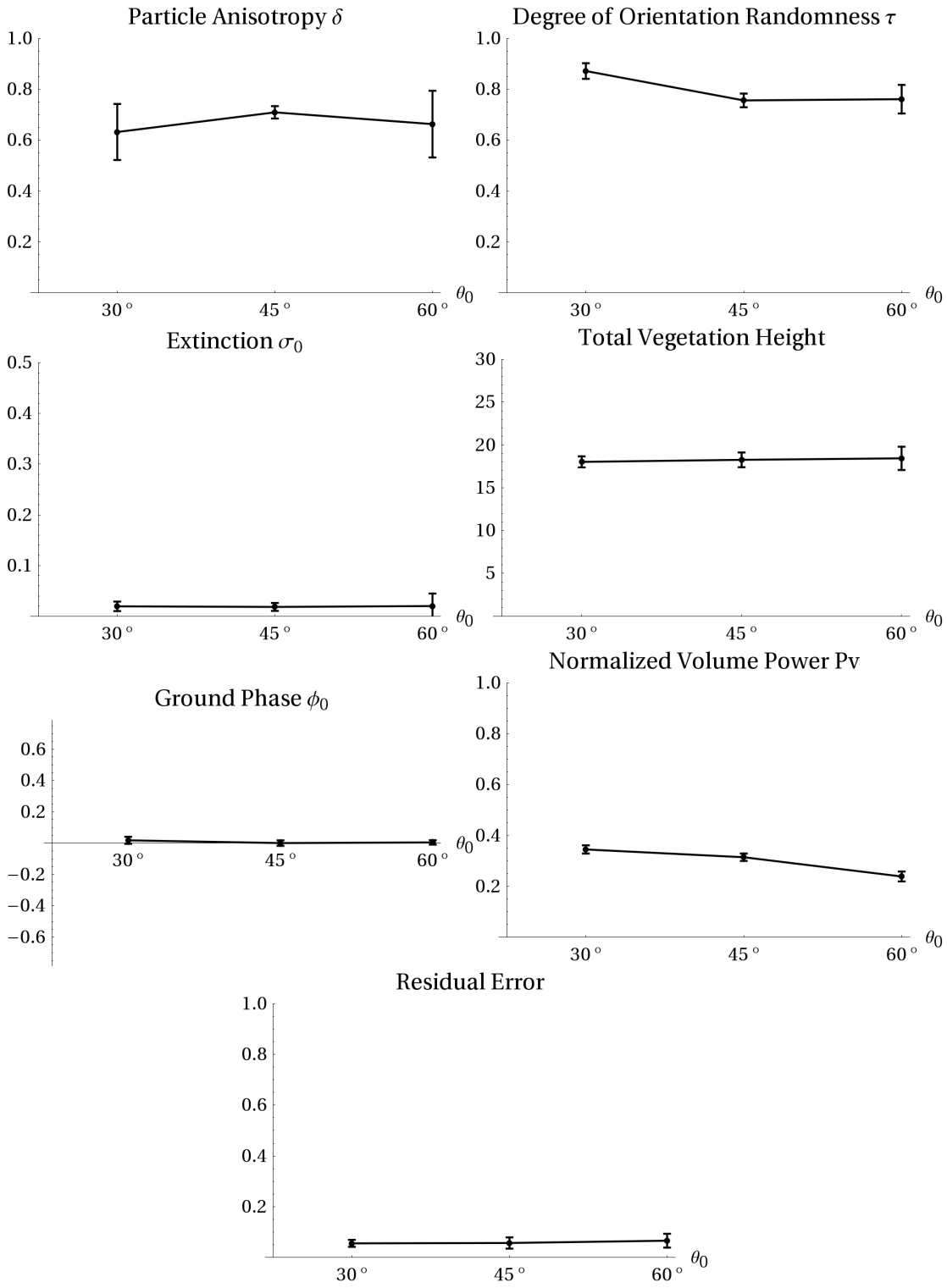

Figure 6.9: Parameter estimation for different incidence angles. Number of looks: 1600; 100 samples per incidence angle.

variance of the vegetation height estimation, which improves for larger baselines. This is as expected since with larger baselines one obtains higher height sensitivity.

Discussion

As these results indicate, the polarimetric interferometric model based parameter inversion performed better over the pine trees, probably because of the more structured and oriented branches. In particular a strong double bounce at L–band could be obtained even over partly rough surfaces. This indicates that polarimetric interferometry might be very powerful over boreal forests. The performance over deciduous trees simulation has led to worse results because at L–band the response is more depolarized and the volume scattering power is widely dominant over double–bounce and surface scattering. If the ground phase could be obtained by other means, e.g. other frequency bands, or LIDAR, or gaps in the forests, then the structural parameters of the forest could be better estimated. However, the characterization of the deciduous trees canopy performed very well, as also for the pine trees.
These experiments have been presented in order to evaluate and demonstrate the parameter retrieval performance over complex tree structures in a controlled environment. The obtained results showed that main characteristics of the given forest stands could be retrieved, and physical interpretations could be provided to all estimated parameters.

6.6 Parameter Retrieval from Repeat–Pass Real SAR Data over Forests

The application of the developed parameter retrieval techniques for real SAR data is conducted on a mountainous temperate forested region in the Traunstein test site. This test site is located near the city Traunstein in the south of Germany. The evaluation test site is shown in Figs. 6.11 – 6.13, depicting the scene in L–band and X–band SAR imagery, and in optical imagery, respectively[(2)]. The topography of the forest stands is relatively flat with only a few steep slopes, as seen in the DEM in Fig. 6.14. The ground truth data is available for 20 validation stands covering 123 hectares, which are delimited in Fig. 6.11. These individual stands were delineated in order to achieve high homogeneity in terms of tree species, height, biomass, and stadium [88]. Quantitative ground truth information has been generated from the forest inventory in 1998 based on a 100×100 meters (1 hectare) grid. It should be noted that the selection of homogeneous areas is subjective. The provided quantitative parameters, as presented in Table 6.5, are naturally subject to variance. The growth stadium of the forest stand is related to the age and the current condition of the trees, classifying the stands into the classes of *Growth*, *Mature* and *Regenerating*. The forest stands can in general be characterized as *mixed forests*. Table 6.5 also presents the dominant tree species as well as up to two other significant tree kinds. 17 of the 20 stands are dominated by coniferous tree species, and only 3 stands are dominated by deciduous tree species. The average tree heights of the evaluation stands range between 12.46 and 36.10 meters with spatial variations inside of the stands of up to 8.6 meters.

[(2)]Note that all three images depict the scene at different times and therefore do not necessary image exactly the same scene. The images are not coregistrated between each other.

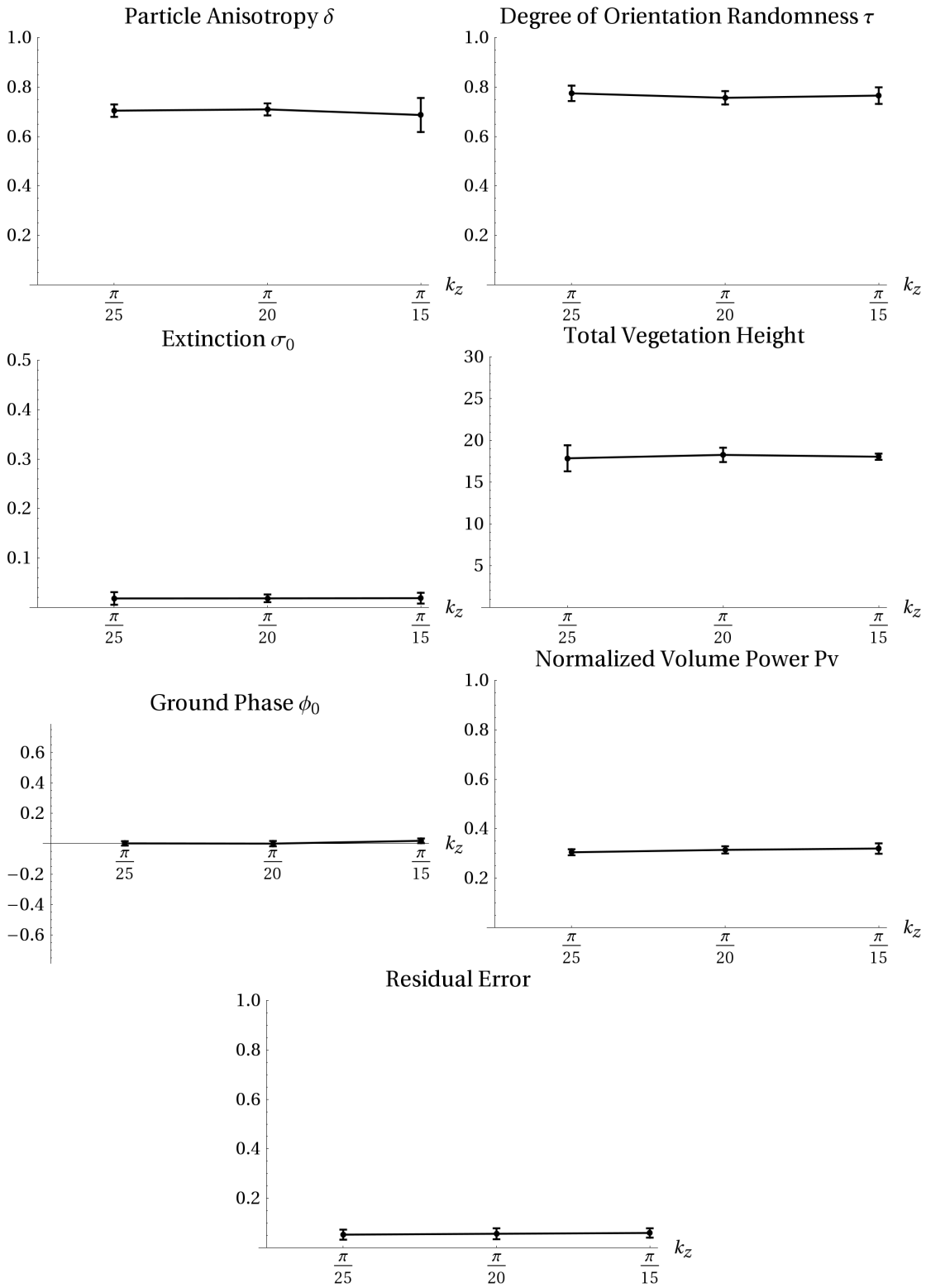

Figure 6.10: Parameter estimation for different baselines. Number of looks: 1600; 100 samples per baseline.

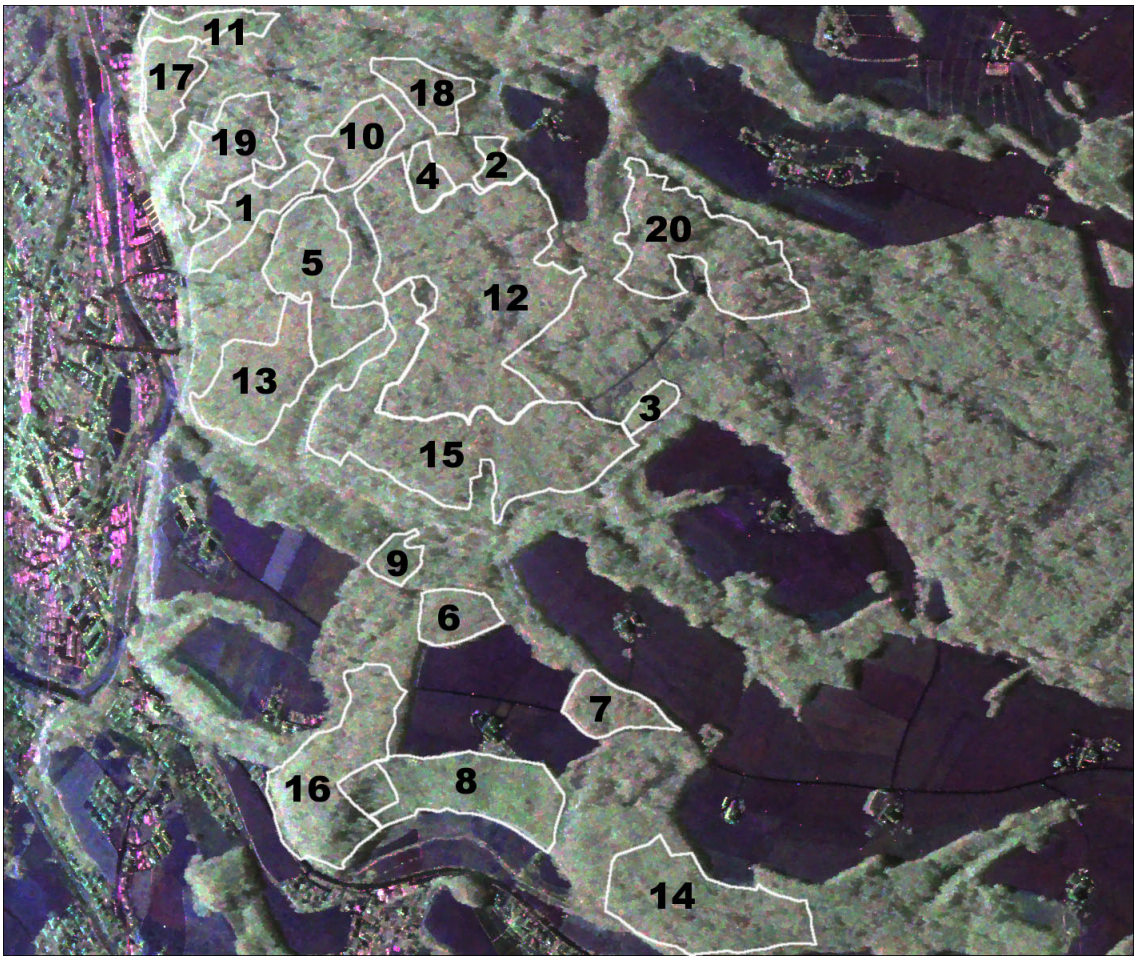

Figure 6.11: Test site Traunstein: L–band SAR image in Pauli basis with delineated forest stands (slant range).

Fully polarimetric and interferometric data at L–band have been acquired by the German Aerospace Center (DLR)'s E–SAR sensor in 2003 in a repeat–pass configuration. The acquisition times and nominal baselines of the four data sets used in this study are presented in Table 6.6. Further characteristics are shown in Table 6.7.

6.6.1 Multi–baseline Multi–Temporal Parameter Inversion Framework

The repeat–pass acquisition mode induces temporal decorrelation which can have significant effects on PolInSAR data coherence and parameter retrieval performance. At the scale of minutes and hours the strongest source of temporal decorrelation over forests is due to wind [76]. Wind is in general non–stationary neither temporally nor spatially. The temporal decorrelation can be higher than all other decorrelation sources. This makes accurate parameter inversion using a single baseline in the repeat–pass configuration practically an impossible task. However, using multiple baselines and assuming that the temporal decorrelation does not affect the ground makes the parameter inversion pos-

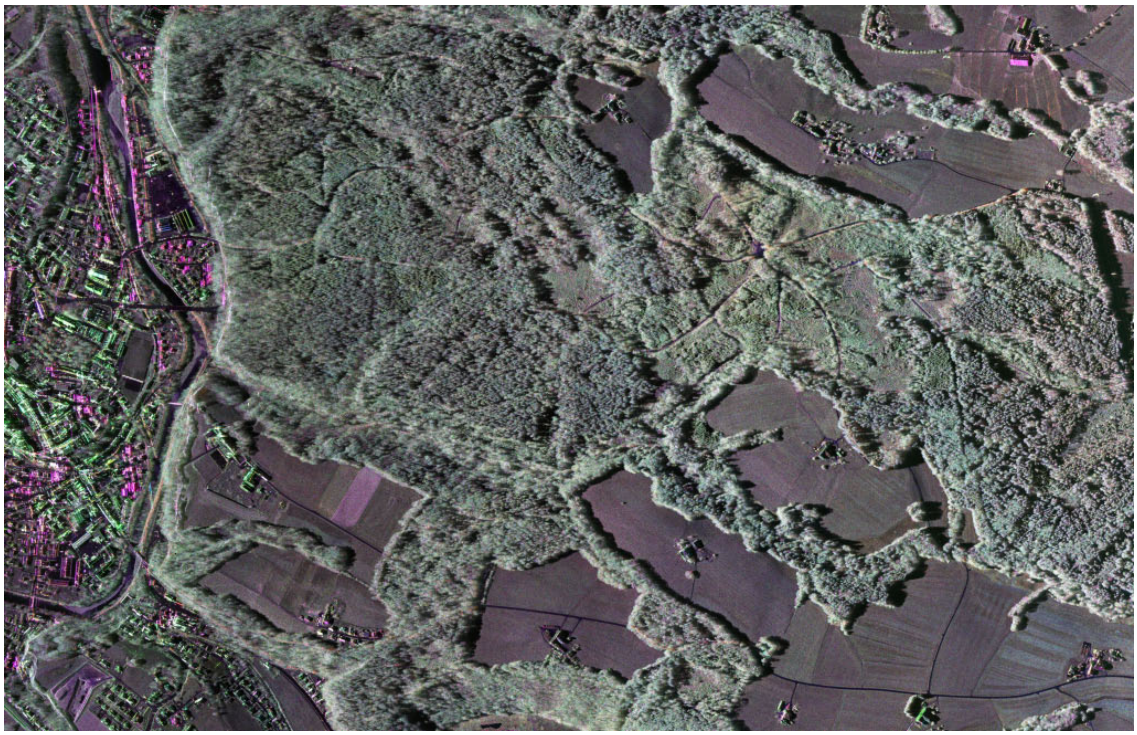

Figure 6.12: Test site Traunstein: high–resolution X–band SAR image acquired by DLR's F–SAR sensor in 2007.

Figure 6.13: Test site Traunstein: optical image.

Stand	Stadium	Dom. species	Dom. type	All species	Avg. height	± height
1	G	Fi	con	Fi-Ta-Bu	12.46m	±2.3m
2	G	Fi	con	Fi	13.00m	±0m
3	G	Ah	dec	Ah-Bu-Fi	13.05m	±0m
4	R	Fi	con	Fi-Bu	18.66m	±3.6m
5	G	Ta	con	Fi-Ta-Bu	19.68m	±8.6m
6	G	Fi	con	Fi-Bu-Ei	26.3m	±1.5m
7	G	Fi	con	Fi-Bu-Ei	26.93m	±2.3m
8	G	Bu	dec	Bu-Ah-Es	27.20m	±3.1m
9	G	Bu	dec	Bu-Fi-La	27.32m	±0m
10	M	Fi	con	Fi-Bu-La	27.43m	±2.2m
11	G	Fi	con	Fi-Bu-La	27.62m	±2.2m
12	M	Fi	con	Fi-Bu-Ta	28.43m	±1.6m
13	M	Fi	con	Fi-Bi-Bu	30.13m	±2.7m
14	M	Fi	con	Fi-Bu-Es	32.49m	±1.6m
15	R	Fi	con	Fi-Bu-Ta	33.14m	±2.7m
16	R	Fi	con	Fi-Bu-Ah	34.34m	±1.8m
17	M	Fi	con	Fi-Bu-Ei	34.59m	±2.5m
18	R	Fi	con	Fi-Ta-Ki	34.66m	±1.4m
19	R	Fi	con	Fi-Ta-Bu	35.23m	±1.2m
20	R	Fi	con	Fi-Bu	36.10m	±1.8m

Table 6.5: Main ground truth characteristics of the 20 forest stands. From left to right: stand number, stadium (G=growth, M=mature, R=regenerating), dominant species (Fi=north spruce, Ki=Scots pine, Ta=white fir, La=Eur. larch, Bu=Eur. beech, Es=ash, Ah=maple, Ei=oak, Bi=birch), type of the dominant species (con=coniferous, dec=deciduous), all significant species, average height, height variation. (Source: [88])

Track	Date and time of acquisition	Nominal baseline
1	11.11.2003, 09:00	master
2	11.11.2003, 08:50	5 m
3	11.11.2003, 08:40	10 m
4	11.11.2003, 08:01	0 m

Table 6.6: Acquisition times and nominal baselines of the SAR data sets.

sible. In the following, a method for multi–baseline multi–temporal parameter inversion will be presented.
For real data, the overall repeat–pass PolInSAR coherence model for baseline i can be represented by

$$\gamma_{i(\boldsymbol{\omega})} = \gamma_{sys}\left(c_{g(\boldsymbol{\omega};\beta,\beta_{vv},\beta_{hv},f_g)}\gamma_{g(\phi_{0_i})} + c_{v(\boldsymbol{\omega};\delta,\tau,f_v)}\gamma_{v(\phi_{0_i},h_v,r_h,\sigma;k_{z_i})}\gamma_{temp_i}\right) \tag{6.11}$$

where we have explicitly denoted the dependence of some parameters on the vertical wavenumber k_{zi}. Since the reference ground phase is different for the different baselines, we have for every baseline a distinctive ϕ_{0_i}, which replaces the ground topography height z_0. Internally, the PolInSAR coherency matrix is normalized from the beginning,

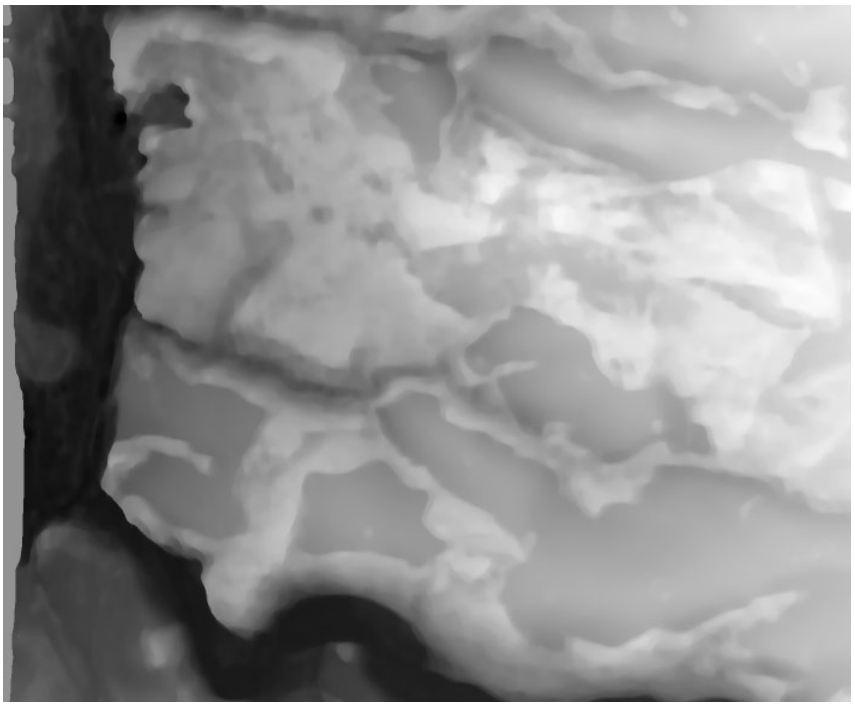

Figure 6.14: Digital elevation model (DEM) of the scene. The topography varies from 600 to 650 meters above the sea level, with only a few steep slopes.

Wavelength	23 cm
Polarizations	HH, HV, VV, VH
Bandwidth	100 MHz
Altitude (above ground)	3 km
Slant range resolution	1.5 m
Azimuth resolution	95 cm

Table 6.7: Characteristics of the SAR imagery.

and the parameters f_g, f_v are replaced by a single parameter, the ground–to–volume ratio at $HH + VV$ polarization $m_V = \frac{f_v}{f_v+f_g}$. The system decorrelation (consisting of thermal, mis–coregistration, mis–calibration and other decorrelation sources) is assumed to be baseline–independent, as are the intensity weights c_g, c_v. The ground is assumed to be temporally stable, whereas the volume experiences additional baseline–dependent temporal decorrelation γ_{temp_i}. This coherence expression resembles the one proposed by Papathanassiou *et al.* in 2000 [107]. Note, that we do not require a model for temporal decorrelation and assume the most general case.
It can be seen that with every baseline we obtain two additional model parameters; the reference ground phase and the temporal decorrelation. At the same time, one obtains with every baseline 10 additional observables (the elements of the $\mathbf{\Pi}_i$ matrix). The model predicts that all coherences from a single baseline are linearly dependent.

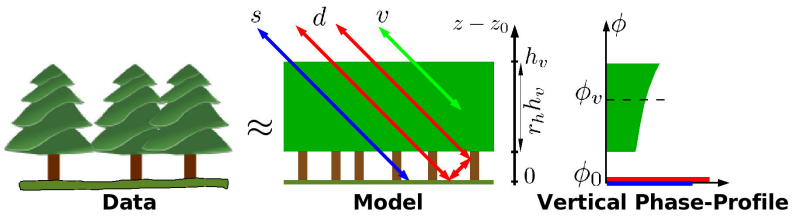

Figure 6.15: PolInSAR forest model properties: polarimetric signatures accounting for ground (surface + double–bounce) and volume scattering; interferometric phase profile for the main scattering contributions.

In summary, the parameter inversion problem consists of the task to retrieve from the data, given in reflection symmetric form, 15 unknowns $\boldsymbol{m}$ (for a single baseline)

$$\boldsymbol{m} = \{f_g, \mathrm{Re}\,\beta, \mathrm{Im}\,\beta, \beta_{22}, \beta_{33}, f_v, \mathrm{Re}\,\delta, \mathrm{Im}\,\delta, \tau, h_v, r_h, \sigma, \gamma_{sys}, \gamma_{temp}, \phi_0\} \quad (6.12)$$

where the first 9 represent the intensities and polarimetric signatures of the ground and the volume layers, and the last 6 represent the interferometric structural parameters. A scheme of considered model properties is presented in Fig. 6.15. Difference in extinction and refractivity is neglected, together with the triple–bounce contribution.
The critical point of the whole parameter retrieval framework is to estimate the interferometric structural parameters correctly. With the knowledge of acquisition system properties, γ_{sys}, which is usually dominated by thermal decorrelation, will be assumed to be known *a priori*. Hence, ϕ_0 is estimable from γ_g.
However, γ_v, a complex–valued term, still depends on additional 4 parameters, h_v, r_h, σ and γ_{temp}. Since in the data we can estimate only γ_v, that provides only two degrees of freedom $(|\gamma_v|, \arg\gamma_v)$, the parameters h_v, r_h, σ and γ_{temp} are ambiguous in a single–baseline acquisition and need further examination.
In addition, the magnitude of γ_v cannot be used for structural parameter estimation since it is perturbed by the unconstrained temporal decorrelation γ_{temp}. Therefore, the retrieval of h_v, r_h and σ needs to be performed solely on the phase of γ_v. One approach is to use multiple baselines in order to increase the number of equations.
The direct model $G(\boldsymbol{m})$, that is related to the forward problem in Fig. 6.1, is given in terms of the coherency matrices by

$$\boldsymbol{d} = G(\boldsymbol{m}) \iff \begin{cases} \mathbf{T} & = f_g \mathbf{T}_g(\beta, \beta_{22}, \beta_{33}) + f_v \mathbf{T}_v(\delta, \tau) \\ \boldsymbol{\Omega} & = f_g \mathbf{T}_g(\beta, \beta_{22}, \beta_{33}) \gamma_g(\phi_0, \gamma_{sys}) + \\ & \quad f_v \mathbf{T}_v(\delta, \tau) \gamma_v(\phi_0, \gamma_{sys}, \gamma_{temp}, h_v, r_h, \sigma) \end{cases} \quad (6.13)$$

where the ground coherency matrix $\mathbf{T}_g = \begin{bmatrix} 1 & \beta & 0 \\ \beta^* & \beta_{22} & 0 \\ 0 & 0 & \beta_{33} \end{bmatrix}$ combines the contributions of surface and double–bounce scattering.
The inverse model is represented as a minimization problem, subject to a set of constraints $\boldsymbol{c}$:

$$\boldsymbol{m} = G^{-1}(\boldsymbol{d}) \iff \boldsymbol{m} = \underset{\boldsymbol{m}|\boldsymbol{c}}{\mathrm{argmin}} \, \|\boldsymbol{d} - G(\boldsymbol{m})\| \quad (6.14)$$

The norm $\|\cdot\|$ is given by the L_2 vector norm of the argument (root mean square misfit minimization). G^{-1} is a multi–dimensional non–linear optimization problem with local minima and possibly non–physical solutions. The set of constraints $\boldsymbol{c}$ is provided to enforce physically reasonable solutions. It proved useful to include into $\boldsymbol{d}$, next to the elements of the PolInSAR coherency matrix, several coherence values with distinctive polarizations to enhance the sensitivity of the parameter retrieval method to structural parameters.
While the problem formulation is straightforward, finding a solution is an art in itself. Using brute–force optimization might lead to undesirable results, and a physically refined approach is recommended (in the manner of [23]). Based on these considerations, a possible multi–stage parameter retrieval framework for a multi–baseline data set has been developed and is presented below[(3)].

Initial Processing

i. SAR image preprocessing: data generation, calibration, coregistration, range spectral filtering, flat earth removal, topography removal, multi–looking operation.

ii. Estimation of the reflection symmetric and polarimetric stationary form.

iii. Estimation of thermal decorrelation and possibly other system decorrelation sources, as for example the coherence bias [151] in case of low number of looks.
The estimated PolInSAR coherence set is shown in Fig. 6.16.(a).

Parameter retrieval

1. Determine the linear structures of the PolInSAR coherence sets (see Fig. 6.16.(b)). Independently for every baseline:
   (a) Fit a line $\mathcal{L}_i$ through the PolInSAR coherence set, in analogy to the *three–stage inversion process* [23].
   (b) Determine the ground phase ϕ_{0_i}.
2. Determine the degree of orientation randomness in the data (see Fig. 6.16.(c)). For all baselines simultaneously:
   (a) Find $\delta', \tau', f_g', f_v', \beta', \beta_{22}', \beta_{33}'$ which minimize (6.14), neglecting for the moment the structural parameters, and only enforcing all $\gamma_{g_i}, \gamma_{v_i}$ to be on the lines $\mathcal{L}_i$.
   (b) Keep only $\tau = \tau'$ for future computation.
3. Determine the structural parameters and temporal decorrelation together with other remaining parameters (see Fig. 6.16.(d)):
   (a) Find common h_v, σ, r_h as well as $\delta, f_g, f_v, \beta, \beta_{22}, \beta_{33}$ and the baseline dependent γ_{temp_i} which approximate the linear structure of the coherences and the polarimetric coherency matrix.

[(3)] Note that for the previous results, only a single numerical optimization has been carried out. When applied to parameter inversion problem with real multi–temporal data, this approach proved to be not robust enough.

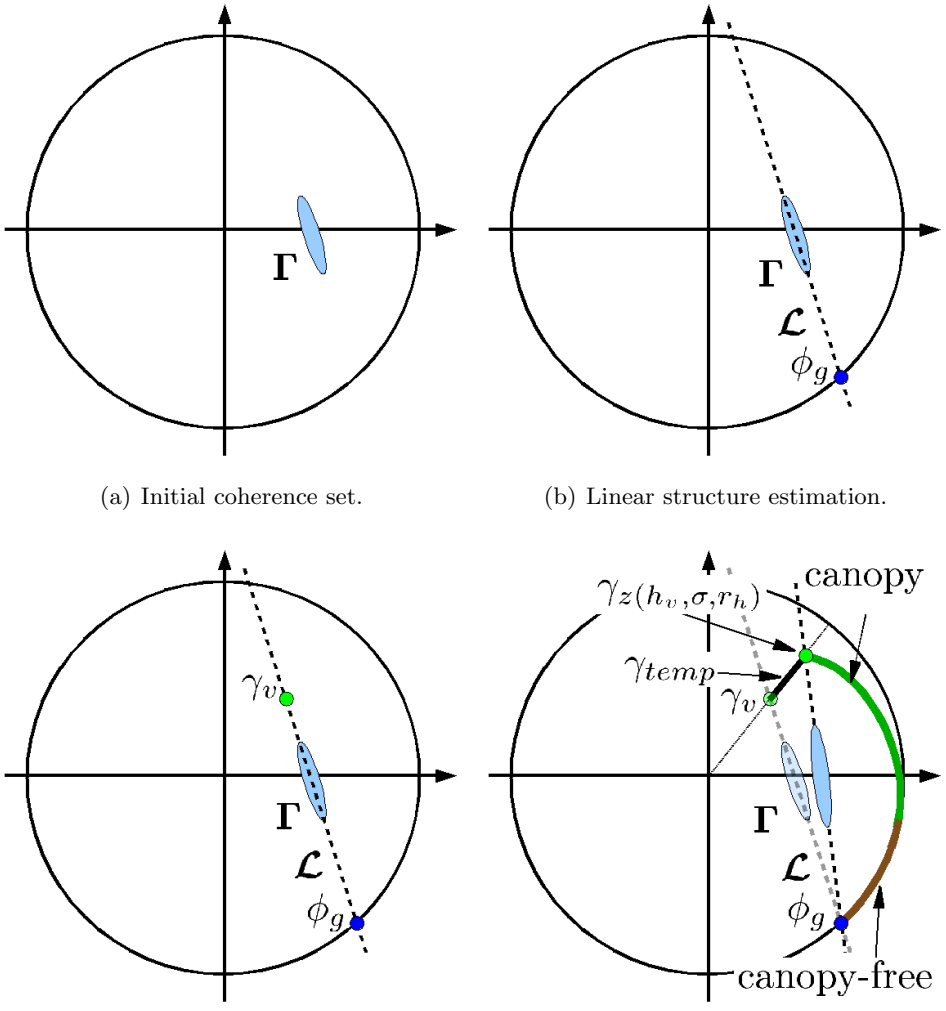

(a) Initial coherence set.

(b) Linear structure estimation.

(c) Estimation of polarimetric signatures, ground–to–volume ratio, and the total coherence of the volume contribution.

(d) Structural parameters estimation.

Figure 6.16: Representation of information extraction from the PolInSAR coherence set in the process of parameter retrieval.

4. If the retrieved parameters are physically not meaningful, either restart using different initialization, or mark this pixel as non–inverted and continue.

For step 1.a) we propose to use the eigenvalues of the contraction matrix $\mathbf{\Pi}$

$$\mathbf{\Pi} = \mathbf{T}^{-\frac{1}{2}} \mathbf{\Omega} \mathbf{T}^{-\frac{1}{2}} \tag{6.15}$$

to estimate the linear structure of the coherences. The line function is estimated in polar coordinates.
Step 1.b) is very important as errors in determining all ground phases correctly will result in erroneous parameter retrieval. Used criteria for identifying the ground phase [23]: (1) polarimetric ordering of coherences, (2) maximal phase distance between the ground and the volume coherence. Other criteria are possible.
Step 2) has been introduced to make the procedure more robust. Theoretically, after step 2) the structural parameters can be directly retrieved from γ_{v_i}, but using the full parameter inversion in step 3) (except τ) provides possibility of further fine–adjustment.
The Nelder–Mead simplex method [114] has been used for the optimization problems in steps 3.(a) and 5.(a). Same comments apply to this optimization strategy, as in section 6.3.
The optimization has been constrained to deliver physically meaningful results, as presented in Table 6.8.

A–priori contraints	Optimization constraints
$\gamma_{sys} = 0.96$	$0.2 \leq m_V \leq 0.98$ $0 \leq \lvert\delta\rvert \leq 1.5$ $0\text{dB/m} \leq \sigma \leq 0.4\text{dB/m}$ $0.4 \leq r_h \leq 1$ $0.25 \leq \gamma_{temp_i} \leq 1$ $5\text{m} \leq h_v \leq 45\text{m}$

Table 6.8: A–priori and optimization constrains used for the experimental parameter retrieval.

6.6.2 Experimental Results

To guarantee good estimates of the covariance matrices and the coherences, the first series of test is conducted using 1800 looks, which with the given slant range and azimuth resolutions correspond to an area of 0.25 ha (slant range geometry). Later on results will be presented for 450, 900 and 1350 looks (1/16, 1/8, 3/16 ha). 3 baselines are used: 1–2, 1–3 and 1–4. The system coherence, which includes thermal, mis–coregistration, mis–calibration and other decorrelation sources, as well as possible temporal decorrelation of the ground contributions was set a–priori to 0.96 independently of the polarization. In reality, this value will be different, and polarization dependent. Using additional information about the acquisition system, data processing and the surface media characteristics, this value can be estimated more precisely. However, the influence of this parameter on the overall parameter estimation is minimal.

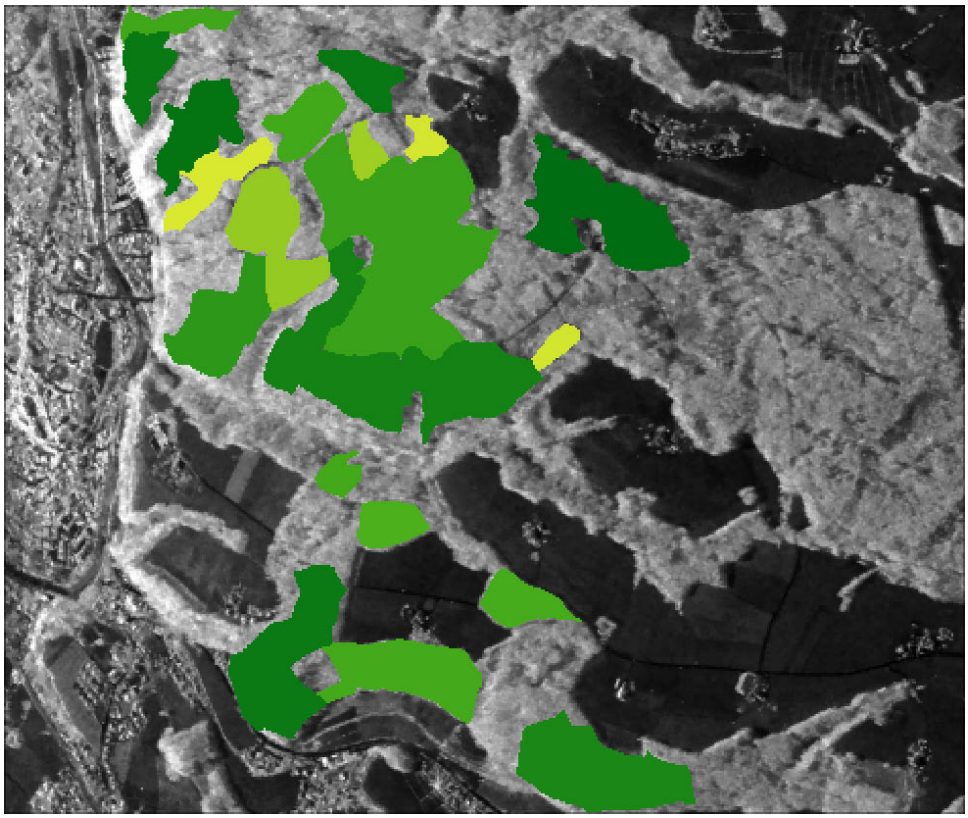

(a) Ground–truth forest height.

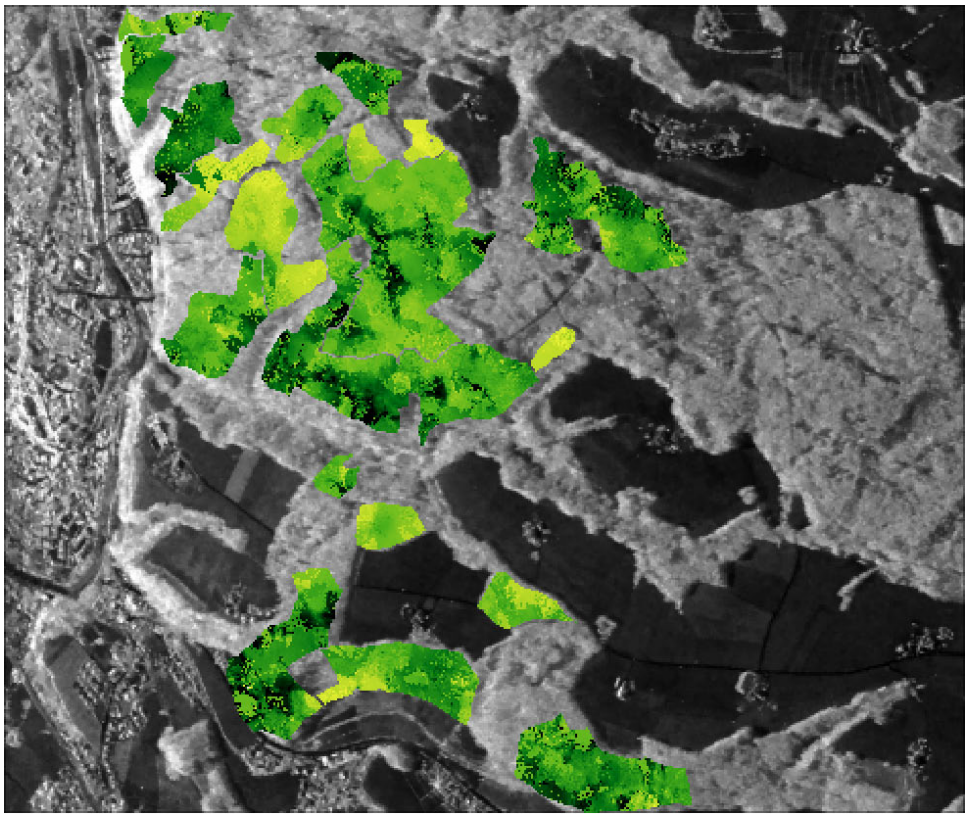

(b) Estimated forest height.

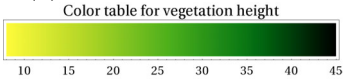

Figure 6.17: Forest height estimation: ground–truth and estimated height images.

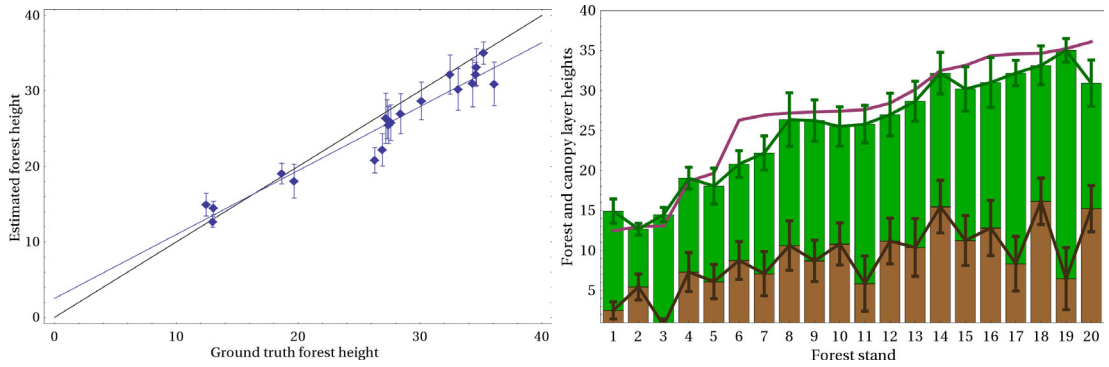

(a) Scatter plot: estimated height (y–axis) over the ground–truth height (x–axis).

(b) Ground–truth height, estimated vegetated height and canopy layer depth.

Figure 6.18: Forest height estimation: evaluation stand analysis.

Vegetation Height Estimation

Figs. 6.17.(a) and (b) show the ground–truth forest heights and the estimated heights. Fig. 6.18.(a) shows the corresponding scatter plot of the heights. These images indicate already that the heights are estimated close to the ground truths, while in some stands the forest heights vary continuously indicating certain inhomogeneities inside the stands. Fig. 6.18.(b) shows the forest heights and the canopy–fill-ratios for the 20 individual evaluation stands. The red line in this plot represents the ground–truth height. The green line represents the estimated heights with the error bars representing the standard deviation of the estimations. The brown line delimits the canopy layer from the non–canopy layer above the ground, and represents the canopy–fill-factor, normalized to the total vegetation height. In average, the forest height is underestimated by 1.6 meters, the average absolute error ($|h_{vest} - h_{vtrue}|$) is 3.97 meters, the average root mean square error (RMSE) is 4.97 meters, and the standard deviation of the height is 4.33 meters. It is interesting to see that the lowest height error (-32cm, RMSE: 1.5m; stand 2) corresponds to the only forest stand which is dominated by a single tree species without other significant species.
The highest error corresponds to stand number 20. The forest heights seems to be underestimated by over 5 meters with RMSE of 7.75 meters. After examination of the characteristics of this stand, we could identify two possible reasons for the high errors. First, the ellipticity of the coherence sets is very high, and the coherence sets are often shrunk to small circles, making it difficult to estimate the linearity of the coherences and introducing severe errors in the estimation of ground phases. Second, looking at the optical image (Fig. 6.13) and at the X–band high–resolution SAR image (Fig. 6.12), one can see that there are several clear–cuts and roads going through this forest stand without being delimited. It is very likely that between the forest inventory in 1998, on which base the evaluation stands have been defined, and the date of radar data acquisition in 2003, there have been significant changes in the spatial structure of this stand. Note that the first indication, the high coherence set ellipticity, can be well explained by the heterogeneous spatial structure of this evaluation stand. Under this evidence (optical and X–band images), it seems likely that the "ground–truth" measurements do not correspond to the *true* forest height of this stand, which appears to be quite heterogeneous.

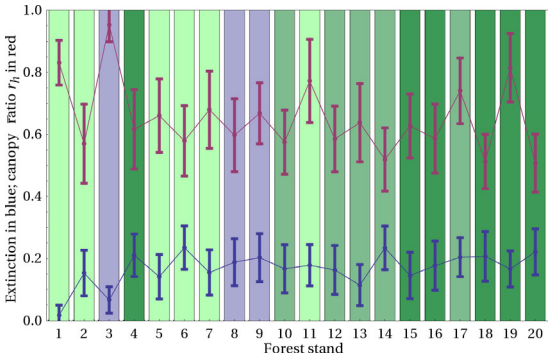

Figure 6.19: Estimation of the extinction and the canopy–fill–factor.

Extinction and Canopy–Fill–Factor Estimation

It was instrumental to introduce the canopy–fill–factor r_h into the model and the parameter estimation procedure to increase the robustness of the procedure. However, together with extinction and the temporal decorrelation this parameter is ambiguous to a certain degree. As can be seen in Fig. 6.19, the canopy–fill–factor is partly correlated with the extinction. Both parameters are very volatile in their ranges. The background colors of the bars represent the forest species type and the growth stadium. The blue bars represented evaluation stands with dominantly deciduous trees. The coniferous (green) stands are in addition classified according to the growth stadium: light green for growth, medium green for mature, and dark green for regenerating forest stands. No binding conclusions could be drawn up to now, except that the only maple dominated forest stand (3) has quite high canopy–fill–factor. However, both parameters are quite volatile in their ranges and it is to early to draw conclusions based on these results.

Orientation Randomness Estimation

Fig. 6.20 presents the performance of the estimation of the orientation randomness. As seen in Fig. 6.20.(b), the standard deviation of this parameter is very low and it enables clear discrimination between the evaluation stands. As discussed in the theoretical part, this parameter depends mostly on the morphology of the tree structures and the incidence angle. The incidence angle dependence is clearly observable in the scatter plot of τ over the incidence angles in Fig. 6.20.(c). Furthermore, one can observe that the young trees (growth stadium) have a steeper slope of τ with incidence angle; e.g. follow τ in the sequence of *growth* stands: 11, 1, 5, 6, 7 (with stand 2 being the only one "outlying" stand).

Effective Particle Scattering Anisotropy Estimation

Surprisingly, the magnitude of the effective particle scattering anisotropy of the vegetation has been estimated to be larger than 1, as shown in Fig. 6.21.(a). It is also quite independent of the evaluation stand and the incidence angle. The estimation is robust with very low variance (average standard deviation is 0.035). However, the particle scattering

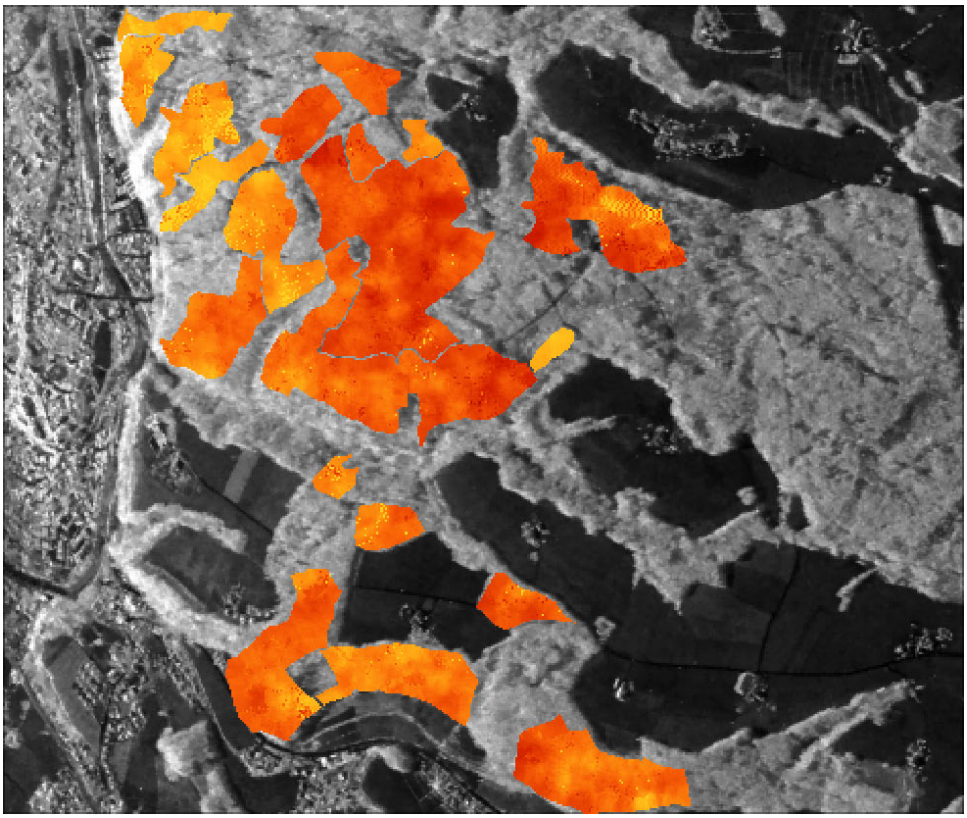

(a) Orientation randomness image.

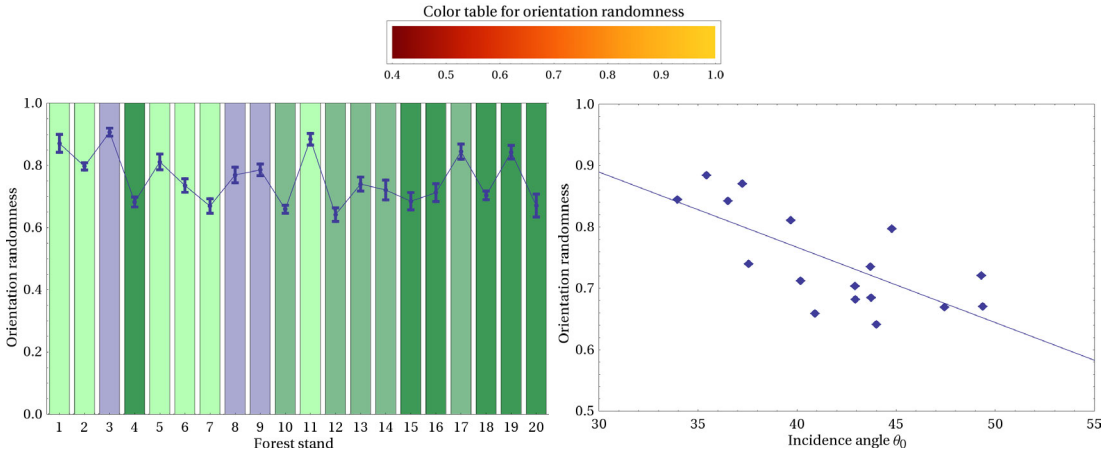

(b) Orientation randomness for all stands.

(c) Orientation randomness over the incidence angle. Only coniferous trees.

Figure 6.20: Estimation of the degree of orientation randomness.

anisotropy phase (see Fig. 6.21.(b)) has a large dynamic range of about $\frac{2}{5}\pi$ over the different evaluation stands.

The similarity of the particle scattering anisotropy magnitude over the evaluation stands might be explained with the fact that we observe relatively *mixed* forests consisting of

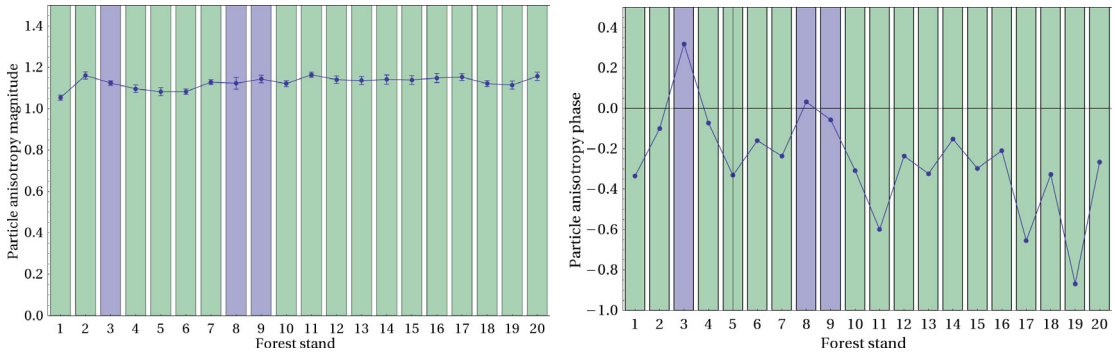

(a) Magnitude (b) Phase

Figure 6.21: Effective particle scattering anisotropy: magnitude and phase estimation.

several tree species in every evaluation stand. Given the different tree species in one sample, one has also to account the distribution of particle shapes, i.e. the range of branches from trunk–like cylinders to medium–thickness branches to thin twigs. The distribution of permittivities of the branches will probably vary slightly between the different tree species, but not in a large extent. It is to expect that the permittivity will be much more affected by the time of the day/year and meteorological aspects than by the differences of given tree species mixes in the evaluation stands which grow under the same conditions. Therefore, it is to expect that one will obtain higher dynamical range of particle scattering anisotropy magnitudes for forests either under different meteorological conditions or at different times of the day or year; also, distinctively different plant morphologies (e.g. agricultural vegetation) should result in distinctive anisotropy magnitudes.
In theory, the particle scattering anisotropy magnitude under the Born approximation for a cloud of simple ellipsoid shapes is assumed to be restricted to the range of $[0, 1]$. The leaving of this range might have one of the following causes. First, it might be an indication for multiple scattering effects in the canopy which are neglected by the Born approximation, but which could result in $|\delta| > 1$. Second, it might be due to other un–modeled effects like a particular distribution of shapes. Third, it might be due to the non–perfectly separated contributions from the ground. Fourth, mis–calibration or processing artifacts can cause this behavior[(4)].
The phase of particle scattering anisotropy is more related to the orientation direction of the particles. In the parameter retrieval from simulated SAR data of coniferous and deciduous trees in section 6.5 we saw a clear distinction of the two tree types in the anisotropy phase. Observing the results in Fig. 6.21.(b) one can see a similar distinction: forest stands dominated by deciduous trees (stands 3, 8, 9; blue background) have positive (or very close to be positive in case of stand 9) phases, whereas the stands dominated by coniferous trees (green background) have negative phases. Since this parameter is related to orientations, it is to expect that it is also sensitive to the incidence angle. This

[(4)]The E–SAR sensor increases the power for the measurement of the polarimetric cross–channels in comparison to co–polar channels. If this system aspect is not completely calibrated in the acquired data, it could lead to higher HV intensity. By dividing the HV intensity by 2 we already obtained $|\delta|$ values inside the theoretical borders of 0 and 1.

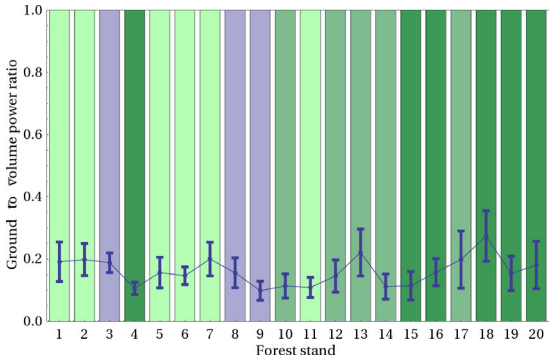

Figure 6.22: Grount–to–volume power ratio estimation.

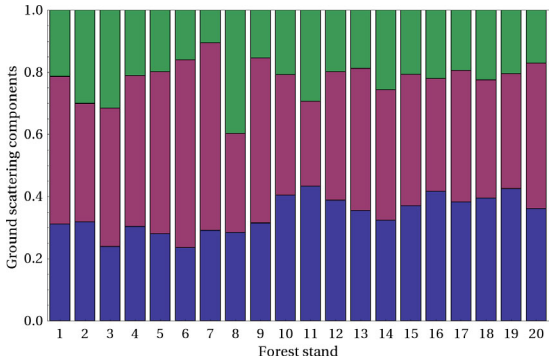

Figure 6.23: Ground scattering components.

hypothesis can be verified, e.g. looking at the first three coniferous stands in the near range, 17, 11, 19, which all have distinctively low phases.

Ground–to–volume Power Ratio Estimation

Fig. 6.22 presents the estimated ground–to–volume power ratios $\frac{P_g}{P_v}$ for all forest stands. This parameter is relatively volatile and has a standard deviation of 0.1. The maximal power ratio is about three times higher than the minimal power ratio. No definitive conclusions about relationships between this parameter and the tree species, or the growth stadium, or the hight could be drawn up to now. An examination of distinctively different forest types and/or different meteorological conditions could be advantageous for further analysis.

Ground Scattering Components Estimation

Fig. 6.23 shows the relative ground scattering components in the Pauli basis for all evaluation stands. Blue corresponds to $HH + VV$, red to $HH - VV$, and green to HV intensities. Although surface and double–bounce terms are larger, the cross–polar component is significant, too. This is an additional indication that the simple first–order Bragg (SPM) model and the first–order double bounce model are insufficient for modeling the ground contributions under the forest.

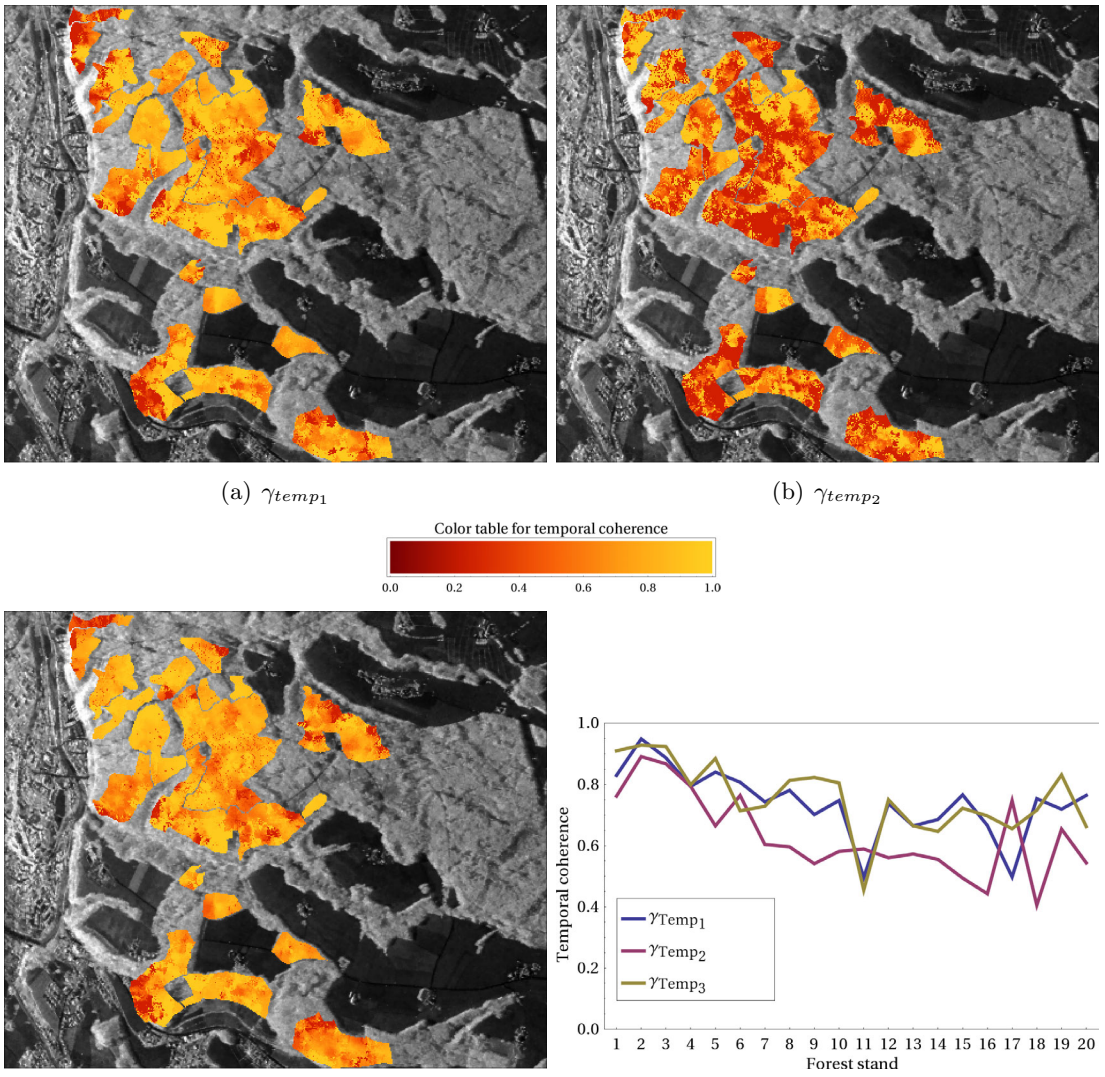

(a) γ_{temp_1} (b) γ_{temp_2}

(c) γ_{temp_3} (d) Temporal decorrelation for all stands.

Figure 6.24: Temporal decorrelation estimation.

Temporal Decorrelation Estimation

The images and the graphs of the estimated temporal decorrelation are shown in Fig. 6.24. The three baselines (1–2, 1–3, 1–4) have nominal perpendicular baselines of 5, 10 and 0 meters, and temporal baselines of 10, 20 and 60 minutes. Over these short temporal periods, the number of minutes between the acquisitions is not authoritative. The temporal decorrelation of the volume at these scales is mostly caused by wind which is non–stationary, neither temporally nor spatially. Because of this behavior, our attempts to model the temporal decorrelation, e.g. by Brownian motion or Markovian model [126], failed. It does not mean that it is not possible, but given the few temporal samples, and the high resolution requirements, the models could not be applied successfully. These effects have to be studied using a larger space of spatial and temporal samples. Therefore,

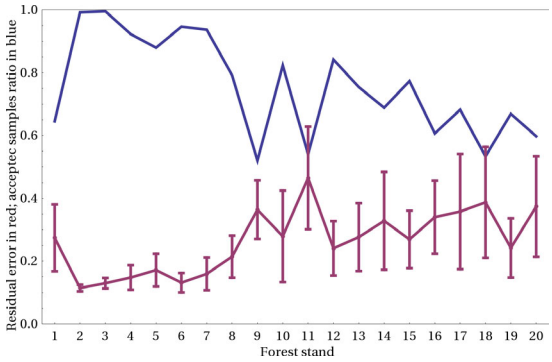

Figure 6.25: Relative number of inverted pixels (blue) and the average normalized residual errors (red).

# of looks	Bias	Abs. error	RMSE	SDEV
1800 looks	-1.51	3.97	4.97	4.33
1350 looks	-1.60	4.34	5.43	4.77
900 looks	-1.75	4.47	5.61	4.88
450 looks	-2.13	4.74	5.87	5.10

Table 6.9: Height estimation statistics for different numbers of looks.

we limited our study to the *estimation* of the temporal decorrelation (assuming it affects only the canopy layer on the given short time scale), in order to remove it and to estimate reliably the vegetation parameters.
As it can be seen, in average the temporal decorrelation is between 0.5 and 0.95. The main observation is: the temporal baseline appears to be less important than the spatial baseline. This behavior is in contrast to previous models of temporal decorrelation, which were based mostly on Brownian motion [171, 126], and needs to be further investigated.

Inversion Performance and Residual Errors

Fig. 6.25 shows the average normalized residual errors and the relative number of inverted pixels. The criteria of acceptance were based on the residual error value and on the success of the inversion procedure to achieve physically reasonable results. This was not always the case due to several reasons. For instance, the inversion process was sometimes trapped in a local optimum or failed to converge, although a reasonable solution existed. It is also possible that the model used for inversion in these given pixels was inappropriate due to significant departure of the medium structure from the modeled medium.
It is expected that by modification of the parameter estimation algorithm and by making it more robust, the performance could be further improved and the number of non–inverted pixels further reduced.

6.6.3 Tests on the Number of Looks

Figures 6.26 and 6.27 show the parameter estimation performance using different numbers of looks with respect to the retrieved forest height and the residual errors, respectively.

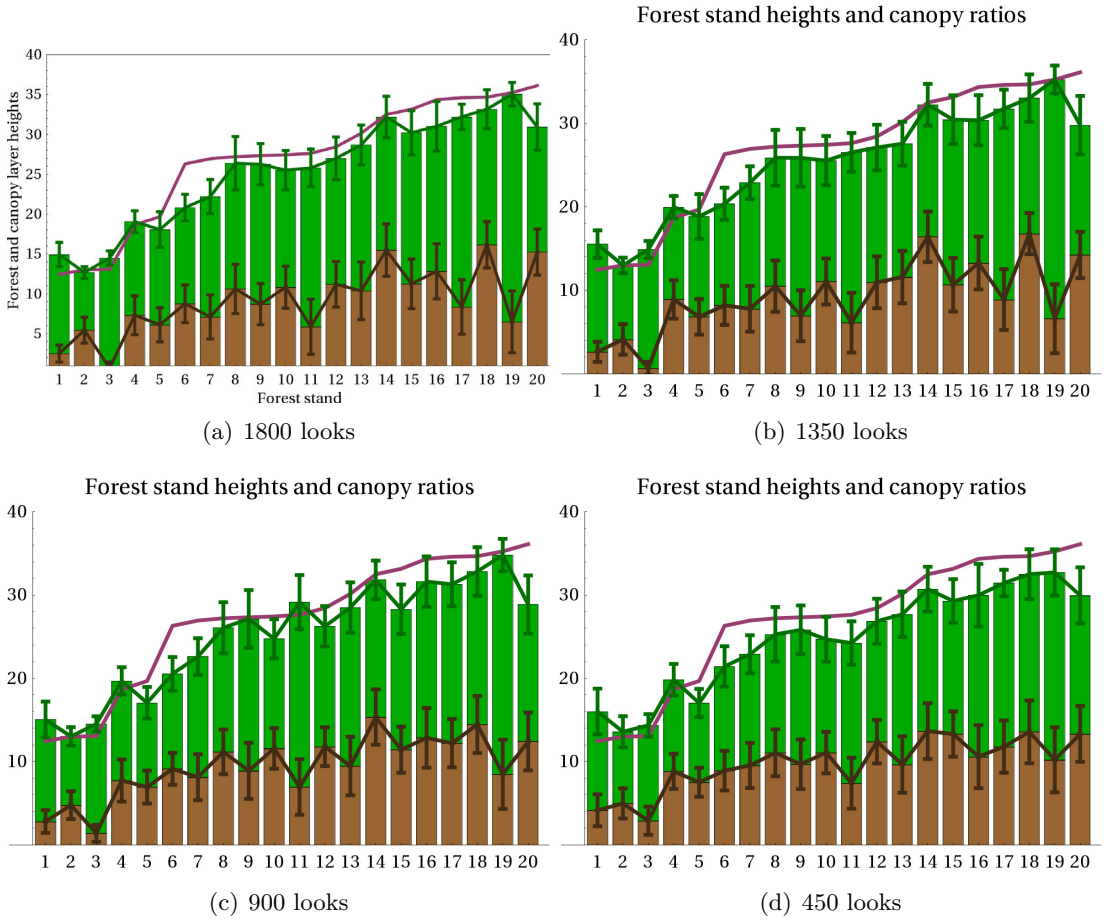

(a) 1800 looks (b) 1350 looks

(c) 900 looks (d) 450 looks

Figure 6.26: Forest height estimation for all forest evaluation stands using different number of looks.

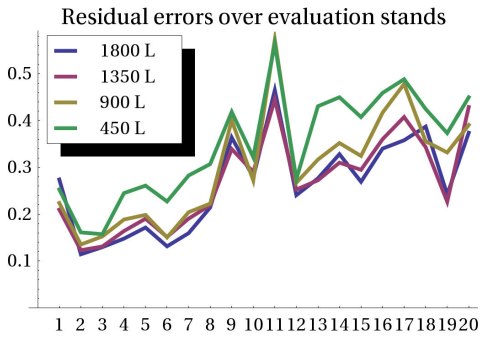

Figure 6.27: Normalized residual errors for all forest evaluation stands using 1800, 1350, 900, and 450 looks for the sample averaging operation.

Baselines	Bias	Abs. error	RMSE	SDEV
1x2, 1x3, 1x4	-1.51	3.97	4.97	4.33
1x2, 1x3, 2x3	-1.62	4.18	5.17	4.48
1x2	2.18	4.08	5.03	4.09

Table 6.10: Height estimation statistics for different baseline combinations.

Table 6.9 presents the results for the forest height estimation errors for the four case scenarios. The bias is given by the average difference between the estimated and the ground–truth forest height $\left\langle {h_v}^{est} - {h_v}^{gt} \right\rangle$, the absolute error is similarly defined $\left\langle |{h_v}^{est} - {h_v}^{gt}| \right\rangle$, the RMSE (root mean square error) is $\sqrt{\left\langle |{h_v}^{est} - {h_v}^{gt}|^2 \right\rangle}$, and SDEV is the common standard deviation of the estimated height, independent of the ground–truth height. These values have been computed independent for every forest stand and in this table the average values over all stands are presented.
The results are according to the expectations: the forest height estimation errors, the height standard deviation, and the residual errors are reduced with a higher number of looks. Reducing the number of looks by a factor of 4 (from 1800 to 450), the RMSE is worsened only by 15-20%. Over some evaluation stands (like stand numbers 2, 3, 4) one obtains always good results, independent of the number of looks, which is an indication for the homogeneous structure and these stands. For the lowest number of looks we see a trend for underestimation of high forest stands.

6.6.4 Tests on the Baseline Choice

Figures 6.28–6.30 and Table 6.10 present the parameter estimation performance using different baselines. In comparing 3–baseline and single–baseline parameter retrieval results, one can observe that the single–baseline results are more biased and overestimated. This indicates, that using a single–baseline it is difficult to estimate the degree of temporal decorrelation; the temporal decorrelation gets underestimated, which results in apparently lower volume coherence values and higher forest height estimates. However, we were still able to obtain very robust and relatively accurate results with an average standard deviation of 4 meters inside an evaluation stand. The same single–baseline data set 1×2 has been analyzed for forest height and biomass estimation in the thesis of T. Mette [88] using the RVoG model and inversion approach [23, 106].

6.7 Conclusions

In this chapter we have at first analyzed the inverse problem of vegetation parameter retrieval from single– and multi–baseline polarimetric interferometric SAR observables. A simple inversion model has been presented which enables us to invert the key vegetation parameters. The model has been evaluated and validated on simple forward modeling simulations, on PolSARPro simulations of coniferous and deciduous forests, and on real SAR data at L–band. The results validated the modeling and the parameter retrieval approach but also opened new questions which need to be addressed.
The limitations for the presented parameter estimation method are determined by model assumptions. Most severe are:

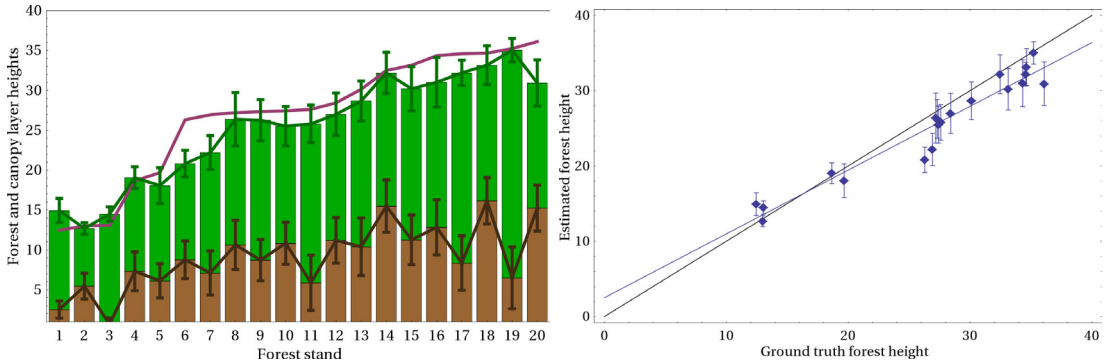

(a) Baselines: 1x2, 1x3, 1x4

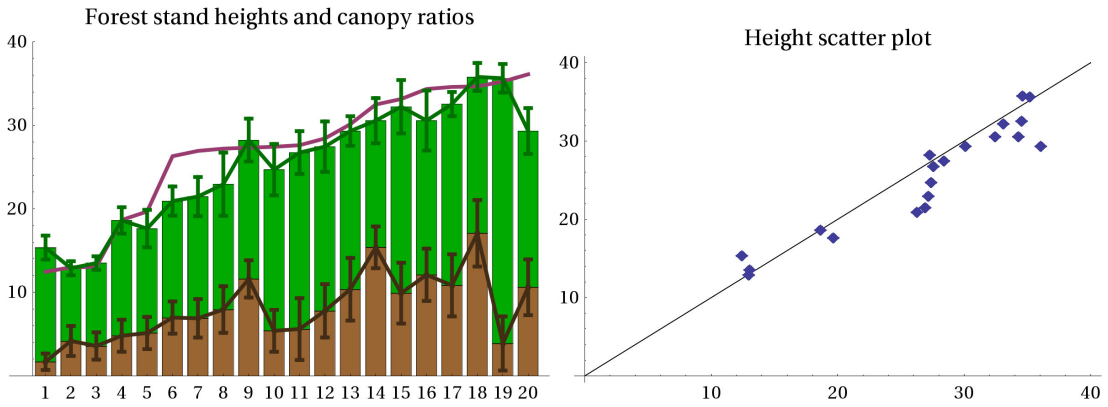

(b) Baselines: 1x2, 1x3, 2x3

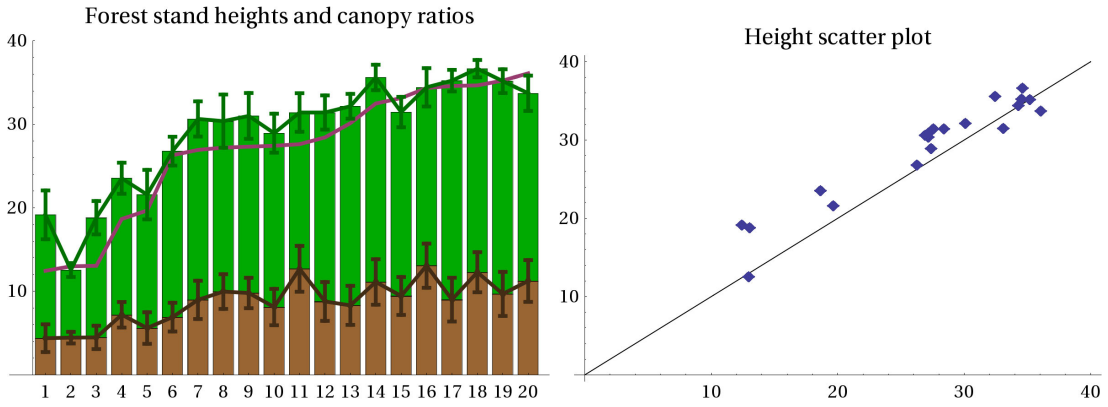

(c) Baseline: 1x2

Figure 6.28: Forest height estimation for all forest evaluation stands using different baseline combinations.

- Terrain slope is assumed to be constant over the region of the averaged samples.
- Vegetation eigenpolarizations and the terrain normal are orthogonal in the polarization plane.

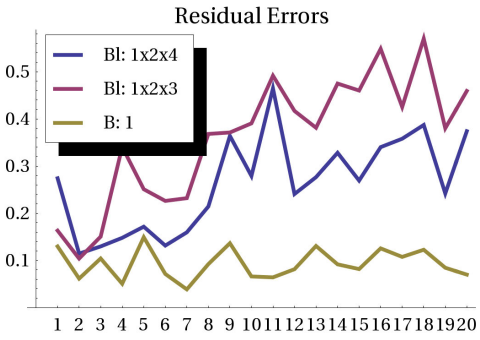

Figure 6.29: Normalized residual errors for all forest evaluation stands for different baseline combinations.

- Simplified vegetation structure assuming vertically uniform and horizontally homogeneous layers.
- Assumption of the average effective particle shape being representable for all particles, and being independent of height and orientation.

The main data set for parameter retrieval evaluation from real SAR data consisted of 3 baselines, 1–2, 1–3, and 1–4, with nominal spatial baselines of 5, 10, and 0 meters and temporal baselines of 10, 20, and 60 minutes, respectively. After pre–processing, 1800 look samples were generated for the evaluation of the parameter retrieval procedure. The evaluation resulted in the following conclusions:

- Despite the temporal decorrelation of the data, relatively good forest height estimates could be achieved with an average underestimation of 1.67m, average absolute error of 3.97m, RMS error of 4.97m, and height standard deviation of 4.33m.
- Based on external observations (X–band and optical images) and the comparison with the retrieved forest heights, it is found that the given rather uniform ground–truth data does not always represent the data correctly. At several evaluation stands it has been observed that the fluctuations in forest height correspond to fluctuations in X–band and optical images but are not represented in the ground–truth data. It is related to the fact that the ground–truth data comes from a forest inventory which was conducted 5 years before the radar data acquisition (although the forest heights have been adapted using appropriate forest growth models [88]). This leaves us with the conclusion that the retrieved forest height parameters are actually better than reported in the previous point.
- The estimated extinction and the canopy–fill–factor have still relatively high standard deviations, partly because these parameters, together with temporal decorrelation, have a non–negligible degree of ambiguity. It might be possible to resolve this ambiguity by using single–pass acquisitions.
- The degree of orientation randomness has been reliably estimated with low variance. It has shown, as predicted, sensitivity to the incidence angle. This parameter has

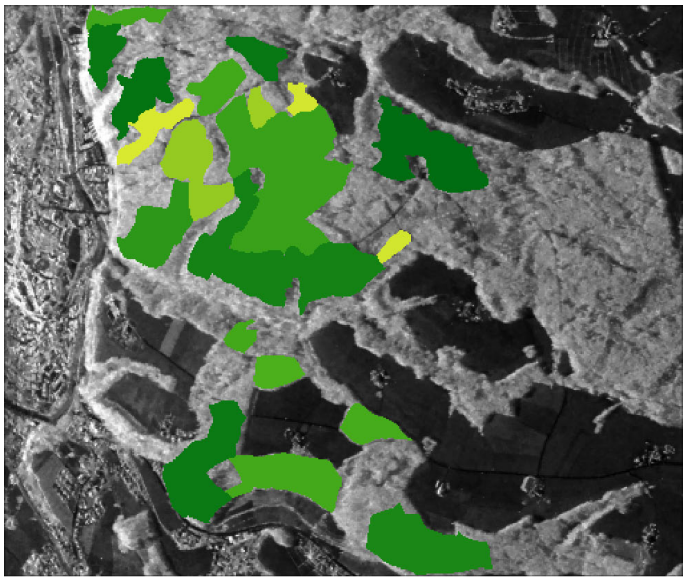

(a) Ground–truth forest height.

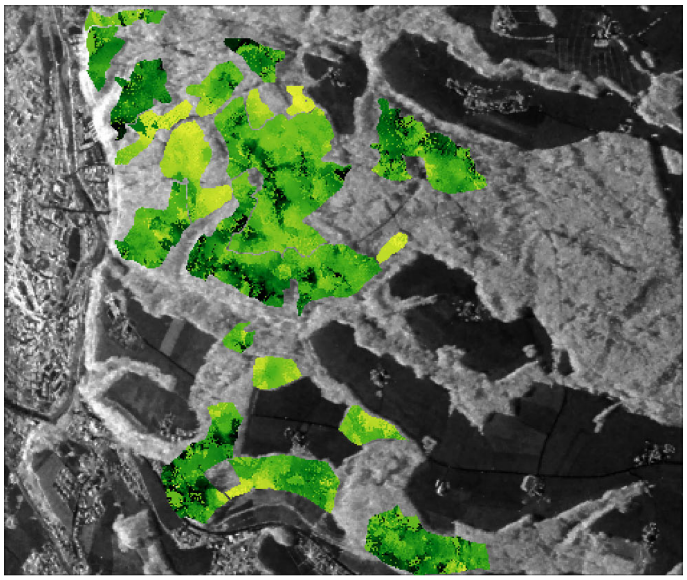

(b) Estimated forest height using 3 baselines: $1 \times 2, 1 \times 3, 1 \times 4$.

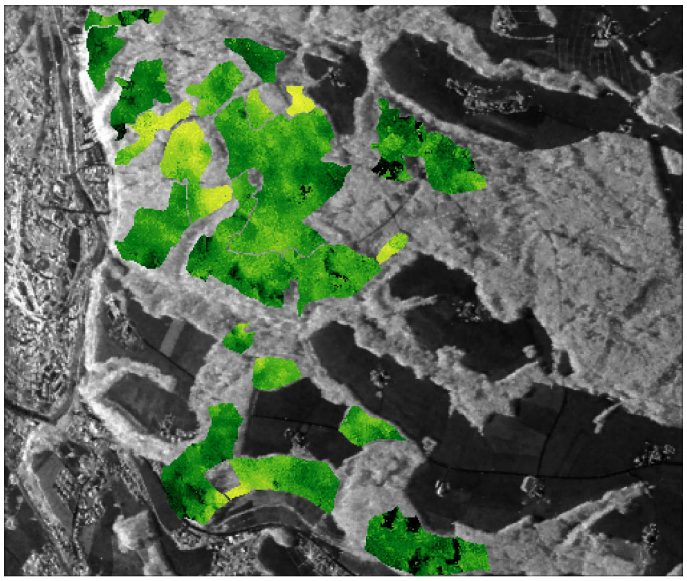

(c) Estimated forest height using 1 baseline: 1×2.

Figure 6.30: Comparison of forest height estimation using 3 and 1 baselines.

the potential to discriminate different vegetation media, in dependence of their morphology. As an example, the only one evaluation stand dominated by young maple trees showed significantly higher degree of orientation randomness than other tree species in the radar mid–range. Multi–angular experiments using this parameter would be very beneficial.

- The retrieved effective particle scattering anisotropy results were surprising since its magnitude was always higher than 1. This might indicate multiple scattering effects inside the canopy. Other possible reasons are the non–removed fractions from ground contributions or mis–calibration of the cross–polar channel. The estimates were reliable with low variances over all evaluation stands. The particle scattering anisotropy magnitude proved to be independent of the incidence angle. It should be dependent on the morphology and the dielectric constant of the vegetation. Particle scattering anisotropy phase helped to discriminate between forest stands dominated by deciduous and coniferous tree species. The phase seems also to be sensitive to the incidence angle.

- The temporal coherence has been estimated for its compensation. At a short temporal scale (minutes to some hours) the temporal decorrelation is mostly caused by wind, which is temporally and spatially non–stationary. The results revealed that at this short time scale the data decorrelates more for larger spatial baselines and for higher forests. In particular, over a larger baseline the data was more decorrelated even if the temporal baseline was smaller.

- Additionally, the ground–to–volume power ratio, the ground scattering components and the ground topography phases have been estimated, and require further analysis.

- For evaluation of the effect of the number of looks, parameter estimation has been performed with additionally 450, 900, and 1350 looks keeping all other procedure parameters the same as for the main evaluation. The experimental results showed that by an increase of the number of looks from 450 to 1800 by a factor of 4, the vegetation height estimation performance could be improved by about 20%. All height estimation performance indicators (bias, absolute error, RMSE, standard deviation) decreased monotonically with increasing number of looks.

- Similarly to the previous point, different baseline combinations have been tried out for parameter retrieval. The results showed that 5 meter single–baseline parameter estimation was able to retrieve forest height with similar RMSE as when using 3 baselines. However, the absolute bias was higher. The forest height results were overestimated and the temporal decorrelation was underestimated. Never the less, the obtained results over a single–baseline data set have been better than previously reported in literature (e.g. in [88]).

Chapter 7

Conclusions

7.1 Summary

This dissertation addresses several topics with the aim to improve the understanding of polarimetric radar interferometry and to provide techniques for vegetation parameter retrieval for remote sensing applications. The basic principles, on which this work is built, are presented in a concise way in the first two chapters. Chapter 2 covers the topics of electromagnetic wave propagation and scattering in random media, and polarimetry principles for scattering media characterization. In Chapter 3, SAR data processing is presented together with system models for single–channel, polarimetric and interferometric SAR imaging modes.

The first part of this thesis focuses on the theoretical framework of polarimetric SAR interferometry (PolInSAR), as it is investigated in Chapter 4. Up to now, the theoretical foundations of polarimetric interferometry, and especially of the PolInSAR coherence set, have not been fully studied and understood. In this study, the mathematical theory of numerical ranges, which governs the coherence set properties, is described and related to properties of PolInSAR covariance matrices, given some common conditions with respect to the illuminated media. Based on these studies, among others, two multi–baseline PolInSAR coherence optimization methods were developed, one unconstrained, using multiple scattering mechanism vectors (MSM), and one constrained using equal scattering mechanism vectors (ESM). These techniques enable us for the first time to use the coherence optimization for polarimetric differential SAR interferometry applications, as well as for multi–temporal and multi–baseline change monitoring with PolInSAR data. The optimization methods were evaluated on multi–baseline multi–temporal data and results were presented in dependence of the filtering technique and the scattering media under consideration.

The second part of the thesis aims to develop a polarimetric interferometric model for characterizing radar response from vegetation which would permit vegetation parameter retrieval from PolInSAR observables.

The state–of–the–art in vegetation parameter inversion for PolInSAR data has been the utilization of the interferometric coherence variation in dependence of polarization to estimate the linear ground–to–volume ratio relationship, which makes the inversion of the forest height and the ground topography phase possible. However, the polarimetric information and the synergy of polarimetry and interferometry have not been used to the full

extent. In Chapter 5, a new model is developed which combines previous PolInSAR–RVoG modeling and inversion approaches with a model–based polarimetric decomposition. The vegetation layer, modeled as a cloud of discrete particles, takes into account the effective particle scattering anisotropy (a parameter incorporating shape, tilt, and dielectric properties of the particles) and the distribution of particle orientations. This model incorporates all zeroth– and first–order scattering contributions for a volumetric layer over the ground, accounting for attenuation and refractivity, as derived for polarimetric and interferometric responses. Therefore, the polarimetric part of the presented model represents a generalization of the Freeman type models. The interferometric part is founded on the derivations by Treuhaft and Siqueira, and Cloude and Papathanassiou.
For the moment, there are two common acquisition modes for single–pass across–track interferometry: the single–transmit and the alternate–transmit modes. They have been already previously combined to acquire single–polarization interferometric dual–baseline data. Furthermore, the theoretical study of interferometric coherence constituents has revealed the potential of a combined hybrid PolInSAR mode (alternate–transmit both–receive) to enhance the separation of surface and double–bounce induced contributions, which is not possible using polarimetry only.
In the final chapter, Chapter 6, the developed forward model is adapted to meet demands to retrieve vegetation parameters from radar observables. In comparison to other approaches, this model enables us to improve the estimation of forest height and ground topography, as well as to retrieve additional parameters related to particle scattering anisotropy, the degree of orientation randomness, the main orientation of the particles, and the ground scattering characteristics.
To deal with repeat–pass PolInSAR required the adaption of the parameter estimation method to temporal decorrelation in the data, which is the major noise source, caused on the given short temporal scale mostly by wind. The final multi–baseline PolInSAR parameter estimation framework is robust against temporal decorrelation and allows to estimate the degree of temporal decorrelation in any particular baseline.
The developed parameter estimation approach has been evaluated on simulated and real airborne SAR data with comparison to ground–truth measurements. The examination of the experimental results (3 baselines, 1800 looks) led to the following main conclusions:

- Forest height estimates: underestimation bias of 1.67m, absolute error of 3.97m, RMS error of 4.97m, and height standard deviation of 4.33m.
- In some regions the retrieved forest heights seem more reasonable than the ground–truth data acquired 5 years before the SAR data acquisition.
- The degree of orientation randomness has been reliably estimated with low variance. It has shown, as predicted, sensitivity to the incidence angle and to the morphology of the trees.
- The retrieved effective particle scattering anisotropy results were surprising due to the fact that the anisotropy magnitude was always higher than 1. This might indicate multiple scattering effects inside the canopy (other possible reasons: residual ground contributions, mis–calibration of the cross–polar channel, or other non–modeled effects).

- The particle scattering anisotropy magnitude proved to be independent of the incidence angle. It should be dependent on the morphology and the dielectric constant of the vegetation particles. Particle scattering anisotropy phase helped to discriminate between forest stands dominated by deciduous and coniferous tree species. The phase seems also to be sensitive to the incidence angle.
- The temporal decorrelation has been estimated: it scales with the effective baseline and the height of the vegetation, which is reasonable. On the short temporal scale (10–60 minutes) the time duration was not very important.
- Further estimated parameters which need further analysis: extinction, canopy–fill–factor, ground–to–volume power ratio, ground scattering components and ground topography phases.
- Increase of the number of looks by a factor of 4 (from 450 to 1800) resulted in height estimation performance improvement of about 20%.
- Single–baseline data showed very good height estimation results, only with an increased overestimation bias, caused by underestimation of the temporal decorrelation.

The accomplishments that have been made in this thesis can be summarized as follows

- Coherence set theory: connection to the numerical range concept. Relationship between the PolInSAR covariance/coherency matrix properties and their projection on the complex coherence plane.
- Multi–baseline PolInSAR coherence optimization: development of two methods which optimize a sum of PolInSAR coherences under the conditions of multiple different or equal projection vectors. Evaluation on a multi–baseline multi–temporal data set.
- Formulation of a polarimetric interferometric vegetation model: zeroth– and first–order scattering contributions of a volume layer over the ground. Parameterization: degree of orientation randomness, main orientation, particle scattering anisotropy, volume layer depth, canopy volume attenuation and refractivity, canopy–fill–factor, ground topography, surface scattering, specular scattering.
- Suggestion for a hybrid single–pass PolInSAR system for enhanced distinction between surface and double–bounce scattering contributions.
- Multi–baseline multi–temporal vegetation parameter retrieval framework for forests. Evaluation on simulated and real data.

7.2 Perspectives

The results of this thesis lead to a variety of different research and application directions:

- The direction for the theoretical studies on coherence set properties is, as of now, uncertain, and only the future can show how it will develop. It was one of the most challenging task of this thesis, partly because it was (and still is) not clear where it leads to. But it was definitively very useful to develop an understanding and *an intuition* for the PolInSAR coherence set as something whole and not mere as a collection of a few discrete coherences corresponding to a few polarizations.

- Multi–baseline PolInSAR coherence optimization methods are going to be applied to multi–channel PolInSAR data, as for example for differential PolInSAR, multi–temporal and/or multi–baseline change monitoring and detection, permanent scatterer identification, and classification. Reigber *et al.* [123, 122] already presented initial optimization results for differential polarimetric interferometry for vegetated areas. Also, it is to expect, that these methods will be very useful for dual– and full–polarization space–borne SAR data. Given the long repeat pass cycles and the resulting temporal decorrelation, coherence optimization will be able to enhance time–series analyses. Especially since in dual–pol mode the physical interpretation is less important, the use of coherence optimization to reduce phase noise for any kind of application is very reasonable.

- The research and application directions for the presented vegetation model and the parameter estimation framework are numerous. Based on this simple model, already a lot of information could be obtained about the evaluated forest stands.
  Even despite the temporal decorrelation; even with a single baseline!
  The presented basic model components are universal and can be applied to various frequencies and for different volumetric media, which provides a wide range of ideas for future research:

  - Vegetation parameter estimation and classification: different tree species, agricultural crops, etc.
  - Evaluation on multiple frequencies, incidence angles, altitudes, etc.
  - Inclusion of multiple various data sources (e.g. multi–baseline, multi–frequency, multi–angular, multi–altitude, etc.) in a single model and parameter retrieval framework for improved robustness and accuracy.
  - Estimation of surface parameters under vegetation, such as soil moisture and surface roughness.
  - Other volumetric structures (with adjusted frequency, and if distorted Born approximation applies): snow, ice, dry soil/sand, precipitation, etc.
  - Combination with conventional or polarization coherence tomography (e.g. [121, 145, 18, 19]) for an improved information extraction from multi–baseline configurations.
  - Multi–temporal monitoring of ecosystem dynamics.

- The presented polarimetric model generalizes the Freeman type polarimetric decompositions. Development of a simple and general framework for a polarimetric decomposition based on the presented model might be advantageous.

- The theoretical prediction of the potential of a single–pass PolInSAR data in a hybrid interferometric mode to enhance the separation of all main scattering components (surface, double–bounce, volume) needs to be evaluated and validated on real data.

In retrospective, probably the most important contribution of this thesis is the formulation of the polarimetric interferometric vegetation model, the theoretical demonstration of meaningfulness and interpretability of this model on simulated data, and, finally, its experimental validation on real data. Some of the main aspects of the model and the parameter retrieval approach include the possibility of multi–source inclusion, robustness against temporal decorrelation, and physical interpretability, which can be useful for various fields in geophysical remote sensing. This approach represents a logical continuation of previous research in this field performed by various authors. It opens up new research and application opportunities and at the same time brings up a number of new questions, which need to be addressed in the future studies.

Appendix

Appendix A

SAR Statistics

A.1 Statistical Distributions of Scattering Signals

This appendix presents briefly the statistics of single– and multi–channel SAR signals for distributed targets. The single–channel scattering coefficients S_i and their multi–channel counterparts in form of scattering vectors $\boldsymbol{k} = [S_1, S_2, \ldots, S_q]$ have to be considered as random variables. The multi–channel scattering vector is composed of q elements, which can be related to polarimetric and interferometric measurements. Considering distributed targets as a random collection of scatterers simplifies the statistical analysis given the assumptions: (1) large number of scatterers, (2) homogeneous spatial distribution with uncorrelated positions, (3) large resolution cell dimensions in comparison to the wavenumber. Under these assumptions the scattered phase has a uniform distribution and under the central limit theorem the backscattering coefficients $S = x + iy$ follow the *complex circular Gaussian distributions* with zero mean and identical variances σ_x^2 for the real and imaginary parts [53]:

$$p(s|\sigma_x^2) = p(x, y) = \frac{1}{2\pi\sigma_x^2} e^{-\frac{x^2+y^2}{2\sigma_x^2}} \tag{A.1}$$

The *joint probability density function* for the amplitude a and phase ψ ($S = ae^{i\psi}$) is given by ($a \geq 0$):

$$p(a, \psi|\sigma_x^2) = \frac{a}{2\pi\sigma_x^2} e^{-\frac{a^2}{2\sigma_x^2}} \tag{A.2}$$

One obtains the *distribution of the amplitude* by marginalizing the previous function by integration over the phase in the range $-\pi$ and π. This delivers the *Rayleigh distribution*:

$$p(a|\sigma_x^2) = \frac{a}{\sigma_x^2} e^{-\frac{a^2}{2\sigma_x^2}} \tag{A.3}$$

The expected value of the amplitude is given by:

$$E[a] = \int_0^\infty a p(a|\sigma_x^2) da = \sqrt{\frac{\pi}{2}\sigma_x^2} \tag{A.4}$$

The distribution of the phase is given by integrating the joint pdf over the amplitude in the range $[0, \infty]$ which delivers a uniform distribution for $\psi \in [-\pi, \pi]$:

$$p(\psi) = \frac{1}{2\pi} \tag{A.5}$$

This shows that a and ψ are uncorrelated (independent), since

$$p(a, \psi|\sigma^2) = p(a|\sigma^2)p(\psi) \tag{A.6}$$

The intensity $I = a^2$ follows the exponential distribution

$$p(I|\sigma_x) = \frac{1}{2\sigma_x^2} e^{-\frac{I}{2\sigma_x^2}} \tag{A.7}$$

and its expected value is given by

$$E[I] = 2\sigma_x^2 \tag{A.8}$$

The scattering vector $\boldsymbol{k}$ follows the *multivariate complex circular Gaussian* distribution:

$$p(\boldsymbol{k}|\boldsymbol{\Sigma}) = \frac{1}{\pi^q |\boldsymbol{\Sigma}|} e^{-\boldsymbol{k}^\dagger \boldsymbol{\Sigma}^{-1} \boldsymbol{k}} \tag{A.9}$$

where q is the dimensionality of the scattering vector (usually =3) and $\boldsymbol{\Sigma} = E[\boldsymbol{k}\boldsymbol{k}^\dagger]$ is the true covariance matrix.
Since S and $\boldsymbol{k}$ have zero mean

$$E[S] = 0, \qquad E[\boldsymbol{k}] = \boldsymbol{0} \tag{A.10}$$

their description requires higher–order statistical characteristics, namely second–order statistics in form of the covariance matrix. If the random medium is homogeneous (the random scattering process can be described as stationary in space), the expect value operation can be replaced by spatial averaging to obtain the estimated (sample) covariance matrix

$$\mathbf{C} = \frac{1}{N} \sum_{i=1}^{N} \boldsymbol{k}_i \boldsymbol{k}_i^\dagger \tag{A.11}$$

where N is the number of *looks* (or pixels) used for the average.
The joint probability of N independent sample scattering vectors $\boldsymbol{k}_i$ can be given by [36]

$$p(\boldsymbol{k}_1, ..., \boldsymbol{k}_N) = \prod_{i=1}^{L} p(\boldsymbol{k}_i|\boldsymbol{\Sigma}) = \frac{1}{\pi^{qL}} \left(\frac{1}{|\boldsymbol{\Sigma}|^L} e^{-L \operatorname{trace}(\boldsymbol{\Sigma}^{-1}\mathbf{C})} \right) \tag{A.12}$$

where $\mathbf{C}$ is the sample covariance matrix and L is the true *effective number of looks* (ENL), see section A.1.2. After variable substitution ($\boldsymbol{k}_1, \boldsymbol{k}_2, \ldots, \boldsymbol{k}_N \rightarrow \mathbf{C}$) one obtains the complex Wishart distribution for the estimated covariance matrix [53, 73]:

$$p(\mathbf{C}|\boldsymbol{\Sigma}, L) = \frac{L^{Lq} |\mathbf{C}|^{L-q}}{\Gamma_q(L)} \left(\frac{1}{|\boldsymbol{\Sigma}|^L} e^{-L \operatorname{trace}(\boldsymbol{\Sigma}^{-1}\mathbf{C})} \right) \tag{A.13}$$

with

$$\Gamma_q(L) = \pi^{q(q-1)/2} \prod_{j=1}^{q} \Gamma(L - j + 1) \tag{A.14}$$

where $\Gamma(z)$ is the *Gamma function* and $\Gamma_q(z)$ is the *generalized Gamma function* for the multivariate case.
One can represent a two–by–two subset of the covariance matrix $\mathbf{C}$ via [64]

$$\mathbf{C}_{[ij]} = \begin{bmatrix} c_{ii} & \sqrt{c_{ii}c_{jj}}d_{ij}e^{i\phi_{ij}} \\ \sqrt{c_{ii}c_{jj}}d_{ij}e^{-i\phi_{ij}} & c_{jj} \end{bmatrix} \tag{A.15}$$

where c_{ii}, c_{jj}, c_{ij} are single elements of $\mathbf{C}$, d_{ij} represents the sample degree of coherence (or correlation) and ϕ_{ij} represents the sample phase difference. $\mathbf{C}_{[ij]}$ also follows the complex Wishart distribution. By marginalizing it one can obtain the distributions of the degree of coherence and of the phase ϕ (which can be the interferometric phase, or polarimetric phase difference). Integrating $\mathbf{C}_{[ij]}$ over c_{ii}, c_{jj} in the range $[0, \infty]$, and over ϕ_{ij} in the range $[-\pi, \pi]$, one obtains the distribution of the degree of coherence:

$$p(d_{ij}|D_{ij}, L) = 2(L-1)(1-D_{ij}^2)^L d_{ij}(1-d_{ij}^2)^{L-2}{}_2F_1(L, L; 1; D_{ij}^2 d_{ij}^2) \tag{A.16}$$

where D_{ij} is the true degree of coherence, and ${}_2F_1(\cdot, \cdot; \cdot; \cdot)$ is the *Hypergeometric function*. It is important to note and to keep in mind that the first moment (expectation value) of (A.16) is biased [150] and requires bias–removal operation.
The distribution of the phase is given by:

$$p(\phi_{ij}|\alpha_{ij}, D_{ij}, L) = \frac{(1-D_{ij}^2)^L}{2\pi}\left({}_2F_1(1, L; \frac{1}{2}; \beta^2) + \frac{\Gamma(1/2)\Gamma(L+1/2)}{\Gamma(L)}\beta(1-\beta^2)^{-(L+1/2)}\right) \tag{A.17}$$

where $\beta = D_{ij}\cos(\phi_{ij} - \alpha_{ij})$, and α_{ij} is the true phase. To improve computational costs, the Hypergeometric function can be replaced by trigonometric and algebraic functions for small number of looks.
The difference between polarimetric and interferometric phases $\Delta\phi_{ij,kl} = \phi_{ij} - \phi_{kl}$ is of importance for multi–baseline and multi–temporal PolInSAR applications. Its distribution can be given as a convolution [64]

$$p(\phi_{ij,kl}|\Delta\alpha_{ij,kl}, D_{ij}, D_{kl}, L) = \frac{1}{Z}p(\phi_{ij}|0, D_{ij}, L) \otimes p(\phi_{kl}|\alpha_{ij,kl}, D_{kl}, L) \tag{A.18}$$

where Z is the normalization factor.

A.1.1 Speckle Filtering

The scattered signal from a random medium is a superposition of scattering contributions from all elements, as expressed in equation (2.44). This coherent summation introduces the so called *speckle* effect, which lets the image appear granular. It is a deterministic interference/diffraction effect which is of major importance for polarimetry and interferometry. However, it is often undesired and is considered as noise. In order to reduce the speckle effect and to estimate the covariance matrices over homogeneous areas and to preserve the borders between different regions, various filters have been developed. Filters based on statistical LLMMSE (local linear minimum mean square error) minimization include the Lee, Kuan [68], Frost filters. More complex locally adaptive filter techniques include the refined Lee filter [72], the Simulated Annealing filter [133], the IDAN filter [164], the Jäger filter, etc.

A.1.2 Estimation of the Equivalent Number of Looks

In section A.1 a distinction has been drawn between the number of looks used for the averaging operation to estimate second order statistics and the true number of looks, the *effective* (sometimes called *equivalent*) number of looks (ENL).
Over homogeneous regions ENL is defined by

$$L = \frac{E[I]^2}{\mathrm{var}[I]} \tag{A.19}$$

Using single polarization data, the conventional (CV) estimation is based on the sample mean and the sample variance of the intensity [104, 4]

$$L^{(CV)}: \qquad L = \frac{\langle I \rangle^2}{\langle I^2 \rangle - \langle I \rangle^2} \tag{A.20}$$

where $\langle \cdot \rangle$ denotes the sample averaging. An alternative (numerical) estimator of L which is based on *fractional moments* (FM) of the intensity has been presented in [48]. Recently, ENL estimators were presented which use the full covariance matrix and with it the full available polarization information [4]. The multivariate generalization of the conventional single–pol estimator is the *trace moment* (TM) estimator

$$L^{(TM)}: \qquad L = \frac{\mathrm{trace}(\mathbf{\Sigma})^2}{\langle \mathrm{trace}(\mathbf{ZZ}) \rangle - \mathrm{trace}(\mathbf{\Sigma\Sigma})} \tag{A.21}$$

where $\hat{\mathbf{\Sigma}} = \langle \mathbf{C} \rangle$ and $\mathbf{Z} = \mathbf{C}$. Additionally a *maximum likelihood* (ML) estimator for ENL for multivariate data is derived in [4] assuming Wishart distribution of the covariance matrices. This estimator requires as well a numerical solution.

A.2 PolInSAR Coherence Set Statistics

In the following, a numerical approach for statistical coherence set analysis is presented with respect to the polarization density. It should be noted, that the analysis of the coherence set with respect to backscattering energy (cf. section 4.4.3) is probably physically more meaningful and the derived expressions can be extended to this case straightforwardly.
To analyze the probability density of PolInSAR coherences in the complex plane, it will prove useful to derive the marginal probability of the complex coherence with respect to the polarization state. But prior to this, one needs to define the joint distribution of the complex coherence and the transmit/receive polarizations. Using the Bayes' theorem, the joint probability density function (PDF) of the sample coherence ($\gamma = de^{i\phi}$) and the scattering polarization vector $\mathbf{\Psi}_\xi$, which determines the true coherence $\xi = De^{i\beta} = f_\xi(\mathbf{\Sigma}, \boldsymbol{\omega}(\boldsymbol{\psi}_\xi))$, can be expressed by

$$p(\gamma, \boldsymbol{\psi}_\xi | \mathbf{\Sigma}, L) = p(\gamma | \boldsymbol{\psi}_\xi, \mathbf{\Sigma}, L)\; p(\boldsymbol{\psi}_\xi). \tag{A.22}$$

This PDF can be interpreted as the joint probability of the sample and the true coherence, γ and $\xi_{(\boldsymbol{\psi}_\xi)}$, for a single polarization.

The conditional probability density for the coherence, given the true coherence, has been derived in [151]:

$$p(\gamma|\boldsymbol{\psi}_\xi, \boldsymbol{\Sigma}, L) = p(\gamma|\xi_{(\boldsymbol{\psi}_\xi)}, L) = \frac{(1-D^2)^L}{\pi\Gamma(L)\Gamma(L-1)} d(1-d^2)^{L-2} \times \left[\Gamma^2(L)\,{}_2F_1(L, L; 1/2, d^2D^2\cos^2(\phi-\beta)) + 2\Gamma^2(L+1/2)dD\cos(\phi-\beta)\;{}_2F_1(L+1/2, L+1/2; 3/2; d^2D^2\cos^2(\phi-\beta))\right] \quad \text{(A.23)}$$

where L is the effective number of looks (ENL), Γ is the Gamma function, and ${}_2F_1$ is the Gauss's Hypergeometric function. This PDF is the "usual" single–pol coherence PDF. The density of scattering polarizations is determined by the assumption of joint uniform distribution of polarization angles in their domains.
The marginal probability of the complex coherence, which represents the coherence density over all polarizations, is obtained by integrating (A.22) over the polarization space:

$$p(\gamma|\boldsymbol{\Sigma}, L) = \iiiint p(\gamma|\xi_{(\boldsymbol{\psi}_\xi)}, L)p(\boldsymbol{\psi}_\xi)d\boldsymbol{\psi}_\xi. \quad \text{(A.24)}$$

With similar reasoning one can derive the expression for the a–posteriori PDF of the true coherence, given the sample covariance matrix and assuming (in the absence of better knowledge) a uniform prior distribution:

$$p(\xi|\mathbf{C}, L) = \iiiint \left[\iint p(\gamma_{(\boldsymbol{\psi}_\gamma)}|\xi', L)d\xi'\right]^{-1} p(\gamma_{(\boldsymbol{\psi}_\gamma)}|\xi, L)p(\boldsymbol{\psi}_\gamma)d\boldsymbol{\psi}_\gamma \quad \text{(A.25)}$$

where the outer integral is taken over the scattering polarization state domain, and the inner, representing the marginal data PDF, is taken over the complex coherence domain, i.e. over the amplitude and phase of the unitary disc in the complex coherence plane.
No analytical forms for the integrals (A.24) and (A.25) can be given at the moment and they need to be solved numerically.

A.3 PolInSAR ML Estimators and Hypotheses Tests

L. Ferro-Famil presented several maximum likelihood (ML) estimators and tests for common PolInSAR assumptions [39]. The test for weak polarimetric stationarity is given by the normalized ML ratio test:

$$\Lambda_{stat,weak} = \frac{\sqrt{|\mathbf{T}_{11}|}\sqrt{|\mathbf{T}_{22}|}}{|\mathbf{T}_3|}, \qquad \text{with } \mathbf{T}_3 = \frac{\mathbf{T}_{11}+\mathbf{T}_{22}}{2} \quad \text{(A.26)}$$

The normalized ML ratio test for strong polarimetric stationarity is

$$\Lambda_{stat,strong} = \Lambda_{stat,weak}\frac{|\mathbf{I}-\hat{\mathbf{P}}|}{|\mathbf{I}-\widetilde{\mathbf{\Pi}}\widetilde{\mathbf{\Pi}}^\dagger|}, \qquad \text{with } \widetilde{\mathbf{\Pi}} = \mathbf{T}_3^{-1/2}\mathbf{\Omega}\mathbf{T}_3^{-1/2}, \hat{\mathbf{P}} = \frac{\widetilde{\mathbf{\Pi}}\widetilde{\mathbf{\Pi}}^\dagger + \widetilde{\mathbf{\Pi}}^\dagger\widetilde{\mathbf{\Pi}}}{2} \quad \text{(A.27)}$$

Bibliography

[1] B. P. Ablitt. *Characterisation of Particles and their Scattering Effects on Polarized Light*. PhD thesis, University of Nottingham, UK, March 2000.

[2] M. Abramowitz and I. A. Stegun. *Handbook of Mathematical Functions with Formulas, Graphs, and Mathematical Tables*. Dover, New York, 1964.

[3] T. L. Ainsworth, L. Ferro-Famil, and J. S. Lee. Orientation Angle Preserving A Posteriori Polarimetric SAR Calibration. *IEEE Transactions on Geoscience and Remote Sensing*, 44(4):994–1003, April 2006.

[4] S. N. Anfinsen, A. P. Doulgeris, and T. Eltoft. Estimation of the equivalent number of looks in polarimetric SAR imagery. In *Proceedings of the International Geoscience Remote Senssing Symposium (IGARSS)*, Boston, USA, July 2008.

[5] J. I. H. Askne, P. B. G. Dammert, L. M. H. Ulander, and G. Smith. C–Band Repeat–Pass Interferometric SAR Observations of the Forest. *IEEE Transactions on Geoscience and Remote Sensing*, 35(1):25–35, January 1997.

[6] J. D. Ballester-Berman. *Retrieval of biophysical parameters of agricultural crops using polarimetric SAR interferometry*. PhD thesis, University of Alicante, Spain, July 2007.

[7] J. D. Ballester-Berman and J. M. Lopez-Sanchez. Coherence Loci for a Homogeneous Volume Over a Double-Bounce Ground Return. *IEEE Geosci. Remote Sensing Lett.*, 4(2):317–321, April 2007.

[8] J. D. Ballester-Berman, J. M. Lopez-Sanchez, and J. Fortuny-Guasch. Retrieval of Biophysical Parameters of Agricultural Crops Using Polarimetric SAR Interferometry. *IEEE Transactions on Geoscience and Remote Sensing*, 43:683 – 694, April 2005.

[9] R. Bamler. A comparison of range-doppler and wavenumber domain sar focusing algorithms. *Geoscience and Remote Sensing, IEEE Transactions on*, 30(4):706–713, July 1992.

[10] R. Bamler and P. Hartl. Synthetic aperture radar interferometry. *Inverse Problems*, 14:R1–R54, 1998.

[11] M. Born and E. Wolf. *Principles of Optics*. Pergamon Press, sixth edition, 1980.

[12] C. Cafforio, C. Prati, and F. Rocca. Sar data focusing using seismic migration techniques. *Aerospace and Electronic Systems, IEEE Transactions on*, 27(2):194–207, March 1991.

[13] W. L. Cameron and H. Rais. Conservative Polarimetric Scatterers and Their Role in Incorrect Extensions of the Cameron Decomposition. *IEEE Transactions on Geoscience and Remote Sensing*, 44(12):3506–3516, December 2006.

[14] W. L. Cameron, N. N. Youssef, and L. K. Leung. Simulated Polarimetric Signatures of Primitive Geometrical Shapes. *IEEE Transactions on Geoscience and Remote Sensing*, 34(3):793–803, May 1996.

[15] S. R. Cloude. Group theory and polarization algebra. *Optik*, 75(1):26–36, 1986.

[16] S. R. Cloude. *Polarimetry: the characterisation of polarisation effects in EM scattering*. PhD thesis, University of Birmingham, Birmingham, October 1986.

[17] S. R. Cloude. Helicity in Radar Remote Sensing. In *Proceedings of the International Geoscience Remote Senssing Symposium (IGARSS)*, pages 411–413, Toronto, Canada, June 2002.

[18] S. R. Cloude. Polarization coherence tomography. *Radio Sci.*, 41:4017– +, August 2006.

[19] S. R. Cloude. Dual baseline coherence tomography. *IEEE Geosci. Remote Sensing Lett.*, 4(1):127–131, January 2007.

[20] S. R. Cloude, J. Fortuny, J. M. Lopez-Sanchez, and A. J. Sieber. Wide–Band Polarimetric Radar Inversion Studies for Vegetation Layers. *IEEE Transactions on Geoscience and Remote Sensing*, 37(5):2430–2441, September 1999.

[21] S. R. Cloude and K. P. Papathanassiou. Polarimetric optimization in radar interferometry. *Electronic Letters*, 33(13):1176–1178, June 1997.

[22] S. R. Cloude and K. P. Papathanassiou. Polarimetric SAR Interferometry. *IEEE Transactions on Geoscience and Remote Sensing*, 36:1551–1565, September 1998.

[23] S. R. Cloude and K. P. Papathanassiou. Three–stage inversion process for polarimetric SAR interferometry. *IEE Proceedings - Radar, Sonar and Navigation*, 150:125–134, June 2003.

[24] S. R. Cloude and E. Pottier. A Review of Target Decomposition Theorems in Radar Polarimetry. *IEEE Transactions on Geoscience and Remote Sensing*, 34(2):498–518, March 1996.

[25] S. R. Cloude and E. Pottier. An entropy based classification scheme for land applications of polarimetric SAR. *IEEE Transactions on Geoscience and Remote Sensing*, 35(1):68–78, January 1997.

[26] E. Colin. *Apport de la polarimétrie à l'interférométrie radar pour l'estimation des hauteurs de cibles et de paramètres de forêt*. PhD thesis, Université Paris 6, 2005.

[27] E. Colin. A Mathematical study about the "Coherence Set" in Polarimetric Interferometry. In *Proceedings of the European Conference no Synthetic Aperture Radar (EUSAR)*, Dresden, Germany, May 2006.

[28] E. Colin and F. Garestier. Polarimetric interferometry applied to high resolution imagery and urban areas. In *Proceedings of the International Geoscience Remote Senssing Symposium (IGARSS)*, Denver, USA, July 2006.

[29] E. Colin, C. Titin-Schnaider, and W. Tabbara. An Interferometric Coherence Optimization Method in Radar Polarimetry for High-Resolution Imagery. *IEEE Transactions on Geoscience and Remote Sensing*, 44(1):167– 175, January 2006.

[30] I. G. Cumming and F. H. Wong. *Digital processing of synthetic aperture radar data: algorithms and implementation.* Artech House, 2005.

[31] J. C. Curlander and R. N. McDonough. *Synthetic Aperture Radar: Systems and Signal Theory.* John Willey & Sons, 1991.

[32] C. Dahon, L. Ferro-Famil, C. Titin-Schnaider, and E. Pottier. Computing the double-bounce reflection coherent effect in an incoherent electromagnetic scattering model. *IEEE Geosci. Remote Sensing Lett.*, 3(2):241–245, April 2006.

[33] P. C. Dubois, van J. J. Zyl, and T. Engman. Measuring Soil Moisture with Imaging Radar. *IEEE Transactions on Geoscience and Remote Sensing*, 33(4):916–926, July 1995.

[34] S.L. Durden, J.J. van Zyl, and H.A. Zebker. Modeling and observation of the radar polarization signature of forested areas. *IEEE Transactions on Geoscience and Remote Sensing*, 27(3):290–301, May 1989.

[35] L. Ferro-Famil. *Télédetection multi-fréquentielle et multi-temporelle d'environnements naturels à partir de données SAR polarimétriques.* PhD thesis, Université de Nantes, France, 2000.

[36] L. Ferro-Famil. *Traitment du signal radar polarimétrique. Aspects théoriques et applications à la télédétection.* Habilitation thesis, Universtité de Rennes 1, France, July 2007.

[37] L. Ferro-Famil, F. Kugler, E. Pottier, and J. S. Lee. Forest Mapping and Classification at L band using Pol-inSAR Optimal Coherence Set Statistics. In *Proceedings of the European Conference no Synthetic Aperture Radar (EUSAR)*, Dresden, Germany, May 2006.

[38] L. Ferro-Famil, C. López-Martinez, and E. Pottier. Analysis of Natural Scene Properties from POLinSAR Data Using Coherence Set Statistics and a Multi-Dimensional Speckle Model. In *Proceedings of the International Geoscience Remote Senssing Symposium (IGARSS)*, Denver, USA, July 2006.

[39] L. Ferro-Famil and M. Neumann. Recent Advances in the Derivation of POL-inSAR Statistics: Study and Applications. In *Proceedings of the European Conference no Synthetic Aperture Radar (EUSAR)*, Friedrichshafen, Germany, June 2008.

[40] L. Ferro-Famil, A. Reigber, E. Pottier, and W. M. Boerner. Scene characterization using subaperture polarimetric SAR data. *IEEE Transactions on Geoscience and Remote Sensing*, 41:2264–2276, October 2003.

[41] R. P. Feynman, R. B. Leighton, and M. Sands. *The Feynman Lectures on Physics*, volume 1,2,3. Addison Wesley, 1964.

[42] T. Flynn, M. Tabb, and R. Carande. Coherence region shape extraction for vegetation parameter estimation in polarimetric SAR interferometry. In *Proceedings of the International Geoscience Remote Senssing Symposium (IGARSS)*, volume 5, pages 2596–2598, Toronto, Canada, June 2002.

[43] L. L. Foldy. The multiple scattering of waves. i. general theory of isotropic scattering by randomly distributed scatterers. *Phys. Rev.*, 67(3-4):107–119, February 1945.

[44] A. Freeman. SAR Calibration: An Overview. *IEEE Transactions on Geoscience and Remote Sensing*, 30(6):1107–1121, November 1992.

[45] A. Freeman. Fitting a Two–Component Scattering Model to Polarimetric SAR Data From Forests. *IEEE Transactions on Geoscience and Remote Sensing*, 45(8):2583–2592, August 2007.

[46] A. Freeman and S. L. Durden. A three-component model for polarimetric SAR imagery. *IEEE Transactions on Geoscience and Remote Sensing*, 34(3):963–973, May 1998.

[47] A. Freeman and S. S. Saatchi. On the Detection of Faraday Rotation in Linearly Polarized L–Band SAR Backscatter Signatures. *IEEE Transactions on Geoscience and Remote Sensing*, 42(8):1607–1616, August 2004.

[48] A. C. Frery, A. H. Correia, and C. C. Freitas. Classifying Multifrequency Fully Polarimetric Imagery With Multiple Sources of Statistical Evidence and Contextual Information. *IEEE Transactions on Geoscience and Remote Sensing*, 45(10):3098–3109, October 2007.

[49] F. Gatelli, A. M. Guarnieri, F. Parizzi, P. Pasquali, C. Prati, and F. Rocca. The Wavenumber Shift in SAR Interferometry. *IEEE Transactions on Geoscience and Remote Sensing*, 32(4):855–865, July 1994.

[50] D. Giuli. Polarization diversity in radars. *Proceedings of the IEEE*, 74(2):245–269, February 1986.

[51] J. L. Gomez-Dans and S. Quegan. Constraint coherence optimisation in polarimetric interferometry of layered targets. In *Proceedings of the International Workshop on Science and Applications of SAR Polarimetry and Polarimetric Interferometry (POLINSAR)*, Frascati, Italy, January 2005.

[52] J. W. Goodman. *Statistical Optics*. Wiley-Interscience, 1985.

[53] N. R. Goodman. Statistical Analysis Based on a Certain Multivariate Complex Gaussian Distribution (An Introduction). *Ann. Math. Statist.*, 34(1):152–177, 1963.

[54] J. O. Hagberg, L. M. H. Ulander, and J. Askne. Repeat-Pass SAR Interferometry Over Forested Terrain. *IEEE Transactions on Geoscience and Remote Sensing*, 33(2):331–340, March 1995.

[55] I. Hajnsek. *Inversion of Surface Parameters from Polarimetric SAR.* PhD thesis, University of Jena, Germany, 2001.

[56] I. Hajnsek, E. Pottier, and S. R. Cloude. Inversion of Surface Parameters From Polarimetric SAR. *IEEE Transactions on Geoscience and Remote Sensing*, 41(4):727–744, April 2003.

[57] R. F. Hanssen. *Radar Interferometry. Data Interpretation and Error Analysis.* Kluwer Academic Publishers, 2001.

[58] R. A. Horn and C. R. Johnson. *Matrix Analysis.* Cambridge University Press, 1990.

[59] R. A. Horn and C. R. Johnson. *Topics in Matrix Analysis.* Cambridge University Press, 1991.

[60] R. Horst. Relations among m sets of measures. *Psychometrica*, 26(2):129–149, June 1961.

[61] H. Hotelling. Relations between two sets of variates. *Biometrika*, 28(3):321–377, 1936.

[62] A. Ishimaru. *Wave Propagation and Scattering in Random Media*, volume 1+2. Academic, San Diego, 1978.

[63] A. Ishimaru. *Electromagnetic wave propagation, radiation, and scattering.* Prentice-Hall, New Jersey, 1991.

[64] M. Jäger, M. Neumann, S. Guillaso, and A. Reigber. A Self-Initialising PolInSAR Classifier Using Interferometric Phase Differences. *IEEE Transactions on Geoscience and Remote Sensing*, 45(11):3503–3518, November 2007.

[65] J. R. Kettenring. Canonical analysis of several sets of variables. *Biometrika*, 58(3):433–451, 1971.

[66] A. S. Khwaja. *Génération rapide de signaux radar d'environment complexes pour la simulation de systèmes imageurs SAR.* PhD thesis, Université de Rennes 1, France, 2008.

[67] E. Krogager. New decomposition of the radar target scattering matrix. *Electronic Letters*, 26(18):1525–1527, August 1990.

[68] F. T. Kuan, A. A. Sawchuk, T. C. Strand, and et P. Chavel. Adaptive noise smoothing filter for images with signal-dependent noise. *IEEE Transactions on Pattern Analysis and Machine Intelligence*, 1985.

[69] R. L. Lang. Electromagnetic backscattering from a sparse distribution of lossy dielectric scatterers. *Radio Sci.*, 16(1):15–30, January 1981.

[70] M. Lax. Multiple scattering of waves. *Rev. Mod. Phys.*, 23(4):287 – 310, October 1951.

[71] P. Leducq. *Traitements temps-fréquence pour l'analyse de scènes complexes dans les images SAR polarimétriques.* PhD thesis, Université de Rennes 1, France, June 2006.

[72] J. S. Lee, M. R. Grunes, and G. de Grandi. Polarimetric SAR speckle filtering and its implication for classification. *IEEE Transactions on Geoscience and Remote Sensing*, 37:2363–2373, September 1999.

[73] J. S. Lee, K. W. Hoppel, S. A. Mango, and A. R. Miller. Intensity and Phase Statistics of Multilook Polarimetric and Interferometric SAR Imagery. *IEEE Transactions on Geoscience and Remote Sensing*, 32(5):1017–1028, September 1994.

[74] J. S. Lee, D. L. Schuler, T. L. Ainsowrth, E. Krogager, D. Kasilingam, and W. M. Boerner. On the Estimation of Radar Polarization Orientation Shifts Induced by Terrain Slopes. *IEEE Transactions on Geoscience and Remote Sensing*, 40(1):30–41, January 2002.

[75] J. S. Lee, D. L. Schuler, and T. L. Ainsworth. Polarimetric SAR Data Compensation for Terrain Azimuth Slope Variation. *IEEE Transactions on Geoscience and Remote Sensing*, 38(5):2153–2163, September 2000.

[76] S. K. Lee, F. Kugler, K. Papathanassiou, and I. Hajnsek. Quantifying temporal decorrelation over boreal forest at l– and p–band. In *Proceedings of the European Conference no Synthetic Aperture Radar (EUSAR)*, Friedrichshafen, Germany, June 2008.

[77] C. K. Li. Lecture notes on Numerical Range. unpublished, June 2005.

[78] F. K. Li and R. M. Goldstein. Studies of Multibaseline Spaceborne Interferometric Synthetic Aperture Radars. *IEEE Transactions on Geoscience and Remote Sensing*, 28(1):88–97, January 1990.

[79] Y. C. Lin. *A fractal–based coherent scattering and propagation model for forest canopies.* PhD thesis, The University of Michigan, 1997.

[80] Y.C. Lin and K. Sarabandi. A Monte Carlo Coherent Scattering Model For Forest Canopies Using Fractal-Generated Trees. *IEEE Transactions on Geoscience and Remote Sensing*, 37(1):440–451, January 1999.

[81] C. López-Martinez, L. Pipia, and K. P. Papathanassiou. Analysis and correction of speckle noise effects on PolInSAR data based on coherent modeling. In *Proceedings of the International Geoscience Remote Senssing Symposium (IGARSS)*, Boston, USA, July 2008.

[82] J. M. Lopez-Sanches. *Analysis and Estimation of Biophysical Parameters of Vegetation by Radar Polarimetry.* PhD thesis, Universidad Politécnica de Valencia, 1999.

[83] E. Lüneburg. Foundations of the Mathematical Theory of Polarimetry. Technical report, EML Consultants, 2001. Final Report Phase I.

[84] E. Lüneburg and S. R. Cloude. Contractions, Hadamard products and their application to polarimetric radar interferometry. In *Proceedings of the International Geoscience Remote Senssing Symposium (IGARSS)*, pages 2224–2226, Hamburg, 1999.

[85] C. López Martinez. *Multidimensional speckle noise. Modelling and filtering related to SAR data.* PhD thesis, Universitat Politècnica de Catalunya, Spain, April 2003.

[86] D. Massonnet and K. L. Feigl. Radar interferometry and its application to changes in the earth's surface. *Reviews of Geophysics*, 36(4):441–500, 1998.

[87] E. Mengi and M. L. Overton. Algorithms for the computation of the pseudospectral radius and the numerical radius of a matrix. *IMA Journal of Numerical Analysis*, 25(4):648–669, March 2005.

[88] T. Mette. *Forest Biomass Estimation from Polarimetric SAR Interferometry.* PhD thesis, Technische Universität München, Germany, 2007.

[89] M. Moghaddam. Effect of medium symmetries in limiting the number of parameters estimated with polarimetric interferometry. In *Proceedings of the International Geoscience Remote Senssing Symposium (IGARSS)*, pages 2221–2223, Hamburg, 1999.

[90] M. Moghaddam and S. Saatchi. Analysis of scattering mechanisms in sar imagery over boreal forest: results from boreas '93. *Geoscience and Remote Sensing, IEEE Transactions on*, 33(5):1290–1296, September 1995.

[91] A. Moreira, J. Mittermayer, and R. Scheiber. Extended chirp scaling algorithm for air- and spaceborne sar data processing in stripmap and scansar imaging modes. *Geoscience and Remote Sensing, IEEE Transactions on*, 34(5):1123–1136, September 1996.

[92] M. Neumann, L. Ferro-Famil, and A. Reigber. Multibaseline POLInSAR Coherence Modelling and Optimization. In *Proceedings of the International Geoscience Remote Senssing Symposium (IGARSS)*, Barcelona, Spain, July 2007.

[93] M. Neumann, L. Ferro-Famil, and A. Reigber. Polarimetric Coherence Optimization for Multibaseline SAR Data. In *Proceedings of the International Workshop on Science and Applications of SAR Polarimetry and Polarimetric Interferometry (POLINSAR)*, Frascati, Italy, January 2007.

[94] M. Neumann, L. Ferro-Famil, and A. Reigber. Estimation of Forest Structure, Ground and Canopy Layer Characteristics from Multi–Baseline Polarimetric Interferometric SAR Data. *IEEE Transactions on Geoscience and Remote Sensing*, June 2008. Submitted.

[95] M. Neumann, L. Ferro-Famil, and A. Reigber. Multibaseline Polarimetric SAR Interferometry Coherence Optimization. *IEEE Geosci. Remote Sensing Lett.*, 5(1):93–97, January 2008.

[96] M. Neumann, M. Jäger, L. Ferro-Famil, and A. Reigber. Statistical Assessment of the PolInSAR Coherence Set for Geophysical Media. In *Proceedings of the European Conference no Synthetic Aperture Radar (EUSAR)*, Friedrichshafen, Germany, June 2008.

[97] M. Neumann, A. Reigber, and L. Ferro-Famil. Data Classification Based on PolInSAR Coherence Shapes. In *Proceedings of the International Geoscience Remote Senssing Symposium (IGARSS)*, volume 7, pages 4852–4855, Seoul, Korea, July 2005.

[98] M. Neumann, A. Reigber, and L. Ferro-Famil. POLInSAR Coherence Set Theory and Application. In *Proceedings of the European Conference no Synthetic Aperture Radar (EUSAR)*, Dresden, Germany, May 2006.

[99] R. G. Newton. Optical theorem and beyond. *American Journal of Physics*, 44(7):639–642, July 1976.

[100] S. V. Nghiem, S. H. Yueh, R. Kwok, and F. K. Li. Symmetry properties in polarimetric remote sensing. *Radio Sci.*, 27(5):693–711, September 1992.

[101] G. Nico, J. M. Lopez-Sanchez, J. Fortuny, D. Tarchi, D. Leva, and A. J. Sieber. Assessment of the Impact of the Polarimetric Coherence Optimisation on Phase Unwrapping. In *Proceedings of the European Conference no Synthetic Aperture Radar (EUSAR)*, pages 523–526, Munich, Germany, May 2000.

[102] A. A. Nielsen. Multiset Canonical Correlations Analysis and Multispectral, Truly Multitemporal Remote Sensing Data. *IEEE Transactions on Geoscience and Remote Sensing*, 11(3):293–305, March 2002.

[103] Y. Oh, K. Sarabandi, and F. T. Ulaby. An Empirical Model and an Inversion Technique for Radar Scattering from Bare Soil Surfaces. *IEEE Transactions on Geoscience and Remote Sensing*, 30(2):370–381, June 1992.

[104] C. Oliver and S. Quegan. *Understanding Synthetic Aperture Radar Images*. Artech House, 1998.

[105] K. P. Papathanassiou. *Polarimetric SAR Interferometry*. PhD thesis, Technische Universität Graz, 1999.

[106] K. P. Papathanassiou and S. R. Cloude. Single–Baseline Polarimetric SAR Interferometry. *IEEE Transactions on Geoscience and Remote Sensing*, 39:2352 – 2363, November 2001.

[107] K. P. Papathanassiou, S. R. Cloude, A. Reigber, and W. M. Boerner. Multi–baseline Polarimetric SAR Interferometry for Vegetation Parameter Estimation. In *Proceedings of the International Geoscience Remote Senssing Symposium (IGARSS)*, volume 6, pages 2762–2764, Honolulu, US, July 2000.

[108] A. Papoulis. *Probability, Random Variables, and Stochastic Processes*. McGraw-Hill, Inc., third edition, 1991.

[109] B. Peterson and S. Ström. T Matrix for Electromagnetic Scattering from an Arbitrary Number of Scatterers and Representations of E(3). *Phys. Rev. D*, 8(10):3661 – 3678, November 1973.

[110] G. Picard. *Modélisation radar des couverts végétaux. Applications à la télédétection de couverts forestiers et agricoles.* PhD thesis, Université Paul Sabatier -Toulouse III, October 2002.

[111] E. Pottier. *Contribution de la polarimétrie dans la discrimination de cibles radar. Application à l'imagerie électromagnétique haute résolution.* PhD thesis, Université de Rennes 1, France, December 1990.

[112] E. Pottier and S. R. Cloude. Application of the "H/A/α" polarimetric decomposition theorem for land classification. In *Proc. SPIE*, pages 132–143, San Diego, USA, July 1997.

[113] J. Praks, F. Kugler, K. P. Papathanassiou, I. Hajnsek, and M. Hallikainen. Height Estimation of Boreal Forest: Interferometric Model-Based Inversion at L- and X-Band Versus HUTSCAT Profiling Scatterometer. *IEEE Geosci. Remote Sensing Lett.*, 4(3):466–470, July 2007.

[114] W. H. Press, S. A. Teukolsky, W. T. Vetterling, and B. P. Flannery. *Numerical Recipes in C: The Art of Scientific Computing.* Cambridge University Press, 2 edition, 1992.

[115] M. Qong. Coherence optimization using the polarization state conformation in PolInSAR. *IEEE Geosci. Remote Sensing Lett.*, 2(3):301–305, July 2005.

[116] K. Raney, H. Runge, R. Bamler, I. Cumming, and F. Wong. Precision SAR Processing Using Chirp Scaling. *IEEE Transactions on Geoscience and Remote Sensing*, 32(4):786–799, July 1994.

[117] R. K. Raney. Hybrid–Polarity SAR Architecture. *IEEE Transactions on Geoscience and Remote Sensing*, 45(11):3397–3404, November 2007.

[118] I. S. Reed, J. D. Mallett, and L. E. Brennan. Rapid Convergence Rate in Adaptive Arrays. *IEEE Trans. Aerosp. Electron. Syst.*, 10(6):853–863, November 1974.

[119] A. Reigber. *Airborne Polarimetric SAR Tomography.* PhD thesis, Universität Stuttgart, 2001.

[120] A. Reigber and L. Ferro-Famil. Interference Suppression in Synthesized SAR Images. *IEEE Geosci. Remote Sensing Lett.*, 2(1):45–49, January 2005.

[121] A. Reigber and A. Moreira. First demonstration of airborne SAR tomography using multibaseline L-band data. *IEEE Transactions on Geoscience and Remote Sensing*, 38(5):2142–2152, September 2000.

[122] A. Reigber, M. Neumann, E. Erten, M. Jäger, and P. Prats. Multi-baseline polarimetrically optimised phases and scattering mechanisms for InSAR applications. In *Proceedings of the International Geoscience Remote Senssing Symposium (IGARSS)*, Barcelona, Spain, July 2007.

[123] A. Reigber, M. Neumann, L. Ferro-Famil, M. Jäger, and P. Prats. Multibaseline coherence optimisation in partial polarimetric modes. In *Proceedings of the International Geoscience Remote Senssing Symposium (IGARSS)*, Boston, USA, July 2008.

[124] A. Reigber and R. Scheiber. Airborne Differential SAR Interferometry: First Results at L–Band. *IEEE Transactions on Geoscience and Remote Sensing*, 41(6):1516–1520, June 2003.

[125] E. J. M. Rignot. Effect of Faraday Rotation on L-Band Interferometric and Polarimetric Synthetic-Aperture Radar Data. *IEEE Transactions on Geoscience and Remote Sensing*, 38(1):383–390, January 2000.

[126] F. Rocca. Modeling Interferogram Stacks. *IEEE Transactions on Geoscience and Remote Sensing*, 45(10):3289–3299, October 2007.

[127] E. Rodriguez and J. M. Martin. Theory and design of interferometric synthetic aperture radars. *IEE Proceedings*, 139(2):147–159, April 1992.

[128] P. A. Rosen, S. Hensley, I. R. Joughin, F. K. Li, S. N. Madsen, E. Rodriguez, and R. M. Goldstein. Synthetic Aperture Radar Interferometry. *Proc. IEEE*, 88(3):333–382, March 2000.

[129] L. Sagués. *Surface and Volumetric Scattering Analysis of Terrains for Polarimetric and Interferometric SAR Applications*. PhD thesis, Universitat Politècnica de Catalunya, Spain, 2000.

[130] L. Sagués, J. M. Lopez-Sanchez, J. Fortuny, X. Fabregas, A. Broquetas, and A. J. Sieber. Indoor experiments on polarimetric SAR interferometry. *IEEE Transactions on Geoscience and Remote Sensing*, 38:671 – 684, March 2000.

[131] M. Santoro. *Estimation of Biophysical Parameters in Boreal Forests from ERS and JERS SAR Interferometry*. PhD thesis, Friedrich-Schiller-University Jena, 2003.

[132] S. Sauer. *Télédétection SAR interférométrique de zones urbaines en bande L à partir de l'utilisation des techniques d'analyse spectrale polarimétrques et multi-bases*. PhD thesis, Université de Rennes 1, France, 2008.

[133] J. Schou and H. Skriver. Restoration of Polarimetric SAR Images Using Simulated Annealing. *IEEE Transactions on Geoscience and Remote Sensing*, 39(9):2005–2016, September 2001.

[134] D. L. Schuler, J. S. Lee, and G. De Grandi. Measurement of Topography Using Polarimetric SAR Images. *IEEE Transactions on Geoscience and Remote Sensing*, 34(5):1266–1277, September 1996.

[135] D. L. Schuler, J. S. Lee, D. Kasilingam, and G. Nesti. Surface Roughness and Slope Measurements Using Polarimetric SAR Data. *IEEE Transactions on Geoscience and Remote Sensing*, 40(3):687–698, March 2002.

[136] P. R. Siqueira. *Wave propagation and scattering in dense random media*. PhD thesis, The University of Michigan, 1996.

[137] M. I. Skolnik. *Introduction to Radar Systems*. McGraw–Hill Book Company, 1962.

[138] R. Snieder. The role of nonlinearity in inverse problems. *Inverse Problems*, 14:387–404, 1998.

[139] R. Snieder and J. Trampert. *Wavefield Inversion*, chapter Inverse problems in geophysics, pages 119–190. Springer Verlag, New York, 1999.

[140] J. C. Souyris, P. Imbo, R. Fjortoft, S. Mingot, and J. S. Lee. Compact Polarimetry Based on Symmetry Properties of Geophysical Media: The $\pi/4$ Mode. *IEEE Transactions on Geoscience and Remote Sensing*, 43(3):634–646, March 2005.

[141] O. Stebler. *Analyse der komplexen Kohaerenz flugzeug- und satellitengestuetzter InSAR-Systeme als Funktion konventioneller und interferometrisch optimierter Polarisationszustaende*. PhD thesis, University of Zurich, 2004.

[142] M. Tabb, T. Flynn, and R. Carande. Estimation and Removal of SNR and Scattering Degeneracy Effects from the PolInSAR Coherence Region. In *Proceedings of the International Geoscience Remote Senssing Symposium (IGARSS)*, pages 1651 – 1653, Toulouse, France, July 2003.

[143] M. Tabb, J. Orrey, T. Flynn, and R. Carande. Phase diversity: a decomposition for vegetation parameter estimation using polarimetric SAR interferometry. In *Proceedings of the European Conference no Synthetic Aperture Radar (EUSAR)*, pages 721–724, Cologne, Germany, June 2002.

[144] A. Tarantola. *Inverse problem theory and methods for model parameter estimation*. SIAM, 2005.

[145] S. Tebaldini and F. Rocca. SAR Tomography over Decorrelating Targets for Forestry Applications. In *Proceedings of the European Conference no Synthetic Aperture Radar (EUSAR)*, Friedrichshafen, Germany, June 2008.

[146] L. Thirion. *Modélasation de l'interaction cohérente des ondes électromagnéticques avec des couverts forestiers*. PhD thesis, Université Paul Sabatier, Toulouse III, France, October 2003.

[147] K. Tomiyasu. Remote Sensing of the Earth by Microwaves. *Proc. IEEE*, 62(1):86–92, January 1974.

[148] K. Tomiyasu. Tutorial review of synthetic-aperture radar (sar) with applications to imaging of the ocean surface. *Proc. IEEE*, 66(5):563–583, May 1978.

[149] R. Touzi and F. Charbonneau. Characterization of Target Symmetric Scattering Using Polarimetric SARs. *IEEE Transactions on Geoscience and Remote Sensing*, 40(11):2507–2516, November 2002.

[150] R. Touzi and A. Lopes. Statistics of the Stokes parameters and of the complex coherence parameters in one-look and multi-look speckle fields. *IEEE Transactions on Geoscience and Remote Sensing*, 34(2):519–531, March 1996.

[151] R. Touzi, A. Lopes, J. Bruniquel, and P. W. Vachon. Coherence Estimation for SAR Imagery. *IEEE Transactions on Geoscience and Remote Sensing*, 37(1):135–149, January 1999.

[152] R. N. Treuhaft and S. R. Cloude. The Structure of Oriented Vegetation from Polarimetric Interferometry. *IEEE Transactions on Geoscience and Remote Sensing*, 37(5):2620–2624, September 1999.

[153] R. N. Treuhaft, S. N. Madsen, M. Moghaddam, and J. J. van Zyl. Vegetation characteristics and underlying topography from interferometric radar. *Radio Sci.*, 31(6):1449–1485, November 1996.

[154] R. N. Treuhaft and P. R. Siqueira. Vertical structure of vegetated land surfaces from interferometric and polarimetric radar. *Radio Sci.*, 35(1):141–178, January 2000.

[155] L. Tsang, J. A. Kong, and K. H. Ding. *Scattering of Electromagnetic Waves: Theories and Applications*, volume 1. John Wiley & Sons, New York, 2000.

[156] L. Tsang, J. A. Kong, K.H. Ding, and C. O. Ao. *Scattering of Electromagnetic Waves: Numerical Simulations*, volume 2. John Wiley & Sons, New York, 2001.

[157] L. Tsang, J. A. Kong, and R. T. Shin. *Theory of Microwave Remote Sensing*. Wiley, New York, 1985.

[158] F. T. Ulaby and C. Elachi. *Radar Polarimetry for Geoscience Applications*. Artech House, Noorwood (MA), USA, 1990.

[159] F. T. Ulaby, R. K. Moore, and A. K. Fung. *Microwave remote sensing: active and passive*, volume 1. Artech House, Boston, London, 1981.

[160] F. T. Ulaby, R. K. Moore, and A. K. Fung. *Microwave remote sensing: active and passive*, volume 2. Artech House, Boston, London, 1982.

[161] F. T. Ulaby, R. K. Moore, and A. K. Fung. *Microwave remote sensing: active and passive*, volume 1–3. Artech House, Boston, London, 1986.

[162] H. C. van de Hulst. *Light Scattering by Small Particles*. Dover, 1981.

[163] J. J. van Zyl, H. A. Zebker, and C. Elachi. Imaging radar polarization signatures: Theory and observation. *Radio Sci.*, 22:529–543, 1987.

[164] G. Vasile, E. Trouve, M. Ciuc, P. Bolon, and V. Buzuloiu. Improving coherence estimation for high-resolution polarimetric SAR interferometry. In *Proceedings of the International Geoscience Remote Senssing Symposium (IGARSS)*, pages 1796–1799, Anchorage, USA, September 2004.

[165] G. A. Watson. Computing the numerical radius. *Linear Alg. Its Appl.*, 234:163–172, February 1996.

[166] M. L. Williams. *PolSARproSim: A Coherent, Polarimetric SAR Simulation of Forests for PolSARPro*, December 2006.

[167] P. A. Wright, S. Quegan, N. S. Wheadon, and C. D. Hall. Faraday Rotation Effects on L-Band Spaceborne SAR Data. *IEEE Transactions on Geoscience and Remote Sensing*, 41(12):2735–2744, December 2003.

[168] H. Yamada, Y. Yamaguchi, Y. Kim, E. Rodriguez, and W. M. Boerner. Polarimetric SAR Interferometry for Forest analysis based on the ESPRIT algorithm. *IEICE Trans. Electron.*, E84-C(12):1917–1924, December 2001.

[169] Y. Yamaguchi, T. Moriyama, M. Ishido, and H. Yamada. Four–Component Scattering Model for Polarimetric SAR Image Decomposition. *IEEE Transactions on Geoscience and Remote Sensing*, 43(8):1699–1706, August 2005.

[170] Y. Yamaguchi, Y. Yajima, and H. Yamada. A Four–Component Decomposition of POLSAR Images Based on the Coherency Matrix. *IEEE Geosci. Remote Sensing Lett.*, 3(3):292–296, July 2006.

[171] H. A. Zebker and J. Villasenor. Decorrelation in interferometric radar echoes. *IEEE Transactions on Geoscience and Remote Sensing*, 30:950 – 959, September 1992.

Résumé

Ce travail concerne différent thèmes qui ont pour objectif d'améliorer la compréhension de l'Interférométrie Polarimétrique Radar (Pol-InSAR) ainsi que de proposer de nouvelles techniques permettant la reconstruction de paramètres liés à la végétation, dans le cadre d'applications de Télédétection. Des études théoriques sont menées afin de définir rigoureusement et d'analyser l'ensemble de cohérences Pol-InSAR ainsi que de développer et d'interpréter les techniques d'optimisation de cohérences à lignes de base multiples. Un modèle interférométrique polarimétrique phénoménologique est développé pour tenir compte d'un milieu volumique situé au dessus d'un sol. Dans le cas de forêts observées en bande L, ce modèle tient compte de la topographie du sol, de la canopée, de la hauteur totale des arbres, de l'atténuation de l'onde, de la réflectivité au sein de la canopée, de la morphologie des arbres prise en compte par la distribution statistique des orientations des branches et leur forme efficace, de la contribution du sol et enfin de l'interaction entre le sol et les troncs. Une méthodologie d'inversion des paramètres de végétation est développée dans le cas des acquisitions monopasse ou multipasses. Dans ce dernier cas, la méthode d'inversion tient compte de la décorrélation temporelle et permet ainsi une estimation pour chaque ligne de base. La performance de l'estimation des paramètres de végétation est évaluée à partir de données SAR simulées et réelles aéroportées en bande L, pour les deux cas de configurations en lignes de base simple ou multiple.

Mots-clés: Télédétection, radar à ouverture synthétique, polarimétrie radar, interférométrie, estimation de paramètres de végétation.

Abstract

This dissertation concerns different topics with the aim to improve the understanding of polarimetric SAR interferometry (PolInSAR) and to provide techniques for vegetation parameter retrieval for remote sensing applications. Theoretical studies are conducted to rigorously define and analyze the PolInSAR coherence set, and to develop and interpret multi–baseline coherence optimization techniques. A phenomenological polarimetric interferometric model, designed for geophysical parameter retrieval, is derived for volumetric media over ground. For forest vegetation observed at L–band, this model accounts for the ground topography, canopy layer and total tree heights, wave attenuation and refractivity in the canopy, tree morphology in the form of the orientation distribution and effective shapes of the branches, surface scattering contribution, and double–bounce ground–trunk interactions. A parameter retrieval framework is developed for single– and repeat–pass acquisitions which is, in the latter case, robust against the temporal decorrelation and permits its estimation in every baseline. The parameter estimation performance is evaluated on simulated and real airborne L–band SAR data in both single– and multi–baseline configurations.

Keywords: Remote sensing, synthetic aperture radar (SAR), radar polarimetry, SAR interferometry, vegetation parameter estimation.